CRANFIELD INSTITUTE OF TECHNOLOGY

SCHOOL OF INDUSTRIAL SCIENCE

PhD THESIS

Academic Year 1983 - 85

PETER G. MILLAR

Corrosion Fatigue Crack Propagation Behaviour of a High Strength Low Alloy Steel in a Synthetic Sea Water Environment

Supervisor: B.S. Hockenhull

December 1986

ABSTRACT

The corrosion fatigue crack propagation behaviour of a high strength low alloy steel, N-A-XTRA 70, in a synthetic sea water solution was tested using S.E.N. specimens subjected to a loading frequency of 0.1 Hz and a load ratio of 0.6. In order to simulate the conditions encountered by a thumb-nail type crack several specimens from each of the microstructural types tested, namely parent plate, heat affected zone and heat treated material, had their crack sides covered by transparent plastic covers. Severe over-protection and slight underprotection conditions were produced using cathodic protection potentials of -1400, -1300, -1200 and -700 mV (S.C.E.).

The Paris relationship $da/dN = C\Delta K^m$ was found to be a useful tool in describing the crack propagation rate data. Results obtained, presented in the form of plots of log da/dN against log ΔK, show that for parent plate, H.A.Z. and heat treated material, covering the crack sides of specimens produces enhanced corrosion fatigue crack propagation rates, at cathodic protection potentials of -1400 and -1300 mV (S.C.E.), when compared to non covered specimens. This trend was also true for H.A.Z. specimens at a potential of -700 mV (S.C.E.). For parent plate specimens, however, covering the crack sides at a potential of -700 mV (S.C.E.) produced reduced crack propagation rates over non covered specimens. It is believed restriced oxygen access may account for these results.

Plots of the Paris exponent m and constant C for the three microstructures tested produced three lines of the form $m = a\ln C + b$ where a and b were found to be dependent upon material parameters.

Comparison of results with BS 4360:50D revealed that N-A-XTRA 70 exhibited superior fatigue performance when tested in air but behaved worse under conditions of free corrosion.

LIST OF CONTENTS

ACKNOWLEDGEMENTS

I would like to express my gratitude to Mr. B.S. Hockenhull, my supervisor, for his help, advice and guidance throughout my studies at Cranfield. This involved leaving me to my own devices when I needed to be left alone and 'kicking my butt' when it needed kicking. Thanks Brian!

I would also like to thank Terry Clifton, Dick Hardwicke, Andrew Baldwin, Ken Nelson, Ray Smith, and the staff of the workshop, for preparing specimens and fixing the testing equipment 'mucho pronto'.

I am indebted to Peter Cook and Colin Matthews for their help with the electron microscope and photographic equipment and also for general help above and beyond the call of duty.

David Callister deserves thanks for many hours of useful argument, discussion and awful cups of tea.

Lastly, but not least, special credit goes to Liz, my wife, for typing this thesis, financially supporting me, and having the belief in me that the good guys make it big in the end!

The Universe and it's inhabitants are governed by certain laws, and so is scientific research. The more notable of these laws include:

Finagle's Laws

1. Do not believe in miracles - rely on them.
2. Experiments must be reproducible - they should fail the same way.
3. Always verify your witchcraft.
4. First draw your curves - then plot your readings.
5. A record of data is useful - it indicates that you've been working.
6. Experience is directly proportional to equipment ruined.
7. To study a subject best - understand it thoroughly before you start.
8. In case of doubt - make it sound convincing.

Murphy's Laws

1. If anything can go wrong, it will.
2. Nothing is ever as simple as it seems.
3. Everything takes longer than you expect.
4. If everything seems to be going well, you have obviously overlooked something.

Gordon's Law

If a research project is not worth doing at all, it is not worth doing well.

NASA's Law

Research is reading two books that have never been read in order to write a third that will never be read.

Cole's Law

Thinly shredded cabbage.

To these must be added Millar's Laws of Corrosion Fatigue:

1. One has to be clever enough to understand what is going on in corrosion fatigue but stupid enough to get involved with it.
2. No matter what time of day a corrosion fatigue experiment starts, it always ends at 5.30 in the morning.

LIST OF FIGURES

LIST OF TABLES

NOTATION

a	Crack length
N	Number of fatigue cycles
K	Stress intensity factor
ΔK	Stress intensity range
K_c	Critical stress intensity factor
K_{1c}	Critical stress intensity for Mode 1 opening
K_{1scc}	Threshold stress intensity level for stress corrosion cracking
ΔK_{th}	Threshold stress intensity range
B	Specimen thickness
w	Specimen width
σy	Yield stress
da/dN	Crack growth rate, per cycle
da/dt	Crack growth rate, per unit time = $1/f.da/dN$
$(da/dN)_c$	Corrosion fatigue crack growth rate
$(da/dN)_{env}$	Environmental crack growth rate
$(da/dN)_r$	Cycle dependent (no environment) crack growth rate
m	Crack propagation parameter
C	Crack propagation parameter
R	Load Ratio
f	Frequency
C.P.D.	Crack Propagation Direction
$\frac{(da/dN)_{env}}{(da/dN)_{air}}$	Crack Propagation Rate (C.P.R.) Enhancement Index

1. INTRODUCTION

In the last decade there has been growing concern about energy shortages. Such shortages would have a major influence on the international economic scene, causing similar problems to those experienced during the energy crises in the early seventies. Moves to seek solutions to these shortages through the development of vast offshore oil reserves, with their immense possibilities, have been greatly intensified on a global scale.

Offshore development projects and technology have advanced hand in hand. Oil and gas exploration and production are now taking place at sites further offshore and in deeper waters year after year. More and more operations are being conducted in severe natural environments, such as the North Sea and inside the Arctic Circle, where the water is very deep, the winds and the waves are extremely violent, and the water temperature is very low. The offshore structures used are tending to increase in size and complexity whilst some platforms have to adopt radically new concepts such as the Conoco tension leg platform which came on stream in late 1984 (figure 1)(Ref 1). Not only is platform size and design breaking new records but the conditions for their use are becoming more severe than ever before.

The steels used in offshore structures do not basically differ from those used in land structures and vessels, however, from the standpoint of construction and use, offshore structures require performances from their constructional materials immensely superior to their onshore counterparts, with the added constraint of needing minimal overall weight in order to generate the necessary excess buoyancy.

In order to satisfy the above criteria, designers and manufacturers have been enticed by the potential benefits of high strength low alloy (H.S.L.A.) steels. These steels are usually achieved by the addition of small amounts of alloying elements followed by a controlled rolling schedule. The major advantages of these steels include enhanced weldability by the use of low carbon contents, increased strength and toughness due to precipitation hardening and controlled rolling techniques, and ultimately a saving in overall weight. If, however, designers and constructors had only to worry about ease of manufacture and weight saving for offshore structures it would indeed be an ideal world. There is one major consideration that cannot be ignored however, and that is environment, or perhaps more importantly it's effects on the service life, safety, and uninterrupted operation of offshore structures.

The oceans are certainly a formidable enemy to offshore structures with a seemingly unabating desire to attack and

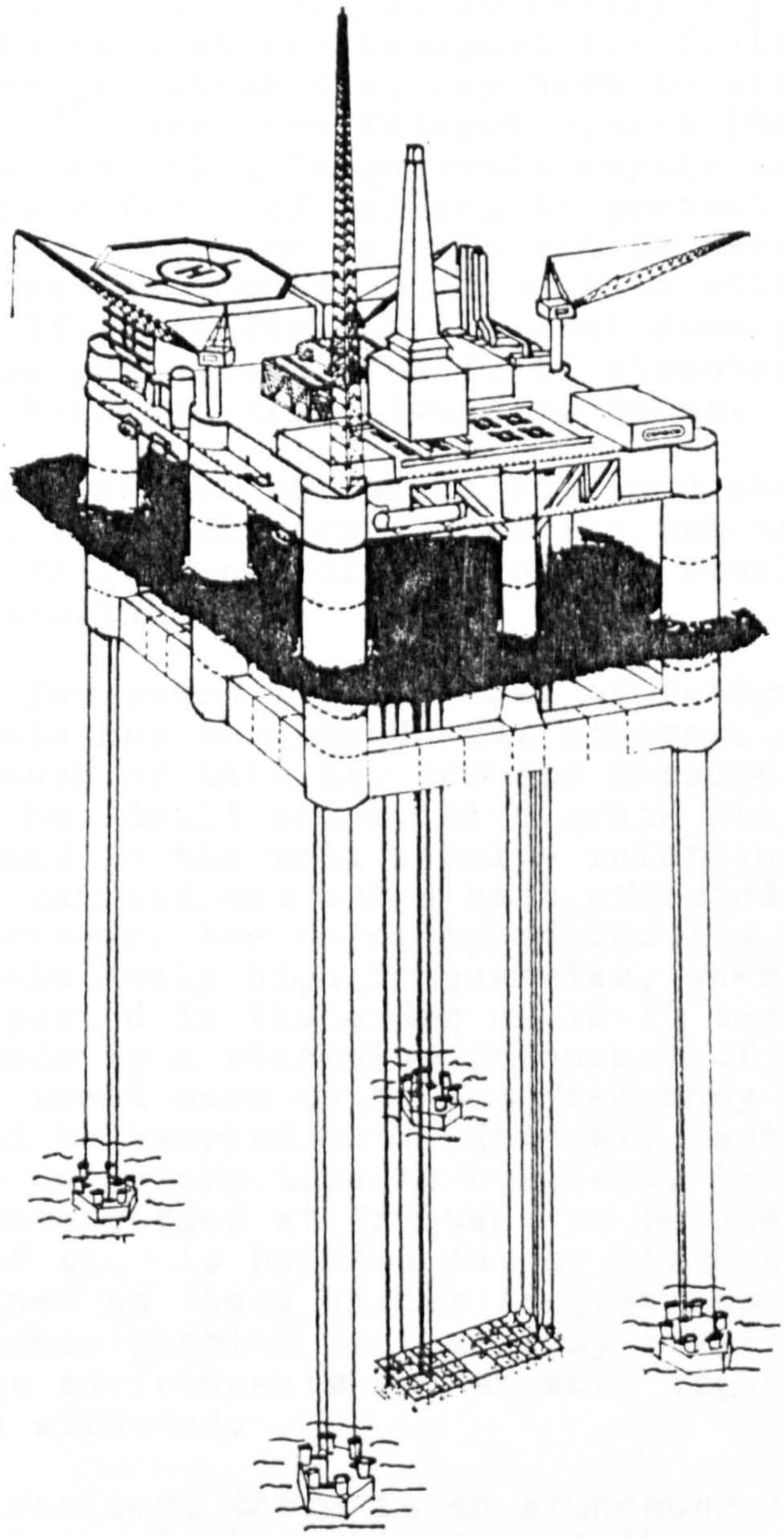

Figure 1. The Conoco tension leg platform (Ref 1)

batter anything placed within their waters. Their most awesome weapon must surely be corrosion fatigue; where the sea is both the corrosive medium and the major source of fatigue loading. This conjoint action generally produces more devastating results than either cyclic stress in air or environmental attack applied separately.

Offshore steel jackets are manufactured using welded tubular constructions with occasional cast nodal joints. They are rife with geometric stress concentrations which are difficult to determine and undoubtedly, in the case

of the welded sections, contain crack-like defects at fatigue critical locations. It is hardly any wonder then that in structures that are designed for finite lives of around 30 years, (in which they may have to withstand approximately 10^9 corrosion fatigue cycles (Ref 2)), that major problems involving large scale repair and maintenance can occur. The effects of failing to prevent or remedy damage caused by corrosion fatigue can be devastating in terms of lost revenue, which may run into millions of dollars a day if a platform has to shut down production, or in the large scale loss of life if disasters such as the Alexander Kjelland are allowed to occur.

In order to prevent the disasters outlined above it is important that research work is carried out to determine the corrosion fatigue performance of the steels to be used in offshore structures.

Over the past few years a great deal of fatigue crack propagation data has been produced. However, it is debatable how relevant much of this is, perhaps because most of the previous work has dealt mainly with crack propagation in parent metal and in the weld metal - relatively little work has been carried out using heat affected zone (H.A.Z.) material. Moreover, the majority of results have been obtained at relatively high frequencies, whereas North Sea waves have a period in the order of 12-15 seconds (Ref 3). This corresponds to a stressing frequency of approximately 0.1 Hz, which would seem to be the frequency at which most research would be carried out. However, tests carried out at 0.1 Hz can take some time to complete, therefore many researchers have worked at frequencies between 300 Hz and 10,000 Hz (Ref 4). As pointed out by Hockenhull (Ref 5), results obtained at these higher frequencies may be misleading. Another problem is that many results are obtained in unrealistic environments and at much higher temperatures than would be expected.

As indicated earlier, there is an abundance of fatigue data for steel in general, but this is not the case for high strength low alloy steels, with again unrealistic frequencies and environments being used. It is hoped that by using a frequency of 0.1 Hz and a synthetic sea water environment in this work that more valid results can be obtained. These may help to show whether the performance in corrosion fatigue of H.S.L.A. steels, in terms of crack propagation rates and fatigue performance in general, is similar to or better than the standard offshore constructional steels, like BS 4360:50D for example. Also it is hoped to ascertain how H.S.L.A. steels compare under conditions of cathodic protection and overprotection.

1.1 Marine corrosion

Exploration of the ocean both by industry and by government has necessitated either the temporary or permanent installation of many types of structures and vessels in marine environments. Carbon steel and the high strength low alloy and alloy steels have been the basic construction materials for these structures and vessels and will continue to be used in the future because of their relative low cost, high strength and good fabricability. However, these materials are being utilised in a very aggressive environment and hence will be subject to some of the worst natural corrosion conditions known. This puts great pressure on the corrosion and design engineers involved in building and maintaining such structures to examine and fully understand where, why and when the steel will corrode and how it can be conserved and protected.

Certain types of high strength low alloy and alloy steels are available that have improved corrosion resistance over that of structural carbon steel in marine atmospheres and in the splash and tidal zones. Under total immersion conditions, however, the low alloy and alloy steels offer no real advantage over carbon steel from a corrosion standpoint.

Before addressing the question of what actually happens to steel when it corrodes, let us first consider the areas of corrosion which must be covered when dealing with offshore structures (Ref 6). These are:

(a) Atmospheric - air, salt spray, rain.

(b) Splash and tidal zones - salt water, salt spray, alternate periods of wet and dry, surface water contaminants such as oil films, marine fouling organisms, wave motion, hurricane and storm damage.

(c) Total immersion zone - water with decreasing levels of oxygen concentration, abrasion from sand and mud, underwater currents, docking of ships and barges.

(d) Mud zone - seawater, sand and muck, anaerobic bacteria.

Because of the differing conditions and mechanisms operating in each of the above sections, the corrosion rate will vary considerably over the whole structure. This can clearly be seen from figure 2 (Ref 7). The rate of corrosion is relatively low (0.1-0.3 mm/yr) for the parts of the structure immersed in the sea bed, the rate increasing around the mud line. This increase is due to

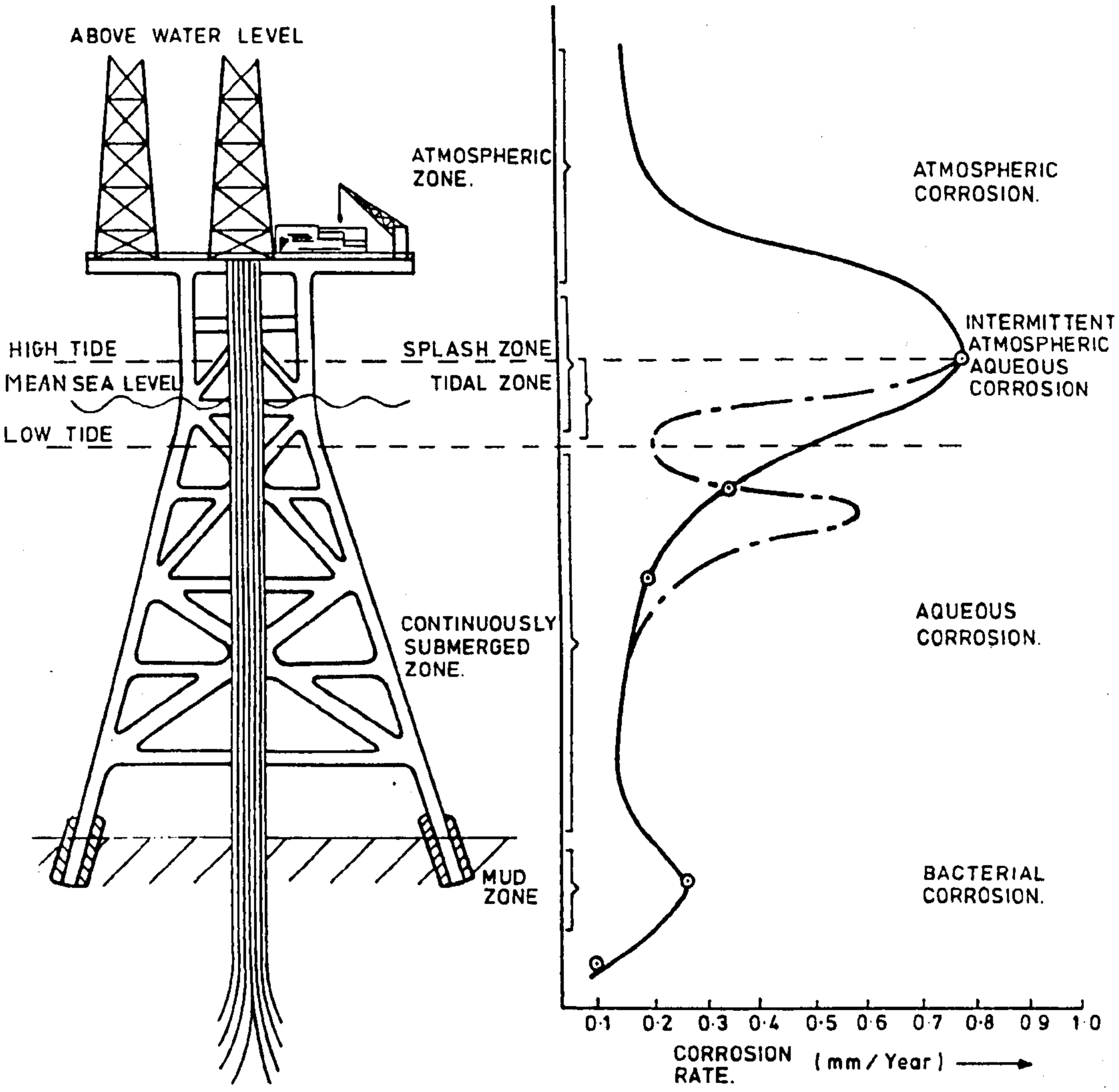

Figure 2. Diagram showing changes in environmental conditions which affect corrosion (Ref 7)

differential oxygen concentration, the activity of bacteria and the scouring action of sand. The total immersion zone has a higher, fairly uniform corrosion rate compared with the buried section, but again differential oxygen concentration causes increased corrosion activity just below the water line.

In the region where the structure is being alternately wetted and dried between high and low tide, a loosely bonded corrosion product is formed in which sea water, with a high oxygen concentration, is retained. This can cause the corrosion rate to climb to as high as four times the rate for any other section. Finally, in the atmospheric region, attack aided by salt deposits can give a high corrosion rate on parts of the structure clear of the high tide but subject to spray. An overall picture of corrosion in the marine environment can be seen in table 1 (Ref 8).

General Behaviour	Corrosion Rate
General subsea corrosion	0.1 - 0.2 mm/yr
Atmospheric zone corrosion	0.05- 0.5 mm/yr
Splash zone	1 mm/yr
Special Problems	
Splash zone risers (100°C)	5 mm/yr
Localised corrosion at welds	4 mm/yr
Ekofisk riser	7 mm/yr

Table 1. Corrosion in the marine environment (Ref 8)

1.1.1 Corrosion of steel in sea water

All common metals are thermodynamically unstable in their refined forms, a forced rather than a natural state, therefore they tend to revert to their natural stable state through the process we call corrosion. There are many textbook definitions of corrosion but it can quite succinctly be put as - 'the alteration of a metal originating at the surface and caused by chemical or electrochemical attack'.

The processes of corrosion take place in the boundary layer of a metal. They are highly complex and depend on many factors. The process begins with the loss of metal ions from the lattice, preferentially at points which possess a higher internal stress condition on account of surface inhomogeneity. A particular feature of these points are the excess electrons left behind, which flow away to surface regions where an electron consuming reaction is taking place. Two different electrode processes thus take place simultaneously in the corrosion of a metal.

From an electrochemist's point of view, corrosion is seen as an electrochemical cell, working at microscopic sites on a piece of metal, passing current (electrons) in a series of oxidation-reduction reactions. The cell works

along the lines of a minute battery with an anode and cathode in a sea water electrolyte. At the anode there is an oxidation reaction involving the loss of electrons and resulting in the steel dissolving into the electrolyte in the form of iron cations.

$$Fe \rightarrow Fe^{++} + 2e^{-} \qquad - (1)$$

At the cathode a reduction reaction occurs which involves some constituent of the electrolyte, thus absorbing the electrons freed at the anode. The flux of electrons (current) flowing between the cathode and the anode is a measure of the corrosion rate of the system.

The two main cathodic reactions of particular importance to marine corrosion are:

(a) The production of hydroxyl ions by the reduction of dissolved oxygen. This occurs in near neutral solutions such as sea water.

$$4e^{-} + O_2 + 2H_2O \rightarrow 4(OH)^{-} \qquad - (2)$$

(b) The production of hydrogen by the reduction of hydrogen ions. This occurs in acidic solutions in the absence of oxygen.

$$2H^{+} + 2e^{-} \rightarrow H_2\uparrow \qquad - (3)$$

In the situation of sea water corrosion the oxygen reduction cathodic reaction is the most important and will clearly depend on the availability of dissolved oxygen, which will vary with depth in the case of sea water. However, in the case of an offshore structure, where pitting and crevice corrosion may be a problem, the hydrogen ion reduction cathodic reaction will be important because it is possible for the environment deep within a crack or crevice to become acidic.

In aerated acid solutions it is possible that both cathodic reactions may act in parallel (competitive reactions). Alternatively, a combined reaction involving both the H^{+} and O_2 species has been postulated to occur in such solutions (Ref 9).

$$4e^{-} + 4H^{+} + O_2 \rightarrow 2H_2O \qquad - (4)$$

The combination of the anodic and cathodic reactions given above produces the overall corrosion reaction in sea water:

$$2Fe + \underset{\text{dissolved}}{O_2} + 2H_2O \rightarrow 2Fe^{++} + 4(OH)^{-}$$

$$\rightarrow \underset{\text{ferrous hydroxide}}{2Fe(OH)_2}$$

$$\rightarrow Fe_2O_3.H_2O + H_2O \qquad - (5)$$

hydrated ferric oxide (rust)

Usually ferrous hydroxide is the first corrosion product to appear on the metal surface, generally somewhere between the anode and the cathode (figure 3). It is a greenish colour which deepens to a darker brown as it is oxidised to form ferric oxide.

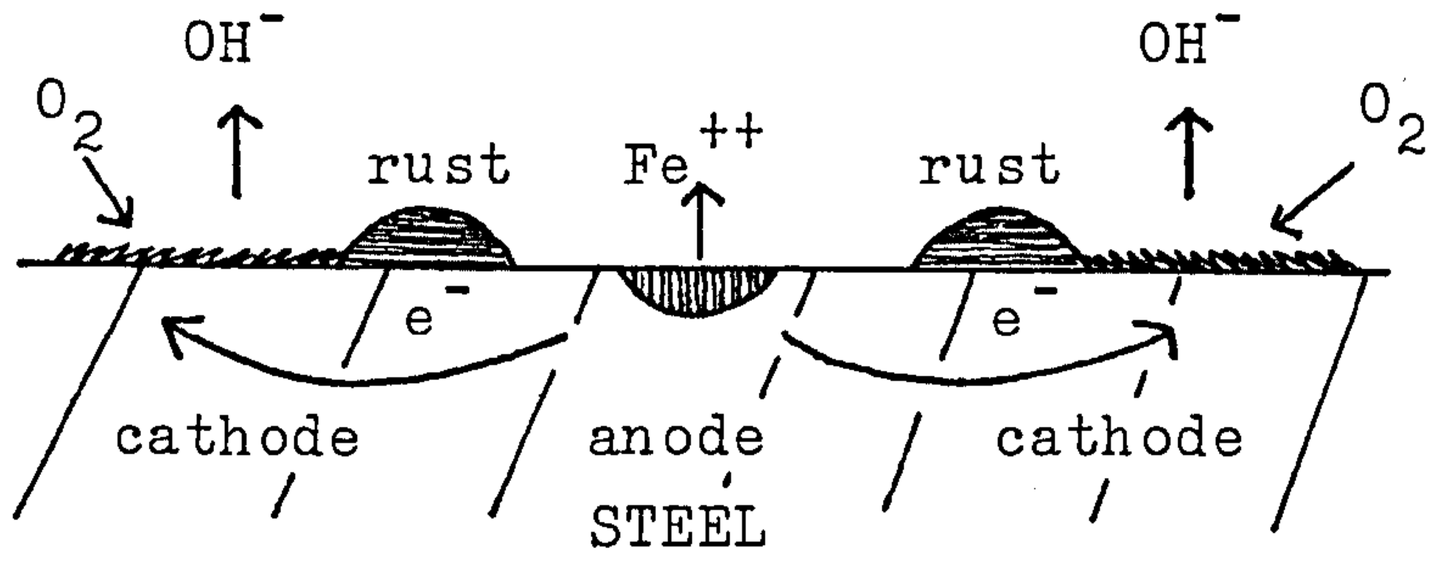

Figure 3. Corrosion cell

The size and distribution of the local electrochemical cells on a metal surface can vary considerably. If the local cathodes and anodes are very small and distributed absolutely uniformly over the surface, corrosion will be uniform and homogeneous. If, however, the cathode is the greater part of the metal surface and there is only a small anodic area, the result is non-uniform, heterogeneous, localised corrosion. This can be explained in simple terms using the 'area rule': Because a corrosion system is electrically neutral externally, the total current (product of current density (J) and surface area (A)) must be equal at the anode and cathode, i.e.

$$(J)\text{anode} \times (A)\text{anode} = (J)\text{cathode} \times (A)\text{cathode} \quad - (6)$$

If (A)anode is very small compared to (A)cathode, then (J)anode must be very large compared to (J)cathode in order to maintain equilibrium. In this way relatively small total corrosion is then concentrated at a few small points, leading to severe local attack (pitting).

One interesting aspect of anode/cathode interaction in an offshore situation has been developed by research at Cranfield (Ref 21). An investigation of BS 4360:50D weldments in sea water using an accelerated corrosion testing technique revealed that the weld corrosion morphology is dependent on the level of heat input. Figure 4 (Ref 22) shows a graphic representation of how different parts of the weld area (parent plate, H.A.Z., weld metal) preferentially corrode depending on the heat energy input used during welding.

The general trend in the results seems to indicate that increasing the weld heat input renders the H.A.Z. more susceptible to anodic dissolution. Considering that corrosion fatigue crack propagation is widely believed to preferentially take place in the H.A.Z., then this finding

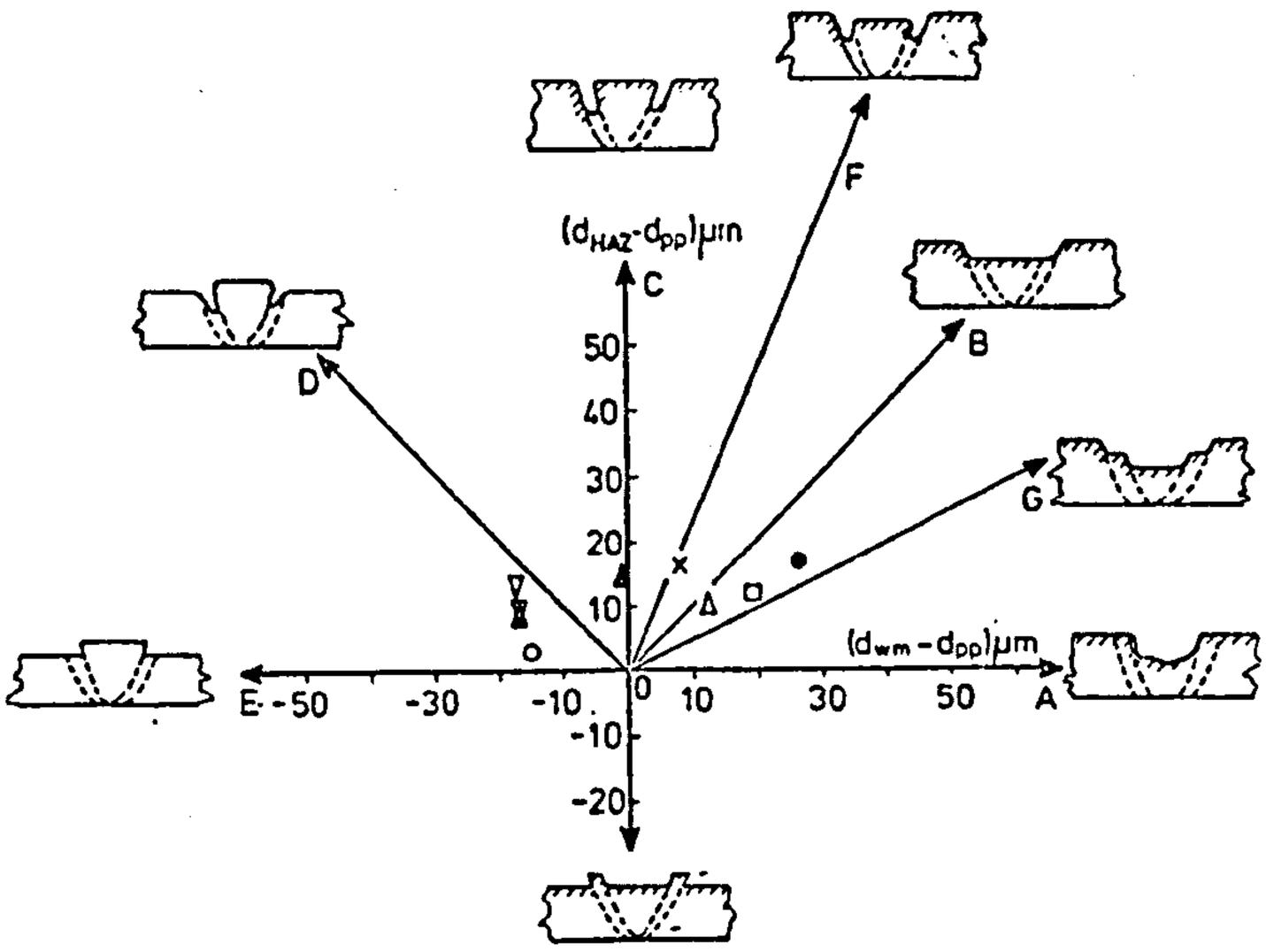

WELD METHOD		HEAT INPUT	
M.M.A.	● M1	1KJ. mm^{-1}	
	□ M3	3KJ. mm^{-1}	
FLUX CORED	Δ F2	2KJ. mm^{-1}	
	o F4	4KJ. mm^{-1}	
	▥ F2 Ni	2KJ. mm^{-1}	HIGH Ni
	x F4(H)	4KJ. mm^{-1}	HEAT TREATED
SUBMERGED ARC	▲ S5	5KJ. mm^{-1}	
	▽ S6	6KJ. mm^{-1}	

Figure 4. Weld corrosion morphology diagram (Ref 22)

proves worrying if it confirms that preferential corrosion and pitting (and hence crack initiation sites) can occur depending on the welding procedure used in construction. However, in order to put the work into perspective, it must be remembered that the actual maximum depth of material loss was 10 microns, which may be considered insignificant in relation to full size structures. Also, the accelerated corrosion technique used may not fully represent actual offshore conditions.

Microstructural features of a steel can have a marked effect on it's corrosion performance. More specifically, manganese sulphide inclusions can be blamed for pitting attack, which for submarine pipelines can result in loss of fluid. The obvious answer to this problem is to use cleaner steels. The H.S.L.A. steel used in this project is one of these cleaner steels in which a sulphur content of 0.004% results in very few manganese sulphide inclusions.

Work carried out by Coburn (Ref 23) has shown that minor additions of elements such as chromium, nickel, molybdenum, and copper to simple ferrite pearlite steels gives only very minor gains in sea water corrosion performance. The presence of several percent nickel and/or chromium is

needed to provide a beneficial effect, but this would incur heavy cost penalties. Other microstructural features such as variations in grain size, the presence of martensite, or changes in the cementite particle size and distribution have been reported to have very little effect on the corrosion behaviour (Ref 24). It is these microstructural features, produced by controlled rolling or quenching and tempering techniques, which account for the strength characteristics of H.S.L.A. steels, rather than the alloying elements.

1.1.2 Factors affecting marine corrosion

Seawater is not just an electrolyte but a complex solution, so there are a number of factors associated with it which can have a profound effect on the corrosion of metals immersed in it. These are:-

(a) Temperature - From a purely kinetic point of view a rise in temperature would be expected, as with other chemical processes, to result in an increase in the corrosion rate. This, however, does not always occur. For example, steel specimens immersed in tropical waters do not necessarily corrode at a greater rate than those in temperate climates. This situation may arise from factors other than temperature, e.g. by difference in oxygen content and fewer marine growths in colder waters.

(b) Depth - The data outlining the effect of depth on corrosion of steel is somewhat limited. As a general rule the rate tends to decrease with increasing depth, although there are many exceptions to this. It is known that oxygen varies with increasing depth, tending to drop at 1000 - 2000 metres and then rise again and that temperature decreases with increasing depth. However, other factors such as pressure and mechanical effects may well be important.

(c) Flow rate - The corrosion of steels in seawater is a function of the availability of dissolved oxygen at the metal - water interface. Therefore, as might be expected, increasing flow rate raises the corrosion rate because it increases the amount of oxygen diffusing to the steel surface. This is quite clearly seen in figure 5 (Ref 10), where the rate seems to level out at around 0.9 mm/yr at about 7.0 m/sec velocity.

Another important factor is that differences in oxygen concentration at different parts of the steel surface can lead to localised corrosion. For example, if there are small areas where the soluble oxygen is deterred from reaching the metal as a result of slow diffusion through rust, and large areas exist where the oxygen remains in ready contact with the steel, pitting will result at the areas where there is a deficiency of oxygen.

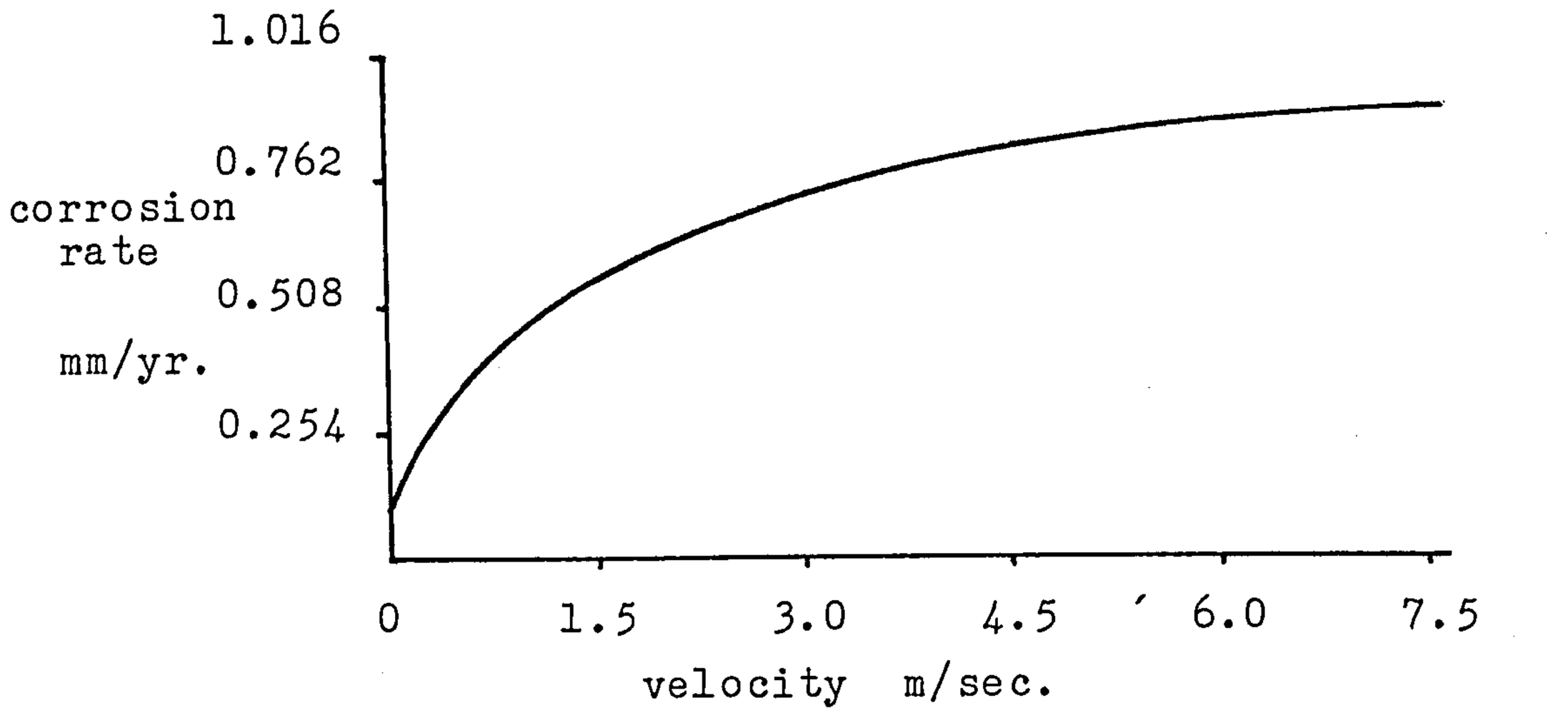

Figure 5. Effect of velocity on corrosion of steel by sea water at atmospheric temperature (Ref 10)

What must be remembered is that in an offshore situation marine growth may decrease the effect of velocity by isolating the metal from the water, or may increase the corrosion by setting up areas of higher velocity with local turbulence.

1.1.3 The galvanic series

Due to the limitations of the e.m.f. series for predicting galvanic reactions, and as alloys are not included (conditions affecting equilibrium of solid alloys and their environment are not well understood), the so called galvanic series has been suggested. This series is an arrangement of metals and alloys in accordance to their actual measured potentials in a given environment. The potentials which determine the position of a metal in this series may include steady state values in addition to truly reversible values and hence alloys and passive metals are included. The galvanic series for metals in contact with sea water is given in table 2 (Ref 11).

The galvanic series provides a good general indication of the likely intensity of corrosion, which is governed by the distance between the alloys in the series. The relative positions of alloys in the series can be influenced by several factors which include temperature, velocity and aeration.

The flow rate of the solution also affects the behaviour of a galvanic cell. In part this arises from the increased oxygen reaching the alloy surface at higher flow rates.

Active (Read down)	
Magnesium	18-8 stainless steel, type 304 (active)
Magnesium alloys	18-8, 3% Mo stainless steel, type 316 (active)
Zinc	Lead
	Tin
Aluminum 5052H	Muntz metal
Aluminum 3004	Manganese bronze
Aluminum 3003	Naval brass
Aluminum 1100	
Aluminum 6053T	Nickel (active)
Alclad	76% Ni-16% Cr-7% Fe (Inconel 600) (active)
	Yellow brass
Cadmium	Aluminum bronze
	Red brass
Aluminum 2017T	Copper
	Silicon bronze
Aluminum 2024T	5% Zn-20% Ni, Bal. Cu (Ambrac)
	70% Cu-30% Ni
Mild steel	88% Cu-2% Zn-10% Sn (composition G-bronze)
Wrought iron	88% Cu-3% Zn-6.5% Sn-1.5% Pb (comp. M-bronze)
Cast iron	Nickel (passive)
Ni-Resist	76% Ni-16% Cr-7% Fe (Inconel 600) (passive)
13% Chromium stainless steel, type 410 (active)	70% Ni-30% Cu (Monel)
	Titanium
	18-8 stainless steel, type 304 (passive)
50-50 lead-tin solder	18-8, 3% Mo stainless steel, type 316 (passive)
	Noble (Read up)

Table 2. Galvanic series in sea water (Ref 11)

This in turn influences oxide films, which tend to become more protective, leading to passivity in the couple. On the other hand, the velocity may be such (particularly if abrasives are present in the water) as to disrupt the protective films and cause a change in the potential of the alloy. Under erosion-corrosion conditions, where passive films are removed from alloys such as stainless steel, galvanic effects may be quite severe.

In an offshore situation, where severe corrosion problems can have potentially disasterous results, great care must be taken to avoid galvanic coupling. This should be quite easy when dissimilar metals are being used. However, work by Schmitt and Phelps (Ref 25) has shown that the corrosion rate of a carbon steel has been significantly increased by coupling with a highly alloyed steel. Even though the solution potentials for the two steels were practically the same, over a long exposure period, when coupled, the higher alloy content resulted in that steel

becoming more noble than the carbon steel. If care is not taken to ensure that weld metal has an alloy content at least equal to that of the base metal, then it is possible that the above situation may arise in welded joints. It is, therefore, important to consider the practical situation when designing or engineering a component or structure for use offshore so that extreme care is exercised in order to prevent unnecessary corrosion problems.

1.2 Corrosion control

Since the corrosion of steel in sea water occurs by electrochemical means, it seems only logical that an electrochemical method should be used in an attempt to slow down and stop it. Cathodic protection is just such a means and can be defined as: "a technique to control corrosion of a metal surface by making that surface the cathode in an electrochemical cell, by means of an impressed direct current or attachment of sacrificial anodes such as magnesium, zinc or aluminium " (Ref 12). The method is far from new - as long ago as 1824, Humphry Davy suggested that the copper sheathing on wooden ships could be prevented from corroding by putting blocks of iron or zinc in contact with the copper at various points on a ship's hull (Ref 13).

Cathodic protection, however, is not the only means of protecting an offshore structure. Since corrosion is basically a reaction between the metal and the sea water environment, simplistic thinking should dictate that the easiest way to stop the metal from corroding is to prevent it reacting with the sea water electrolyte. To this end various coating and cladding systems have been developed. These are shown along with their applications in figure 6 (Ref 14).

Even though coatings are recognised as a very efficient form of protection, there are a number of problems encountered with them. A major problem is damage to coatings due to transportation, handling, installation and during service. Cathodic overprotection, which will be discussed later, can cause disbondment of coatings. Alternatively, water ingress may result from osmosis which can then lead to ionic discharge and subsequent hydrogen formation at the metal-coating interface.

Due to alternate submergence and aeration, the splash zone is the most critical area of protection and it is subject to corrosion/erosion. An early practice of increasing the thickness of steel in members of this zone has been largely discontinued because of the extreme depth of corrosion pitting. Coatings or claddings are now generally used and these include wrought iron, fibreglass, stainless steel, Neoprene, and the most widely used,Monel (an alloy

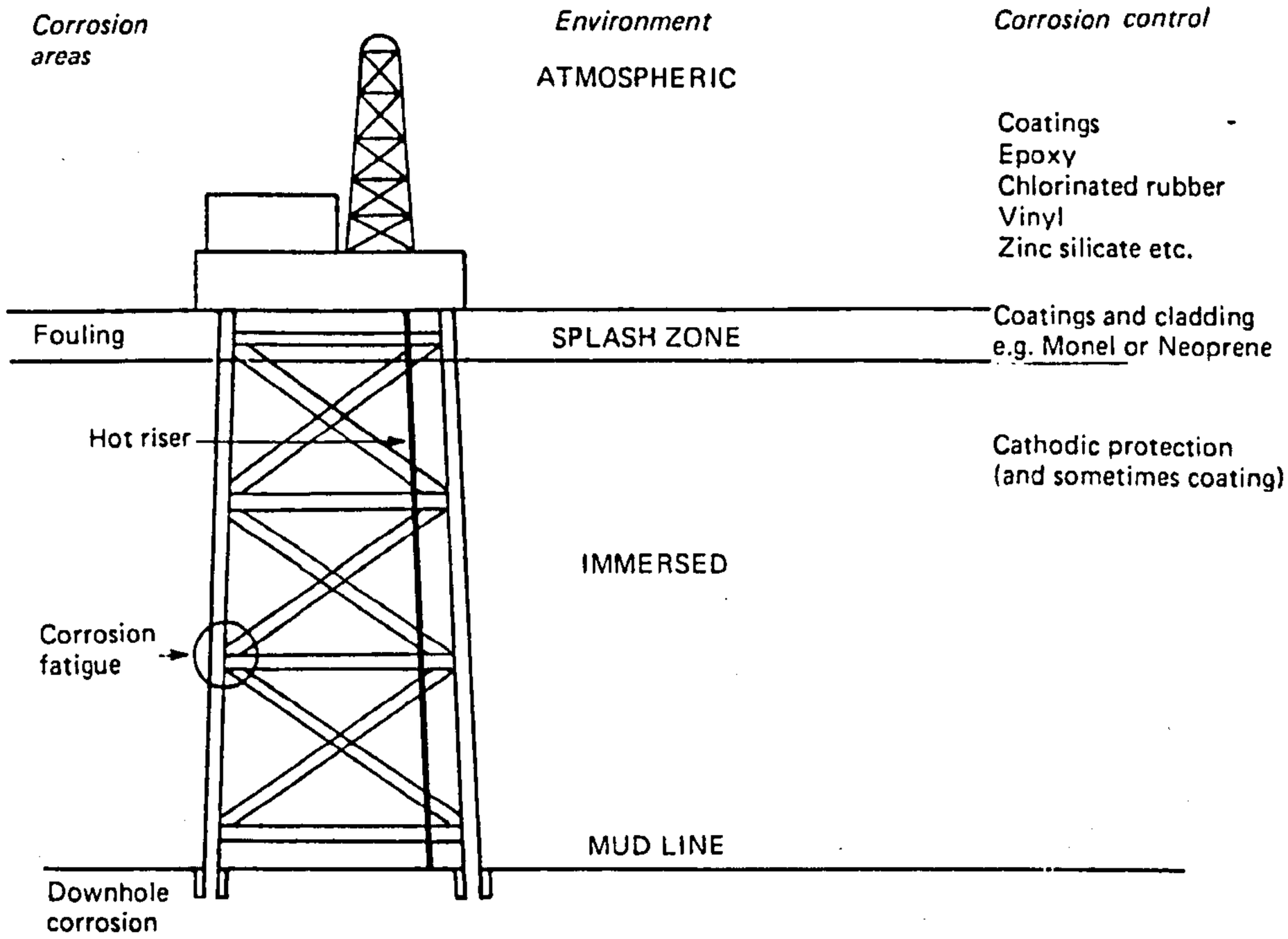

Figure 6. Offshore structure: areas of corrosion and types of control (Ref 14)

of nickel and copper). Monel is usually applied to the riser pipes in the region of the splash zone, where the cathodic protection system is not fully effective, and in these conditions, which are highly erosive (corrosion rates up to 5mm/yr have been encountered (Ref 15)), other coating systems do not perform satisfactorily. In addition to being resistant to corrosion attack, such coatings must withstand mechanical abuse from impact and abrasion by vessels and mooring lines.

Given the two major types of corrosion control, the ideal solution would be a combination of both coatings and cathodic protection. However, many offshore structures rely solely on cathodic protection for the submerged zone, but this should not be the case. For optimum corrosion protection a cathodic system should not be used without prior painting of the structure because, even with the limitations of coatings, they reduce current demands by an order of magnitude or more. Moreover, coated structures are far more tolerant of design shortcomings in the cathodic protection systems.

Even though corrosion protection systems can represent up to ten percent of total platform investment (Ref 16), the large overall investments, the extremely high cost for submarine repairs, and the financial repercussions incurred by shut down and loss of product, dictates a most serious consideration of corrosion control.

1.2.1 Cathodic protection

When iron or steel is corroding in sea water, atoms of iron leave the metal surface as ferrous ions, as shown in equation 7.

$$\text{Anodic reaction:} \quad 2Fe \rightarrow 2Fe^{++} + 4e^{-} \qquad - (7)$$

The electrons remain in the metal making it negatively charged with respect to the sea water. The process of corrosion, therefore, involves a flow of electricity from the metal to the sea at the site of the corrosion, which is called the anode. The current must return to the metal elsewhere, to complete the circuit, and the areas where it does so are called cathodes. If electrons are supplied to the iron from some external source, i.e. a current is imposed, then the anodic reactions will be supressed and the potential of the metal will be lowered. If the potential of the metal is lowered sufficiently, then no current will flow between the anodes and the cathodes on the metal surface, the passage of ferrous ions leaving the surface will be arrested, and corrosion will be reduced. This is called cathodic protection because it involves making the whole of the metal surface a cathode, i.e. a receiver of current.

It is possible to determine when the potential of the corroding structure has been polarised to the open circuit potential of the most active anode point. This potential can be measured against standard reference electrodes; the values for several of these electrodes are given below in table 3 (Ref 17).

Reference Electrode	Protective Potential
Calomel	- 780 mV
Silver - Silver Chloride	- 810 mV
Copper - Copper Sulphate	- 850 mV

Table 3. Protective potentials of steel measured against various reference electrodes in sea water (Ref 17)

Another way of explaining cathodic protection is in terms of the potential/current (Evans) diagram (figure 7). Under freely corroding conditions, i.e. the anodic and cathodic reactions are occurring at the same rate, the potential of the metal will be E_{corr}. The corresponding current I_{corr} (I_W) represents in electrical terms the corrosion rate.

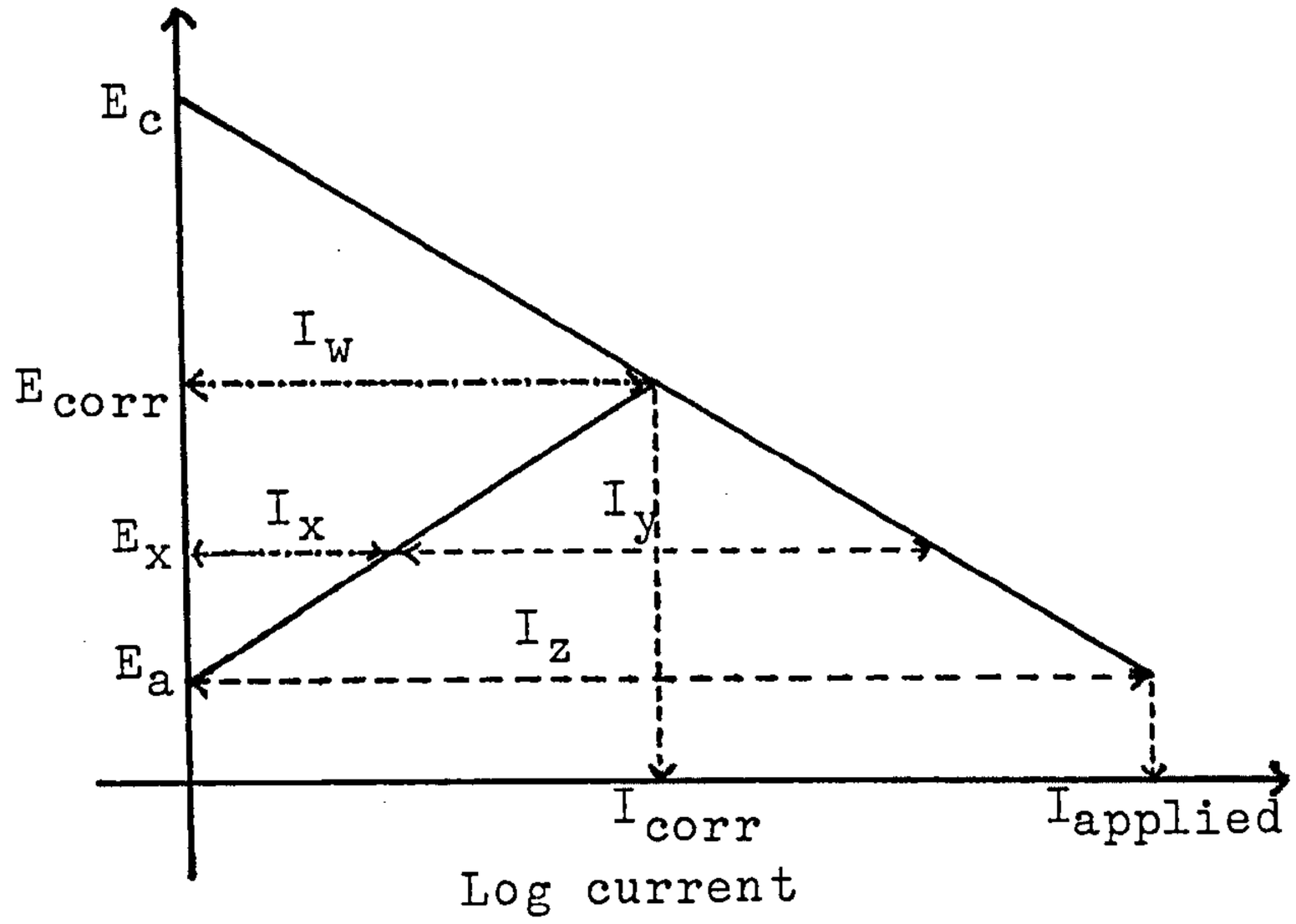

Figure 7. Potential/current (Evans) diagram (Ref 11)

To achieve full protection an externally applied current is employed to depress E_{corr} until it reaches E_a. At this point the whole metal surface will be at the same potential and no corrosion currents will flow. $I_{applied}$ (I_z) is the external current required to supply the additional electrons necessary to lower the potential and give complete cathodic protection.

If the externally applied current is not great enough (I_y), then the overall metal potential will only be depressed to E_x. This will leave a residual corrosion current of (I_x), indicating that the metal is only partially protected. Although some corrosion will occur it will be less than the amount experienced without cathodic protection. Conversely, if excess current is externally applied so that the potential is lowered below E_a, then not only will there be an unnecessary expenditure of current, but other detrimental effects may occur. The applied current causes a cathodic reaction resulting in the reduction of oxygen or the evolution of hydrogen (reactions 8 and 9).

Cathodic reactions

$$O_2 + 2H_2O + 4e^- \rightarrow 4OH^- \quad \text{(neutral pH)} \qquad - (8)$$

$$2H^+ + 2e^- \rightarrow 2H^o \rightarrow H_2 \text{ (gas)} \quad \text{(lower pH)} \qquad - (9)$$

This tends to make the solution alkaline in the vicinity of the protected metal and may cause problems with paint

films that are subject to saponification. In situations where hydrogen is evolved, problems such as blistering and rupture of coatings may occur. Where high strength steels are used, excessive hydrogen may enter the steel and cause hydrogen embrittlement problems.

Speaking electrochemically, cathodic protection involves the supply of electrons to the corroding steel such that no local corrosion currents can occur. This can be achieved in two ways on offshore structures:

(1) By applying a current through an external source, usually a low voltage d.c. supply situated on board, the technique being known as the impressed current system.

(2) By forming a galvanic cell using a block of suitable metal, e.g. magnesium, aluminium or zinc alloys, which is connected electrically to the structure. The use of the aforementioned metals ensures that they will have a more negative potential than the steel structure and electrons will flow freely from these anodes into the steel. This is called the sacrificial anode system because the attached metal is sacrificed to protect the steel structure.

1.2.1.1 Impressed current systems

The basic principle for both impressed current systems and galvanic, sacrificial anode systems is the same in both cases, except that the impressed current system energizes inert or relatively inert anodes by means of an external energy source. A rectifier is customarily used to convert normally available alternating current to direct current. The current is then introduced into the electrolyte by means of anodes specially designed for long life under 'forced' anodic conditions. Many different types and sizes of anodes are available for use in impressed current systems; graphite (specially treated with heated linseed oil), high silicon cast iron, lead-silver alloy, and platinum with titanium, niobium or tantalum as a base metal on a steel former, each having special design, installation and operating characteristics.

The usual installation consists of a transformer/rectifier control unit and a number of anodes (most frequently lead/silver alloy or platinum where physically abusive environmental conditions exist) installed in parallel. Where environmental conditions have wide variations requiring fluctuation in current output, automatically controlled units monitored by a special reference electrode are employed. On most offshore structures, the impressed current anodes are attached to the structure legs (or cross bracing members) in an appropriately dispersed geometric

pattern throughout the underwater area of the structure (see figure 8, Ref 17). The attachment is accomplished by means of non-conducting hardware (usually heavy duty plastic fittings) inasmuch as the anodes and the entire positive half of the circuit must be electrically isolated from the structure.

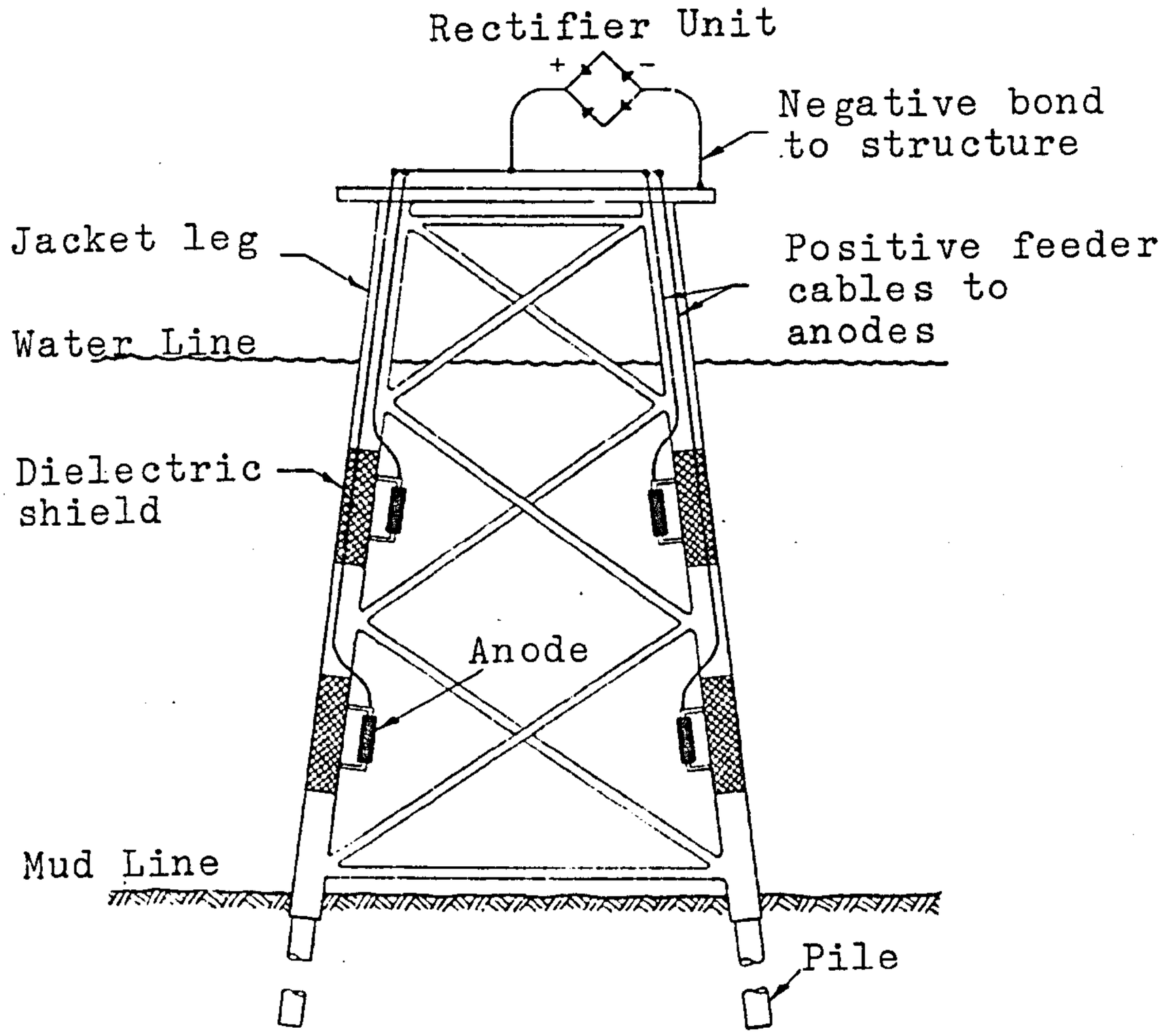

Figure 8. Schematic diagram for an impressed current system (Ref 17)

Sacrificial anode systems produce the required current to protect an offshore structure by means of an electrochemical reaction using a metal less noble than the metal to be protected as the sacrificial anode. For protecting steel, cast iron, or copper, the anode material may be magnesium, zinc or aluminium. The number, size, type and location of the anodes are determined by a detailed study of the structure to be protected and the environmental conditions which the structure will be subjected to.

As a general rule, galvanic anodes are employed when:

(a) current requirements are not excessively high,
(b) alternating current is not available,
(c) water or soil resistivity is relatively low,
(d) cathodic interference problems exist,
(e) the structure will be relatively unattended by operating personnel.

Since this project uses an impressed current system, sacrificial anode systems will not be discussed.

1.2.1.2 Current requirements

One of the most imprecise areas of cathodic protection is the determination or estimation of the current density required to give adequate corrosion protection. Current density requirements are not static; they are dependant on several factors including sea water resistivity, oxygen concentration, temperature, turbulence, flow rates and wave height. As may be expected, the current density requirements increase with the transition from relatively calm summer months to the much more turbulent winter period. Furthermore, an initially uncoated structure will experience it's greatest current density demand during the first few months on station, while polarization films and calcareous deposits are formed on the surface as a result of the discharge of the cathodic protection current. Once formed, these films and deposits will reduce the current demand although damage and dislodgement due to storms may increase the variability of current demand. Geographical location may also cause variations, as shown by table 4 (Ref 19).

LOCATION	CURRENT DENSITY mA/m^2		
	INITIAL	MEAN	FINAL
NORTHERN NORTH SEA	160	120	100
SOUTHERN NORTH SEA	130	100	90
ARABIAN GULF	120	90	80
INDIA	120	90	80
AUSTRALIA	120	90	80
BRAZIL	120	90	80
GULF OF MEXICO	100	80	70
WEST AFRICA	120	90	80
INDONESIA	100	80	70
BURIED PIPELINES	50	40	30
RISERS (in shafts with running sea water)	180	140	120
RISERS (in shafts with stagnant sea water)	120	90	80
SALINE MUD (ambient temperature)	25	20	15

Table 4. Minimum design current densities for protection of fixed offshore steel platforms (Ref 19)

It is possible to calculate the theoretical current density requirements prior to film formation and polarisation using Faraday's laws. 86 mA/m^2 is considered to be the value for steel in sea water (Ref 18). This value is noticeably different from those quoted in the table above and serves to show how cathodic protection can never really be an exact science.

One other major factor influencing current density calculations is surface area. This is itself a very imprecise factor and some offshore cathodic protection systems have been based on calculations of surface areas some 25% lower than the actual areas (Ref 20). It must be remembered to include all ancillary steelwork. This constitutes: pile guides, pile sleeves, conductor frames and guides, riser clamps, temporary buoyancy provisions, flooding and grating pipework, mud mats, well tubing, export pipelines, and other structures in contact with the platform. Furthermore, allowances are often not made for surface roughness, weld profile, manufacturing tolerances and edge effects.

In summing up cathodic protection one thing should be remembered; no matter how good the system is, be it impressed, sacrificial or hybrid, it cannot be installed and then forgotten about. The imprecise nature of our knowledge of current density requirements, anode distribution, and system efficiency in a highly dynamic sea water environment, means that cathodic protection systems should be constantly monitored for performance. This monitoring should encompass fixed and changing locations and take account of bad weather conditions, when the system will be stretched to it's maximum requirements. It is only with constant surveillance and adjustment that cathodic protection systems can achieve their optimum performance levels.

1.3 Corrosion fatigue

Metal fatigue has long been recognised as one of the major causes, if not the major cause, for failure of engineering structures in service. When this mechanical damage is allied to electrochemical damage in the form of corrosion fatigue, the problem is greatly accentuated. There have been many definitions of corrosion fatigue, that of Wei (Ref 26) is as good as any and states; "Corrosion fatigue is a generic term that is used to describe the phenomenon of cracking (including environment enhanced fatigue crack growth) in materials under the combined actions of an applied cyclic stress and a corrosive (agressive) environment". In an offshore environment both the cyclic stresses and the corrosive environment are ever present and their effects on the corrosion fatigue performance of 'standard' constructional steels such as BS 4360:50D are reasonably well understood. When high strength steels are introduced

however, this level of knowledge of material performance decreases. If we are to design and construct safe and efficient offshore structures for use in deeper and more hazardous waters, then this knowledge level must increase, particularly in situations where the length of time between inspection periods must be determined.

In trying to assess the corrosion fatigue performance of a H.S.L.A. steel, the situation must be looked at first in terms of all the variables which can affect the whole system. The relevant variables can then be examined in detail. Table 5 (Ref 26) lists most of the significant variables in any fatigue life consideration.

Mechanical Variables

- Maximum stress or stress intensity factor
- Cyclic stress or stress intensity factor range
- Stress ratio or load ratio
- Cyclic load frequency
- Cyclic load waveform (for constant amplitude loading)
- Load interactions in variable amplitude loading
- State of stress
- Residual stress
- Mean stress

Geometrical Variables

- Crack size and relation to component dimensions
- Crack geometry
- Component geometry adjoining crack
- Stress concentrations associated with design

Metallurgical Variables

- Alloy composition
- Distribution of alloying elements and impurities
- Microstructure and crystal structure
- Heat treatment
- Mechanical working
- Preferred orientation of grains and grain boundaries
- Mechanical properties (strength, fracture toughness, etc.)

Environmental Variables

- Temperature
- Pressure
- Types of environment
- Partial pressure of damaging species in gaseous environments
- Concentration of damaging (or beneficial) species in aqueous or other liquid environments
- Electrochemical potential
- pH
- Viscosity
- Velocity of environment
- Coatings

Table 5. List of variables associated with fatigue crack growth (Ref 26)

As the work undertaken in this project concentrates on one particular steel in a set environment, many of the outlined variables will be constant for the duration of the experimental work. Before considering the effects of these variables, we must first look at the major method used to analyse these parameters, namely fracture mechanics.

Linear elastic fracture mechanics (L.E.F.M.) is basically an expansion of the idea that under a cyclic loading regime, any component containing a fatigue crack will have an associated lifetime, expressed in number of cycles (for a given frequency), and stress level for that crack at any particular instant in time. For constant amplitude loading the correlation between the stress intensity factor, the stress, and the crack length can be given by:

$$\Delta K = \Delta\sigma\sqrt{\pi a} \qquad - (10)$$

where $\Delta K = K_{max} - K_{min}$
$\Delta\sigma = \sigma_{max} - \sigma_{min}$
a = crack length

From this a fundamental relationship between the fatigue crack growth rate da/dN (which is the slope of the crack length plotted against the number of cycles) and the stress intensity factor range can be obtained.

The characteristic sigmoidal shape of a da/dN - ΔK fatigue crack curve is shown in figure 9 (Ref 27).

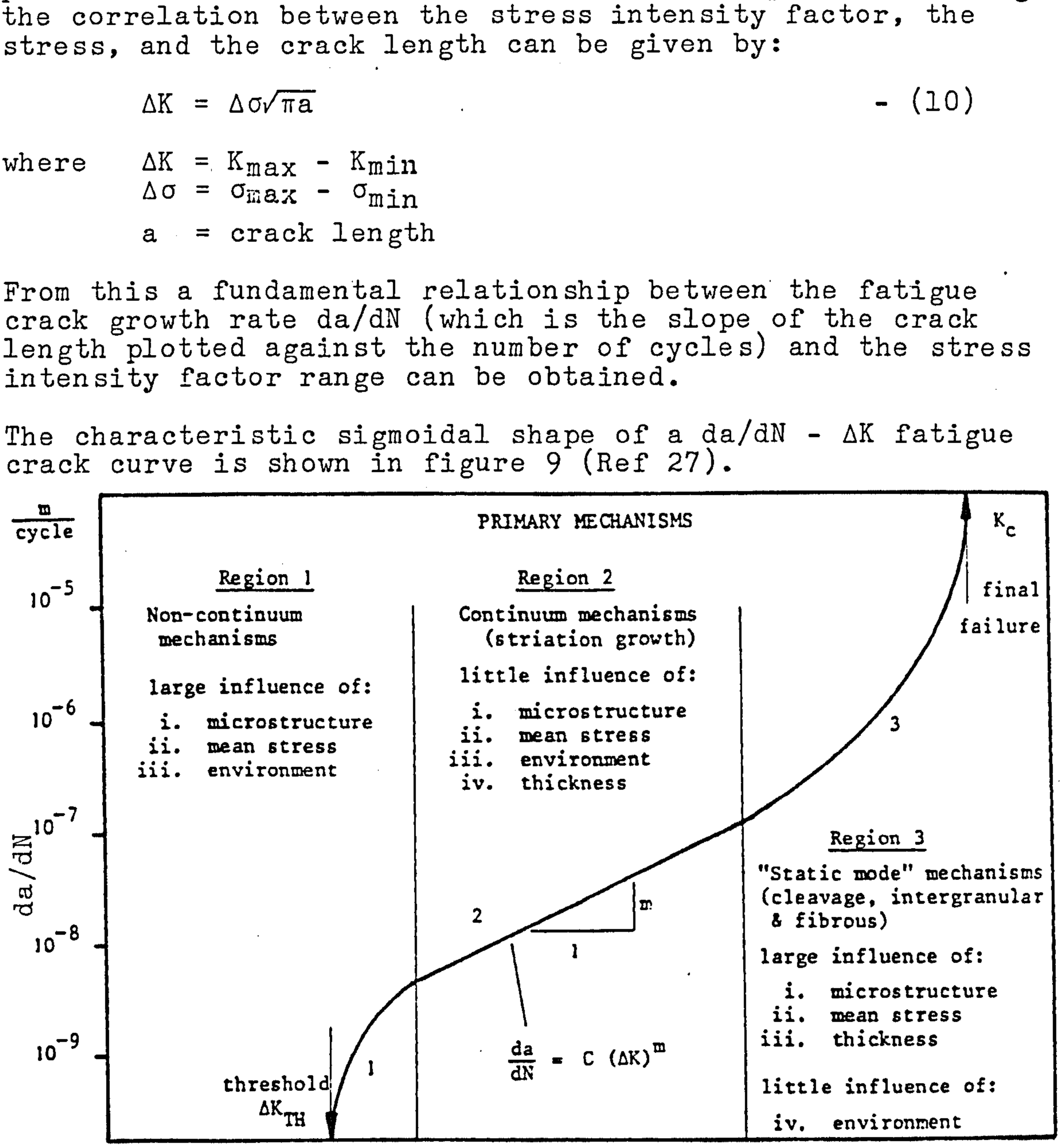

Figure 9. Characteristics of the fatigue crack growth rate curve log da/dN - log ΔK (Ref 27)

The curve is generally divided into three regions according to the curve shape, the mechanisms of crack extension, and various influences which affect the shape. In region 1 there is a threshold value, ΔK_{th}, below which cracks do not propagate or are less than a certain detectable size. Above this value the crack growth rate increases relatively rapidly with increasing ΔK. In region 2 there is often a linear relationship between log da/dN and log ΔK. Finally in region 3 the crack growth rate rises to an asymptote where the maximum stress intensity factor K_{max} in the fatigue stress cycle rises towards the critical stress intensity factor K_c, although in practice test specimens will develop a plastic hinge before this is reached.

The observation of a stress intensity, dependent on material and environment, below which no measurable crack growth is observed, has led workers to suggest that this corresponds to a real threshold ΔK_{th} below which the crack growth rate is zero. The existence of such a point would be of great interest both for design purposes and for fundamental studies. At such a point the crack can be considered to be in a state of equilibrium - the requirements for crack growth being just fulfilled. In practice the minimum detectable crack velocity is limited by drift/error in the crack length measurement systems, or more often, by the resolution of the measurement technique. Hence below the observed ΔK_{th} the crack velocity may not be zero, but simply slower than could be detected. This has often led cautious workers to refer to their observed threshold as an apparent ΔK_{th}. This raises the question as to whether a true ΔK_{th} exists at all, and if it does, how accurate is the apparent ΔK_{th} as a measure of the true value?

There have been many attempts to describe the crack growth rate curve by crack growth laws which are usually semi or wholly empirical formulae fitted to a set of data. The two most widely known are:

$$da/dN = C(\Delta K)^m \qquad \text{- the Paris equation - (11)}$$

$$da/dN = \frac{C(\Delta K)^m}{(1-R)K_c - \Delta K} \qquad \text{- the Forman equation - (12)}$$

where:
- da/dN = crack growth rate, per cycle
- ΔK = stress intensity range = $K_{max} - K_{min}$
- R = stress ratio = $\sigma_{min}/\sigma_{max}$
- K_c = critical stress intensity factor
- m = linear gradient
- C = the intercept of the extension of the linear portion of the curve, on a log-log plot, until it meets the da/dN axis at $\Delta K = 1$.

Although the Paris relationship continues to enjoy widespread popularity in the field of offshore engineering,

it has some very serious limitations. If it is considered in relation to the fatigue crack growth curve shown in figure 9, then the Paris equation does not prove to be totally satisfactory. It is only valid for the intermediate range of growth rates (region 2), failing to offer reliable data for the threshold (region 1) and final failure (region 3) sections.

Several attempts have been made to improve the correlation between crack growth rate and the stress intensity factor. Forman's equation introduces several elements which enable it to describe the final failure region and the intermediate region. This equation has been proven in several research laboratories to give reasonable approximations to test results for several aluminium alloys. A further modification was carried out by Klesnil and Lucas (Ref 28) which included ΔK_{th}.

$$da/dN = \frac{C(\Delta K^m - \Delta K_{th}{}^m)}{(1-R)K_c - \Delta K} \qquad - (13)$$

This gave a good fit to test data but ΔK_{th} had to be determined experimentally.

With the somewhat confusing and even contradictory array of crack growth relationships, it is important to be able to select one that best explains the fatigue behaviour for a given set of environmental and loading conditions. The Paris equation, despite it's limitations, still remains the strongest contender at the present time, primarily because it is most easily manipulated, but also due to the fact that a great deal of experimental data generated fits it's general form over a considerable range of practical circumstances. However, the lack of R in the equation is important, as will be discussed later.

Several observations can be made when considering the usefulness of fatigue crack growth relationships :-

1) The majority of relationships assume that the fatigue crack opens in mode I only. Factors which take account of mixed mode opening and secondary cracking are generally not included in order to stop the equation becoming too complex and unwieldy.

2) The Paris equation gives good correlation with fatigue crack propagation data for both high and low strength steels tested in an air environment.

3) The alternate relationships developed to take account of the effects of stress ratio (R), threshold stress intensity (ΔK_{th}) and fracture toughness (K_{1c} or K_c), retain dependence on regression analysis and are based on individual alloy systems. This makes them suspect when

applied to high strength steels in sea water environments.

4) The constants C and m in the Paris equation are generally believed to be environmental and material parameters respectively.

5) The relationships do not include reference to or make allowance for the effects of material inhomogeneity or the interaction of stress systems in the advancing crack front, which frequently causes the crack front to assume a 'bowed' profile.

6) The ability of ΔK to correlate crack growth rate data depends to a large extent on the fact that the alternating stresses causing crack growth are small compared to the yield strength. Therefore, crack tip plastic zones are small compared to crack length, even in a very ductile material.

7) In terms of aquiring experimental data, there is general difficulty in measuring crack propagation rates of the order of 10^{-9} m/cycle or less. This further contributes to the scatter of data points, particularly in the threshold region. A further source of error arises from the interaction of stress systems referred to in point 5 above. This effect can result in significant errors in crack length measurement, particularly if optical measurement techniques are used.

8) Generally speaking, because different mechanisms may be operating in each region of the fatigue crack growth rate curve, any single equation which attempts to describe the overall behaviour must include many parameters. This may not only make the equation extremely complicated, but it may also limit it's usefulness to a specific material - environment system.

9) The fatigue crack growth rate relationships can be successfully used to represent a large amount of data in a condensed analytical form which is advantageous in computerised life calculation techniques.

The major problem associated with Paris type relationships is that they apply to an essentially elastic situation. However, there will be an associated plastic region at the crack tip which is not accounted for. In effect, the yield stress, σy, is exceeded at the crack tip and a plastic zone develops. If the plastic zone is small compared with the plate thickness, transverse yielding is restricted and conditions near the crack tip still approximate to plane strain throughout most of the plate thickness. When the elastic zone size becomes comparable with the thickness, the stress state at the crack tip changes to plane stress. It is this crack tip plasticity which is the basis for striation mechanisms of growth, which have provided the basis for the majority of all quantitative models of fatigue crack propagation.

The precise mechanism of striation formation has yet to be established, although it is generally accepted that it involves alternate blunting and resharpening of the crack tip. In a model first proposed by Laird and Smith (Ref 29), the area of the crack tip is increased during the loading part of the cycle, after which the tip becomes blunted, only to be resharpened during the unloading portion by buckling of the new crack surface. Under such conditions, growth is controlled by the local crack tip alternating plastic strain and thus when applied to propagation under linear elastic conditions, the growth rate would be expected to be dependent on ΔK. A mechanism put forward by Tomkins (Ref 30) proposes that intense localised shear deformation on planes of maximum shear gradient at the crack tip leads to the creation of new fracture surfaces by shear decohesion at the crack tip. This shear decohesion is mooted to be the process of crack blunting by which the strain singularity, existing at the crack tip, is relieved.

It is worth considering these two models in relation to the work proposed for this project, where the R ratio = 0.6. The question that must be asked is: if the crack tip resharpens during the unloading part of the cycle, becoming 'fully sharp' when the crack is fully closed; what happens if the R ratio is greater than 0 and the fatigue crack does not fully close? Will the crack growth rate slow down?

Intuitively, compressive stresses are largely ineffective in causing fatigue damage, so it seems reasonable to suggest that a wholly tensile stress cycle should be more damaging than one which is all or partially compressive. Measurements of crack propagation rates of BS 4360:50D under freely corroding conditions in sea water using R values in the range -1 to +0.85 by Johnson and Bretherton (Ref 31) revealed that an increase in the R ratio enhanced the crack propagation rate, the effect becoming saturated for R values between 0.5 and 0.7. The work of Elber (Refs 32,33) has suggested that the plastic zone left in the wake of a growing fatigue crack causes the crack to be closed at the tip during the lower portion of the fatigue cycle, even under tension/tension loading (see Fig 10, Ref 32).

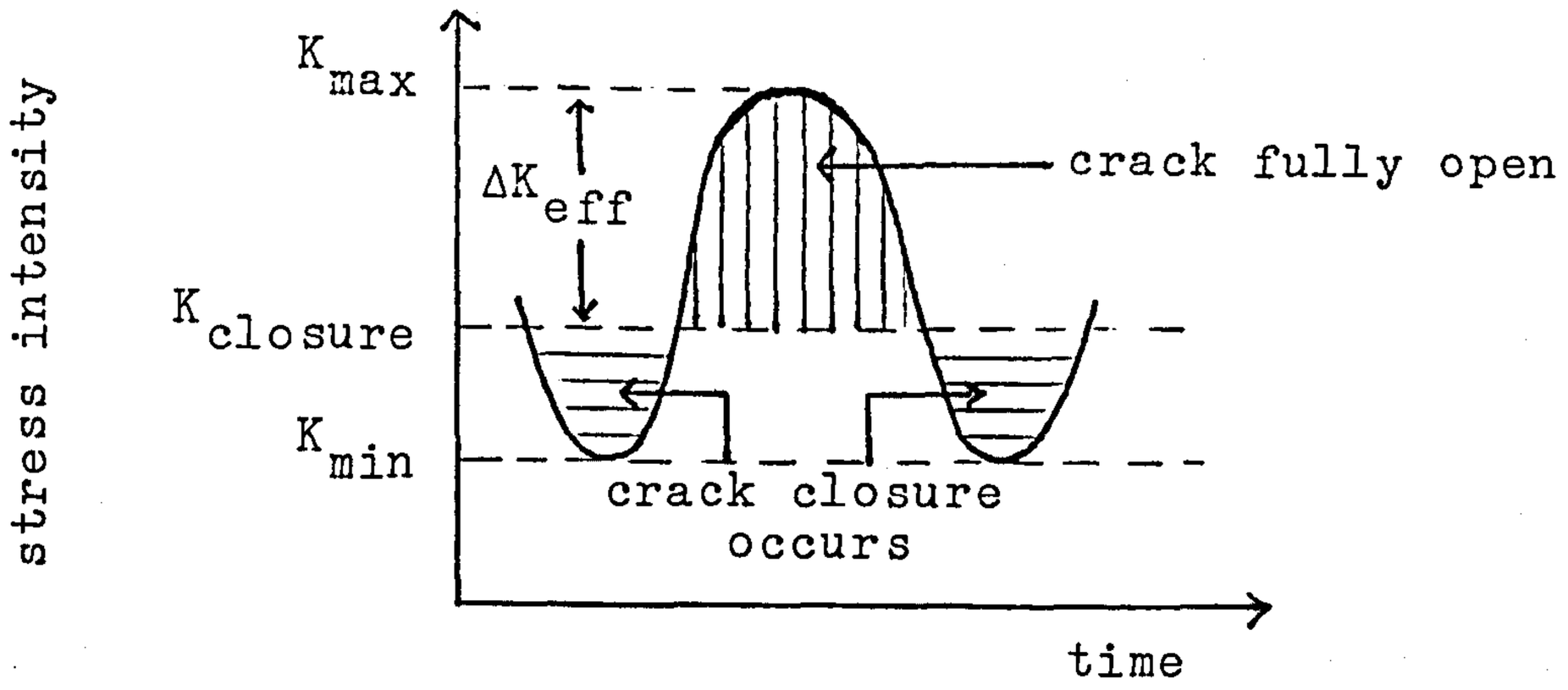

Figure 10. Crack closure schematic (Ref 32)

Elber found that residual stresses exceeding yield stress magnitude could be left acting on the fracture surfaces on an unloaded fatigue crack and proposed that growth was controlled by an effective stress intensity factor range, ΔK_{eff}, defined by:

$$\Delta K_{eff} = K_{max} - K_{op} \qquad - (14a)$$

where: K_{op} is the stress intensity level at which the crack opens.

This ΔK_{eff} will be less than the applied stress intensity factor range ΔK.

Elber went on to propose that for R ratios between -0.1 to 0.7, the proportion of the stress range during which the crack was open, U, was given by:

$$U = 0.5 + 0.4R \qquad - (14b)$$

Consideration that the effective stress intensity range at the crack tip was not simply proportional to the applied dynamic load but instead was critically influenced by the degree of closure, led Elber to propose the following modification to the Paris equation:

$$da/dN = C(\Delta K_{eff})^m = C(U\Delta K)^m \qquad - (14c)$$

Substitution for U from equation 14b in terms of the known quantity R gives:

$$da/dN = C\left[(0.5 + 0.4R)\Delta K\right]^m \qquad - (14d)$$

The validity of these studies, and it must be remembered that the results of Elber were obtained using aluminium alloys, is questionable following research by Lindley and Richards (Ref 34). Crack sectioning studies have shown that at the lower limit of a loading cycle, cracks could be closed locally at the surface but remain open in the interior. Work by Irving, Robinson and Beevers (Ref 35) suggests that results obtained from compliance methods (used by Elber) only detect closure loads in the plane stress regions and that the crack closure has no validity in effectively plane strain situations.

Another major consideration must be given to the R ratio when a comparison has to be made between different sets of data obtained under different R ratios. Lindley and Richards (Ref 36), using a bainitic steel with a yield strength of 618 MPa, have shown that for an increase in R ratio from 0 to 0.8, the threshold stress intensity range ΔK_{th} decreases from 8.2 to 2.6 MPa$\sqrt{m}$. This is significant when considered in relation to welded joints where the influence of geometrical stress concentration factors and increased levels of residual stress could be expected to

increase the effective level of the R ratio. Any associated reduction in the ΔK_{th} coupled with the unavoidable defects due to welding may have a deleterious effect on the early stages of fatigue crack propagation in the welded region. It has already been mentioned that an increase in R ratio is believed to increase the crack propagation rate. Therefore in the case of a high strength steel in an offshore environment subjected to purely tensile fatigue loading and perhaps overprotection, it is easy to see that a serious corrosion fatigue crack initiation/propagation situation may arise. A point to bear in mind, however, is that the data produced by Lindley and Richards, and similar results by Stewart (Ref 37), were for steels tested in ambient air. Therefore, any extrapolation to offshore conditions must be done with care.

In recent years two notable concepts have been proposed to explain corrosion fatigue crack propagation. In the first of these, Wei and Landes (Ref 38) suggested that the mechanical and environmental contributions to crack growth could be algebraically summed. This was given the name 'The Linear Summation Hypothesis'. Briefly it states that the corrosion fatigue crack propagation rate is equal to the linear sum of the individual contributions of the environmental rate of attack and of the cycle dependent (no environmental effect) fatigue crack propagation rate. This is expressed in equation form as :-

$$(da/dN)_c = (da/dN)_{env} + (da/dN)_r \qquad - (15)$$

where the subscripts denote:
c = corrosion fatigue
env = environmental
r = cycle dependent (no environmental effect).

Wei and Landes further postulated that the environmental contribution could be expressed in the form:-

$$(da/dN)_{env} = \int_t (da/dt).K(t)dt \qquad - (16)$$

where the integral is taken over one period of loading and K = stress intensity.

This gave a final equation thus:-

$$(da/dN)_c = (da/dN)_r + \int_t (da/dt).K(t)dt \qquad - (17)$$

Using this hypothesis they were able to satisfactorily predict the rates of corrosion fatigue cracking in several high strength steels in both hydrogen and humid air. However, it is believed (Ref 30) that their success was probably because of the dominance of the environmental term and that the reference term forms only a baseline indicating little evidence of real summation.

The second model was proposed by Austen and Walker (Ref 39), called 'The Process Competition Model'. The basis of this model is that the processes of stress corrosion and fatigue are mutually competitive, not additive as in the Wei and Landes model. It is assumed that the crack will propagate by the fastest available mechanism pertinent to the prevailing stress intensity. This implies that corrosion fatigue crack growth plots can be constructed by combining fatigue and stress corrosion plots, ensuring compatibility of variables in terms of da/dN and ΔK, and taking the fastest rate throughout.

This model suggests that the threshold stress intensity K_{1scc}, above which stress corrosion cracking occurs, is the separation point between two distinct types of corrosion fatigue crack growth behaviour. These are defined as:-

True corrosion fatigue - this identifies the behaviour where fatigue crack growth rates are enhanced by the presence of an aggressive environment through a synergisism of corrosion and cyclic loading. This is below K_{1scc} behaviour and applies to materials which do not stress corrode such that $K_{1scc} \simeq K_{1c}$.

Stress corrosion fatigue - this describes the phenomenon of static load stress corrosion under fatigue conditions. This occurs whenever the stress intensity in the fatigue cycle is above K_{1scc}.

Figure 11 (Ref 39) characterises both of these conditions and the most common type of behaviour which includes both true and stress corrosion fatigue throughout.

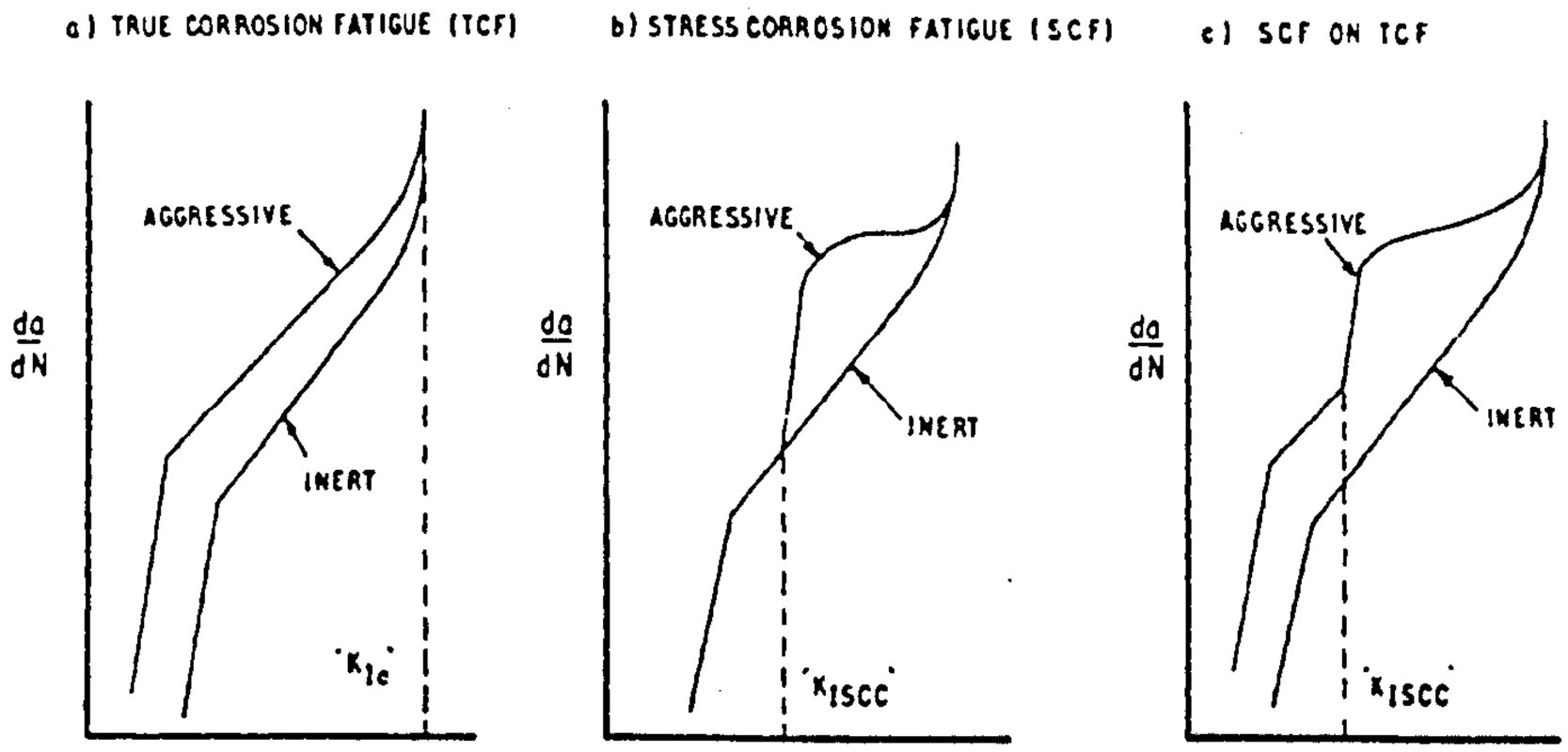

Figure 11. Basic types of corrosion fatigue crack growth behaviour (Ref 39)

Interestingly enough, this model gave good predictions for a H.S.L.A. steel in 3.5% NaCl solution.

It is a widely held view that structural steels in sea water environments exhibit true corrosion fatigue behaviour

and are not susceptible to 'classic' stress corrosion crack propagation. However, work carried out under the UKOSRP project (Ref 40) has shown that this may not be the case under all circumstances, and steel/environment conditions which normally exhibit true corrosion fatigue behaviour have been found to show effects characteristic of stress corrosion related propagation mechanisms. If this is the case then suspect systems involving high strength steels and conditions of severe overprotection should be very prone to stress corrosion fatigue.

Understanding the mechanisms of corrosion fatigue crack growth requires consideration of the kinetics of the various processes likely to be involved. These major processes are illustrated schematically in figure 12 (Ref 41).

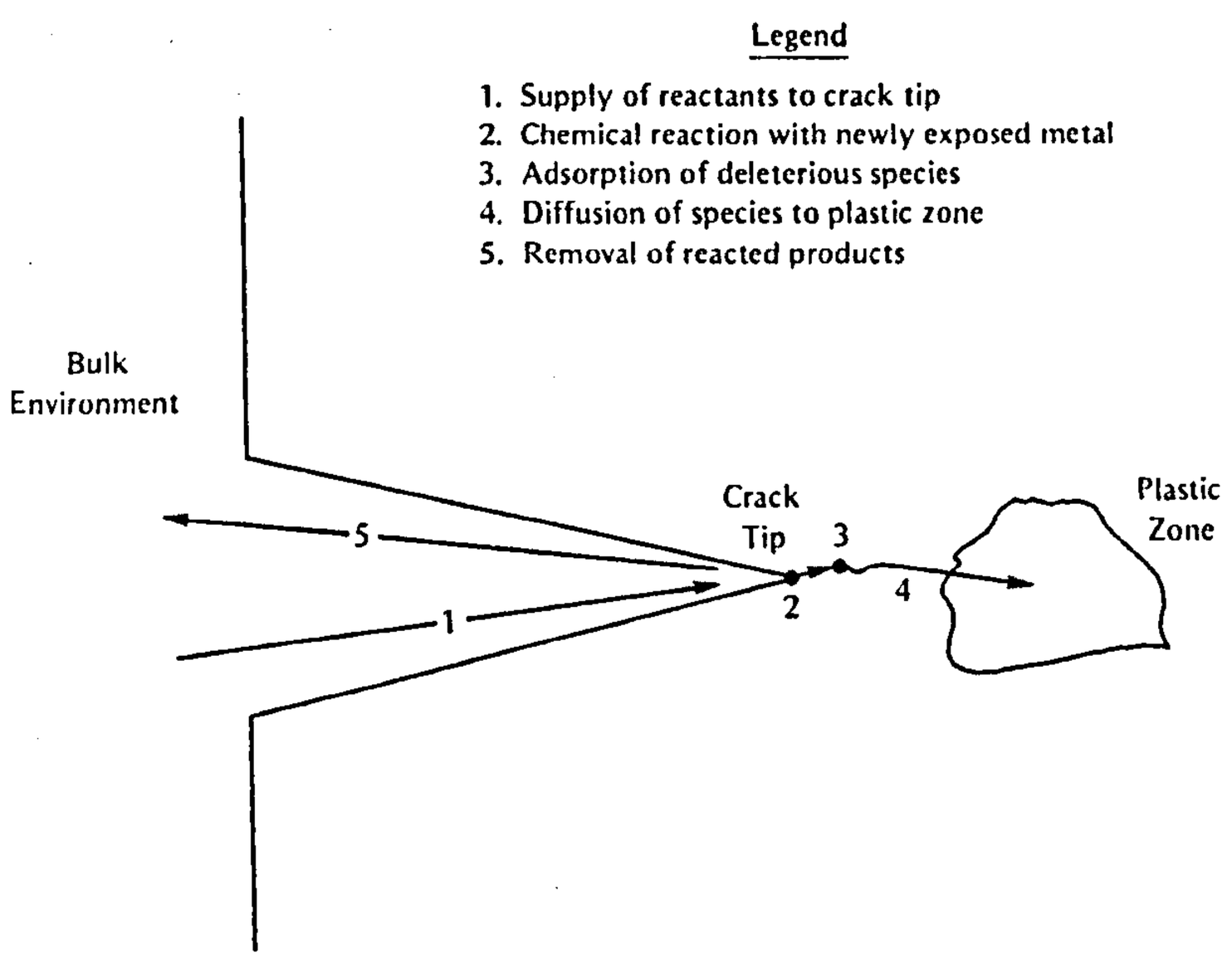

Figure 12. Schematic of processes involved near crack tip during corrosion fatigue (Ref 41)

First, the reactants present in the bulk environment must be supplied to the crack tip region. The local solution near the crack tip generally will be different in nature from the bulk solution. The local crack tip chemistry may be affected by the presence of corrosion products and deposits. Therefore, the rate of removal of these products is important as a build up at the crack tip may alter local stresses just by their physical influence on crack closure.

As newly cracked material is produced near the crack tip

by fatigue processes, this material reacts with the local environment, thus the mechanical fracturing process synergistically interacts with the chemical attack. It is generally believed that the mechanistic effects of aqueous environments on crack propagation rates involve essentially two processes: anodic dissolution of bare or partially corroded metal at the crack tip, and hydrogen embrittlement. Their effects are quite different, as dissolution involves changes in the crack tip geometry, whereas hydrogen embrittlement can affect the material ahead of the crack tip.

In the simplest case, anodic dissolution of material at the crack tip is responsible for the environmental contribution to corrosion fatigue crack growth. The highly deformed material in the plastic zone ahead of the crack contains a high concentration of slip bands which are more susceptible to corrosive attack than the surrounding metal. This corrosive dissolution competes against the constant mechanical resharpening of the crack tip and if it is rapid enough then crack blunting may occur. This is especially true in highly aggressive conditions at high ΔK levels, where the plastic zone is fairly large. Since the process is a time dependent function, it will also be affected by frequency. Lowering the cyclic frequency allows the corrosion effects to act for longer, causing dissolution enhanced rates of crack growth to increase. There is, however, a specific frequency range which results in the maximum effect of corrosion, which according to Atkinson and Lindley (Ref 42) lies between 0.1 and 0.01 Hz.

The hydrogen embrittlement process of crack growth is not independent of the anodic dissolution process, since the hydrogen may be produced as a result of the crack tip anodic dissolution. The hydrogen is absorbed at the metal surface then diffuses to the zone ahead of the crack tip where it causes localized embrittlement. The exact method of this embrittlement is still not fully understood (the main contenders will be discussed in the stress corrosion cracking section), but this localized hydrogen embrittlement process is believed to be responsible for accelerated corrosion fatigue crack growth in high strength steels (Refs 43,44) and is obviously of great importance whenever cathodic protection is involved.

In general high strength steels are not used to fabricate large structural members, as are the low to medium strength steels. Instead they are used in machinery, equipment, and selected critical structural components where their high strength capability is needed to produce desired performance. It is now worth returning to the list of variables presented at the start of this section and reviewing the effects of the more relevant ones on the corrosion fatigue of high strength steels.

1.3.1 Strength and microstructure

As can be seen in figure 13 (Ref 45), increased tensile strength does not significantly improve the high cycle corrosion fatigue strength of steels under free corrosion conditions in saline solutions.

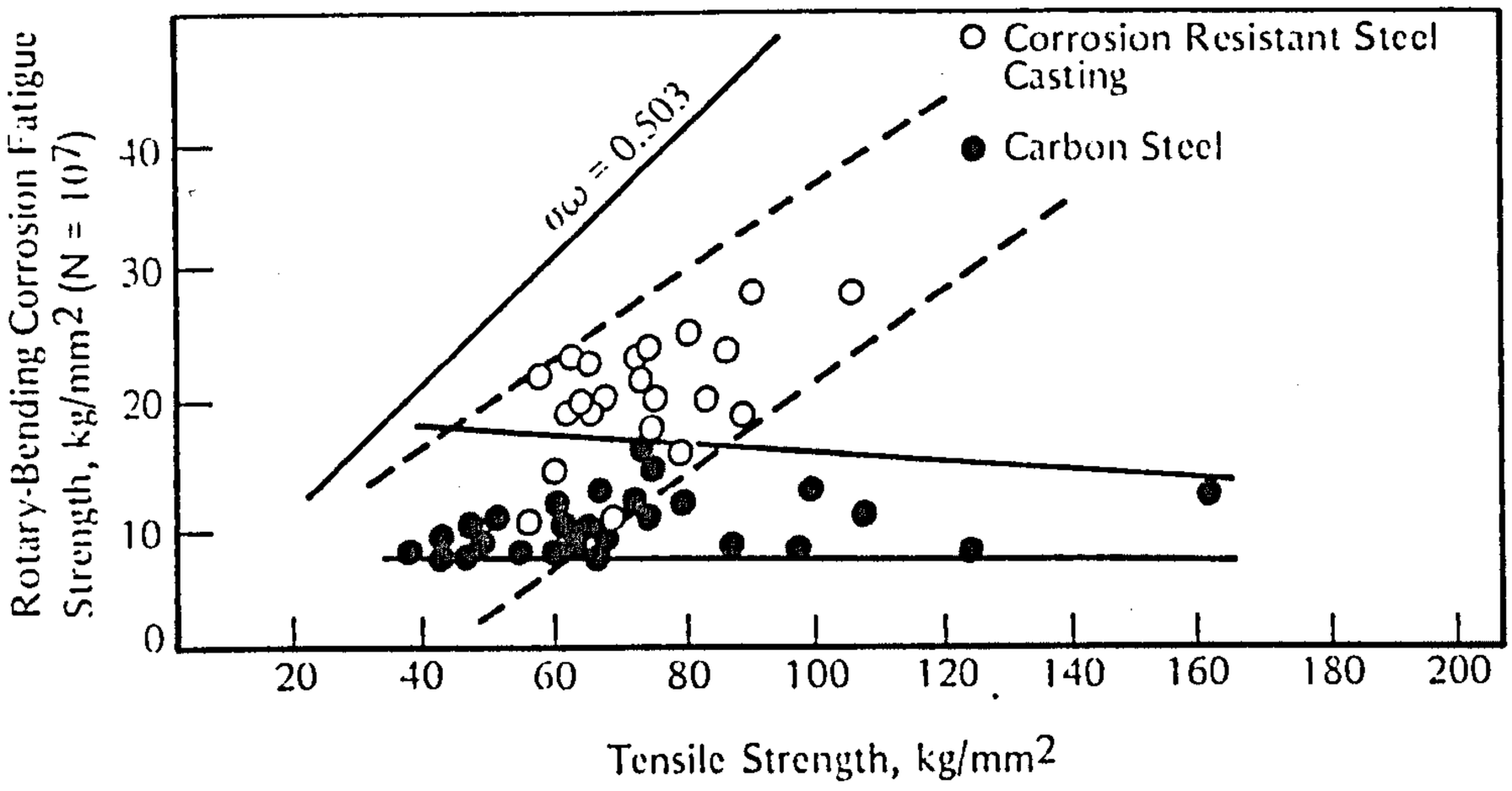

Bending frequency: 1,450 to 3,000 cpm

Figure 13. Correlation between ultimate tensile strength and corrosion fatigue strength at 10^7 cycles to failure of carbon and alloy steels in salt water and sea water (Ref 45)

Unless high strength steels are protected in some manner, little benefit derives from using them in marine environments if they are subjected to cyclic loading. However, as noted before, commonly used methods of cathodic protection may make high strength steels more susceptible to hydrogen embrittlement mechanisms and hence enhanced rates of crack propagation may occur. As a direct consequence of this, it seems reasonable to suggest that microstructural features known to improve tensile strength and high cycle fatigue strength in air would thus be of little benefit in corrosion fatigue conditions. Indeed, work carried out by Masumoto and Akaishi (Ref 46) has shown no improvement in corrosion fatigue strength by reducing grain size or changing the microstructure from lamellar pearlite to dispersed cementite.

1.3.2 Frequency

It is generally believed that decreasing frequency increases da/dN values at intermediate ΔK levels (Refs 39,47,48,49). In their studies using 3.5% NaCl solution, Austen and Walker (Refs 39,47) varied frequency from 64 Hz to 0.25 Hz.

As can be seen in figure 14 (Ref 47), da/dN values dramatically increased with decreasing frequency at intermediate ΔK values, whereas there was little frequency effect at very high and very low ΔK values.

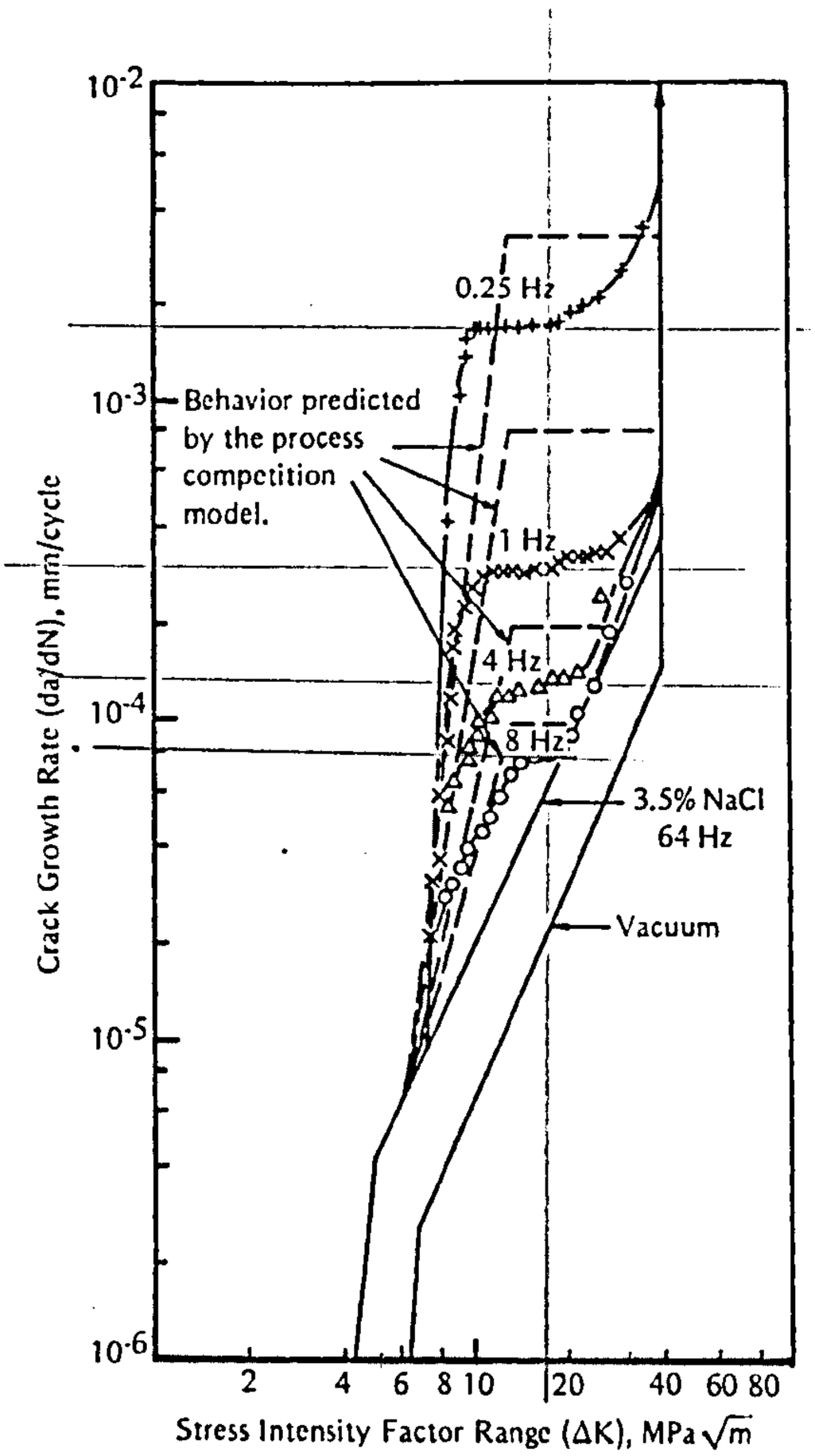

Figure 14. Effect of cyclic frequency on corrosion fatigue crack growth rate of 835M30 steel in 3.5% NaCl solution (Ref 47)

It must of course be remembered that this data was obtained in a sodium chloride solution and not in sea water, therefore care must be taken when directly comparing these results. However, this environment should have little effect on the general trend associated with frequency and high strength steels.

For BS 4360:50D, Scott and Silvester (Ref 50) found that decreasing the frequency from 10 to 1 Hz had little effect on crack growth rate but decreasing it to 0.1 and 0.05 Hz resulted in crack growth rates 4 to 5 times those in air, when ΔK was about 20 MPa√m at R = 0.1 in sea water at 20°C. Below this ΔK level there was no significant frequency effect.

1.3.3 Stress ratio

There is a fair amount of controversy regarding the effect of stress ratio on corrosion fatigue. Austen and Walker (Refs 39,47) examined the influence of R using a quenched and tempered martensitic steel. For tests at 75 Hz and in a 3.5% NaCl solution, they found no effect of varying R from 0.31 to 0.73. However, at r = 0.8 and 0.9, there were accelerated crack growth rates, especially at low ΔK values. When the frequency was decreased to 4 Hz, increasing R from 0.1 to 0.8 gave large increases in da/dN values at intermediate levels of ΔK, and reduced the ΔK_{th} value.

This is a similar result to that found by Pook and Greenam (Ref 51), who showed that high R ratios increased crack growth rates at low values of ΔK.

Austen and Walker have suggested that high R ratios can be quite deleterious to corrosion fatigue crack growth resistance of high strength steels because they may cause K_{max} to be greater than K_{1scc} and hence the environment effect, discussed earlier, will have a much more important effect.

1.3.4 Temperature

It has been shown by Scott and Silvester (Ref 50) that reducing the temperature of sea water from 20°C to 5°C reduced the crack growth rates by a factor of approximately 2. This result was obtained for BS 4360:50D at 0.1 Hz in natural sea water, so it must be considered to be very relevant with respect to offshore conditions where the temperature on the surface ranges from 0° to 12°C. However, it is generally believed that variations within this range of temperature are expected to have only a minor effect in actual offshore situations. One interesting point to note for sub-arctic offshore applications is that cold (-2°C) sea water may cause the dissolution of calcareous scale, as inferred from the observations of Barrett and Taylor (Ref 52) who noticed that such coatings would form during summer months and disappear during winter months on platforms in Cook inlet, Alaska.

1.3.5 Cathodic protection

From the literature it seems that a moderate degree of cathodic protection may be useful in mitigating corrosion fatigue of high strength steels in sea water. The lower the stress level imposed upon the steel, then the better the behaviour will be. Below an optimum potential there appears to be a general pattern of increasing crack growth with decreasing potential (increasing protection). More negative potentials in general appear to be damaging,

more so the higher the strength and the higher the cyclic stress. The optimum potential mentioned, in order to give minimum crack growth, may be specific to a given steel.

Some of the findings of different researchers show markedly different results. Gallagher (Ref 49) found that, at best, cathodic protection does not have any significant effect on high strength steel crack growth rates. Bogar and Crooker (Ref 53) showed that polarising a high strength steel to -1.05 V (Ag/AgCl) caused faster growth than freely corroding conditions. Vosikovsky (Ref 54), using the same steel, found that cathodic protection was capable of decreasing crack growth rate at moderate potentials though it did not restore behaviour to that in air. On the other hand, Pettit (Ref 55), working with smooth steel specimens having a 990 MPa yield strength, reported restoration of fatigue life to match that in air at intermediate potentials.

It is interesting to note the findings and recommendations of Scott and Silvester (Ref 40) after investigating BS 4360: 50D as part of the U.K. Offshore Steels Research Project. They observed that cathodic polarisation to potentials more negative than -0.7 V (on the silver/silver chloride scale) increased crack growth rates so that the maximum acceleration factor of five was observed at -1.0 V. In the light of this, they concluded that in practice in offshore installations cathodic protection potentials more negative than -0.85 V (on the silver/silver chloride scale) should be avoided.

It is without doubt that in the cases of overprotection the major source of damage is hydrogen embrittlement, the effects being worse the higher the steel's strength. The improvement due to 'correct' cathodic protection may be caused by the calcareous deposits within the crack, which reduce crack closure, since Hartt and Hooper (Ref 56) found little improvement in corrosion fatigue life using NaCl solutions. These solutions would obviously not contain the necessary magnesium and calcium salts needed for the formation of calcareous deposits. These calcareous deposits will be discussed in their own section.

1.3.6 Welded joints

Since the majority of offshore structures are fabricated using welded joints and these joints are often at geometrical locations where corrosion fatigue damage is likely to occur, then the effects of geometric configuration and residual stress cannot be ignored. In welded components, geometric configuration plays a dominant role in that corrosion fatigue cracking often initiates at the toe of the weld where stress raisers or notches are present. In addition to this, the microstructure of the metal in this region will be altered from that of the base metal by the welding process. Residual stress concentrations occur

when the weld cools. Contraction of the weld metal relative to the cool parent metal results in the creation of tensile stresses in the weld metal with balancing compressive stresses in the parent plate.

To date, the results produced by several researchers (Refs 57,58,59) show varying effects due to residual stresses, and remedial action needed to alleviate them, upon the crack propagation rate during corrosion fatigue. Booth (Ref 59) demonstrated that the grinding of weldments produced an improvement in fatigue strength for specimens tested in synthetic sea water. This improvement was not, however, as large as that found with joints tested in air. Vaessen and De Back (Ref 60) found that although grinding and plasma dressing improved corrosion fatigue resistance, T.I.G. dressing and modification of the weld toe angle from 70° to 45° gave only a slight improvement in corrosion fatigue strength.

Overall research into welded joints can be summarised by the following:-

1) Compressive residual stresses substantially raise the fatigue resistance of welds, so actions which induce these stresses, such as shot peening, are recommended.

2) Tensile residual stresses decrease the fatigue resistance in welds. Actions such as fabrication followed by weld dressing and heat treatment are recommended to reduce internal residual stresses and improve weld profiles.

3) Compressive residual stresses are primarily responsible for improved fatigue resistance in the heat affected zone.

4) High hardness values in the H.A.Z. associated with welding are detrimental to the corrosion fatigue performance of welded joints. Care should be taken to keep hardness values below 350 Hv to avoid lamellar tearing and hydrogen induced cold cracking.

1.4 Stress corrosion cracking and hydrogen embrittlement

Any discussion on the corrosion fatigue of high strength steels must consider the possibility of stress corrosion cracking (S.C.C.) and it's influence on crack propagation. Until relatively recently, design criteria and remedial actions against stress corrosion have been based primarily on ensuring an operational tensile stress below some threshold level and avoiding a 'susceptible' alloy/environment system. It has since been realised, however, as more systems are investigated and as the definition of the word susceptible changes with the need to design structures with long lives, that the list of cracking systems is forever

changing. In fact, it has been shown that pure metals, as well as alloys, can undergo environment enhanced cracking; that many alloys can crack in pure water or water containing very small concentrations of anions, and that the superposition of a dynamic or cyclic stress on the system can increase the likelihood of cracking.

There is indeed a great need to understand the interrelationships between the mechanisms of stress corrosion cracking, corrosion fatigue and hydrogen embrittlement. Figure 15 (Ref 61) illustrates these interrelationships and suggests that most practical situations involving ductile alloy/aqueous environment systems probably lie in the centre of the diagram.

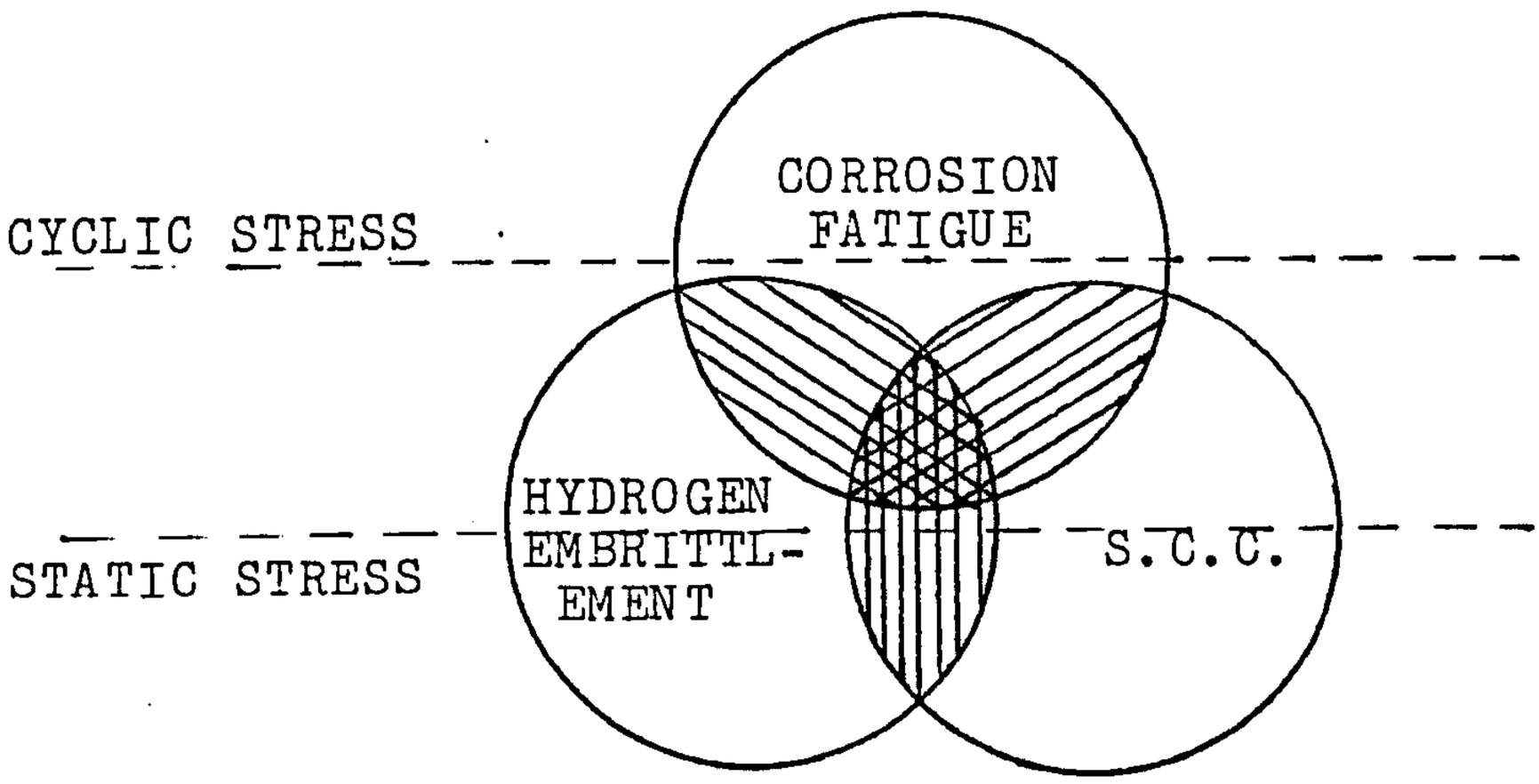

Figure 15. Venn diagram illustrating interrelationships between stress corrosion cracking, corrosion fatigue and hydrogen embrittlement (Ref 61)

A brief summary of the requirements for stress corrosion cracking reveals the following factors (Ref 5):-

1) a susceptible alloy composition,
2) a susceptible microstructure,
3) a specific aggressive environment,
4) a sustained tensile stress.

In recent years the most significant development in the characterisation of stress corrosion cracking susceptibility has been the use of fracture mechanics concepts, as previously discussed in the fatigue section. It has been found that S.C.C. data may be interpreted using the stress intensity (K_1) approach, K_1 signifying mode I crack opening stress intensity. Figure 16 shows a generalized representation of the stress corrosion crack growth rate, da/dt (where t is time), as a function of K_1.

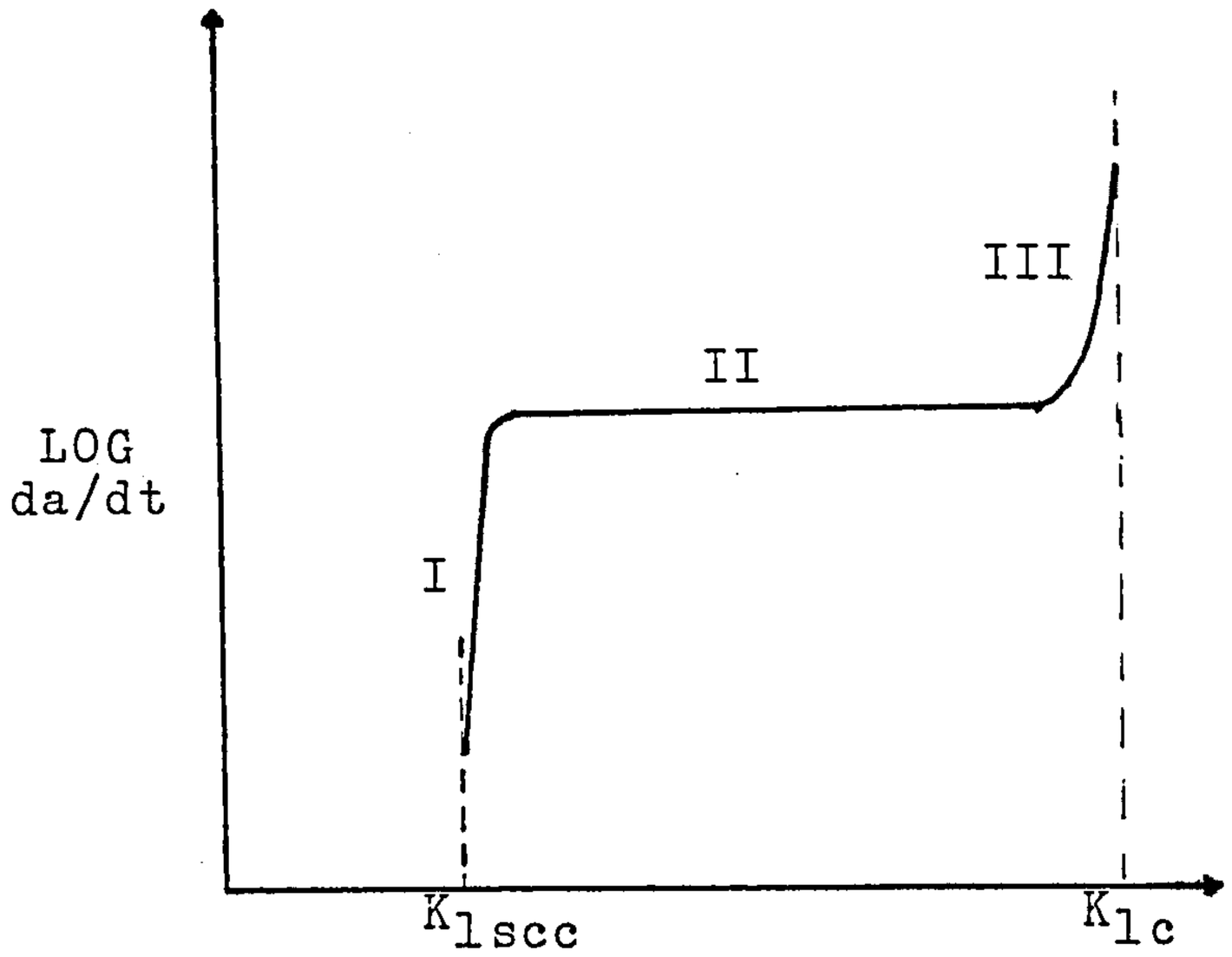

Figure 16. Stress corrosion crack growth as a function of K_1

It must be noted that this representation bears a striking resemblance to that encountered for fatigue, the major difference being that in region II the crack growth rate is virtually independent of stress intensity for S.C.C., whereas it increases considerably with stress intensity for the fatigue curve. In regions I and III of figure 16 the crack growth rate depends strongly on stress intensity, with region III often not being observed owing to a fairly abrupt transition from region II to unstable fast fracture. In region I there is a so called threshold stress intensity, designated K_{1scc}, below which cracks do not propagate under sustained load for a given material - environment system. This threshold stress intensity is an important parameter which may be determined by time to failure tests in which pre-cracked specimens are loaded at various stress intensity levels, thereby failing at different times, as shown schematically in figure 17 (Ref 62).

K_{1scc} provides a convenient separation point between those stress intensity levels that do and do not induce determinable rates of environmentally assisted crack growth. For those materials exhibiting the above K_{1scc} behaviour, the rate of environmental cracking, under sustained loads, can be extremely influential on the rate of corrosion fatigue cracking. Below K_{1scc} the environmental effect requires the conjoint action of the environment and the fatigue cracking mechanism, because the material will not be subject to failure by a pure stress corrosion cracking mechanism. (Ref 63).

When considering stress corrosion cracking in relation to structural steels in a sea water environment, care must be

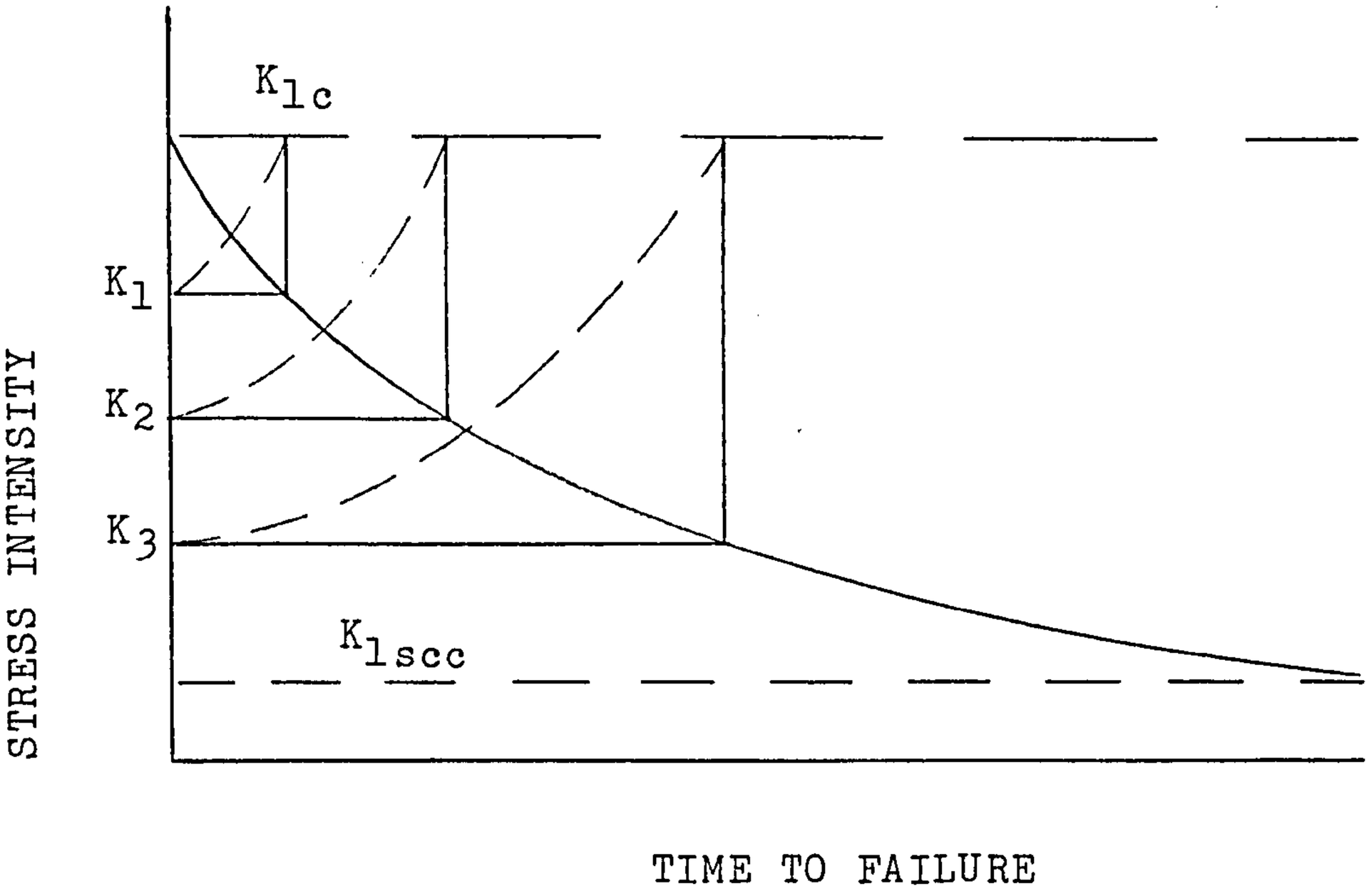

Figure 17. Stress intensity versus time to failure (Ref 62)

taken when assessing data. Work carried out by McMahon (Ref 64) has shown that K_{1scc} values are dependent upon the time taken to conduct the test, the type of test and the conditions used. As an offshore structure may have a design life in excess of 25 years, extrapolation of data gained in a 1000 hour experiment may not be practicable. Other complications may arise due to various effects of marine growths, exposure conditions, oxygen content and temperature, all of which would vary continuously for long exposure times in sea water.

A schematic relationship between the yield strength of steel and the steel's susceptibility to S.C.C. in sea water has been suggested by Jones, figure 18 (Ref 65).

Most offshore structures will follow the trend shown by the pre-cracked specimens because crack initiation sites will already be present due to welding defects. It would seem to suggest from figure 18 that steels with a yield strength of below 850 N/mm^2 would give little cause for concern regarding susceptibility to S.C.C.; however, in the H.S.L.A. steels used offshore not only will the parent plate material approach these values, but a more worrying aspect is the values of yield strength that may occur in the H.A.Z.

Work carried out by Hart (Ref 66) at the Welding Institute has produced a correlation between hardness value and yield strength for H.A.Z., parent plate and welded material (Fig 19, Ref 66).

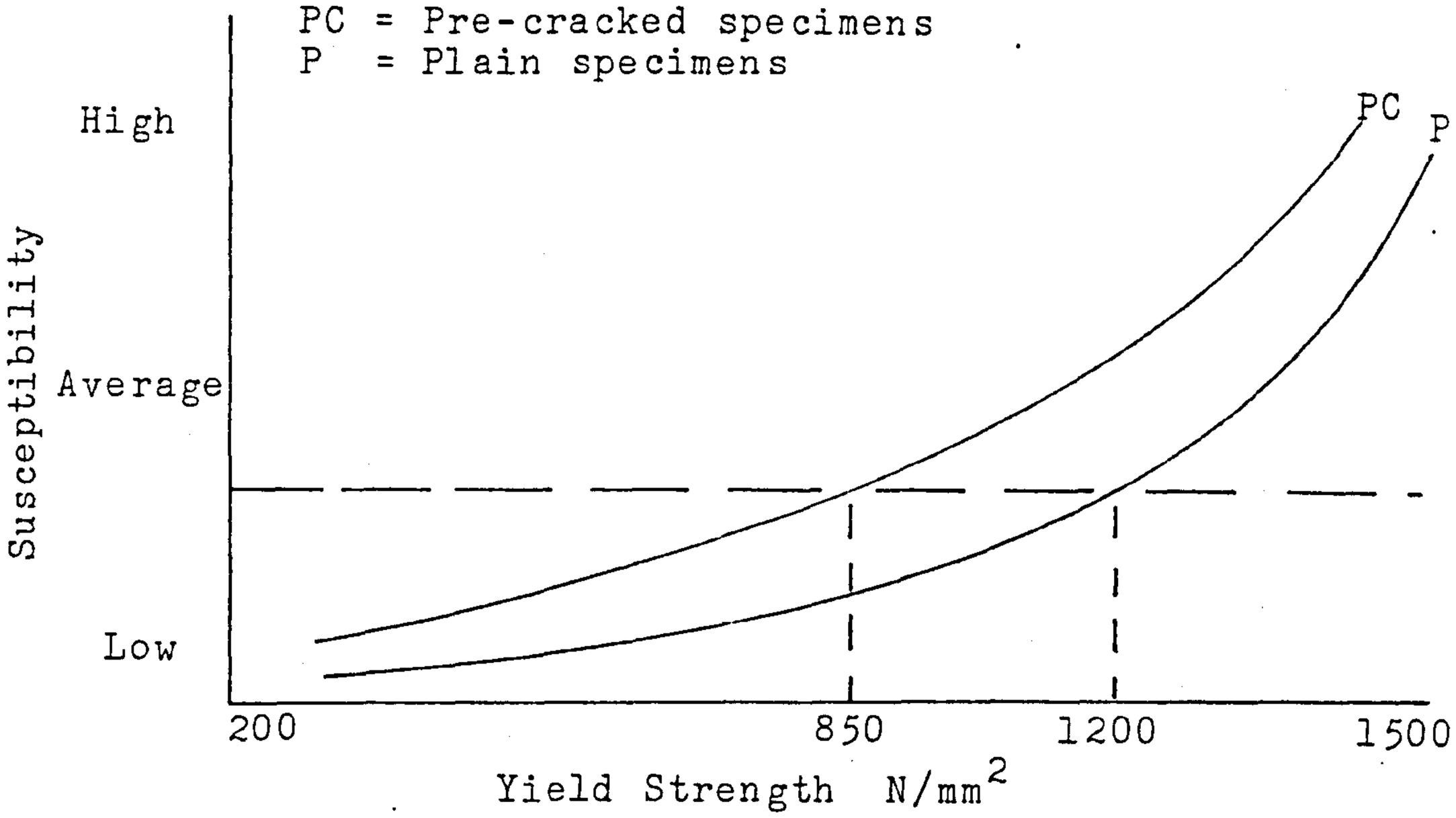

Figure 18. Susceptibility to S.C.C. as a function of yield strength (Ref 65)

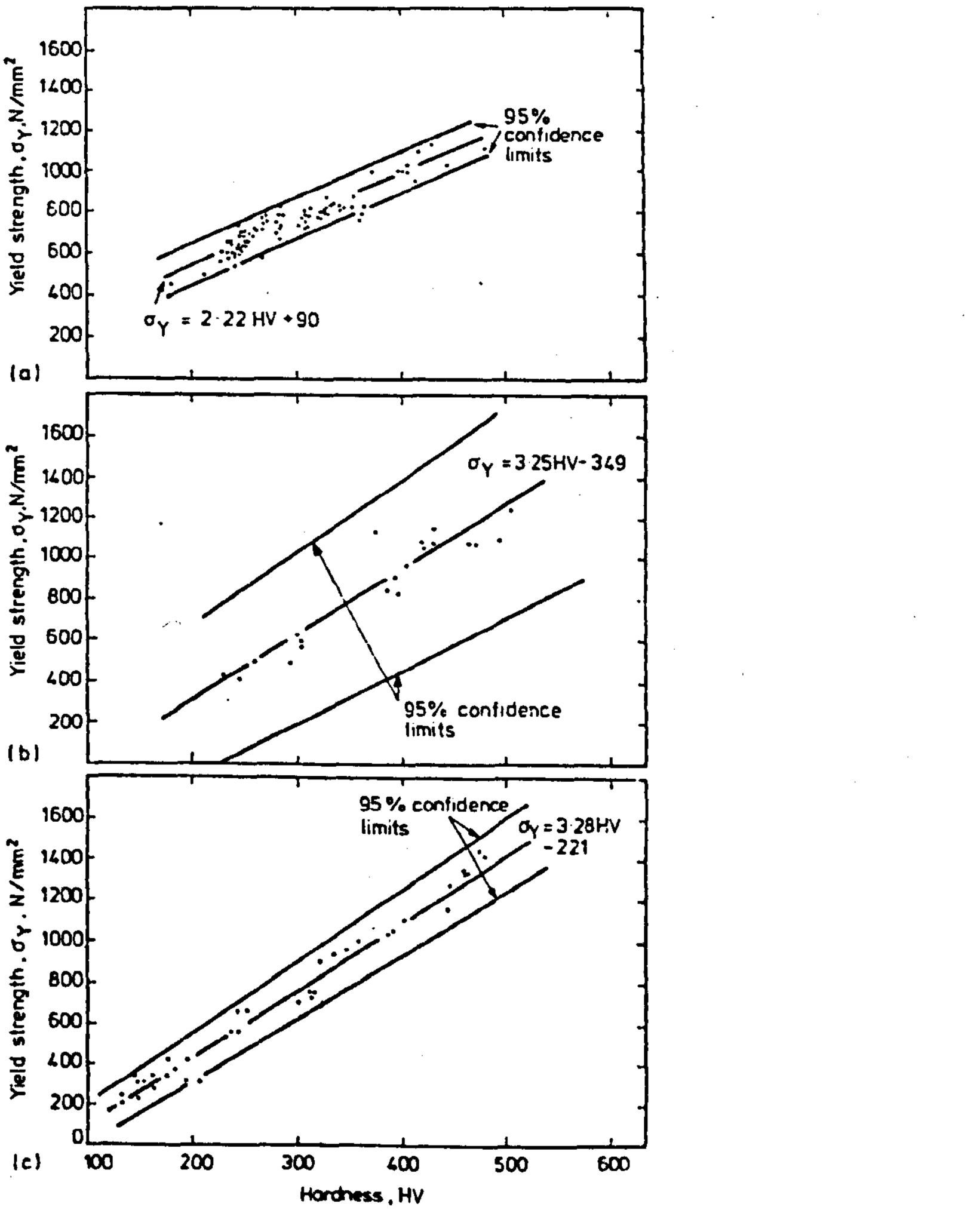

Figure 19. Correlation between hardness and yield strength (Ref 66)

Using this correlation it can be seen that a H.A.Z. hardness value of 450 Hv (which is not unreasonable for a H.S.L.A. steel) can translate to a yield strength of over 1000 N/mm^2. Clearly this means that welded high strength steels may pose a problem when used in offshore situations because any susceptibility to S.C.C. will only be exaggerated once cathodic protection is applied. Hovland (Ref 67) has shown that for steels with strength levels between 900 and 1212 N/mm^2 severe stress corrosion cracking was evident, exhibiting typical brittle behaviour at potentials between -1100 and -1300 mV (S.C.E.). What is particularly interesting in Hovland's results is the fact that the small amounts of hydrogen liberated at -780 mV (S.C.E.) seem to be enough to cause S.C.C. behaviour in these higher strength steels. This means that even so called 'correctly protected' structures that use high strength steels may be at risk from hydrogen induced stress corrosion cracking.

This now raises the whole question of the role of hydrogen in corrosion fatigue in an offshore environment. Hydrogen is without doubt one of the main species involved in the corrosion of steel and it's ability to accelerate and cause failure is well known throughout the offshore industry, both in the welding and construction side and in the operation side, the problem becoming worse as the steel strength level increases.

Several theories have been proposed to explain the mechanisms of hydrogen embrittlement. These theories basically fall into two groups:

a) <u>Pressure theory</u>

This idea was originally proposed by Zapffe (Ref 68) and subsequently modified by several researchers (Refs 69,70, 71,72,73). This theory proposes that hydrogen embrittlement results from the precipitation of hydrogen gas at defects such as inclusions, and the expansion of microcracks and voids due to the gas pressure. Tetelman (Ref 74) briefly summarises the theory by pointing out that the gas pressure lowers the applied stress necessary to cause crack growth. Thus, below the yield strength,unstable fracture occurs from the tip of the crack when:

$$\sigma_f = P = \sqrt{\frac{2E\gamma_p}{\pi C}} \qquad \sigma_f << \sigma_y \qquad - (18)$$

where: σ_f = applied stress
σ_y = yield stress
P = gas pressure
E = Youngs modulus
C = ½ crack length
γ_p = work done in initiating unstable fracture at the crack tip.

b) Decreasing strength theory

This theory was first put forward by Petch and Staples (Ref 75) and has been modified subsequently (Refs 76,77). Basically this theory proposes that the presence of dissolved hydrogen lowers the cohesive strength of the iron lattice in a way similar to that occurring in liquid metal embrittlement. In this model the decrease in cohesive strength results in a decrease in the surface energy of fracture and hence in a lowering of the applied stress necessary for crack propagation.

Even now the sequence of events at or near the tip of a crack in the presence of hydrogen remains a controversial subject. Oriani and Josephic (Ref 78) have proposed a decohesion thoery where decohesion at the crack tip is associated with a critical local concentration of hydrogen. In this model the tensile stress distribution in the crack tip region is the driving force for increasing the local hydrogen concentration. When this hydrogen concentration reaches a critical level fracture occurs. Oriani and Josephic have neglected plasticity near the crack tip, and it has been suggested (Ref 79) that as a result of local yielding the highest maximum tension will be attained ahead of the crack tip. Gerberich and co-workers (Refs 80,81), taking account of the stress field for small scale yielding near the crack tip, have proposed that molecular hydrogen forms fissures internally at a distance from the crack tip which is approximately equal to the crack tip opening displacement.

For high strength steels, a model developed by Raj and Varadan (Ref 82) suggests that crack propagation is by the initiation of a secondary crack ahead of the crack tip, and by the interaction between this crack and the primary crack. The secondary crack forms in the region of maximum tensile stress in the stress field of a sharp crack with small scale yielding. The micromechanism for the initiation of the secondary crack is the stress level and the formation of a two dimensional cluster of hydrogen atoms in the grain boundary which initiates the secondary crack. The main crack advances in jumps by coalescing with the secondary crack.

Although all the models discussed attempt to throw light on the hydrogen enhancement effect of crack growth, in the reality of a true corrosion fatigue situation the rate of growth per cycle is governed by the distance ahead of the crack that the hydrogen atoms can penetrate. In other words, the extent of embrittled material that the growing fatigue crack can pass through in each cycle is limited by the diffusion distance of hydrogen atoms. This diffusion distance will be dependent upon the hydrogen concentration at the crack tip surface and the form of concentration profile and hence will vary with the degree of cathodic protection/overprotection potential.

In terms of the effects of material composition and microstructure on susceptibility to hydrogen embrittlement, the major factor is the material hardness and strength level. As a general rule hardened structures are deleterious, and the risk of environmental hydrogen cracking is very much greater in quenched material than in annealed or normalized steel.

With regards to the permeability of hydrogen in steel, the major factor is the form in which the carbon is present. Table 6 (Ref 83) lists the results of several investigators in which different steel compositions were used. However, each one chosen was capable of being heat treated to several structures.

STEEL USED	METAL MICROSTRUCTURE	RELATIVE PERMEABILITY
0.84% C	Martensite	1.00
0.50% Mn	Lower Bainite	1.00
	Globular Cementite	3.59
	Troostite (fine globular carbides)	3.91
	Annealed steel	4.78
	Sorbite (growth of troostite)	7.00
	Normalized steel	7.43
0.59% C	Martensite	1.00
	Coarse Lamellar Pearlite & Ferrite	1.57
	Very Fine Pearlite & Ferrite	2.79
0.26% C	Martensite	1.00
0.25% Ni	Tempered Martensite (at 550°C)	1.04
	Fine Bainite	1.57
	Coarse Bainite	1.95
	Coarse Lamellar Pearlite	2.16
	Fine Lamellar Pearlite	2.98

Table 6. Permeation of hydrogen in steels heat treated to produce various microstructures (Ref 83)

From the results it can be seen that the lowest permeability was detected for the martensitic structures. The bainitic stuctures had lower permeabilities than the pearlitic structures but there is a difference in the results for the coarse and fine varieties of each. The effectiveness of the annealed and tempered structures in permeating hydrogen is generally high. As a very general conclusion for this it could be said that the more massive forms of carbide particles (spheroidal or globular cementite, pearlite, and certain tempered carbides) offer considerably less resistance. Martensite, in which the carbon atoms are retained in a dilated and strained iron lattice, affords

the most resistance to hydrogen passage. Therefore, hydrogen permeability tends to increase with increasing temperature of formation or transformation of the micro-constituent.

In the final summary of hydrogen problems in steel, several points can be made:

(1) The stronger or harder the steel, the more susceptible it is to hydrogen damage.

(2) Addition of substitutional alloying components like chromium and nickel cause an increase in the hydrogen solubility and a decrease in the apparent diffusivity of hydrogen in the alloy.

(3) The form of the carbide is particularly important, with martensitic structures being less permeable to hydrogen than normalized structures, however, the martensitic structures are more hydrogen sensitive.

(4) Cold working and welding usually increase the hydrogen susceptibility; annealing and tempering decrease it.

For the offshore situation, high strength steels offer many advantages in terms of weight saving and reduced fabrication charges, but these benefits are made at the cost of decreased performance with respect to hydrogen, and in an offshore environment hydrogen is a major problem. The role of hydrogen will be further discussed with reference to the actual results obtained in this project in a later section.

1.5 Calcareous deposits

It has long been recognised by corrosion engineers that calcareous deposits have a profound effect on the efficiency and effectiveness of offshore cathodic protection systems and on the mechanisms involved in propagating a corrosion fatigue crack. Depending on certain conditions, the most important of which is the cathodic current and it's ability to cause an increase in the electrolyte pH adjacent to the cathodic metal surface, these deposits may form on the cathodic metal surface in seawater. The deposits are in effect inorganic compounds, notably calcium carbonate ($CaCO_3$), magnesium carbonate ($MgCO_3$) and magnesium hydroxide ($Mg(OH)_2$), the solubility limits of which decrease with increasing pH, meaning that they are normally insoluble in sea water at a neutral to slightly alkaline pH.

On consideration of the importance of these deposits and their effect on cathodic protection and corrosion fatigue in the offshore industry, there is evidence that (or it has been suggested that) calcareous deposits intervene in the following ways (Refs 84,85,86,87,88,89) :-

(1) They reduce the flux of dissolved oxygen from bulk solution to the metal.

(2) They reduce the current density necessary to effect a given cathodic potential.

(3) They enhance the 'throwing power' of the cathodic protection.

(4) They reduce the overall magnitude of local action cells (uniform corrosion) if cathodic protection is removed.

(5) They mechanically interfere with crack closure.

(6) They reduce the effective stress intensity range at the crack tip, thus reducing closure and the rate of crack propagation.

Despite the importance of these calcareous films, there is not a great deal of information on the interrelationships between deposit properties and the influential variables which determine their formation.

1.5.1 Mechanisms of calcareous deposit formation

For most cathodic surfaces in aerated sea water, the principal reduction reaction is:

$$O_2 + 2H_2O + 4e^- \rightarrow 4OH^- \qquad - (19)$$

If the potential is more negative than the reversible hydrogen potential, then a second reaction also occurs:

$$4H_2O + 4e^- \rightarrow 2H_2 + 4OH^- \qquad - (20)$$

Either way, the hydroxyl ion is a reaction product which causes an increase in the pH of the electrolyte adjacent to the cathodic metal surface. In other terms, an increase in OH^- ions is equivalent to a corresponding decrease in H^+ ions. Figure 20 (Ref 91) is a schematic representation of this situation, the pH at the metal/electrolyte interface being determined by the rate of OH^- ion production and the subsequent removal of these ions by diffusion or convection or both. This pH profile is influenced by several factors including electrolyte composition, temperature and electrolyte velocity.

As the pH increases, the ionic products of various compounds increase until the respective solubility product is exceeded. For sea water, pH is controlled by the carbon dioxide system, the important reactions being:

$$CO_2 + H_2O \rightarrow H_2CO_3 \qquad - (21)$$

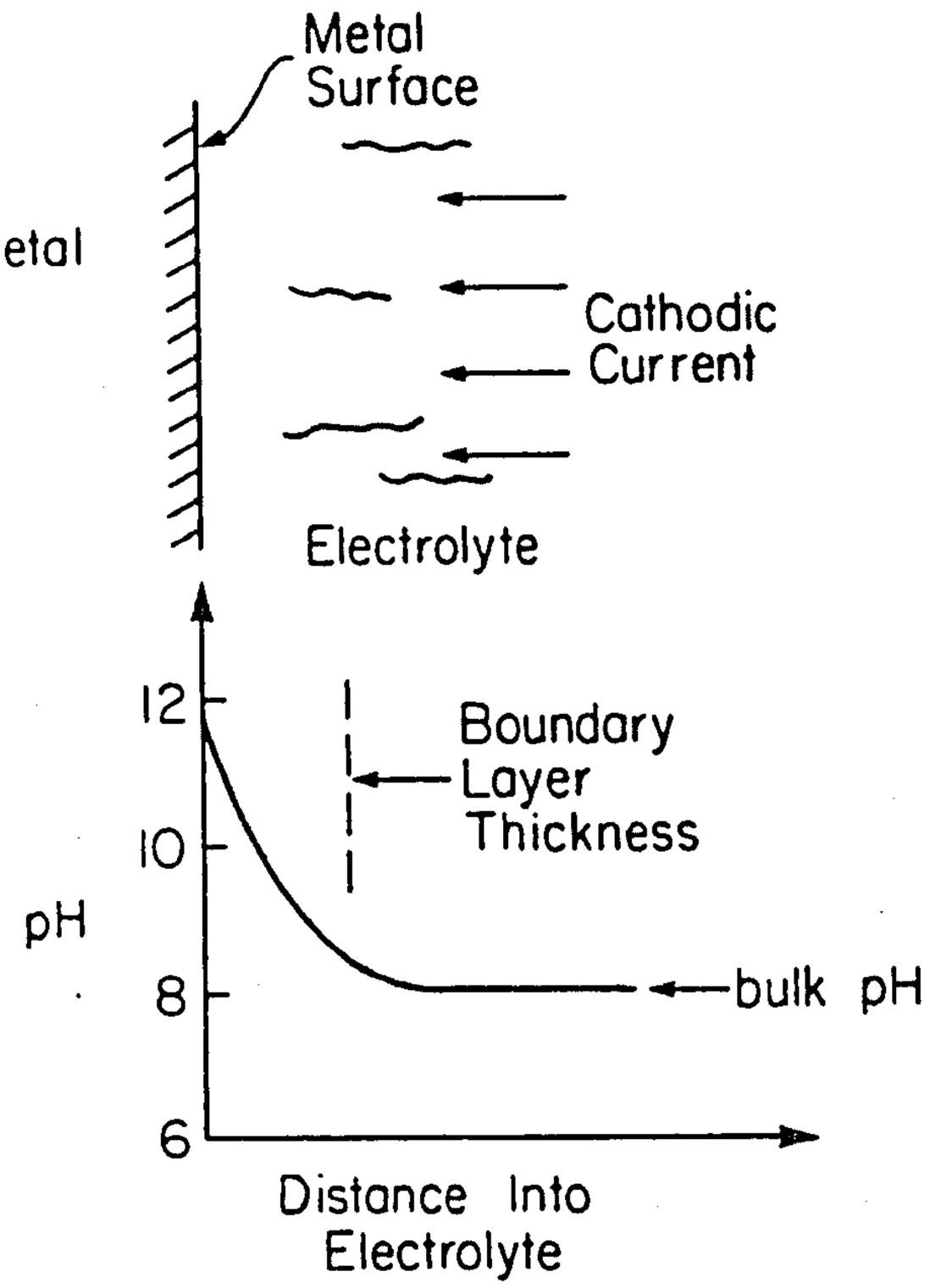

Figure 20 Schematic illustration of the pH profile in the electrolyte adjacent to a cathodically polarised metal surface (Ref 91)

$$H_2CO_3 \rightarrow H^+ + HCO_3^- \quad - (22)$$

$$HCO_3^- \rightarrow H^+ + CO_3^{--} \quad - (23)$$

If OH^- ions are added as a consequence of either of the above cathodic processes (reactions 19 and 20) then the reactions:

$$OH^- + HCO_3^- \rightarrow H_2O + CO_3^{--} \quad - (24)$$

$$CO_3^{--} + Ca^{++} \rightarrow CaCO_3 \text{ (ppt)} \quad - (25)$$

are expected. As soon as the solubility product of $CaCO_3$ is reached, the local OH^- concentration increase allows precipitation of $Mg(OH)_2$ as well, according to:

$$Mg^{++} + 2OH^- \rightarrow Mg(OH)_2 \text{ (ppt)} \quad - (26)$$

These last two reactions are possible for pH values greater than 8.3 and 9.3 respectively. The overall result of equations 21 to 26 is the precipitation of calcareous deposits on the cathodic surfaces in sea water.

The term 'calcareous deposits' is rather misleading; it implies that the surface films found on the cathodic surfaces are composed solely of calcium carbonate, and this is far from correct. The data shown in table 7 (Refs 84,90) indicates that calcareous deposits contain a significant amount of magnesium, especially at higher current densities. The data shown, and X-ray spectroscopy carried out by the author on similar samples, suggest that the magnesium is present primarily as $Mg(OH)_2$ and $MgCO_3$. This is not unreasonable considering the solubility limits and the major ion composition of sea water.

ION	CURRENT DENSITY (mA/cm^2)			
	Freely Corroding	0.054	0.108	0.431
% Na	1.37	0.72	0.85	1.03
% Fe	13.30	3.78	3.46	2.12
% Si	-	0.65	1.77	0.41
% Cl	-	0.44	0.84	0.55
% CO_3	36.20	44.62	32.62	14.70
% Ca	22.80	28.91	20.88	6.73
% Mg	0.86	6.51	13.53	29.47
% Sr	-	0.14	0.06	0.006
% OH (calc.)	-	8.37	18.18	38.52

Table 7. Analysis of calcareous deposits (Refs 84,90)

1.5.2 Properties of calcareous deposits

In order to fully understand the properties of calcareous deposits we must be able to identify not only why they occur, but also when and how they form and the factors which influence their development. The overall properties of calcareous deposits; structure, growth, chemistry, nucleation, etc.; are considered to be affected by five major variables (Ref 91):

(1) Potential/ current density / time
(2) Sea water chemistry
(3) Velocity / agitation of sea water
(4) Temperature
(5) Substrate surface condition.

The more important of these will be discussed separately.

Potential / current density / time

Wolfson and Hartt (Ref 92) observed that the current density decreased with increasing time, and in most

instances achieved a relatively constant value after approximately 100 hours. They attributed this reduction and achievement of steady state conditions in part to the build up of calcareous deposits on the metal surface. Figure 21 (Ref 92) represents a typical current density decay plot for three carbon steel specimens polarized to -780 mV, -930 mV and -1030 mV (S.C.E.) in natural sea water.

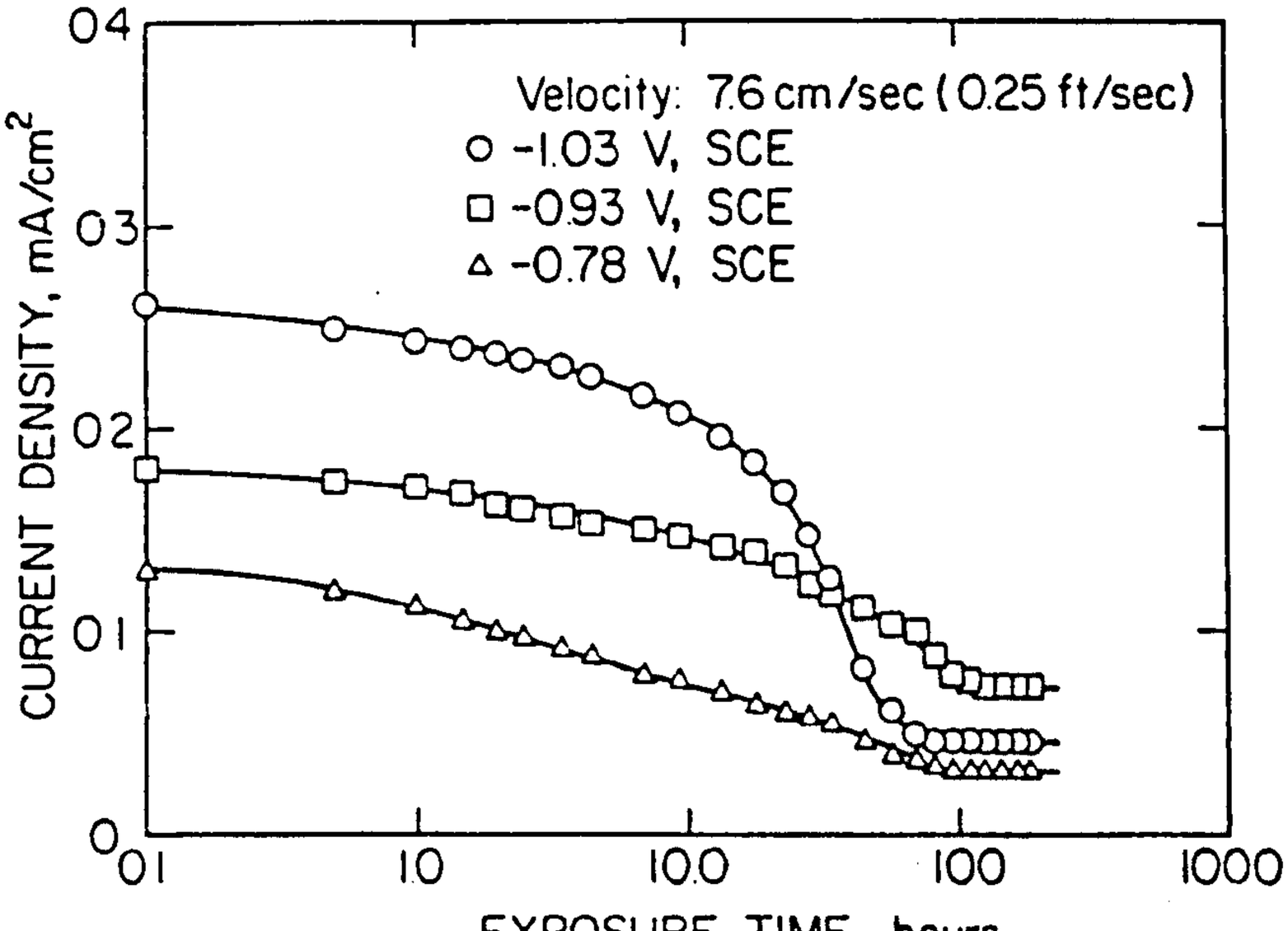

Figure 21. Decrease in current density for steel specimens cathodically polarized in sea water as a function of exposure time (Ref 92)

A point to note in the above figure is how the current density of the -1030 mV (S.C.E.) specimen behaved in relation to the other two potentials. The initial ordering of current densities was in proportion to the magnitude of cathodic polarization, as should be expected. Also, the current density decay for the initial ten hours of exposure was almost the same in each case. Subsequently, however, the decay rate for the -1030 mV (S.C.E.) specimen increased, leading to current densities which after 30 hours were less than for -930 mV (S.C.E.). Presumably, some property of the calcareous deposits formed at the most negative potential was unique in comparison with the other two potentials, and this upset what otherwise may have been a common potential / current density exposure relationship for all three specimens. No explanation was given for this strange behaviour, although it was suggested that it may have been caused by greater specific resistivity of the -1030 mV (S.C.E.) deposit as a consequence of some aspect of it's chemistry or structure or even both.

Experiments by Humble (Ref 84) illustrated how deposit chemistry and properties depended on the magnitude of cathodic current. He found that the concentration of certain ions, namely Na^{+}, Si^{4+} and Cl^{-}, was relatively independent of current density in the range investigated, whereas other ions (Fe^{2+}, CO_3^{2-}, Mg^{2+}, Sr^{2+} and OH^{-}) exhibited an upward or downward trend. The decrease in the Fe^{2+} ion was probably due to the decrease in the corrosion of the specimen as a consequence of the cathodic protection. For the other ions, the variations are probably due to solution chemistry modifications caused by the differing current densities.

Velocity / agitation of sea water

Research by Wolfson and Hartt (Ref 92) has shown that as the velocity of sea water increased, the calcareous deposit film thickness decreased. Figure 22 (Ref 92) illustrates this and also demonstrates that the effect is similar for several different cathodic protection potentials. It was suggested that the reason for the overall effect was the influence of velocity upon the electrolyte pH adjacent to the metal surface.

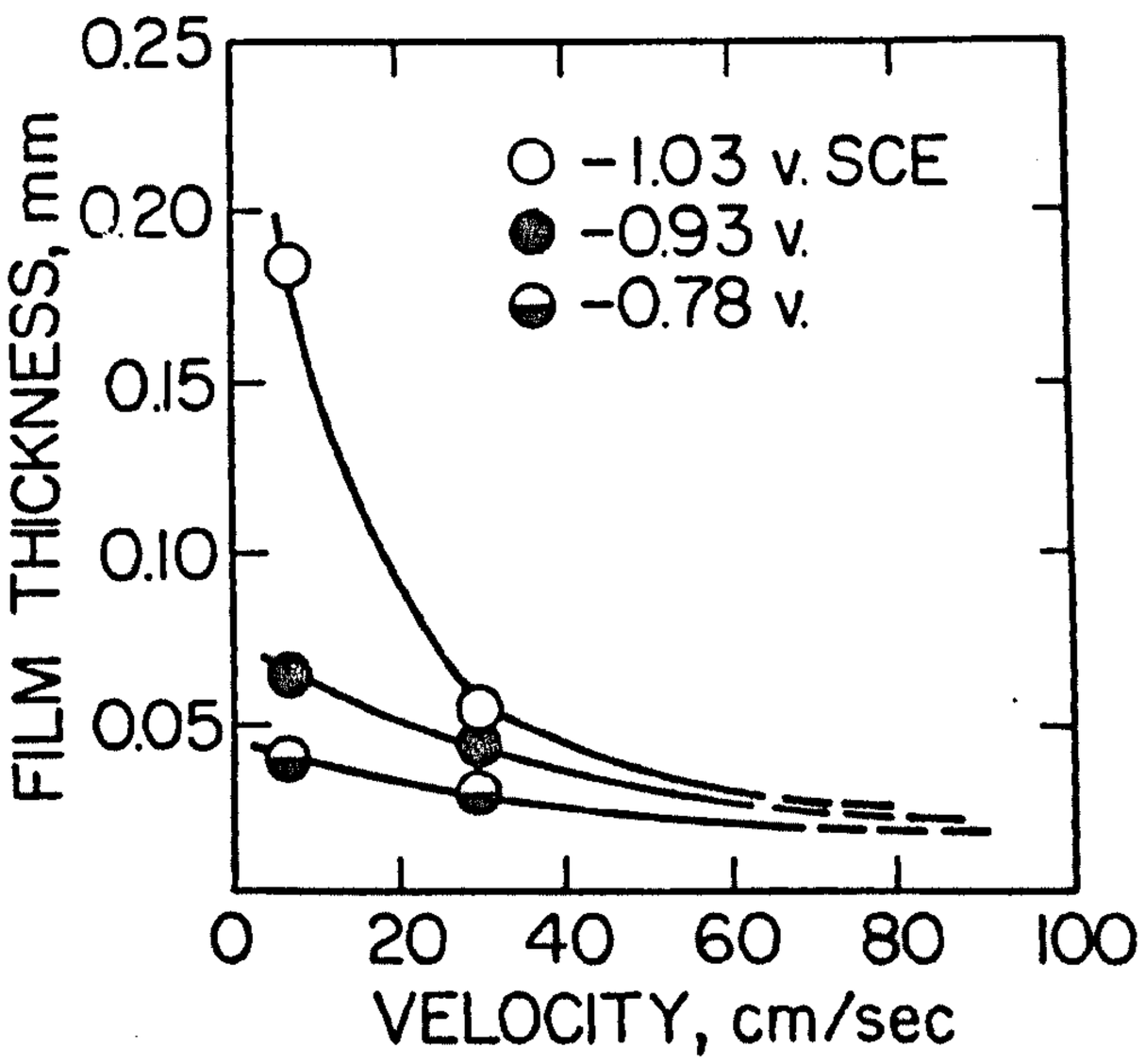

Figure 22. Plot of calcareous deposit film thickness as a function of nominal sea water velocity (Ref 92)

Temperature

Work by Guillen and Felin (Ref 93) has shown that the overall effect of increasing temperature is to increase the amount of calcareous deposit (gauged by weight gain over a 48 hour period). Although the data is limited, it

is consistent with the belief that calcareous deposits form more readily on metal surfaces in warm waters than in cold waters. However, it is possible that other factors such as water movement and chemistry may be influential.

As well as being beneficial in reducing the corrosion rate of steel in sea water (Ref 1), it has been suggested by Scott, Thorpe and Silvester (Ref 94) and Endo, Komai and Suzuki (Ref 89) that calcareous deposits can be helpful in reducing the effects of corrosion fatigue by a plugging action which impedes crack closure (Fig 23, Ref 95).

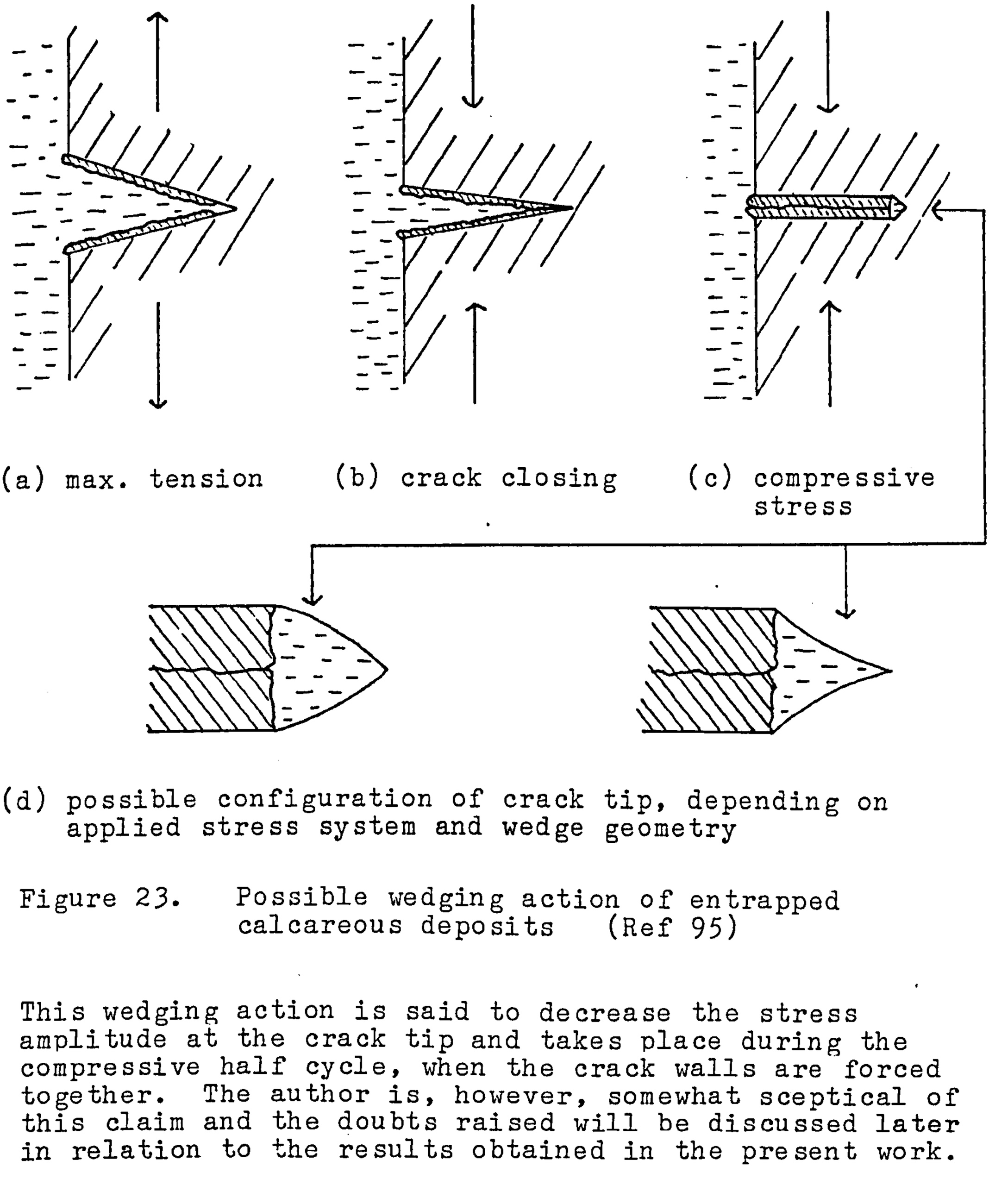

Figure 23. Possible wedging action of entrapped calcareous deposits (Ref 95)

This wedging action is said to decrease the stress amplitude at the crack tip and takes place during the compressive half cycle, when the crack walls are forced together. The author is, however, somewhat sceptical of this claim and the doubts raised will be discussed later in relation to the results obtained in the present work.

1.6 Sea water environment

In order to optimize the performance of materials utilized offshore, it is important that a comprehensive understanding of the nature of the medium to which they will be exposed is achieved. Sea water is perhaps the most aggressive natural environment on this planet. It has some distinctive features which are not common in other natural aqueous solutions and which have a very profound influence in accelerating corrosion reactions. The prime characteristic from the corrosion point of view is the salinity of the sea, a consequence of various chlorides, but there are several other properties which should be appreciated by designers and engineers alike. One example of this can be seen in figure 2 (page 5).

The corrosion rate of many alloys can be greater on parts of an offshore structure that are not continuously immersed in sea water. Therefore, anyone designing or engineering a component using only the life estimations based on total immersion could be in for a nasty shock.

The most important zone is the sea itself, because it is the chemical nature of the sea water that influences corrosion in marine environments. Sea water is also rather more than a solution of chemicals, it is rarely free of suspended particles and the surface is in constant turbulence; the various particles are liable to promote erosion and the unceasing surface movement ensures that, except in a few inshore areas, the sea is always well oxygenated. Sea water is also a biological medium and it's corrosion characteristics can be influenced by the continual biological activity taking place both in open water and on the ocean bed.

There are two major constituents of sea water that are often overlooked when considering the medium. These are animal and vegetable life forms, and they can have both a direct and indirect influence on corrosion. On offshore structures the sheer weight of marine growths can affect not only corrosion by differential aeration but can also influence the dynamic loading of the structure and cause impingement attack by restricting flow in certain areas. It is very difficult to cater for these problems because marine life is subject to a myriad of factors such as water temperature, salinity, depth, distance from the shore, pollution, etc.

1.6.1 Synthetic sea water

Whenever it is necessary to evaluate a material's corrosion and/or corrosion fatigue performance in sea water, the researcher faces an important choice: should natural sea water be used, or a synthetic substitute ? Each solution offers certain advantages and disadvantages.

The natural environment contains the corrosive elements as they naturally occur and requires no simulation. The disadvantage is that all natural marine environments are not identical and can change. A synthetic environment can be engineered to exhibit selective control of certain components of the environment while reducing the effect of or negating others. The major disadvantage of a synthetic environment is that it may not accurately simulate the corrosive and hostile nature of the natural sea water solution.

Many researchers have worked to develop tests in synthetic environments which simulate corrosive behaviour in natural marine environments. The main reason that these tests have been developed is to take advantage of some aspect of the synthetic sea water solution to allow a more rapid and more convenient assessment of a material's corrosion behaviour.

Designing a test environment to simulate corrosion and/or corrosion fatigue behaviour in natural sea water can present many problems. For example, sea water is much more than a solution of sodium chloride and should be viewed as a complex living medium. It contains a myriad of biological species and organic and inorganic matter. Also, a unique property of sea water, compared to many synthetic solutions, is it's buffering capacity.

The most common solutions used to simulate sea water are 3.5% NaCl and synthetic sea water. The synthetic sea water solution, supplied by B.D.H. Chemicals Ltd. for this research work (which complies with DEF 1053 / BS 3900) includes the major inorganic constituents in natural sea water. The solution offers a convenient method of conducting laboratory evaluations, but the results of corrosion tests can be significantly different from those conducted in natural sea water. The relative effects of natural and synthetic sea water and a 3.5% NaCl solution onthe corrosion and corrosion fatigue of high strength steels have been investigated (Ref 53). Substantially different results were obtained; the rates of fatigue crack growth varied by as much as a factor of three, with the natural sea water causing faster crack growth than either of the synthetic environments. However, it must be noted that simple corrosion tests in 3.5% NaCl solutions on mild steel have shown the synthetic solution to give corrosion rates up to three times that of natural sea water. The difference is normally attributed to the deposition of calcium or magnesium salts found in the natural sea water onto cathodic areas (Ref 96).

As a general summing up on the use of sea water as a test medium several points must be noted:

(1) Marine environments are extremely complex media and can affect the outcome of material evaluation tests in many ways.

(2) The use of synthetic environments should be approached with caution, given the multitude of variable factors which can influence the behaviour of materials in these environments.

(3) If correlations are established between test results in synthetic and natural environments for a given material, care should be exercised before applying the same test to other materials or alloy systems.

(4) Extreme caution should be exercised when extrapolating results obtained for small scale specimens in synthetic sea water to large scale structures in natural sea water.

2. OBJECTIVES

1) To assess the corrosion fatigue crack propagation behaviour of a high strength low alloy steel, N-A-XTRA 70, for microstructures associated with parent plate and heat affected zone configurations immersed in synthetic sea water.

2) To examine the surface deposits generated by cathodic protection and determine their effect on the corrosion fatigue crack propagation behaviour of N-A-XTRA 70, for parent plate and heat affected zone microstructures.

3) To modify the standard single edge notch specimens by the addition of transparent plastic covers on the sides of the notch and crack and assess the corrosion fatigue crack propagation behaviour of N-A-XTRA 70 as outlined in (1) above.

4) To assess the effect of various degrees of under-protection and over-protection on the corrosion fatigue crack propagation behaviour of N-A-XTRA 70 for microstructures associated with parent plate and heat affected zone configurations.

5) To assess the viability of computerised methods for generating da/dN and ΔK values from experimental data.

3. EXPERIMENTAL

Due to the fact that earlier work had been carried out on corrosion fatigue by Shepherd (Ref 97), Thompson (Ref 98) and the author (Ref 99), a corrosion fatigue test rig and well defined experimental procedure were already in operation for this project. All experimental work was carried out using pre-cracked, single edge-notched (S.E.N.) specimens which were subjected to fatigue using a three point bend load configuration.

In an attempt to simulate North Sea environmental conditions, the corrosion fatigue testing was carried out with the test specimens completely immersed in a flowing, aerated, synthetic sea water solution. A loading frequency of 0.1 Hz and a solution temperature of 8°C were chosen to best represent the average 14 second wave period and average temperature (Ref 3) experienced in the North Sea. In order to simulate a fatigue crack in a constant state of tension, a load ratio of 0.6 was chosen.

3.1 The test machine

The test machine used throughout this project is a further development of the one designed for use by Shepherd in 1977 for corrosion fatigue testing under three point bending conditions (Ref 97). The machine, based on an existing high frequency electro-hydraulic fatigue testing machine, with specimen tank and associated electronic controls are shown in figure 24.

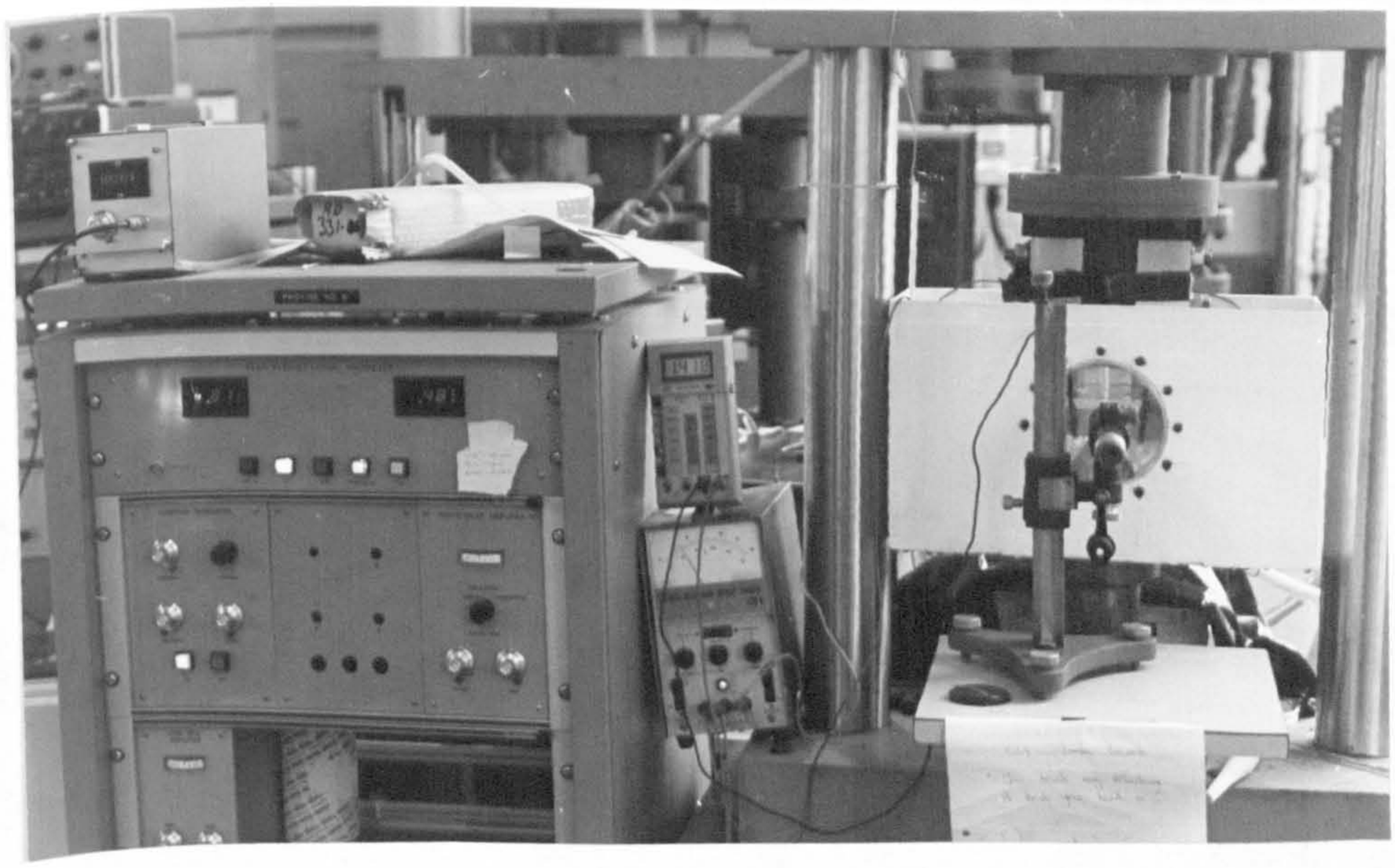

Figure 24. Test machine and associated electronics

Mounted to an upper central pillar and electrically insulated by a paxolin block are two fixed steel rollers. These oppose the load which is applied to a specimen, supported by and acted on by a lower central steel roller. This roller is pillar mounted to the specimen tank bottom, a clear silicone sealant giving a watertight seal. The specimen tank has two clear perspex observation parts cut on opposite sides, thus allowing optical crack measurement of both sides of the specimen to be carried out. The complete specimen tank sub-assembly is mounted via a paxolin spacer, again for electrical insulation, to a steel balance plate which is assembled to an adaptor plate fixed to the end of the hydraulic ram extension. With this arrangement there is no need for a seal around the ram extension as would be the case if the tank were stationary and the ram moved through the tank bottom.

A schematic block diagram of the control system for the fatigue machine is shown in figure 25. Control is achieved by means of a simple load controlled closed-loop servo system. The output from the function generator is sinusoidal, triangular and square wave outputs may also be obtained , the amplitude and mean load being variable. This signal is passed through an error measuring circuit to the servo amplifier which is connected to a summing amplifier. The output from the servo amplifier is passed to the servo-hydraulic control valve (Moog valve), which in turn controls the flow rate and direction of mains pressure hydraulic fluid to the double acting hydraulic ram.

Under the action of mains hydraulic pressure, the ram moves until resistance to movement is encountered, caused by the presence of the specimen or until the ram reaches the end of its travel if the specimen is not present. When resistance to movement, caused by the central pillar and roller coming into contact with the specimen, is encountered, load is applied to the specimen, the magnitude of which is registered by the load cell. Under load, the load cell provides an output signal which passes through and is amplified by the load cell amplifier and is then fed to the error measuring circuit. The output signal from the error measuring circuit is used to reduce the input to the servo amplifier. The reduced input is amplified and loading of the specimen is continued until the signal fed back from the load cell, via the load cell amplifier, is sufficient to cancel out the signal from the function generator and reduce the input to the servo amplifier to zero. At this stage, the ram will continue to exert a constant load on the specimen until the output from the function generator is altered. This is the process by which sinusoidal loading is applied to the specimen.

In this machine the only moving parts are the ram and the tank mass, and during fatigue this movement is negligible,

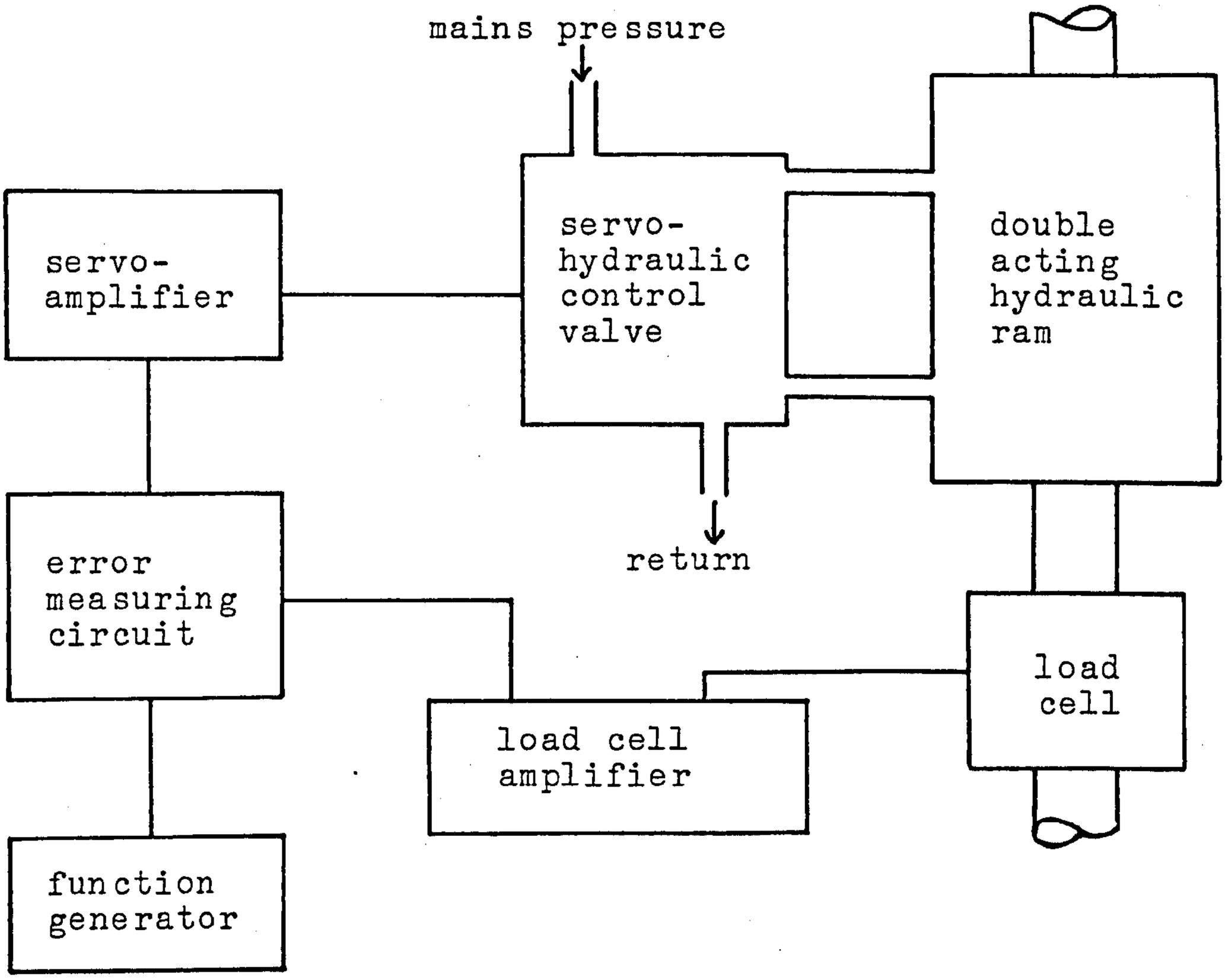

Figure 25. Schematic diagram of the load controlled, closed-loop, servo control system

which creates low inertia in the system and hence provides extremely good system response. The only adjustments that need to be made are occasional alterations of the load and offset controls to compensate for slow drift.

3.2 Materials

The specimens used in this project were all prepared from N-A-XTRA 70, a high strength low alloy quenched and tempered steel, manufactured by Thyssen Stahl Aktiengesellschaft of West Germany. This material is normally available in the thickness range of 3 to 50 mm, with a maximum width of 4000 mm (depending on thickness) and a maximum length of 14000mm (Ref 101). The plate material delivered to Cranfield was 30 mm thick. The manufacturer's chemical composition is given in table 8 (Ref 101), which can be compared with the N.E.I. International Combustion Limited analysis of the parent plate material and the weld metal as used in the fatigue specimens.

The steel's blend of properties, as shown in tables 9 (Ref 103) and 10 (Ref 102), arise not only from it's chemical composition but also because of it's process route, namely quenching and tempering.

	Chemical composition in % wt.												
	C	Si	Mn	P	S	Cr	Mo	Zr.	N	Al	Ni	Cu	Ti
*1	0.2 max.	0.4-0.8	0.7-1.2	0.025 max.	0.025 max.	0.5-1	0.2-0.6	≤0.12	/	/	/	/	/
*2	0.16	0.59	1.07	0.01	0.006	0.74	0.34	0.08	0.012	0.036	/	/	/
*3	0.16	0.64	1.05	0.016	0.004	0.7	0.39	/	/	0.04	0.1	0.07	0.023
*4	0.07	0.28	1.25	0.017	0.003	0.13	0.52	/	/	0.03	0.05	0.09	0.006

* Reference : 1 Thyssen AG : General information
2 Thyssen AG : Plate delivered to C.I.T.
3 NEI INTERNATIONAL COMBUSTION LTD : Parent material
4 NEI INTERNATIONAL COMBUSTION LTD : Weld metal

Table 8. Chemical composition of N-A-XTRA 70 and of weld metal (Ref 101)

Plate thickness mm	Specimen orientation	Yield strength MPa	Tensile strength MPa	Elongation %	Reduction in area %
10	longitudinal	731	845	20	65
25	"	738	852	20	66
50	"	712	827	19	63
10	tranverse	746	858	18	62
25	"	739	849	19	60
50	"	721	834	18	61

Table 9. Deformation data for N-A-XTRA 70 (Ref 103)

specimen orientation	Impact work (J) minimum values				
	Temperature				
	$-75^{o}C$	$-60^{o}C$	$-40^{o}C$	$-20^{o}C$	$\pm 0^{o}C$
longitudinal	27	30	40	50	60
transverse		27	30	35	40

Table 10. Impact strength of N-A-XTRA 70 ISO-V notch specimen (Ref 102)

After initial hot rolling when the material's microstructure consists of upper bainite, a heat treatment regime is instigated. It commences with heating to temperatures above $920^{o}C$ (A_3) at which austenisation takes place and carbides are largely dissolved. This is followed by rapid cooling by means of a pressurised water quench, resulting in a transformation of the structure at the martensite or lower bainite stages, as seen on the time-temperature transformation curve in figure 26 (Ref 102). Due to the low carbon content of the material, martensite with a cubic lattice is formed at temperatures higher than $400^{o}C$. This martensite has a low distortion and is very tough. The lower bainite, characterised by well distributed carbides, is also very tough. The less tough upper bainite as well as pearlite and ferrite are not formed at these high cooling rates.

After quenching, the steel is tempered at temperatures between 650 and $720^{o}C$, producing an extremely fine ferrite substructure with well distributed fine carbide and nitride precipitates which help to promote a fine grain size. This small grain size is a decisive factor in obtaining the strength and toughness of the steel.

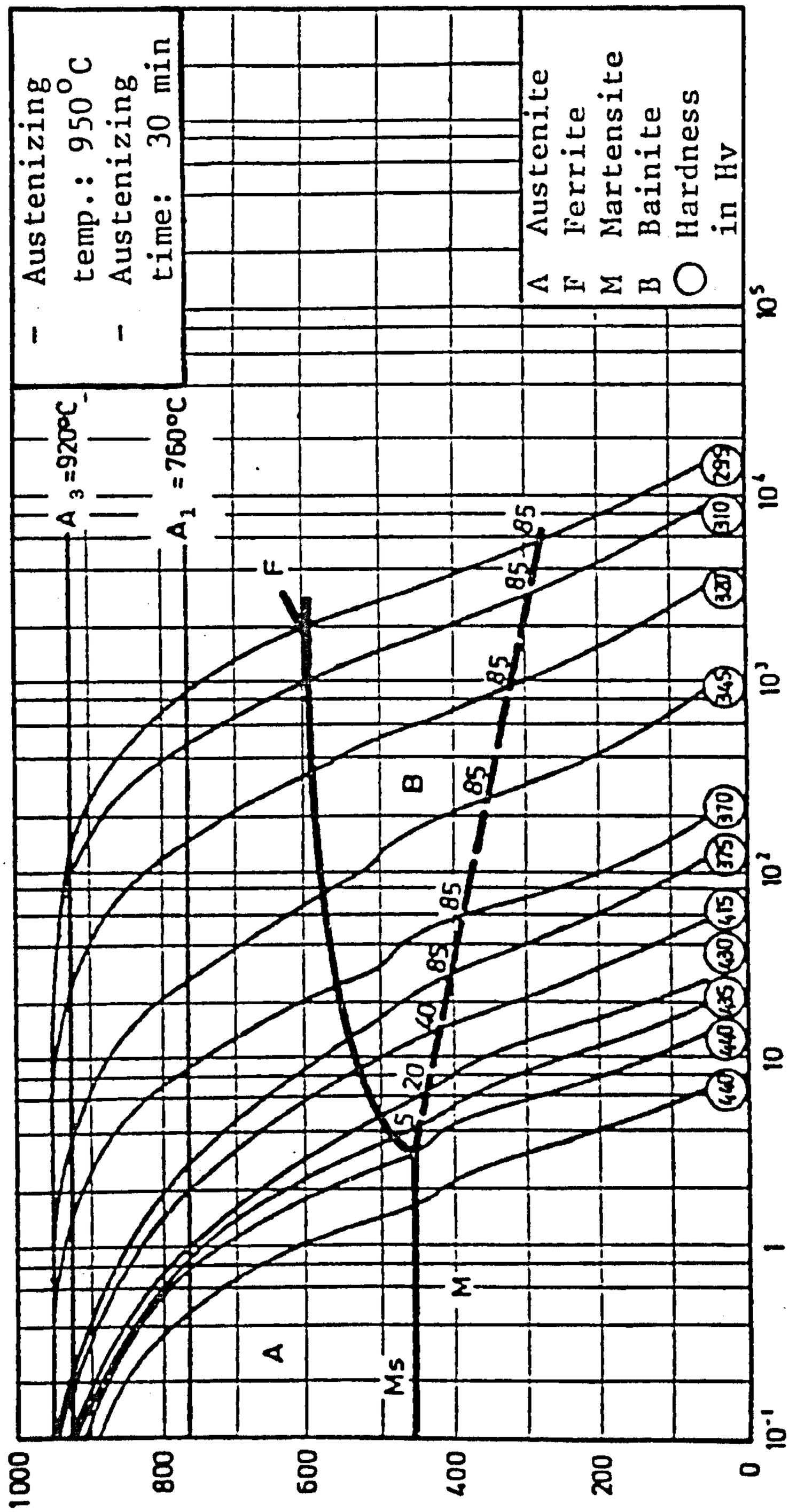

Figure 26. Time-temperature-transformation curve for N-A-XTRA steels (Ref 102)

3.3 Welding procedure

The welding of N-A-XTRA 70 may be accomplished with any proven process, either in a workshop or on site. However, to obtain welds with no cracks and full load bearing strengths, the following requirements must be met :- (Ref 101)

* The use of suitable alloy consumables to obtain such mechanical properties in the welded material as will meet the requirements.

* The humidity should be excluded during welding to ensure low hydrogen percentages in the weld in order to prevent the occurrence of cold cracking.

* A choice of adequate thermal cylces during welding to obtain sufficiently high cooling rates in the H.A.Z. in order to reach the required mechanical properties.

For welding heavy gauge material, pre-heating should be carried out at a temperature in the range 100-200^{o}C. This is due to the fact that as the thickness increases, post weld internal stresses also increase.

For this project, welding was carried out using the sub-merged arc technique. The equipment consisted of a Hagglunds LSIT 1200 amperes power source and a Hagglunds HSA welding head. This automatic unit worked above a traversing table, the speed of which was controlled by a Kopp variator.

The welding operation consisted of eight runs, the operating parameters of which can be broken down into the following subsections.

3.3.1 Plate preparation

The preparation of the plate is illustrated in figure 27. An asymmetrical, Vee shaped bevel was chosen to obtain a straight H.A.Z. in order to facilitate fatigue crack growth exclusively in the H.A.Z. material.

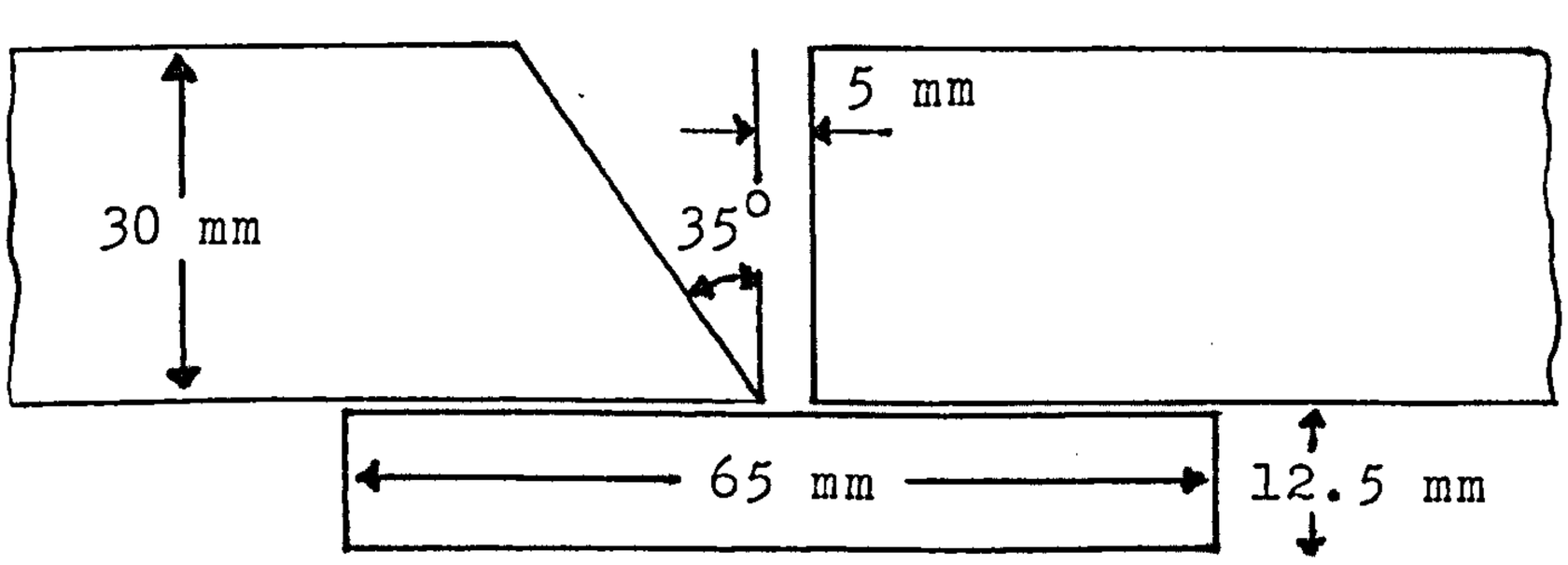

Figure 27. Plate preparation

3.3.2 Welding parameters

Welding process	:	submerged arc welding (SAW)
Joint type	:	butt weld
Bevel	:	asymmetrical V-35°
Welding position	:	flat
Back gauging	:	yes
Filler wire	:	SD3 Mo,4mm diameter
Flux	:	OP41TT
Preheating	:	none
Interpass temperature	:	150°C
Current	:	500 A
Voltage	:	30 V
Welding speed	:	300 mm/min
Number of runs	:	8 (see figure 28)
Heat input	:	3 KJ/mm

During the welding, if the interpass temperature was greater than 150°C, the plate was allowed to cool before the next run. There was no heat treatment after welding. Table 11 (Ref 104) gives the welding rod and flux analysis.

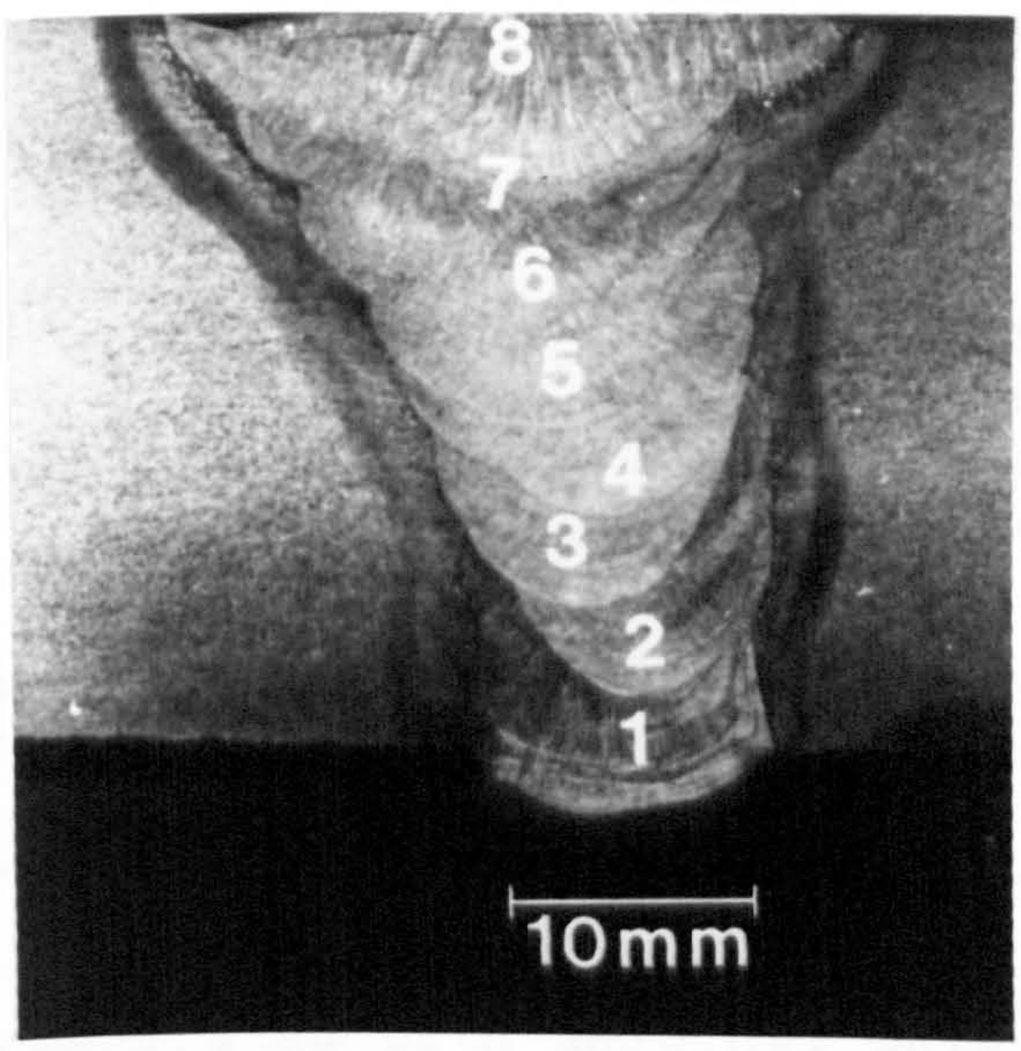

Figure 28. Macrograph showing welding sequence

Welding Rod : SD3 Mo x 4mm diameter

C	Mn	Si	Mo
0.05-0.08	1.2-1.5	0.25-0.4	0.5

Flux coating : OP41TT

$SiO_2 + TiO_2$	CaO + MgO	Al_2O_3 + MnO	CaF_2
10%	35%	20%	30%

Table 11. Welding rod and flux analysis (welding rods were baked at 300°C for 2 hours prior to welding) (Ref 104)

3.4 Test specimens

All test specimens were manufactured from N-A-XTRA 70 steel in either the as-received parent plate condition or the submerged arc welded parent plate. The plates used for both the welded and parent specimens were cut from the original steel plate in such a way that the longitudinal axis of the specimens were parallel to the rolling direction. This allowed for projected fatigue crack propogation at 90^{o} to the rolling direction, as shown in figure 29.

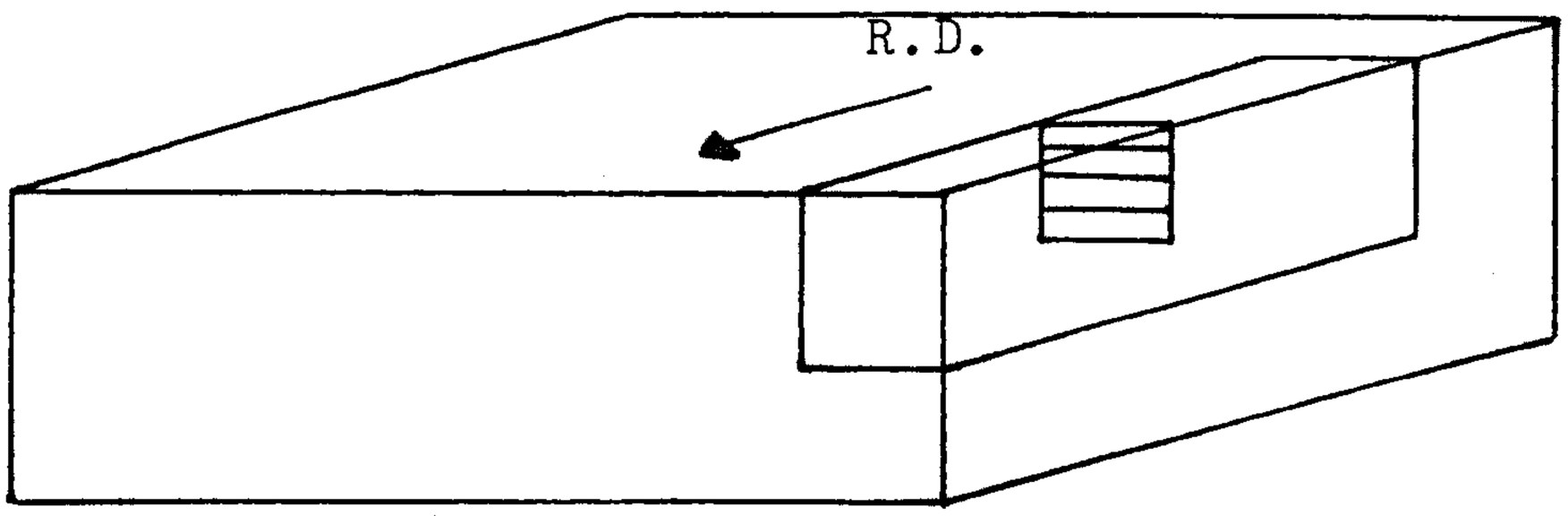

Figure 29. Schematic of specimen position in rolled plate

All specimens were designed and manufactured in accordance with BS 5762 : 1979 (Ref 105), as shown in figure 30. These all had a 60^{o} Vee notch machined into them to a depth of 8mm. In the case of the welded specimens, this notch was situated in the heat affected zone. This enabled the fatigue crack to grow through the H.A.Z. during the course of the experimental run (Fig 31).

Before any prefatigue or test run, the notch area was polished with emery paper and finally with diamond paste of 6µm grade, followed by thorough cleaning and drying, in order to facilitate crack length readings.

Due to the fact that the high hardness values produced in the H.A.Z., associated with welding, were considered to be important, it was decided to test material which had been heat treated to give a hardness value of over 350 Hv. This value is typical of that found in the H.A.Z. by the author (Ref 99) and is also considered to be critical for hydrogen cracking (Ref 100).

To this end, heat treatment consisting of $950^{o}C$ for 30 minutes, water quenching, $550^{o}C$ for 30 minutes and finally air cooling, was performed on several N-A-XTRA 70 specimens. This produced a hardness value of 380 ± 8 Hv for the material whilst still retaining a fine tempered martensite and lower bainite microstructure.

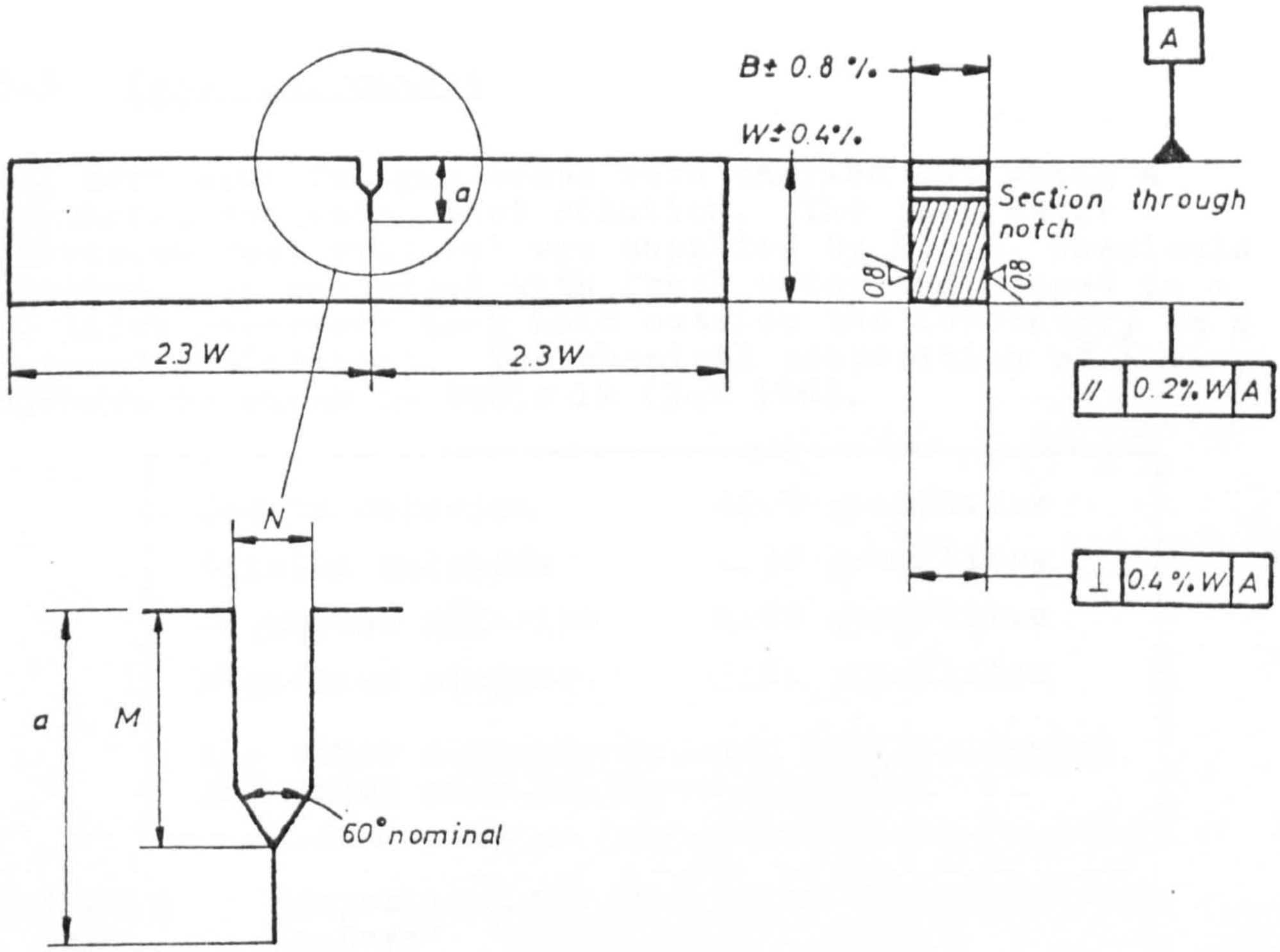

Width (W) = 26mm
Thickness (B) = 0.5 W = 13mm
Half loading span (L) = 2 W = 52mm
Notch width (N) = 1.5mm
Effective notch length (M) = 8mm
Effective crack length (a) = 0.45 W to 0.55 W (11.7 to 14.3mm)

Figure 30. Proportional dimensions and tolerances for bend test pieces according to BS 5762:1979 (Ref 105)

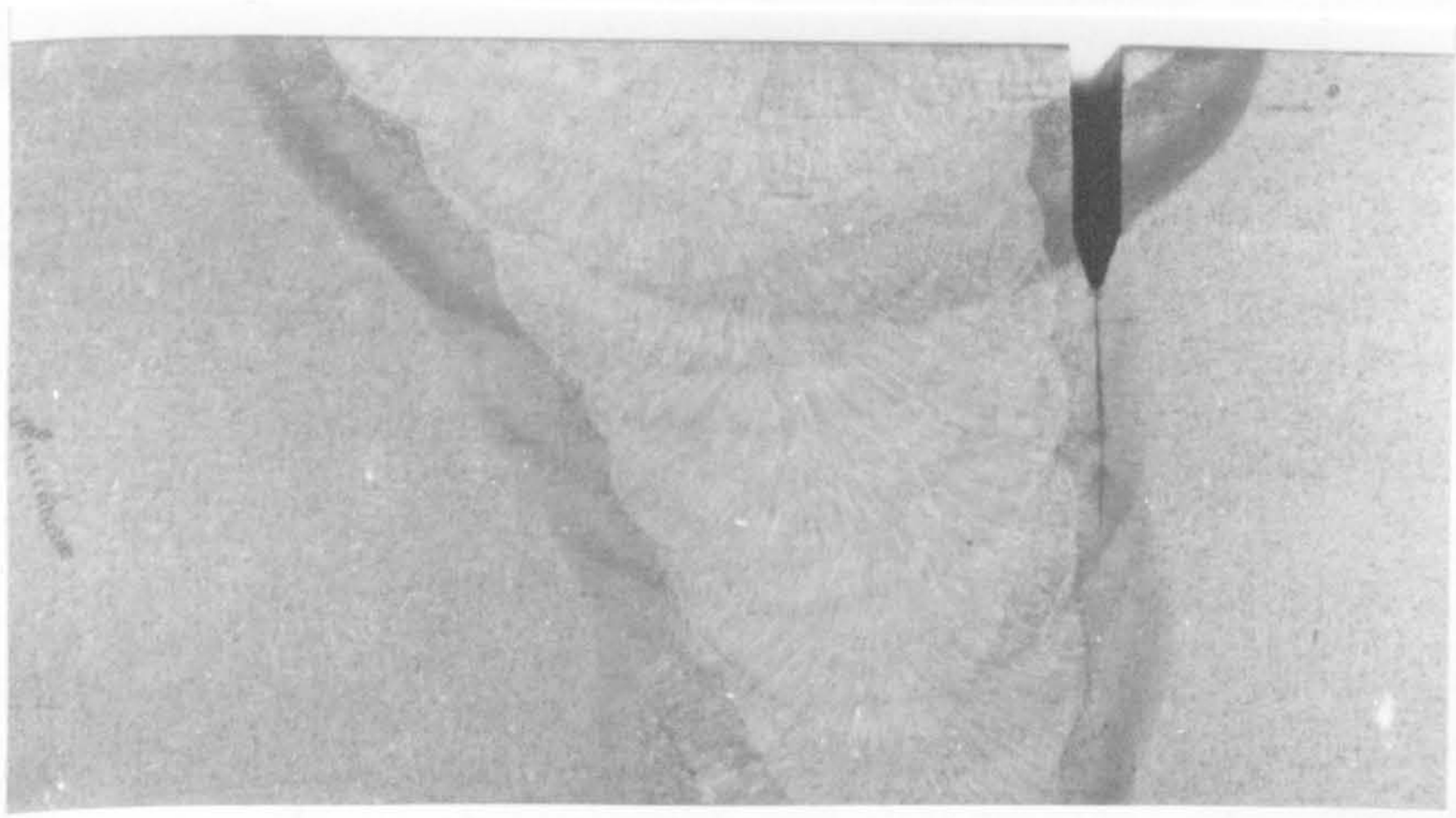

Figure 31. Macrograph showing machined notch and subsequent corrosion fatigue crack growth in the H.A.Z.

3.5 Test environment

All corrosion fatigue tests were carried out using a synthetic sea water test solution. The 'Sea Water Corrosion Test Mixture' was supplied by B.D.H. Chemicals Limited. It was mixed with fresh water and housed in a 90 litre reservoir tank held outside the laboratory in a covered emplacement. The chemical composition of the mixture is shown in table 12 (Ref 106).

Sodium chloride	24.9 gram/litre
Calcium sulphide	1.50 gram/litre
Magnesium chloride	2.99 gram/litre
Magnesium sulphate	2.00 gram/litre

Any other elements present are incidental and exist only as trace elements.

Table 12. Composition of 'Sea Water Corrosion Test Mixture' (Ref 106)

The reservoir tank was fitted with a copper coil which contained circulating cooling water from a refrigeration unit. Polystyrene insulation on five sides of the tank helped to maintain the solution at a temperature of around 8°C, while a cover helped to reduce evaporation losses. The interior of the specimen tank was coated with Lacomit to minimise corrosion of the tank and prevent a galvanic reaction between the specimen and the tank.

The test solution, the pH of which was approximately 7, was circulated through the specimen tank at a rate of around 2 litres/minute. It entered at the top of the tank through a nozzle arrangement, which caused vigorous aeration, and was bled off at the bottom, as shown by figure 32.

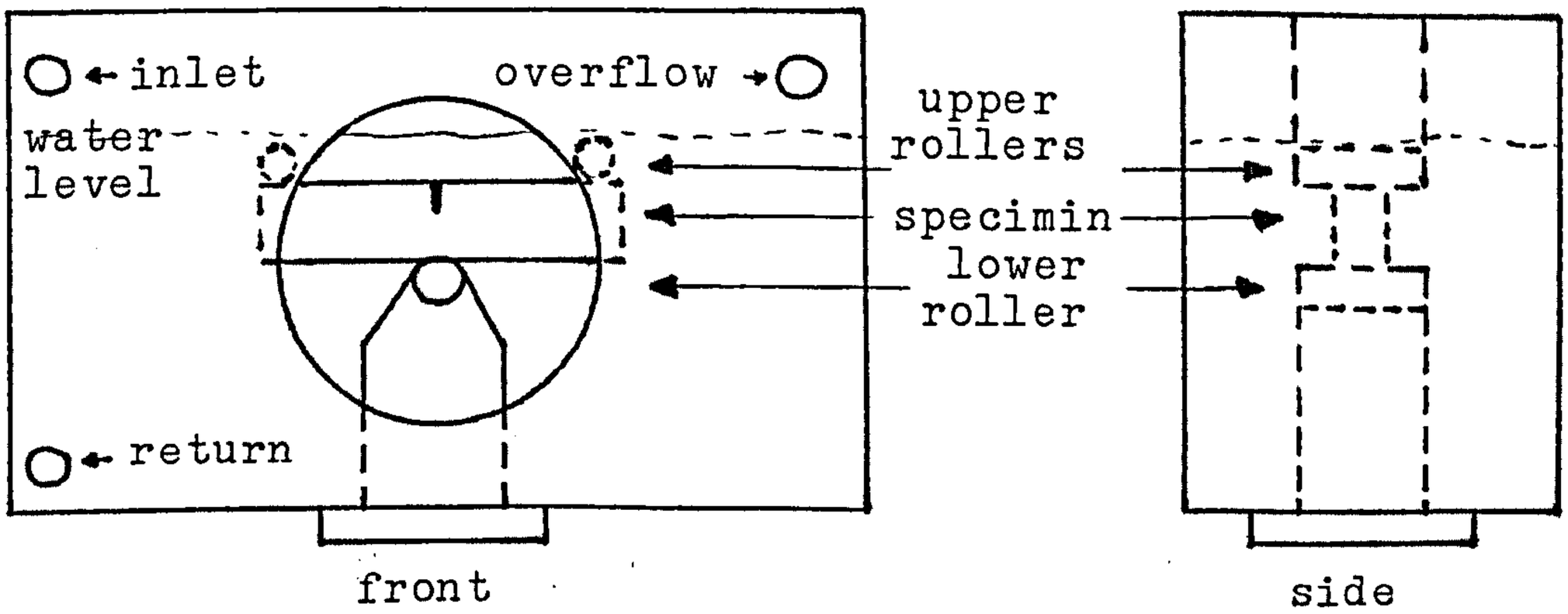

Figure 32. Schematic illustration of specimen arrangement and water level control

The water level was maintained such that the specimen was fully immersed at all times. The return pipes stopped short of the water surface in the reservoir tank, thus enabling the water to free fall and hence aid aeration of the solution bulk.

3.6 Cathodic protection system

As a consequence of the relatively small size of the test specimens used and the difficulty expected in producing a small enough sacrificial anode range to cover the potential conditions envisaged for the test program, it was decided to continue using the impressed current system that the author had found satisfactory in earlier work (Ref 99). The apparatus consisted of a stabilised power source which was used to control the potential applied to the specimen, a digital multimeter to monitor this potential, a saturated calomel electrode (S.C.E.), and a platinum electrode. The whole system was connected as shown in figure 33.

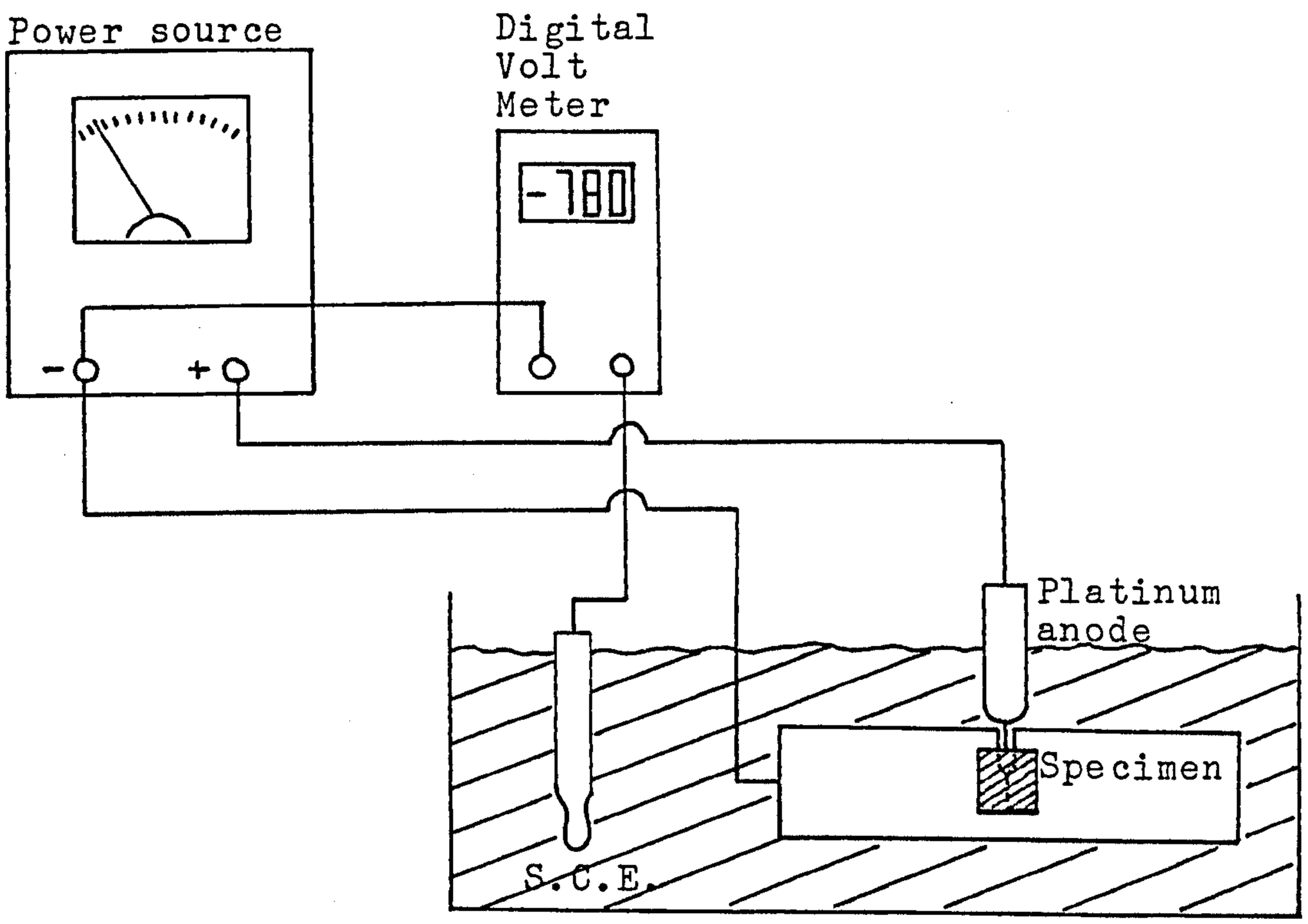

Figure 33. Schematic diagram for impressed current cathodic protection experimental layout

Since the cathodic protection potential was controlled by a stabilised power source, it was necessary to monitor and manually adjust it occasionally. At the start of each test this was frequently necessary due to the specimen polarising and the system 'settling down'. Figure 34 demonstrates how the potential will change due to polarisation.

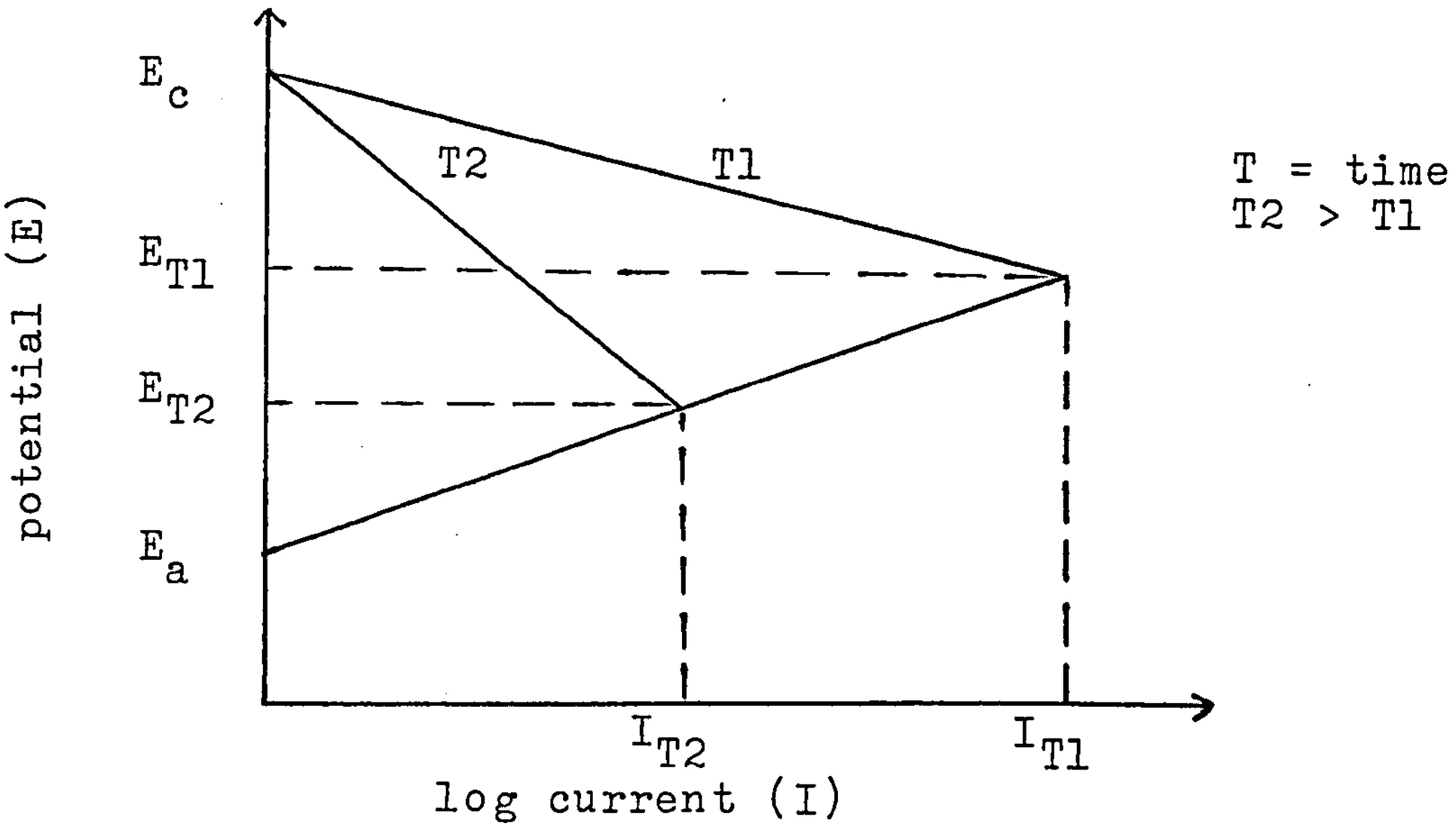

Figure 34. Reduction in potential and current due to polarisation

3.7 Crack growth measurement

In all cases, during the experimental work carried out in this project, crack length measurements were made using a vertical travelling vernier microscope, magnification X 10, mounted on a wooden platform securely fixed to the side of the fatigue testing machine (Fig 24). The accuracy of this method and all sources of possible error will be discussed in the results section.

Except in the case of correctly protected specimens, it became increasingly difficult to measure the crack length as the test progressed. This was due to the formation of corrosion products and surface films or calcareous scales in the overprotected case. It was also necessary to allow for the pumping action of the growing fatigue crack. In order to facilitate accurate crack length measurement, a method was developed in which the specimen surface around the crack tip was cleaned before each reading. To this end a short bristle paint brush was used to gently remove the surface deposits. This technique did not prove to be detrimental to the testing and had no adverse effect on the fracture surface deposits, fatigue crack propagation or potential measurement.

Despite the limitations and restrictions caused by using the optical crack growth measurement technique (discussed later), the method has been proved to be effective and satisfactory for corrosion fatigue studies (Refs 97,98,99,). For fatigue crack propagation in air the electrical (D.C.) potential drop (P.D.) technique has found much favour. This

method involves measurement of the electrical potential change with increasing crack length. Extensive reviews by Aronson and Ritchie (Ref 107) and Gangloff (Ref 108) have shown that P.D. techniques are technically complex and subject to crack length measurement errors by such things as probe positioning and applied electric current. These error - inducing factors are a serious cause for concern when the technique is applied in the context of corrosion fatigue, where any cathodic protection current may influence the readings and, in the case of a sea water environment, there will be an electrically conducting medium within the crack. For these reasons, and the satisfactory performance reported earlier for the optical measurement method, it was decided that an electrical measurement system would offer no clear advantages and therefore the decision was made to use the optical method.

3.8 Experimental procedure

Corrosion fatigue tests were carried out on specimens where the fatigue crack was initiated and propagated through the parent plate and on specimens where the fatigue crack was initiated and propagated through the heat affected zone material, under the following environmental conditions:

1) Free corrosion
2) -700 mV (S.C.E.) $\pm$ 1.0 mV (S.C.E.)
3) -780 mV (S.C.E.) $\pm$ 1.0 mV (S.C.E.)
4) -1300 mV (S.C.E.) $\pm$ 1.0 mV (S.C.E.)
5) -1400 mV (S.C.E.) $\pm$ 1.0 mV (S.C.E.)
6) Initial correct protection at -780 mV (S.C.E.) then severe overprotection at -1300 mV (S.C.E.) and finally back to correct protection at -780 mV (S.C.E.)
7) In air at ambient temperature and relative humidity (parent plate only)
8) Heat treated material at -1400 mV (S.C.E.)

In each of the categories several specimens had both sides of the crack covered with a transparent plastic sheet. This was done in order to stimulate an actual 'real' crack where the sea water environment entered only from the top and not the sides (Fig 35).

It was believed that S.E.N. type specimens did not give a true representation of corrosion fatigue and environment ingress associated with a 'thumb nail' crack. Specimens were modified to include the plastic covers in an attempt to discover if the corrosion fatigue crack propagation behaviour was influenced by the S.E.N. specimen design.

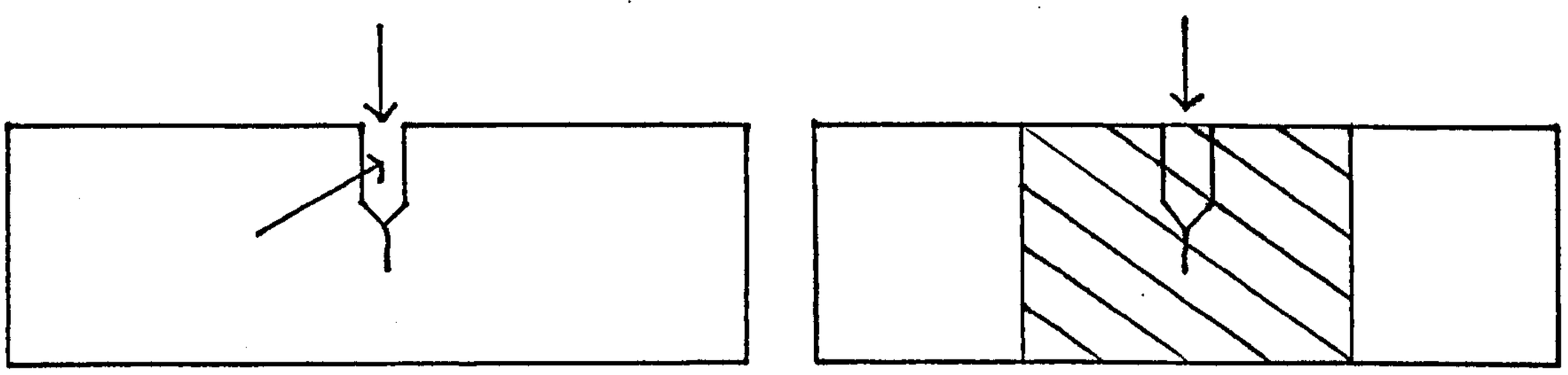

Figure 35. Schematic representation of plastic modification to normal S.E.N. test specimens

All specimens in groups 1 to 8 inclusive were initially prefatigued at 20 Hz. Experimental loads + 10% were used to initiate the prefatigue crack from the machined starter notch. Overall, all test specimens had a comparable initial fatigue crack length of 13.00 ± 0.20 mm.

3.8.1 Experimental procedure for fatigue tests in air

Before the specimen was taken from a moisture free environment, a dummy bar was positioned in the fatigue testing machine (less sea water) and the fatigue loads adjusted to equal those of actual experimental proportions. The test machine was then run for approximately twenty minutes to allow the machine, the servo hydraulics, and the associated electronics and instrumentation to stabilise at their working temperatures. At the end of this period the dummy bar was replaced by the specimen. The position of the specimen in the fatigue machine was such that the notch was directly above the centre of the lower roller. When it had been lined up correctly the ram was raised. By means of the offset control and the gain control, the maximum and minimum loads were attained. These were checked by reference to the peak and trough digital meters incorporated in the control panel. The test was allowed to continue at a frequency of 0.1 Hz, maximum load 8.14 KN, minimum load 4.88 KN and an R value of 0.6. Once started the test was run continuously until the specimen failed. At this stage it was stored in a moisture free environment pending detailed examination.

3.8.2 Experimental procedure for corrosion fatigue tests at free corrosion potential

The procedure outlined in the air experiment was followed

except for the following modifications:
With the specimen in position, the test machine was set to a nominal holding load at the level of the calculated experimental mean. Next the simulated sea water test solution was admitted to the specimen tank. It's temperature was already down to the experimental value of $8^{o} \pm 2^{o}C$ since the refrigeration unit was never switched off. In this condition the specimen potential was allowed to stabilise, which for free corrosion was -663 ± 1 mV (S.C.E.), this occuring after 4 or 5 hours. The cyclic load was then applied and the corrosion fatigue crack propagation test carried out.

Once the specimen had failed it was removed, washed in distilled water and with isopropyl alcohol, and dried with a warm air blower. The specimen was then clamped in a vice and broken in two using a hammer. One side of the fracture surface was cut up and mounted on a stub in preparation for examination in a scanning electron microscope (S.E.M.).

3.8.3 Experimental procedure for fatigue test at a cathodic protection potential of -780 mV (S.C.E.)

The procedure followed was similar to that outlined in section 3.8.2 above except for the following modification:
With the static load in effect, the necessary electrical connections were made as shown in figure 33. The simulated sea water test solution was admitted to the tank and the power supply adjusted to force the specimen potential down to -780 ± 10 mV (S.C.E.). Again, the potential was allowed to stabilise before the cyclic load was applied and the test instigated.

3.8.4 Experimental procedure for corrosion fatigue tests at cathodic protection potentials of -1300 and -1400 mV (S.C.E.)

The general procedure was identical to that detailed in section 3.8.3 above, amended for potential readings of -1300 and -1400 mV (S.C.E.) respectively.

3.8.5 Experimental procedure for corrosion fatigue tests at cathodic protection potentials of -780 mV (S.C.E.) with temporary overprotection of -1300mV (S.C.E.)

The general procedure was similar to that described in section 3.8.3 above. However, the following modifications were carried out:
The test was allowed to continue with the specimen potential

reading -780 mV (S.C.E.) until the measured crack length had reached approximately 15.5 mm. The power supply was then adjusted to provide a specimen potential of -1300 ± 10 mV (S.C.E.). This situation continued until approximately 2800 cycles had elapsed, when the power supply was again adjusted to give a specimen potential of -780 mV (S.C.E.).

In the cases where the fracture surfaces of the over-protected specimens were to be examined by the S.E.M., a procedure was developed for removing the often tenacious calcareous deposits. This involved washing the surfaces in water and then dilute inhibited hydrochloric acid, ultrasonic cleaning in gramosol, washing with alcohol and drying with a hot air blower. This process was repeated several times in the case of the more adherent deposits.

Throughout the tests, experimental readings of crack length, a, were recorded periodically after suitable crack increments by means of a vertical travelling vernier microscope. The corresponding number of cycles, N, were read from an electro-mechanical device linked to the testing machine. The crack growth rates, da/dN, were calculated graphically by the tangent to curve technique from plots of a against N.

A finite difference method was used after each reading to obtain an immediate indication of the crack growth rates. As the finite difference calculations between successive values result in erratic gradients, they were not used to produce the da/dN versus ΔK plots.

The stress intensity factor, K, and the stress intensity range, ΔK, were calculated using the formula recommended in BS 5447:1977.

$$K = \frac{3PL}{Bw^{3/2}} \quad Y \qquad -(27)$$

where: P = applied load
B = specimen thickness
Y = f(a/w) = stress intensity factor coefficient
a = effective crack length
w = specimen width
L = half loading span

However $L = 2w$

hence

$$K = \frac{6PY}{Bw^{\frac{1}{2}}} \qquad -(28)$$

where $Y = 1.93(a/w)^{\frac{1}{2}} - 3.07(a/w)^{3/2} + 14.53(a/w)^{5/2}$
$- 25.11(a/w)^{7/2} + 25.80(a/w)^{9/2}$ $\qquad -(29)$

Measurement of the crack length was carried out with the test machine in motion. Previous research, which used a method in which the fatigue load was halted (Ref 97), found that there was a high probability that crack blunting could occur. It is possible that this may lead to subsequent retardation of crack propagation when the fatigue loading was restarted. Obviously greater care was needed with the dynamic method of crack measurement. During the course of the project, however, this technique caused no problems and resulted in no significant errors.

4. RESULTS AND DISCUSSION

4.1 Summary table of all corrosion fatigue tests

Test No.	Crack Path	Specimen Potential mV (SCE)	Sides Covered	Comments
1	Parent Plate	-780,-1300,-780	Yes	
2	"	-700	No	Top face above water ~30 mins, mid test
3	"	-1400	Yes	
4	"	-1300	No	
5	"	-780,-1300,-780	No	Power failure, test aborted
6	"	Free Corrosion	No	
7	"	-780,-1300,-780	No	
8	"	Laboratory Air	No	
9	"	-1400	No	Test aborted to examine microstructure
10	"	-1400	Yes	
11	"	-700	Yes	
12	"	-1200	Yes	
13	"	Laboratory Air	No	
14	"	-1300	Yes	
15	"	-780	No	
16	"	-1400	No	
17	"	-700	Yes	
18	"	-1400	Yes	
19	"	Free Corrosion	No	Severe difference in front & back crack lengths, test aborted
20	"	-1300	Yes	

continued ....

continued ....

Test No.	Crack Path	Specimen Potential mV (SCE)	Sides Covered	Comments
21	Parent Plate	-700	No	
22	"	-780,-1300,-780	Yes	
23	"	-780	No	
24	"	-1300	No	
25	H.A.Z.	Free Corrosion	No	Water drained from tank ~2 hrs near end of test
26	"	-780,-1300,-780	Yes	
27	"	-780,-1300,-780	Yes	
28	"	-1400	No	
29	"	-700	Yes	
30	"	-1400	No	
31	"	-700	Yes	
32	"	-780,-1300,-780	No	
33	"	-700	No	
34	"	-780,-1300,-780	No	
35	"	-700	No	
36	Heat Treated	-1400	No	
37	"	-1300	Yes	Only one of each type tested due to insufficient specimens
38	"	Free Corrosion	Yes	
39	"	-1400	Yes	

Table 13. Summary table of all corrosion fatigue tests

4.2 Assessment of a, N analysis techniques

In order to generate meaningful data from any corrosion fatigue experiments it is necessary to identify the pertinent variables associated with the expected service conditions encountered by the material under test in it's intended applications. Table 14 presents some of the variables which can have a significant effect on the corrosion fatigue crack growth rate properties of a high strength low alloy (H.S.L.A.) steel in sea water, and ultimately the life of any component constructed from this material.

MATERIAL VARIABLES
Composition
Microstructure - inclusion content
Processing
ENVIRONMENTAL VARIABLES
Sea water chemistry
Temperature
Protection from environment - cathodic protection etc.
LOADING VARIABLES
Load spectrum
Stress Ratio
Frequency
Constraint
Type of loading - uniaxial - complex

Table 14. Factors that can influence corrosion fatigue crack growth behaviour

The material, environmental, and loading variables noted above are generally well recognised as important factors in predicting fatigue life and as a result considerable effort is usually expended in identifying and subsequently controlling these variables during testing. There are, however, additional and often neglected aspects of fatigue crack growth rate testing which must be considered. These are the variables associated with the analysis of test data, including those data processing methods used to convert the raw test data (crack length versus elapsed cycles) to crack growth rate data (growth rate versus stress intensity range). Often these analytical variables can have as much or more influence on the measured rate of crack growth and predicted component life than the testing variables listed

in table 14. Consequently it is important to recognise the significance of these parameters in fatigue crack growth rate testing and formulate an optimum method of analysing test results.

4.2.1 Methods of data processing

The major problem encountered in converting a versus N data to crack growth rate data (da/dN versus ΔK) is that of determining the derivative (slope) of a function, a = f(N), which is known only at certain points obtained by a and N measurements during the actual test. At present, at least six different data processing techniques are being used to analyse fatigue crack growth data (Ref 136). However, these techniques can be classified into three basic categories:-

(1) Graphical techniques.
(2) Finite difference techniques.
(3) Numerical curve fitting techniques.

Examples of each of these techniques are illustrated and described below.

(1) Graphical

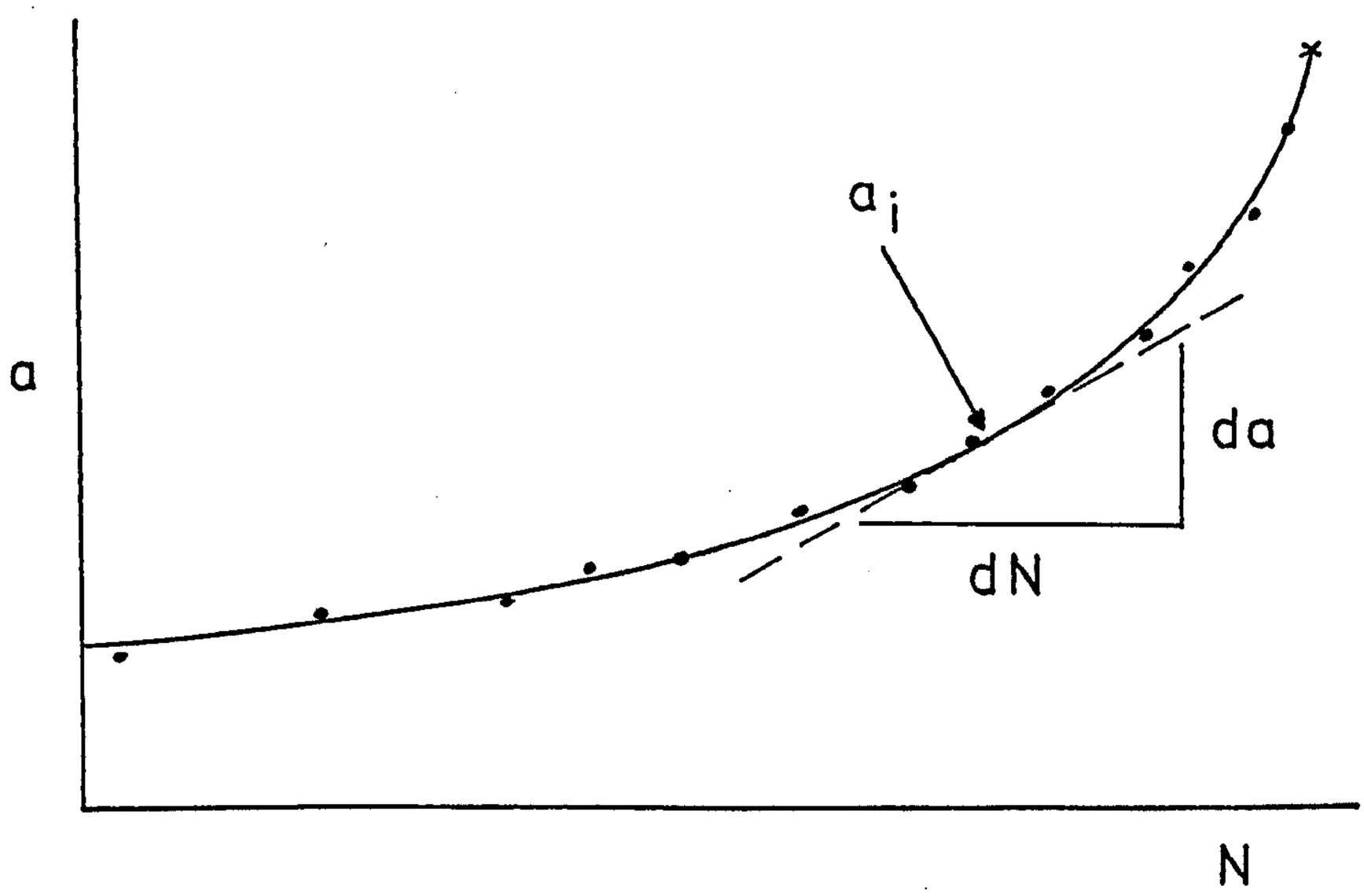

Figure 36. Graphical method for determining crack growth rate (da/dN)

The graphical method of determining crack growth rate (da/dN) from a versus N plots simply involves visually fitting a smooth curve through the plotted data and estimating the rate of growth at a given crack length, a_i, from the slope of a straight line drawn tangentially to the curve at a_i. The corresponding ΔK value is computed using the crack length at the point of tangency, namely a_i.

The most obvious and widely voiced critisism of this technique is that of 'experimental error'. Human failings such as defective eyesight and the researcher integrity may be called into question, and there is little doubt that occasionally results may be 'massaged' to fit the expected trend. No more so is this true than with the very first part of the a versus N plot; it is here that quite a bit of scatter can occur, especially in corrosion fatigue tests where not only can the scatter be caused by inhomogeneity of the material but also the 'settling down' of the system, i.e. water temperature, cathodic protection potential or specimen polarisation. This scatter can have quite a significant effect in the next analysis technique.

(2) <u>Finite difference</u>

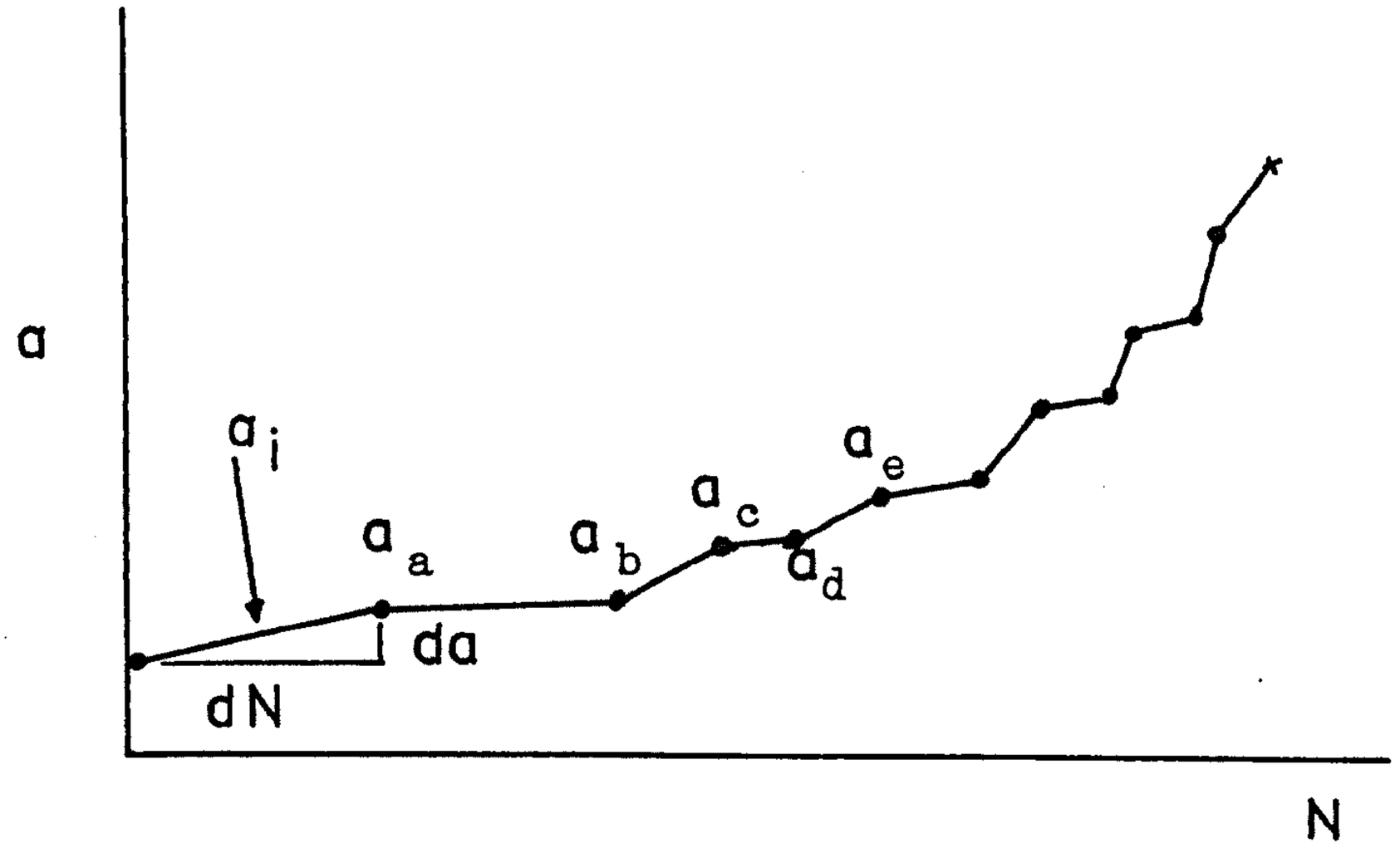

Figure 37. Secant method for determining crack growth rate (da/dN)

The most commonly used finite difference method of analysing fatigue crack growth data is the secant or point to point technique. This method involves calculating the

crack growth rate from the slope of the straight line connecting two adjacent points on the a versus N plot. Therefore the rate da/dN is simply:

$$da/dN = \frac{a(i+1) - a_i}{N(i+1) - N_i} \qquad - (30)$$

Since da/dN is the average crack growth rate over the $a(i+1) - a_i$ increment, the average crack length $(a(i+1) - a_i)/2$ is normally used to calculate ΔK.

The major disadvantage with this method is the effect that sharp changes in the slope between sets of adjacent points has on the overall da/dN versus ΔK plot.

If, for example, the slopes are analysed for the points a_b, a_c, a_d, a_e, then it can be seen that the slope a_b to a_c is steep, the slope a_c to a_d is less steep and the slope a_d to a_e increases in steepness again. This may cause the da/dN versus ΔK curve to exhibit a negative slope in places where it should theoretically be positive.

The failing in the above two techniques is but one reason why the seemingly impartial and increasingly ubiquitous microcomputer was considered to be a more effective method of generating da/dN values. Another major factor is that a computer can access and assimilate vast quantities of numerical data both extremely quickly and (providing it has been programmed correctly) accurately.

(3) Numerical curve fitting

The numerical curve fitting methods currently in use in the analysis of fatigue crack growth data include several sophisticated techniques of fitting data with complex polynomial expressions. Of these there are two relatively simple methods: the least squares technique and the incremental polynomial technique.

a) The least squares technique

This is a very common method for fitting a curve $a = f(N)$ to a set of data points (a_1,N_1), (a_2,N_2), (a_3,N_3) ..... (a_m,N_m). The method is based upon the concept of minimising the sum of the square errors $e_1^2 + e_2^2 + e_3^2$ ..... $+ e_m^2$, where e is the error associated with a certain set of points. That is, for a given a value, say a_i, e_i is the difference between the data point a_i and a value $a = f(N_i)$ which is read from the fitted curve (see Fig 38).

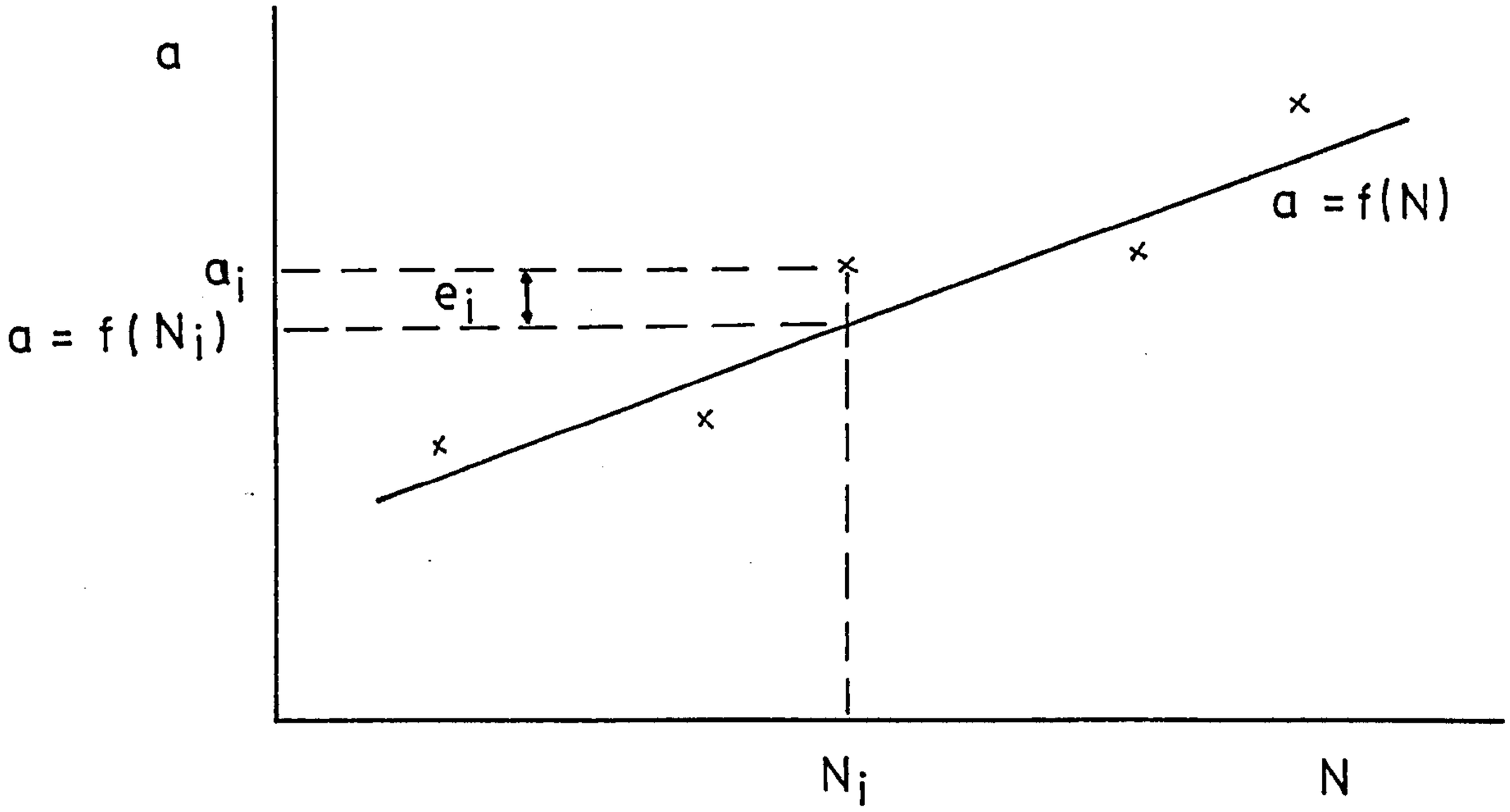

Figure 38. Error associated with fitted curve

The method is commonly applied to power functions, exponential functions and to polynomials. In either case the method requires solving a set of simultaneous, linear, algebraic equations, where the unknown quantities are the constants in the equation for the curve. For example, suppose we wish to pass the power function

$$a = pN^q$$

through a set of M data points. This would involve solving the following two equations for p and q.

$$M \log p + \{\Sigma_{i=1}^{M} \log N_i\} q = \Sigma_{i=1}^{M} \log a_i \quad - (31)$$

$$\{\Sigma_{i=1}^{M} \log N_i\} \log p + \{\Sigma_{i=1}^{M} (\log N_i)^2\} q =$$

$$\Sigma_{i=1}^{M} (\log N_i)(\log a_i) \quad - (32)$$

where Σ indicates summation, e.g.

$$\Sigma_{i=1}^{M} \log N_i = \log N_1 + \log N_2 + \log N_3 \ldots + \log N_M$$

Notice that these are linear algebraic equations in terms of the unknowns log p and q. Once log p has been determined it is very simple to obtain the constant p.

For both an exponential curve

$$a = pe^{qN} \qquad - (33)$$

and a polynomial

$$a = c_1 + c_2N + c_3N^2 ..... + c_{q+1}N^q \qquad - (34)$$

the coefficients p, q, c_1, c_2, c_3 ..... c_{q+1} are determined by solving a system of equations.

b) <u>The incremental polynomial technique</u>

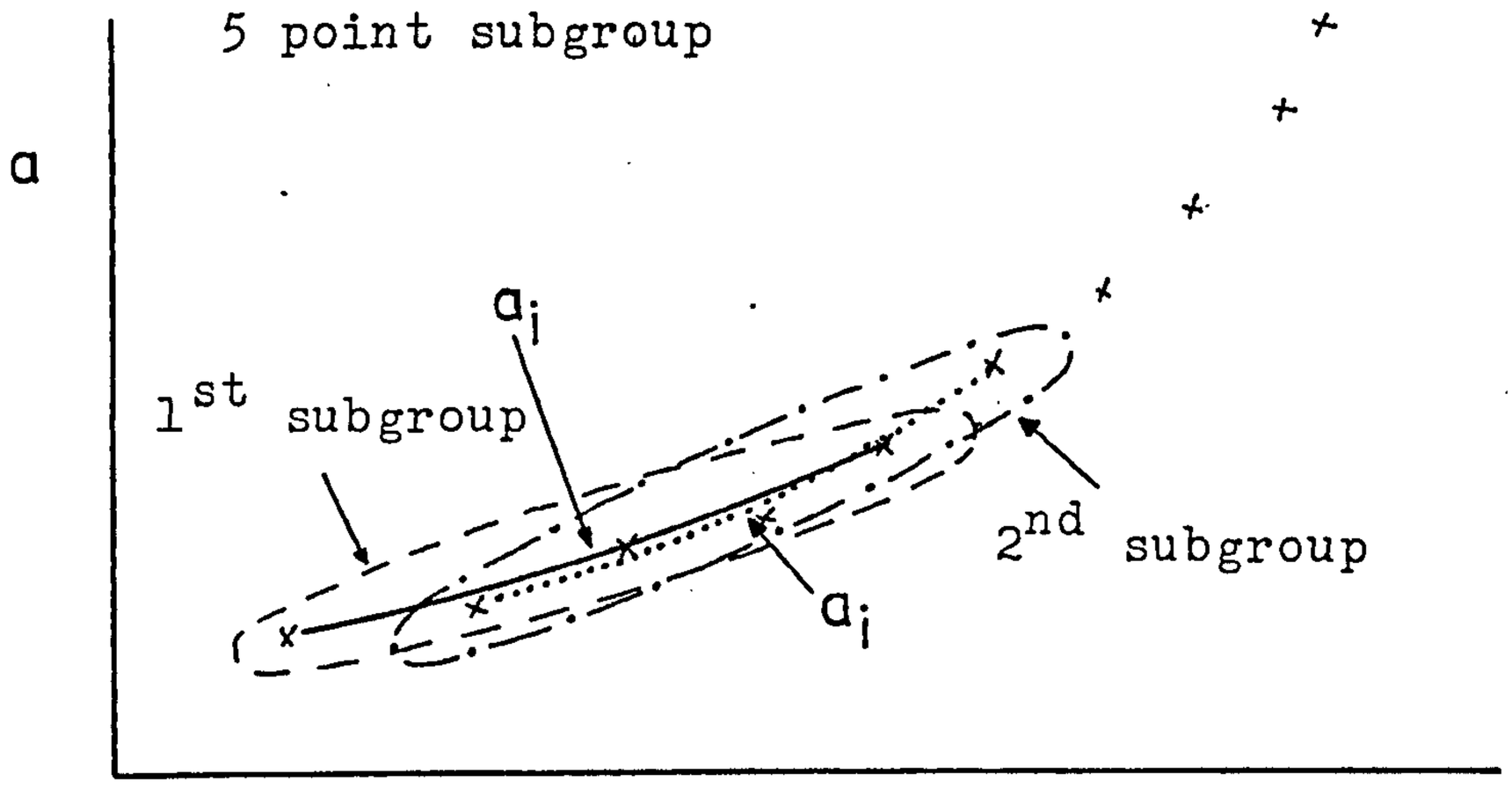

Figure 39. Incremental polynomial

The incremental polynomial technique involves fitting a second order polynomial (parabola) to sets of successive data points (usually 5 to 7 points). The form of the equation for this local fit is :-

$$a = b_0 + b_1(N-c_1/c_2) + b_2(N-c_1/c_2)^2 \qquad - (35)$$

where b_0, b_i and b_2 are the regression parameters which are determined by the least squares criterion, that is, to minimise the square of the deviations between observed and fitted values of crack length (Ref 137) over the local range of crack lengths. The parameters c_1 and c_2 are used to scale the input data, thus avoiding numerical difficulties in determining the regression parameters. When using a five point subgroup the local range is given by

$$a_{i-2} \leqslant a \leqslant a_{i+2}$$

hence

$$c_1 = (N_{i-2} + N_{i+2})/2 \ , \quad c_2 = (N_{i+2} - N_{i-2})/2$$

The rate of crack growth at a_i is obtained from the derivative of the above parabola (equation 35), which is given by:-

$$da/dN = b_1/c_2 + 2b_2(N_i - c_1) \ / \ c_2^2 \qquad - (36)$$

Usually the ΔK value associated with this da/dN value is computed from the fitted crack length, $\hat{a}_i$, which corresponds to the median number of cycles, N_i, over the local elapsed cycle range. The value N_i is used in the above expression to calculate da/dN. The reasoning behind using these particular values of a and N is simple. The recorded N_i value is used since this variable is essentially error free, having been simply read from a digital counter. The recorded crack length, a_i, on the other hand, always contains a certain amount of measurement error, human or mechanical. By using a regression technique to determine $\hat{a}_i$, this error is recognised and an attempt is made to establish a best estimate of the true crack length.

Due to the differing natures of the above methods of crack growth rate data analysis and the differing levels of sophistication used in each, it is obvious that there are certain limitations which can affect the characterisation of the fatigue crack growth behaviour. As mentioned before, the graphical method suffers very badly from subjectivity and without doubt different researchers could produce quite markedly different results from the same test data. The major limitation with the technique is in essence the basis of the technique, i.e. where should one draw the curve in order to give the best fit? Any procedure suffering from subjectivity is open to the judgement of being unable to produce consistent, reproducible results.

The finite difference techniques, which are based on point to point differences, tend to magnify variations in the a versus N test data and consequently may yield excessive variability in the processed data. In addition, this variability is sensitive to the interval between successive crack length measurements.

Given the limitations of the above two techniques, it seems that the almost impartial numerical curve fitting methods could provide a technique for generating consistent, reproducible and limited error fatigue crack propagation

rate results. The only cloud on this seemingly blue horizon is the fact that most numerical curve fitting techniques employ a least squares regression analysis, which may include excessive 'smoothing' of the a versus N data and can mask important specimen - microstructure - environment behaviour.

4.2.2 Comparison of techniques

In order to compare the traditional graphical curve fitting technique, the secant technique, and the numerical curve fitting methods, a least squares regression analysis program was written for a Sinclair ZX Spectrum micro-computer (Refs 138,139). The main action of the computer program (listed in Appendix B) was to work out the equation of 'best fit' for inputted values of a and N, using the technique of least squares regression. The program allowed several computations of the data until the equation 'best fitting' the data points was obtained. This was apparently so when the sum of square errors generated was very small. On finding this 'best' equation, the program performed a first differentiation on it giving the slope at any point on the curve and hence da/dN. The final stage of the program computed the ΔK values corresponding to the generated da/dN values using the formula :-

$$\Delta K = \frac{6\Delta P f(a/w)}{B w^{\frac{1}{2}}} \qquad - (37)$$

$$\text{where } f(a/w) = 1.93(a/w)^{\frac{1}{2}} - 3.07(a/w)^{3/2} + 14.53(a/w)^{5/2} - 25.11(a/w)^{7/2} + 25.80(a/w)^{9/2} \qquad - (38)$$

In order to investigate the accuracy and usefulness of the computer analysis we must look at several sets of data. The first set is from a corrosion fatigue test using a welded specimen cathodically protected at a potential of -850mV (S.C.E.). It can be argued that this type of experimental set up should severely test the program's ability to produce accurate, meaningful results, since scatter and/or errors due to environmental effects such as hydrogen, calcareous deposits and corrosion may be expected.

Figure 40 shows a plot of a against N for this data. It's general form is as would be expected, with a gradual increase in the slope until a is approaching final failure (at the higher values of N) when the slope increases dramatically.

Using the analysis program, the equation of 'best fit' for this data was found to be:

$$a = 12.91 + 0.26N - 0.03N^2 + 0.004N^3 - 0.0002N^4 + 0.000006N^5 \qquad - (39)$$

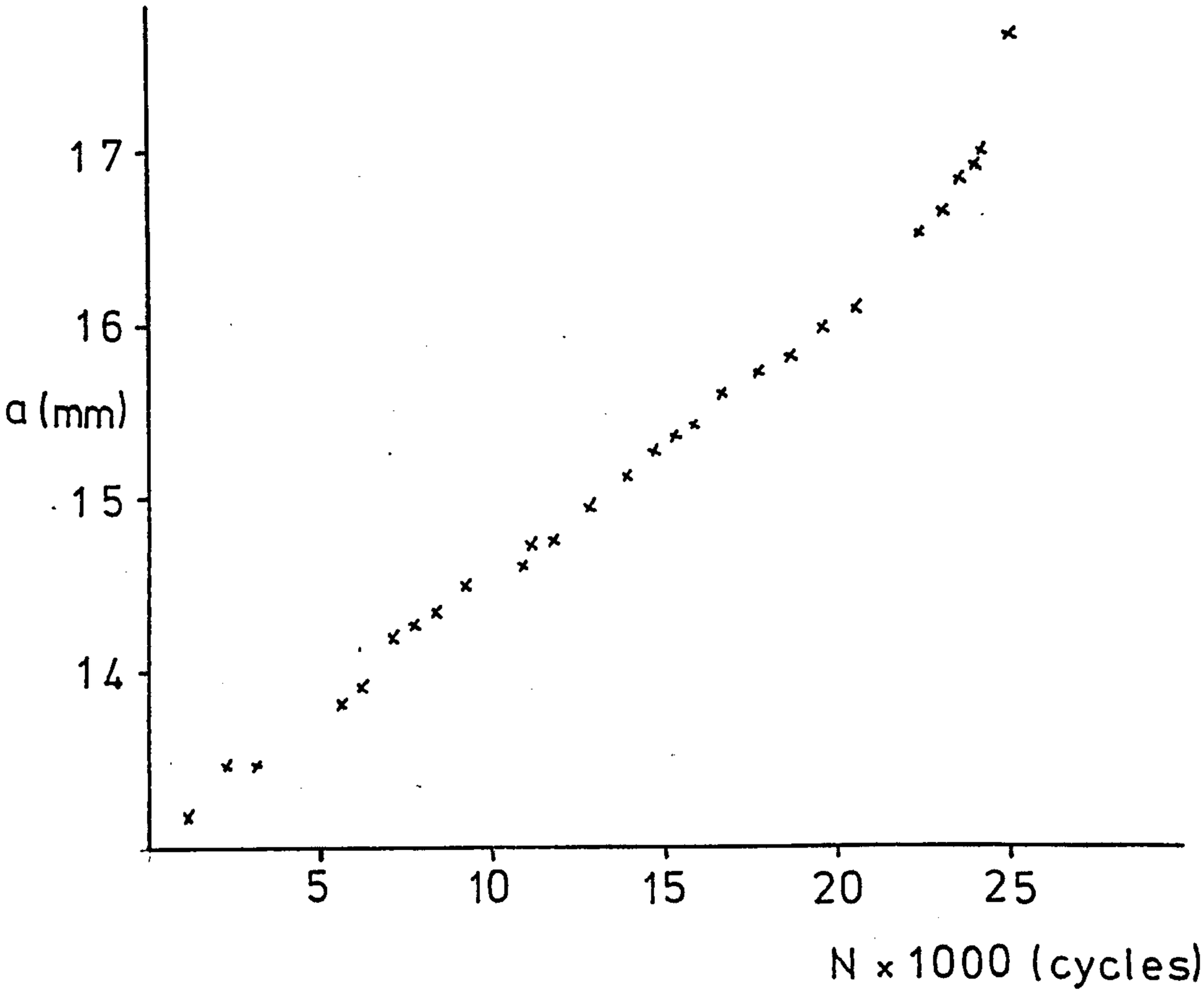

Figure 40. a versus N plot

An examination of the calculated values of a (table 15) shows that they are reasonably close to the original inputted values of a obtained by measurement during the test, the sum of square errors being very small indeed.

For comparison, several other equations were generated for the above a versus N data, these being lower order polynomials than the 'best fit' polynomial which had a maximum power of N^5. These can be seen in table 16 overleaf.

The equation generated in case (1) of table 16 was

$$a = 13.19 + 0.11N + 0.02N^2 \qquad - (40)$$

whereas that in case (2) was

$$a = 12.85 + 0.24N - 0.0097N^2 + 0.0003N^3 \qquad - (41)$$

It is quite apparent from these results that as the complexity of the 'best fit' equations increases, the calculated a values approach the actual inputted a values. How the computed da/dN values behave can only be assessed by plotting them in comparison with those obtained by the more traditional methods of analysis, namely the tangent to curve and secant methods.

N	a	a_{calc}	ΔK	da/dN x10^{-7}
1312	13.20	13.20	16.91	1.99
2327	13.47	13.39	17.50	1.69
3388	13.47	13.56	17.50	1.52
5642	13.82	13.89	18.31	1.45
6300	13.92	13.98	18.55	1.46
7221	14.22	14.12	19.30	1.50
7750	14.27	14.20	19.43	1.53
8440	14.32	14.31	19.56	1.56
9385	14.50	14.45	20.05	1.59
10100	14.62	14.57	20.38	1.60
11130	14.72	14.73	20.66	1.59
11805	14.79	14.84	20.86	1.58
13017	14.95	15.03	21.33	1.52
14020	15.15	15.18	21.94	1.46
14790	15.29	15.29	22.38	1.41
15350	15.34	15.37	22.54	1.37
16000	15.42	15.46	22.80	1.33
16812	15.61	15.57	23.44	1.31
17561	15.67	15.67	23.64	1.31
17918	15.74	15.71	23.89	1.32
18863	15.82	15.84	24.17	1.39
19720	16.00	15.97	24.83	1.53
20710	16.12	16.13	25.27	1.82
22668	16.62	16.58	27.26	2.89
23272	16.78	16.76	27.94	3.39
23680	16.89	16.91	28.42	3.79
24114	16.95	17.08	28.68	4.27
24460	17.05	17.25	29.13	4.69
25108	17.74	17.58	32.49	5.59

SUM OF SQUARE ERRORS = 0.14695969

Table 15. Results of computer analysis for 'best fit' of a versus N data

(1)		(2)	
a_{calc}	da/dN x10^{-7}	a_{calc}	da/dN x10^{-7}
13.33	1.13	13.14	2.15
13.45	1.17	13.36	1.99
13.58	1.22	13.56	1.84
13.87	1.32	13.94	1.58
13.96	1.34	14.04	1.52
14.08	1.38	14.18	1.45
14.16	1.40	14.26	1.42
14.25	1.43	14.35	1.38
14.39	1.47	14.48	1.34
14.50	1.50	14.58	1.33
14.65	1.55	14.71	1.32
14.76	1.57	14.80	1.32
14.95	1.62	14.96	1.35
15.12	1.67	15.10	1.39
15.25	1.69	15.21	1.44
15.34	1.72	15.29	1.47
15.46	1.75	15.39	1.53
15.60	1.78	15.51	1.61
15.73	1.81	15.64	1.69
15.60	1.83	15.70	1.73
15.97	1.87	15.87	1.85
16.13	1.90	16.03	1.97
16.33	1.94	16.24	2.13
16.71	2.02	16.69	2.49
16.84	2.05	16.84	2.62
16.92	2.07	16.95	2.71
17.01	2.08	17.07	2.80
17.08	2.09	17.16	2.88
17.22	2.13	17.36	3.04

Table 16. Results of computer analysis for lower order polynomials

Figures 41 & 42 show separate plots for the two traditional methods and the computer generated results. It is quite obvious that the traditional graphical method exhibits a recognisable Paris plot, whereas the secant technique generates many points which seem to lie in a sloping pattern. The criticism of subjectivity that is so often levelled at the tangent to curve method must now also be levelled at the secant method. Although the points seem to follow a definate trend, confusion and error may arise when trying to draw a representative line through them. There is no doubt that a multiplicity of lines with any number of slopes could be drawn through the scatter of points. It is for this reason that the author, in the confines of this project, believes the secant method to be totally inadequate as an analysis tool for producing Paris plots.

Figure 42 shows the da/dN versus ΔK curves generated by the least squares regression analysis method. It can be seen that when the equation with the least sum of squared errors and highest degree polynomial (and hence the 'best fit' for the a, N data) is used, the curve obtained is totally unlike a normal Paris plot.

Consideration of figure 43 may help to explain what is happening when the computer generated da/dN versus ΔK curve undulates instead of steadily increasing. In an effort to faithfully follow the points, the exact fit line will change it's slope from steep at X to less steep at Y, to steep at Z. This will be reflected in the values of da/dN which will be high, lower and high respectively since the da/dN value of each point is the slope of the tangent at each point. This will cause a Paris plot to undulate, as in the 'best fit' case in figure 42. The 'smoothed fit' line in figure 43 has a steadily increasing slope which will translate to steadily increasing da/dN values.

As the equation used to explain the a versus N points becomes less complex and the 'smoothed' curve is used to generate da/dN values, it could be expected that the Paris plot would also lose the undulation shown in the 'best fit' curve in figure 42. However, the two less complex equations generate curves which bear little relation to the curve produced by the graphical method.

One explanation of this anomaly can be put quite simply: in analysing the a versus N data the computer program tries to fit a single curve to what may in effect be three distinct curves. Figure 44 shows a simplified theoretical a versus N curve.

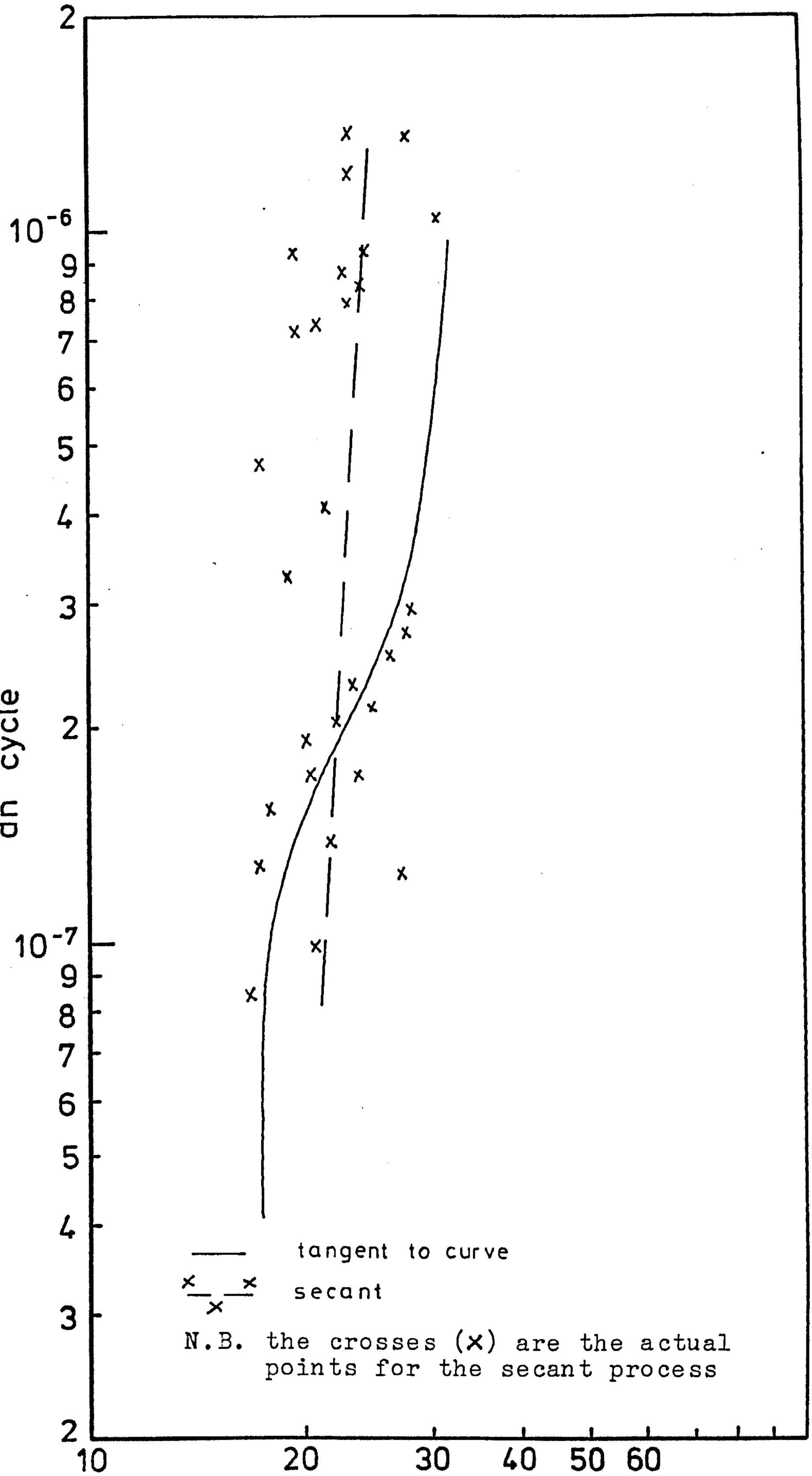

Figure 41 . Paris plots for a welded specimen (-850mV S.C.E) generated by the traditional methods

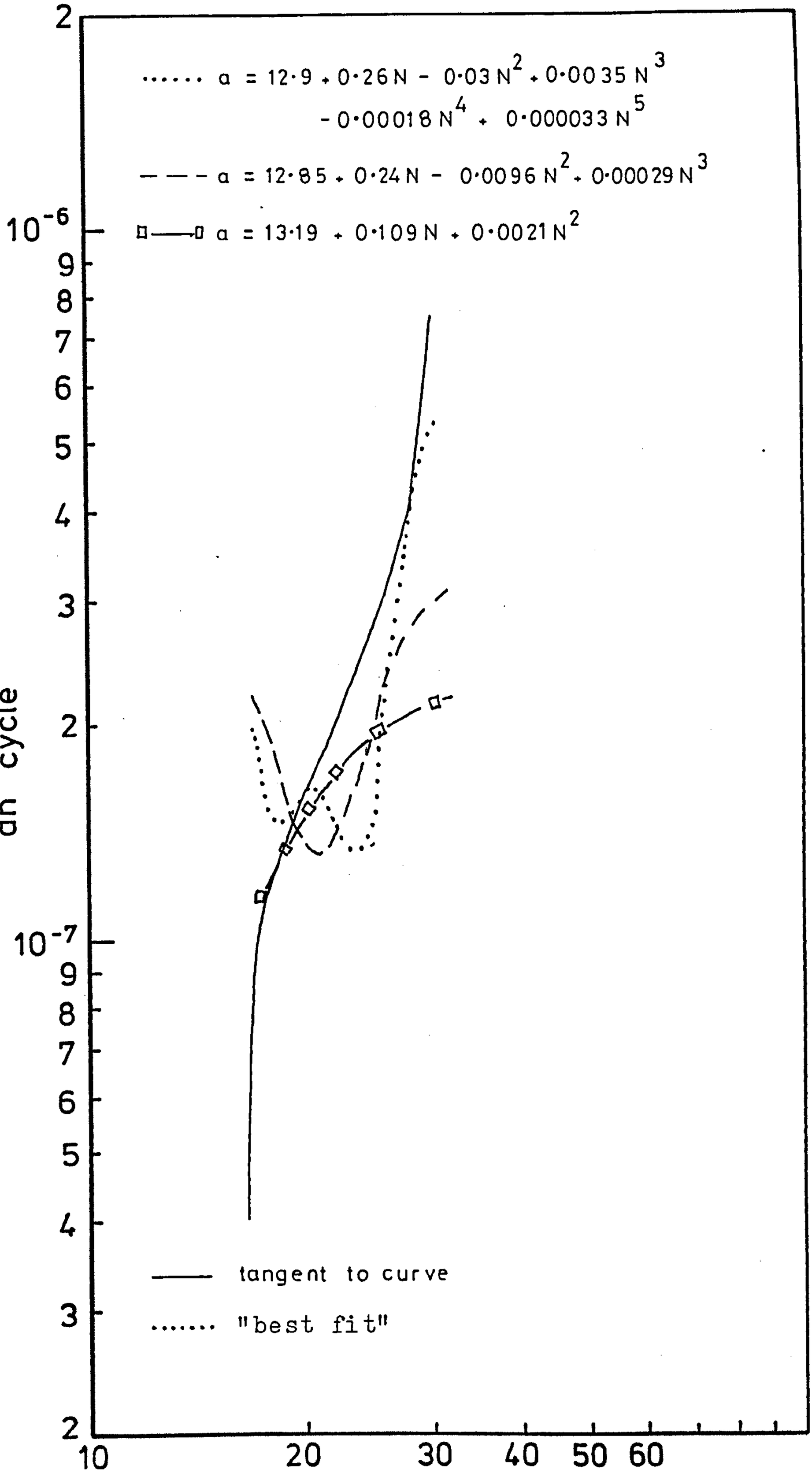

Figure 42. Paris plots for a welded specimen (-850mV S.C.E.) generated by various polynomial eqtns.

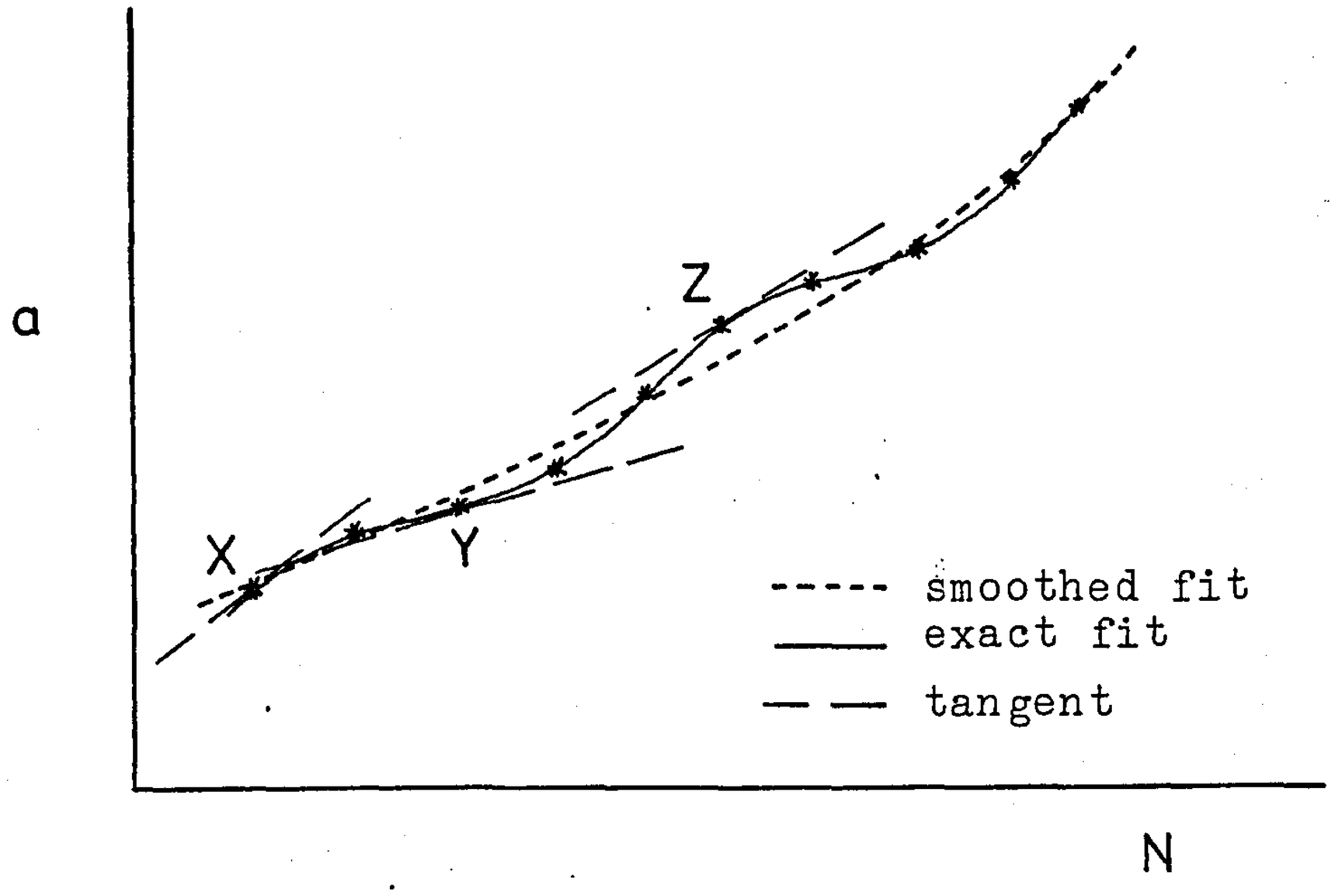

Figure 43. Exaggerated a versus N deviations

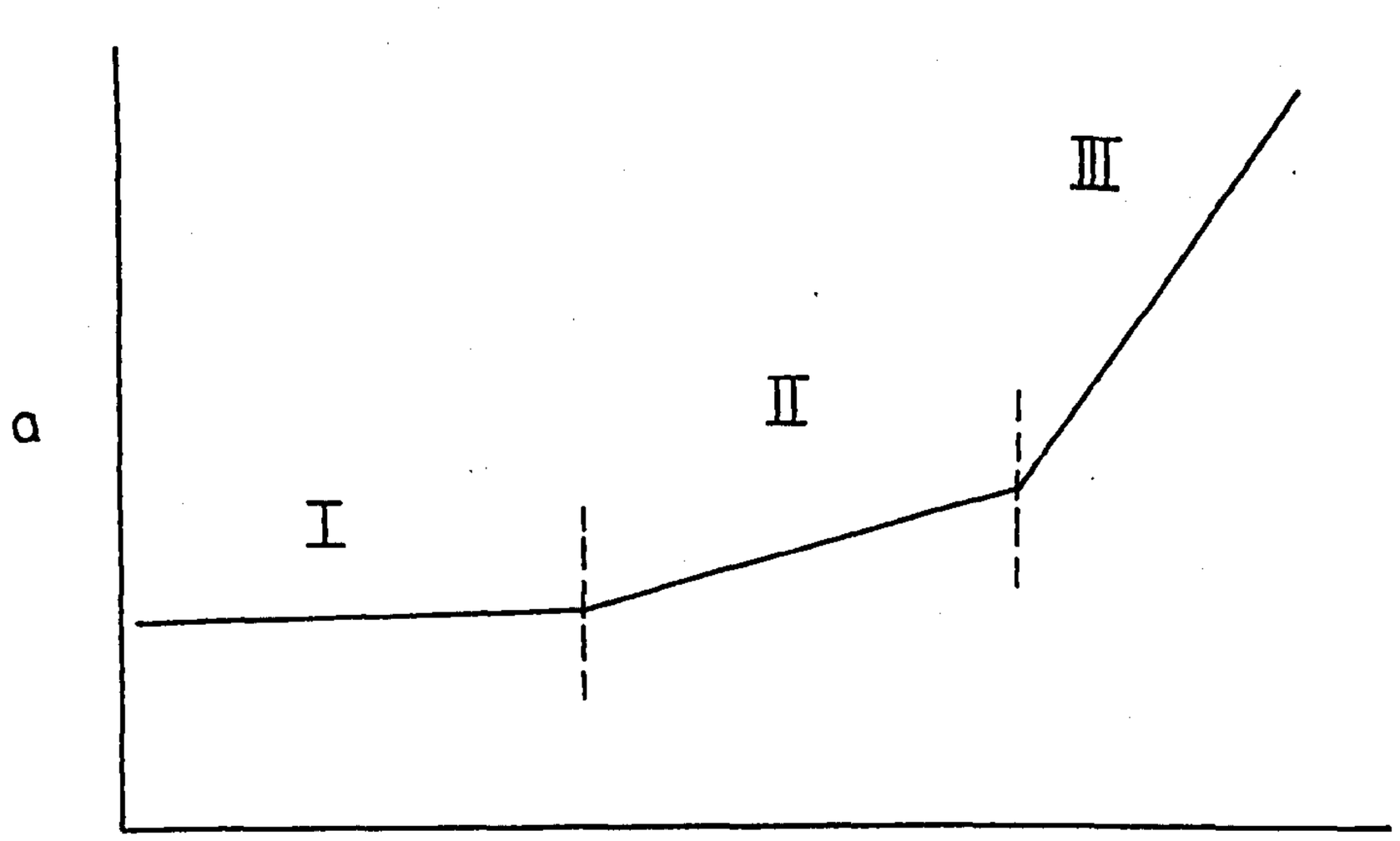

Figure 44. Simplified theoretical a versus N curve

Region I is the initiation or threshold area of the fatigue crack. This initiation or very slow growth may have taken thousands of cycles and may have resulted in a region of curve which is horizontal or very slightly inclined. Region II is after initiation and threshold

and is when the fatigue crack may be growing at a steady rate. Region III is the approach to final failure where the fatigue crack growth rate should be accelerating towards the point where failure occurs.

It must be remembered that the lines in figure 44 have been drawn straight for reasons of simplicity but may in fact be curved or undulating slightly due to material inhomogeneity, environmental or loading conditions etc.

A simple way around the problem of the three separate regions is to use the numerical analysis program to analyse sets of data points from each region. However, this may not be as easy as it sounds because there is a problem of deciding where one region ends and the next begins. The results of such an operation on the previous set of a versus N data can be seen in table 17. Subsequently the da/dN versus ΔK plot is shown in figure 45. Although the plot is in three distinct parts the overall view shows some semblance of a typical Paris curve; however it bears little relation to the 'original' graphical method curve. Examination of the computer print-out will show that the spread of da/dN values for region I is virtually the same as for region II. This indicates that for this particular set of a, N data, region I is very small and may have lasted only up to 2000 cycles, therefore the majority of data points analysed as region I may infact belong to region II. As mentioned earlier, this is more than likely a human error in the decision of regional delimitations.

The next step in the numerical analysis technique was to use the incremental polynomial method and to this end the program was rewritten, incorporating a five point subgroup analysis. The da/dN versus ΔK plot generated by this technique is compared with the plot from the graphical technique in figure 45. Like the 'best fit' polynomial it shows undulations at the low ΔK end but it is, however, quite a bit better than any of the polynomial curves. This is a reflection of how the moving subgroup takes account of any region factor when it adds the next point and drops the last as it analyses each subsequent subgroup.

Having looked at the performance of the computer analysis technique on a typical 'worst' case specimen, it was decided to compare it with a parent plate specimen fatigued in air. This is arguably the best condition in which to test the computer program because of the lack of environmental and cathodic protection effects.

The in air specimen was analysed in much the same way as the corrosion fatigue specimen. This time however, the results were much more favourable and can be seen in figure 46, which shows a Paris plot for the results using the graphical technique, a single run analysis, and a three run analysis.

REGION I

N	a	a_{calc}	ΔK	da/dN x10^{-7}
1312	13.20	13.19	16.91	1.21
3388	13.47	13.47	17.50	1.41
5642	13.82	13.81	18.31	1.62
6300	13.92	13.92	18.55	1.68

REGION II

N	a	a_{calc}	ΔK	da/dN x10^{-7}
7221	14.22	14.21	19.31	1.24
7750	14.27	14.27	19.44	1.27
8440	14.32	14.36	19.57	1.29
9385	14.50	14.48	20.05	1.33
10100	14.62	14.60	20.38	1.35
11130	14.72	14.72	20.66	1.39
11805	14.79	14.81	20.87	1.41
13017	14.95	15.00	21.34	1.46
14020	15.15	15.14	21.95	1.50
14790	15.29	15.25	22.39	1.52
15350	15.34	15.34	22.55	1.54
16000	15.42	15.44	22.81	1.57
16812	15.61	15.57	23.44	1.60
17561	15.67	15.69	23.65	1.62
17918	15.74	15.74	23.89	1.64

REGION III

N	a	a_{calc}	ΔK	da/dN x10^{-7}
18863	15.82	15.88	24.17	3.42
19720	16.00	15.94	24.82	3.71
20710	16.12	16.08	25.27	1.70
22668	16.62	16.55	27.25	3.14
23272	16.78	16.75	27.94	3.58
23680	16.89	16.91	28.41	3.88
24114	16.95	17.08	28.68	4.20
24460	17.05	17.23	29.13	4.46
25108	17.74	17 53	32.49	4.93

Table 17. Results of computer analysis for three distinct regions

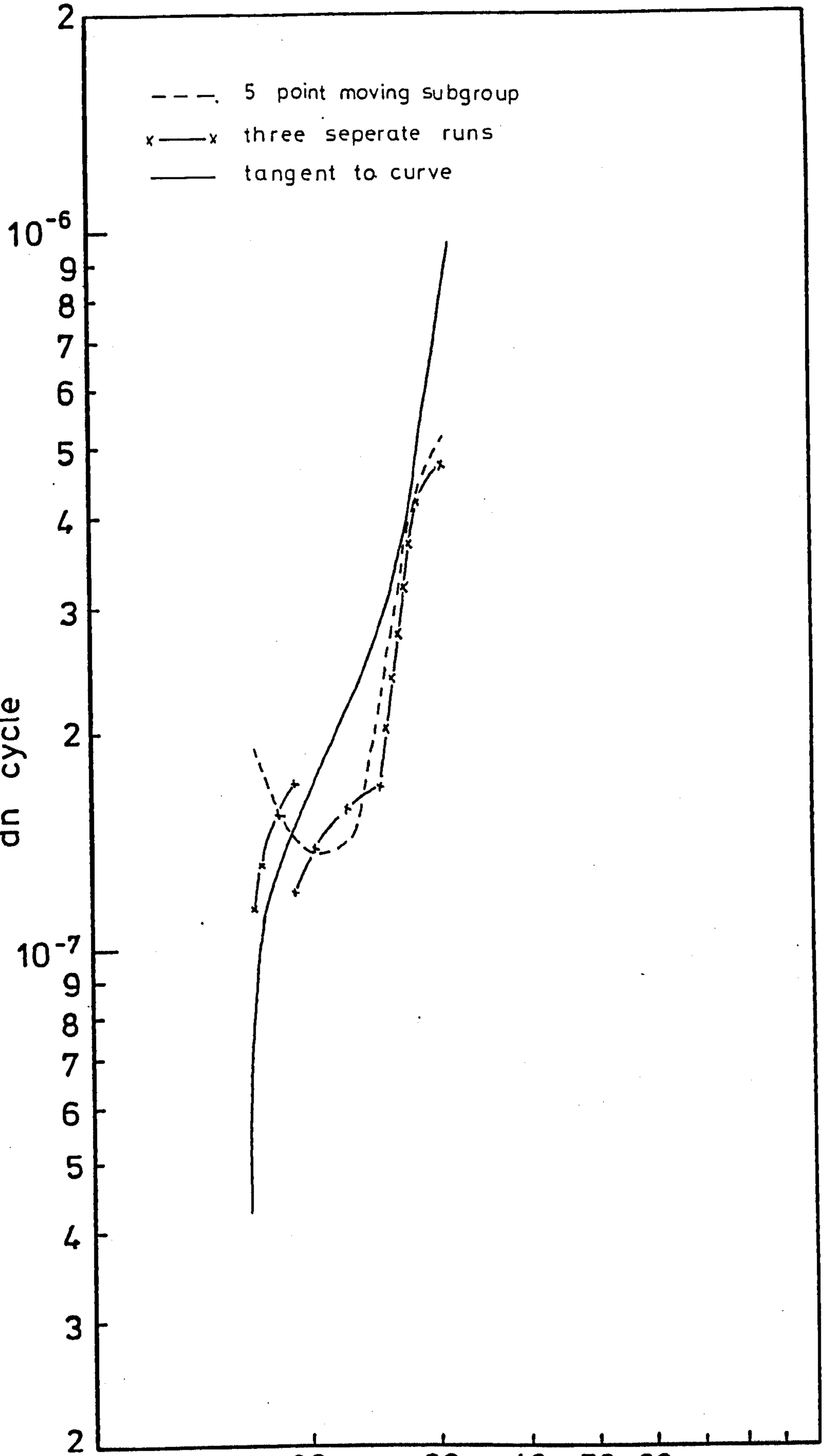

Figure 45. Paris plots for a welded specimen (-850mV S.C.E.) generated by 3 computations and a 5-point incremental polynomial

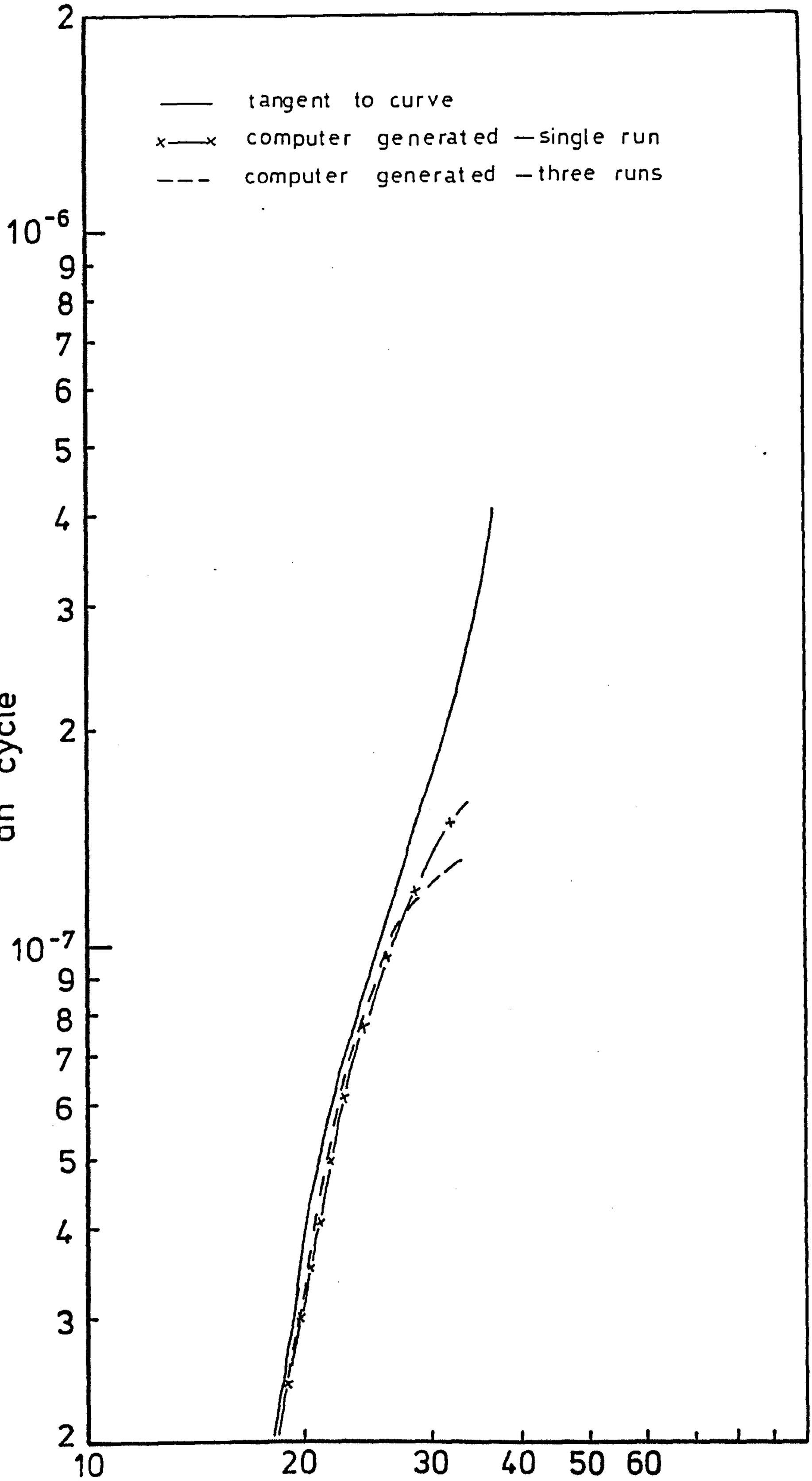

Figure 46. Paris plots for a parent plate specimen (in air) generated by two computer analyses and a graphical method

In both cases the computer generated results show a striking faithfulness to the tangent to curve results, especially at the lower ΔK reaches of the graph. It is only when the higher ΔK region is encountered that the computer generated results show a marked divergence from the traditional method results.

It is without doubt that the computer programs written to find the equation of 'best fit' for a set of a versus N data points worked well. They also proved excellent at differentiating this equation and generating the ΔK values. However, except for the in air case, the da/dN results obtained left a lot to be desired when compared with the graphical method. It seems that when a more complex polynomial equation is used to describe the a versus N curve a better fit for the data is obtained. The only problem is that if any variability exists in the data at the initiation and final failure regions then this 'best fit' equation will pick up on it and the da/dN values will suffer accordingly. 'Smoothing out' the a versus N curve by using a less complex polynomial may remove the undulations but it does not account for the a, N plot sufficiently well enough to produce a reasonable Paris plot.

Breaking the a, N data up into regions does tend to produce slightly better results than just a straightforward polynomial approach, but the major problem of human error and subjectivity associated with delimiting the regions is not removed. The final computer analysis method of an incremental polynomial proved to be not much better and, like the previous computer variations and the secant method, it proved susceptible to data scatter, especially in the threshold and final failure regions.

It is possible to postulate several reasons for the variability of a versus N data. First there is the scatter induced by measuring the actual crack, then scatter associated with material inconsistencies and inhomogeneity, then variability due to environmental conditions, sea water, and potential etc., if it is a corrosion fatigue test. One major reason for scatter may be that measurement of the surface of a fatigue crack that is under plane stress does not exactly mirror what is happening in the plane strain bulk of the specimen. For this reason measurement of the crack on both sides of the specimen (where possible) and use of an average crack length may prove beneficial.

Other mechanisms of subcritical crack growth such as crack growth under static load may be interacting with fatigue crack growth in the initiation and threshold region,

whereas the ΔK values and crack lengths corresponding to the final failure region may be approaching the fully plastic limit values for the specimen and the mode I ΔK may no longer be an appropriate parameter to characterise the driving force for fatigue crack growth in this region.

Several researchers (Refs 136, 140) have similarly compared secant and numerical data analysis techniques. Their conclusions state that data processing methods based on numerical curve fitting techniques over a local region, such as the incremental polynomial method, represent near optimum methods for situations where ample raw data is available. The graphical method was not assessed due to it's subjective nature. However, it must be remembered that in undertaking their comparison, these researchers considered a set of hypothetical test data which represented idealized fatigue behaviour and added a uniform error to the crack length measurements. It is a debatable point whether the incremental polynomial technique would have proved as good had it been subject to the sort of variable data produced in a 'real' fatigue test.

Overall it must be said that in this comparison it seems that the graphical method gave the 'best' Paris plot when used to analyse the raw data even though it is without doubt the most subjective of all the techniques. The secant method is very unreliable and suffers badly from sensitivity to crack length measurement interval and raw data scatter. The computer numerical analysis methods are really of little value other than to indicate the general trends of the a versus N data. However, saying that, it does not mean that they should be dismissed out of hand since they do tend to give better performances if used to analyse data generated from in air fatigue experiments where there is less data scatter (due to environment and difficulty of measurement). Moreover, during the course of the project a few computer analyses did produce reasonable Paris plots.

Even though in this project the computer analysis techniques did not prove to be as useful as it was at first hoped, the use of computer programs to analyse fatigue crack propagation is growing. Bureau Veritas, one of the major certification authorities, now uses a computer analysis program to calculate $\Sigma = ni/Ni$ (Miners Rule) according to a given S.N. curve and discretized load histogram, and also calculation of the sum of the damage by crack propagation for a given load distribution (Ref 141).

Due to the random nature of fatigue crack growth and the fact that it is occurring in an inhomogeneous material, then it is hardly surprising that data scatter is present. Since subjective judgements are involved and no completely satisfactory procedure has been defined, it is gratifying that fatigue crack growth data obtained by different

investigators on similar materials usually agree reasonably well, although there may be considerable variation in the amount of scatter. It will never be possible to completely eradicate the errors produced by the variability in data but it is possible, by using either a computer analysis or a subjective human analysis, to reduce the magnitude of the error, providing care and time is taken. This holds true not only in the analysis of results, but also in the setting up and monitoring of the experiment.

4.3 Operating parameters

Prior to any corrosion fatigue testing, all specimens were pre-fatigued in accordance with BS 5762:1979. The frequency used was 20 Hz and the R ratio was 0.1. BS 5762:1979 states that the pre-fatigue length should be such that a/w was within the range 0.45 - 0.55 (where a is the crack length and w is the specimen thickness). Since the specimen thickness used in this project was 26mm, the above standard specification allowed a total length of machined notch and pre-fatigue crack of between 11.7 and 14.3 mm. In an effort to maintain a consistent corrosion fatigue crack start length, all specimens were pre-fatigued to a total crack length of approximately 13 ± 0.2 mm. In keeping with the standard specifications this involved growing the last 1.28 mm in not less than 50,000 cycles. This ensured that the crack tip was sharp enough for fatigue crack initiation. It was usual practice to perform the pre-fatigue immediately prior to carrying out the corrosion fatigue test. When this was not the case, the pre-fatigued specimen was held in a desiccator before testing.

The corrosion fatigue testing machine used in this project derived the hydraulic pressure for the servo hydraulic system from a single hydraulic pump running at a nominal pressure of 0.586 MPa (85 lbs/sq in). Unlike other testing machines in the laboratory, the corrosion fatigue 'rig' was the only one served by a separate hydraulic pump. The other testing machines were served by a hydraulic 'main' which caused problems of electrical and hydraulic surges when one of the machines on the ringmain was started up or shut down. This was not a problem for the corrosion fatigue testing machine used in this project because of the isolated system.

During operation the applied loads were monitored continuously by a pair of digital peak and trough meters (Fig 24). The accuracy and reliability of these meters was established during the first experiment by linking them electronically to a digital voltmeter and chart recorder and cross-checking the actual outputs with the reported outputs. This procedure was carried out several times during the total period of the project work and the control system was found to consistently produce loads that were within approximately ± 0.25% of the maximum load.

At the start of the experimental work it was noticed that a slight fluctuation in the peak and trough meter readings occurred whenever the inspection lamp, used to illuminate the specimen during crack length measurements, was switched on and off. This lamp was fed from an auxiliary power socket on the testing machine. Although the peak and trough load readings fluctuated by less than 3%, it was considered

desirable to try to eliminate this fluctuation, especially as it was found that if an electric arc welder was used in the laboratory, the meter readings fluctuated continuously. As a consequence, all testing machines were subsequently isolated from the main electrical circuit.

During the course of the experimental work, the sea water solution was maintained at a temperature of approximately 8°C. As the refrigeration unit was housed outside the laboratory, there was a variation of approximately ± 2°C in the temperature during the winter and the summer months. Typically the test solution warmed during the daylight hours and cooled down in the early hours of the morning. However, for any one test, the maximum temperature variation was ± 1.5°C. As discussed in the literature survey, there is sufficient evidence to show that an increase in temperature from 5°C to 20°C doubles the crack propagation rate. The effects of the temperature variation in this work were considered to be too small to be of major significance, and hence to all intents and purposes will be ignored as a dominant factor.

Throughout the period of the project, the corrosion fatigue testing equipment, it's associated electronics and the ancillary equipment gave excellent service and proved to be very reliable. This high level of performance was consistent throughout the period of use and as a consequence has generated confidence in the validity of the experimental data obtained.

4.4 Crack growth measurement

As described in the experimental section, whenever a corrosion fatigue experiment was being carried out, the measurement of the crack length, and hence the crack growth, was made optically using a travelling vernier microscope. Although this method is relatively simple and easy to use, erroneous readings may arise if care is not taken. The major source of error is likely to arise from the optical crack measurement system.

In order to ascertain the resolution level of the microscope used for the duration of this project, a relatively simple experiment was carried out. Measurements were made of graduations on an engraved Leitz scale, from which a frequency distribution was plotted. From these results the mean accuracy and standard deviation was found for the microscope. In this case it was found to be able to discriminate to within 5 microns on any reading.

The majority of other errors are purely operator induced and can be eliminated provided the operator is vigilant and careful when taking readings. To ensure that errors were kept to a minimum, the light source illuminating the specimen was held in the same position for each reading,

thus negating any optical lengthening or shortening of the crack due to shadows. However, it must be said that in the author's opinion some method in which a light source could be brought extremely close to the crack would be an advantage; perhaps an optical fibre arrangement. Readings of crack length were always taken when the specimen was under maximum loading so that errors in length could not arise due to the flexing of the specimen because of the difference in force acting on it from maximum and minimum loads.

Any problems associated with optical crack measurement in air are greatly magnified when under conditions of corrosion fatigue. Obviously, the major sources of error in these cases are the corrosion deposits which accumulate on the specimens. These must be removed before any measurements can be taken, since even a light build-up of surface deposits can obscure the crack tip completely. During the actual experimental work it was found that the calcareous deposits were quite easily removed, even the very thick deposits generated at severe overprotection potentials (e.g. -1300 mV S.C.E.) as shown by figure 47.

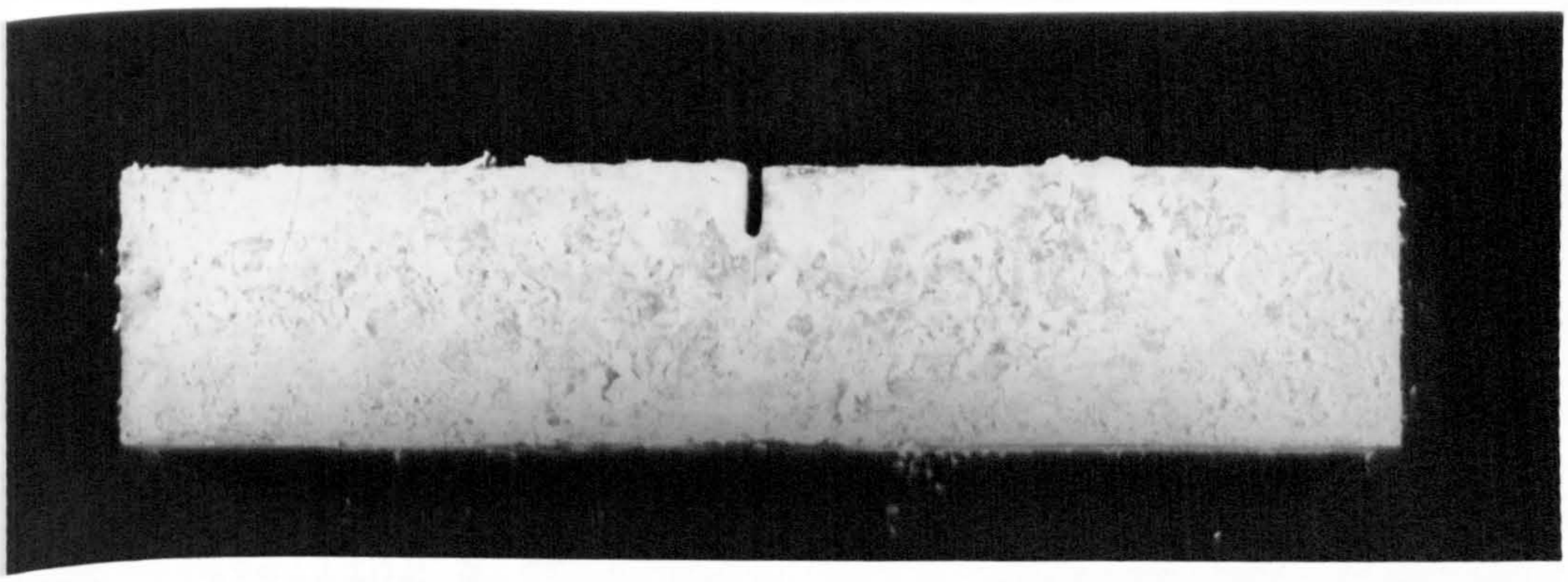

Figure 47. Calcareous deposit build-up generated at -1300 mV S.C.E.

The clean, bright metallic surface which was revealed afforded excellent conditions for 'correct' crack length measurements. This was not the case, however, for the free corrosion experiments. Even though the corrosion products were easily removed, as described in the experimental section, the pitted and generally corroded surface which was uncovered proved a difficult surface from which to discern the correct crack length. Unfortunately, because no greater care and consideration could be taken than was already employed for other conditions, it was a problem that had to be tolerated.

Owing to the nature of fatigue crack advance and the

interrelation between plane stress and plane strain conditions, there will be a curvature of the crack front in the through thickness direction (Fig 48a).

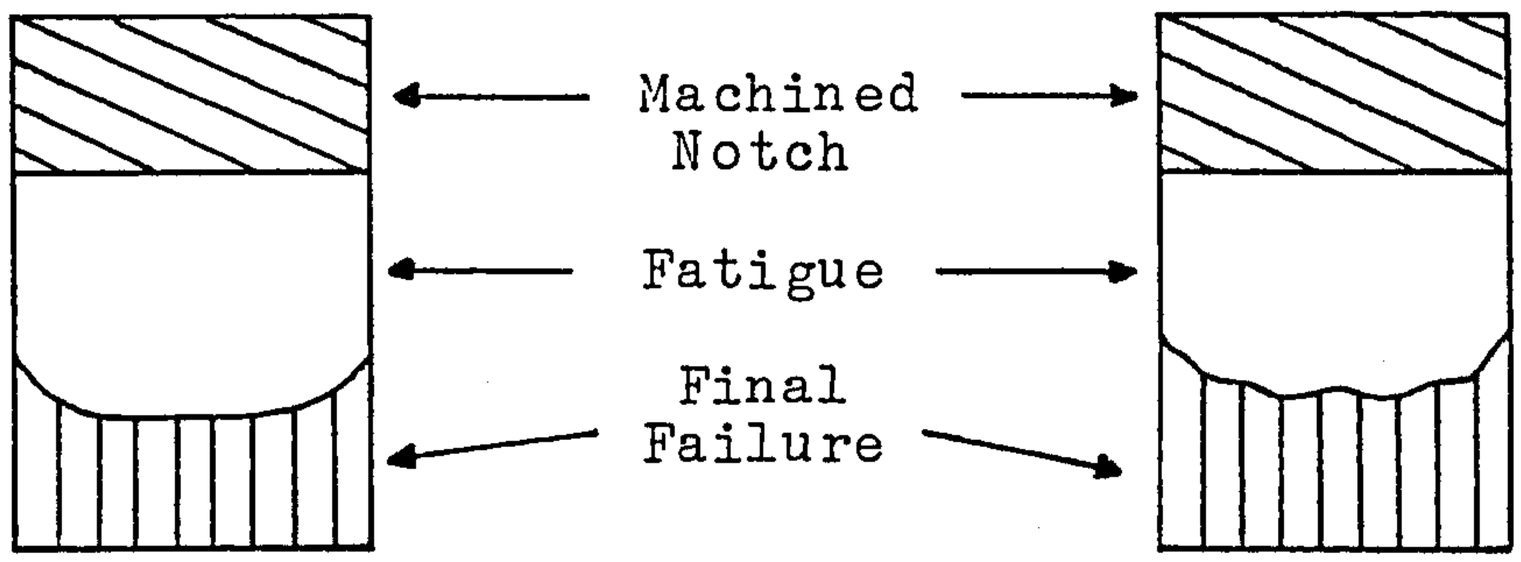

(a) (b)

Figure 48 (a) Idealised crack front profile
(b) More realistic crack front profile

Even this curvature may not be uniform because of erratic crack advance due to variables such as corrosive environment effects, inhomogeneous material, secondary cracking, inclusions and second phase particles (Fig 48b). This crack curvature may also be compounded by incorrect specimen alignment on the load and reaction rollers or by non-parallel/horizontal alignment of the rollers themselves. It was not unusual during this project for the measured crack lengths at the front and back of the specimen to differ by up to approximately 1.0 mm. In order to counter-act this problem, great care was taken in positioning the specimens on the rollers and only one side of the crack face was measured. Severe differences in the front and back crack lengths led to the abandonment of the experiment. Other miscellaneous effects can usually be attributed to operator error and include misalignment of the microscope cross-wires, defective eyesight, and accidental disturbance of the travelling microscope. When this latter situation occured, new 'base line' measurements were made by re-measuring the total crack length from the top of the 8mm notch.

Obviously, all of the above errors in measurement can have a serious effect on the results obtained in terms of a versus N plots, which in turn effect the da/dN versus ΔK plots. For instance, if an allowance is made for the fact that the actual crack length is longer than measured, due to the curvature effect, then the ΔK values calculated would be higher than if no allowance was made. This means that the crack propagation curve would be shifted to the right and consequently, for a given ΔK value, the corresp-onding crack propagation rate would be lower. Since the results generated in this project used the shorter crack length measured at the specimen surface, it may be generally concluded that the crack propagation rates recorded are fractionally overestimated for any given ΔK value.

It is without doubt that the optical crack measuring technique is prone to some serious disadvantages (Table 18), however, the majority of these can be overcome provided the operator is aware that they can occur and takes the time and effort to ensure that the probability of any occurrence is at a minimum. Throughout the period of this research work the optical method of crack growth monitoring was found to cause no problems in operation and gave satisfactory results. It is the author's opinion that the major errors in da/dN versus ΔK analysis of fatigue performance arise from the plotting and interpretation of the a and N results.

ADVANTAGES OF OPTICAL CRACK MONITORING
1) Unit cost is low in comparison to other monitoring techniques.
2) The equipment is portable, technically simple, reliable and relatively independent of operator skill.
3) The method requires no special modifications nor enhancements for use on corrosion fatigue systems.
4) Resolution of crack length to within 5 μm is possible.
5) Equipment is extremely easy to use and set up.
DISADVANTAGES OF OPTICAL CRACK MONITORING
1) Operator integrity must be high if errors are not to arise due to subjectivity.
2) The technique is labour intensive and cannot be 'rigged' for automatic control.
3) Only surface breaking cracks may be monitored so the technique can only monitor plane stress crack behaviour.
4) Crack needs to have no restriction to access and must be well illuminated.

Table 18. Advantages and disadvantages of optical crack monitoring

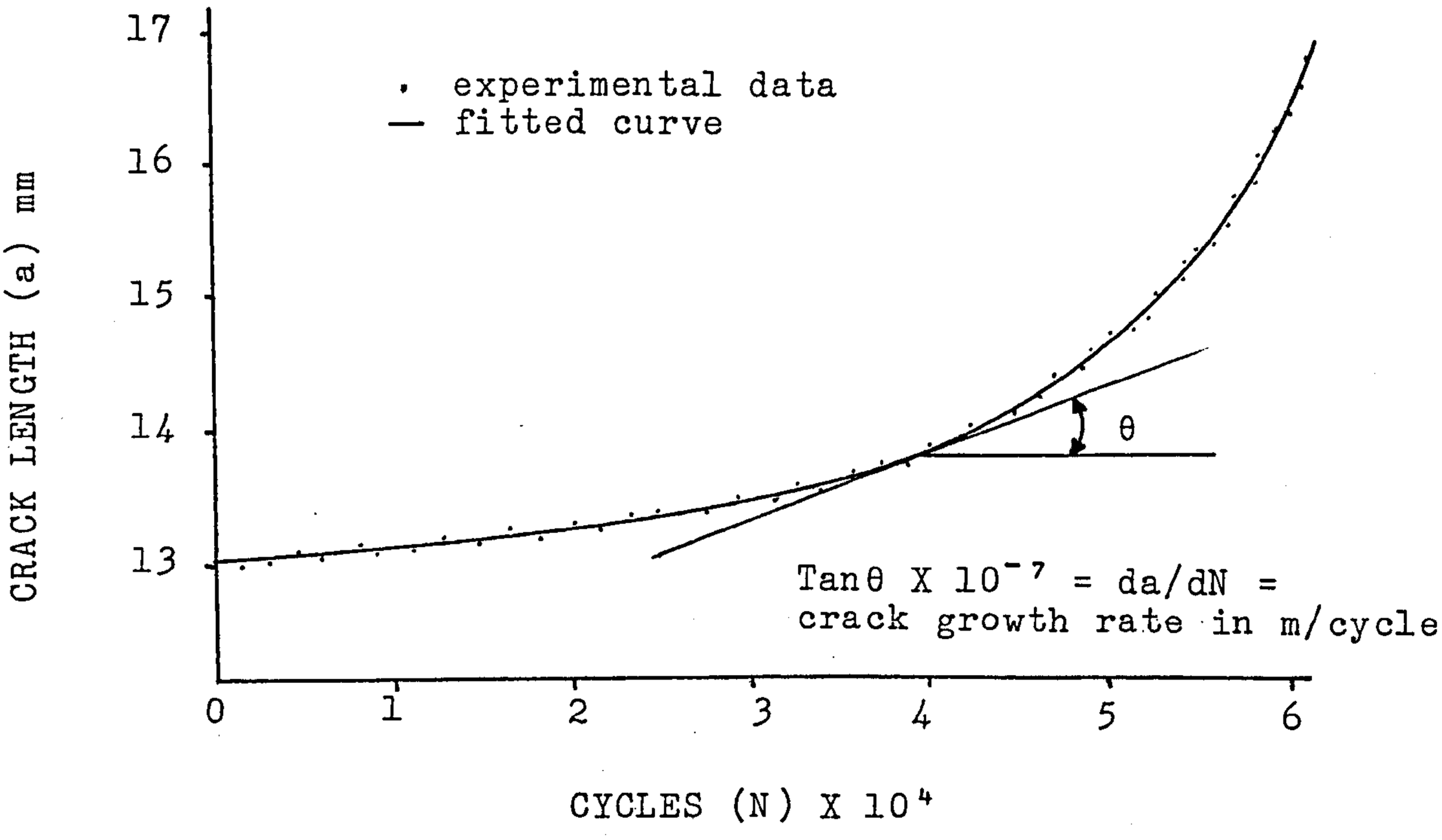

Figure 49. Typical graph of crack length against number of cycles for corrosion fatigue in the H.A.Z.

Figure 49 represents a typical a versus N plot for a H.A.Z. specimen. The fitted curve was drawn using a French Curve and is considered to be the line of best fit. However, a few questions must now be asked:-

- Can it truly represent what has actually occurred or does it give a very simplified view ?

- In all the stages of the curve is the scatter of the points due to experimental error, settling down of the system, or actual variation in incremental crack growth due to metallurgical variables in the specimen ?

- What effect will the corrosive environment and/or protective potential have on the scatter of the points ?

- If the scales of the axes are quite small then what effect will the actual size of the pencil or pen data points have on the induced error ?

- How accurately can the tangential angle be read ?

- How much difference will an accuracy of 0.5^{0} or 1.0^{0}

make to the da/dN results ?

- How will the accuracy of the microscope readings affect the results ?

Some of these questions will be quite difficult to resolve, others quite easy, the last question being perhaps the easiest.

If it is assumed that a pencil point can make a mark in the region of 0.25 mm (250 μm), then the resolution of the measurement found for the microscope (0.005 mm or 5 μm) will really be insignificant. It seems that the error caused by using a blunt pencil will be far greater than any caused by the 0.005 mm resolution of the microscope. Obviously this will also depend on the size of the scale used for plotting the points. For this project it was found that a scale of 2 mm equals 1 mm of crack growth gave the best results in terms of ease of measuring the tangential angle.

For this project the angle varied from around 3^0 at the start of the test to around 50^0 at the end. If an error of 0.5^0 is assumed in the measurement of the angle, then it can be shown that this error may produce some surprising results. In the early stages of the experiment when the angle is low, an error of 0.5^0 can result in a difference error in the range -16.69% to +16.70% in the da/dN values. At the end of the experiment, however, when the angles are far greater, the difference error in the da/dN values can be in the range -1.75% to +1.79%.

Several points must be made with reference to these findings. Firstly, since the values of da/dN versus ΔK are plotted on a log - log scale, the size of the above errors are not significant. Secondly, it can be shown that the bigger the angle the bigger the error range in the da/dN values. For this project the large errors occurred at initiation when the Paris equation is not relevant.

For these operator errors it is assumed that the researcher will be aware of them and if they occur it can only be hoped that the researcher will make them consistently. More worrying aspects will be the effects of microstructure, specimen metallurgy, environment, protection potential, and any resultant reactions producing hydrogen, calcareous deposits and pH changes. From a macroscopic viewpoint it is often convenient to regard a metallic material as a homogeneous continuum and basing engineering calculations on this assumption does not generally lead to serious error. However, in the fatigue response of a metallic material, scatter and errors arise precisely because it is not a homogeneous continuum when considered on a microscopic scale. For this project it can be assumed that micro-structural and metallurgical factors will have small effects because, unlike the banded structure of BS 4360:50D,

N-A-XTRA 70 has a very homogeneous, unbanded microstructure. Since the environment was consistent for all corrosion fatigue experiments, any overall effect will be the same for each specimen. The effects of protection potential and any associated products can be seen better in terms of the overall corrosion fatigue performance and will be discussed later when the actual results are assessed. However, it is the author's view that their effects on the point by point nature of the a versus N curve are very difficult to ascertain exactly but they must be acknowledged when viewing any results.

All the values of da/dN were determined by the tangent to curve method. As previously described, this involved fitting a curve through the a versus N data generated and then fitting a tangent to each of the points associated with that curve. The da/dN value was obtained from the angle the tangent subtended with the x axis of the plot. Measurement was made using a draughting set square which incorporated a 180° protractor with a resolution of ±0.5° of arc. The tangent function of this angle was multiplied by the scale factor for tan 45° associated with the particular a versus N curve to give the da/dN value for that point. It can be clearly seen that any errors in the da/dN values are caused by the human subjectivity of the researcher in deciding the position of the tangents to the points and measuring the subtended angles.

In order to show the extent of the scatter associated with a versus N readings and the subsequent scatter in da/dN versus ΔK, two tests are analysed fully in the following figures. Figures 50 and 51 show the plots of a against N for corrosion fatigue tests 3 (-1400 mV S.C.E.) and 17 (-700 mV S.C.E.). Figures 52 and 53 are the respective log/log plots of da/dN versus ΔK for these tests. It can be clearly seen that in both tests the degree of scatter in the a versus N plots is quite small, thus enabling quite smooth da/dN versus ΔK plots to be drawn. Since the scatter is so small it is felt that there is no need to incorporate error bands on the log/log da/dN versus ΔK plots, nor is it necessary to show individual data points when the scatter of these points about the mean line drawn through them is very small.

In conjunction with the assessment of a versus N analysis techniques previously discussed, it is the author's belief that the tangent to curve method for producing da/dN values is superior to any of the other techniques considered. The small error range, reproducibility and constant quality of results generates a high degree of confidence in the ability of the tangent to curve method to produce da/dN data that accurately reflects the material's crack growth behaviour.

The graphical presentation of the results of this work are to be found grouped together at the back of the thesis for ease of reference (pages 188 to 206).

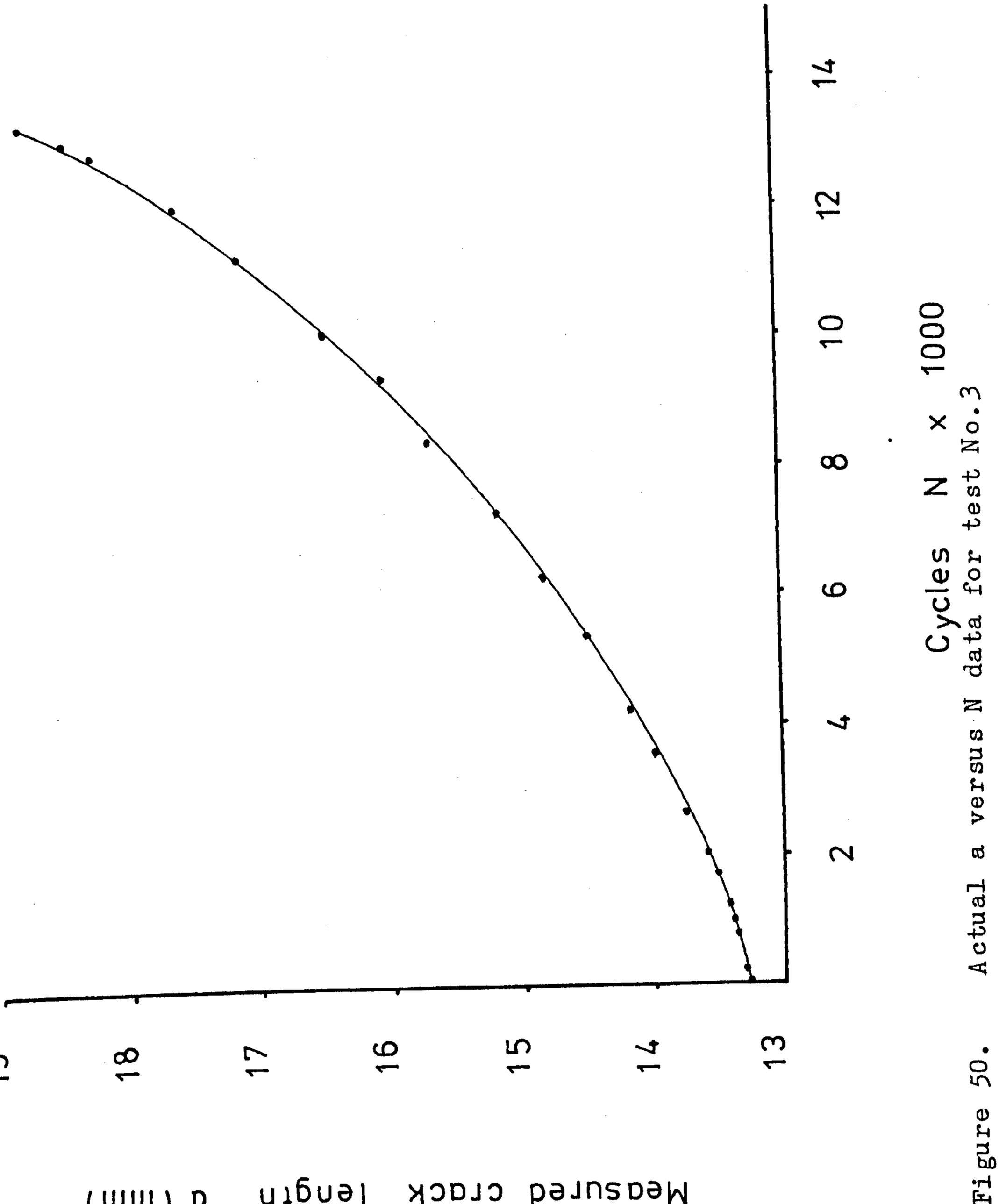

Figure 50. Actual a versus N data for test No.3

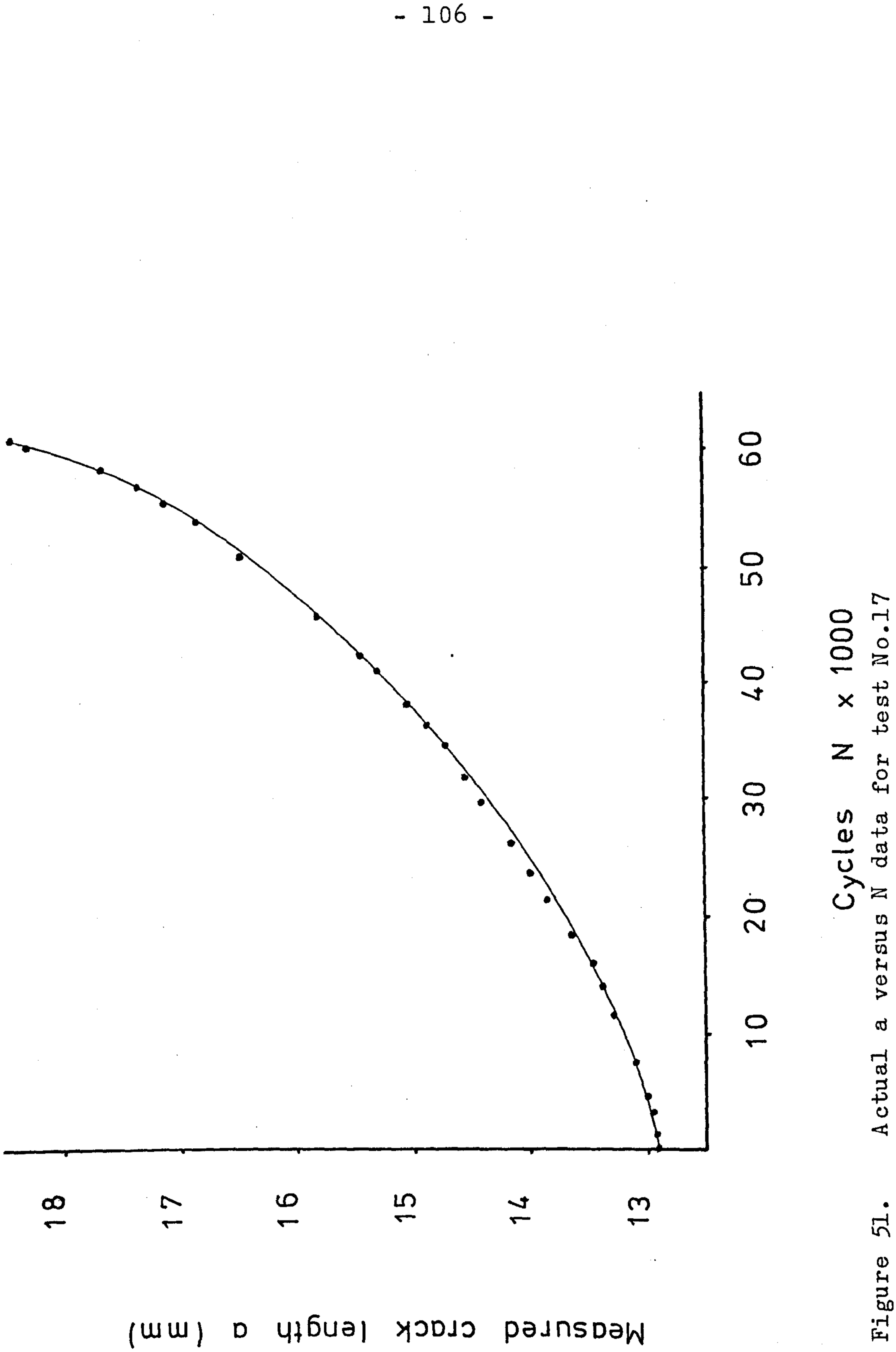

Figure 51. Actual a versus N data for test No.17

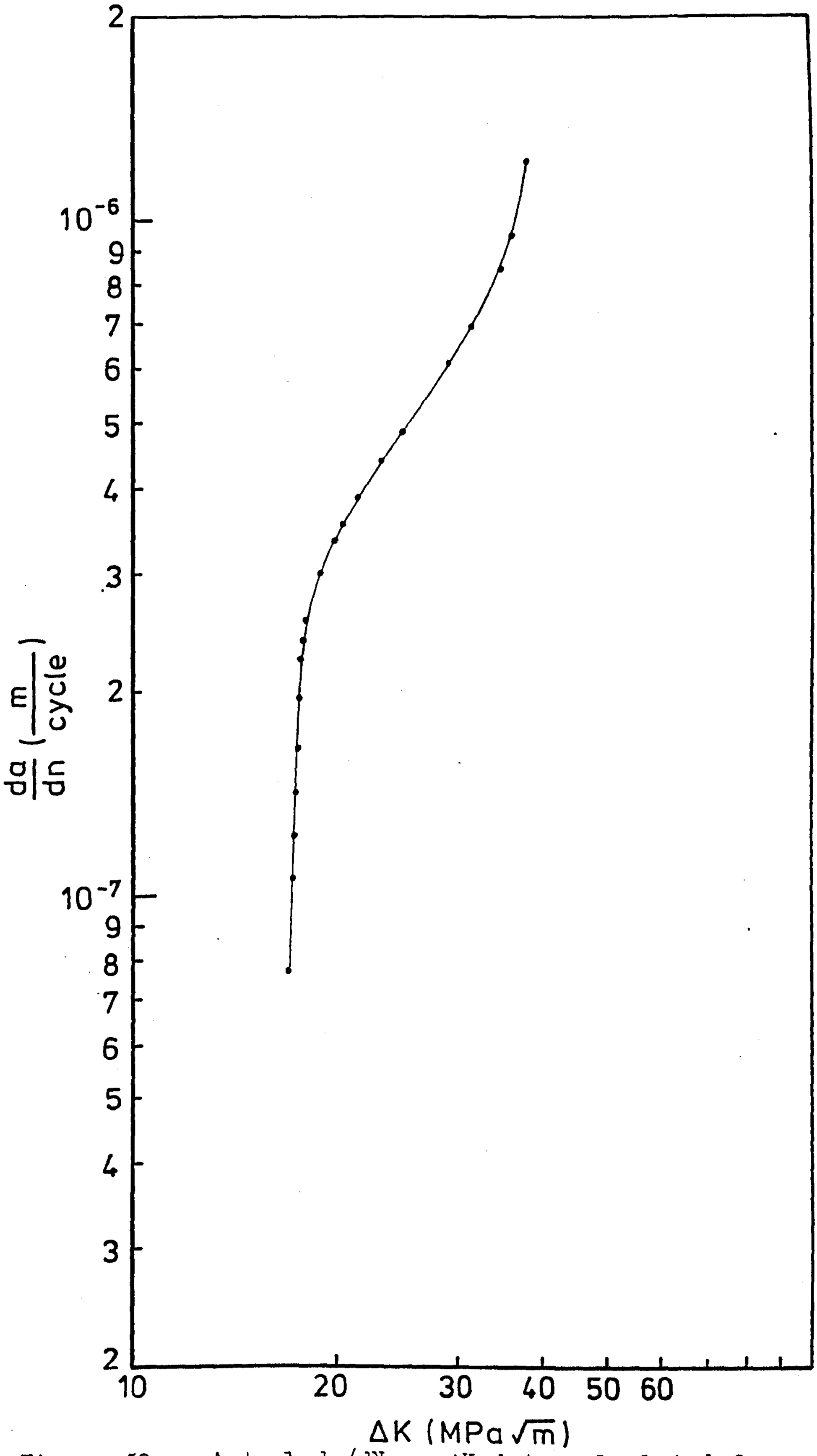

Figure 52. Actual da/dN vs ΔK data calculated from test No.3 showing minimal scatter

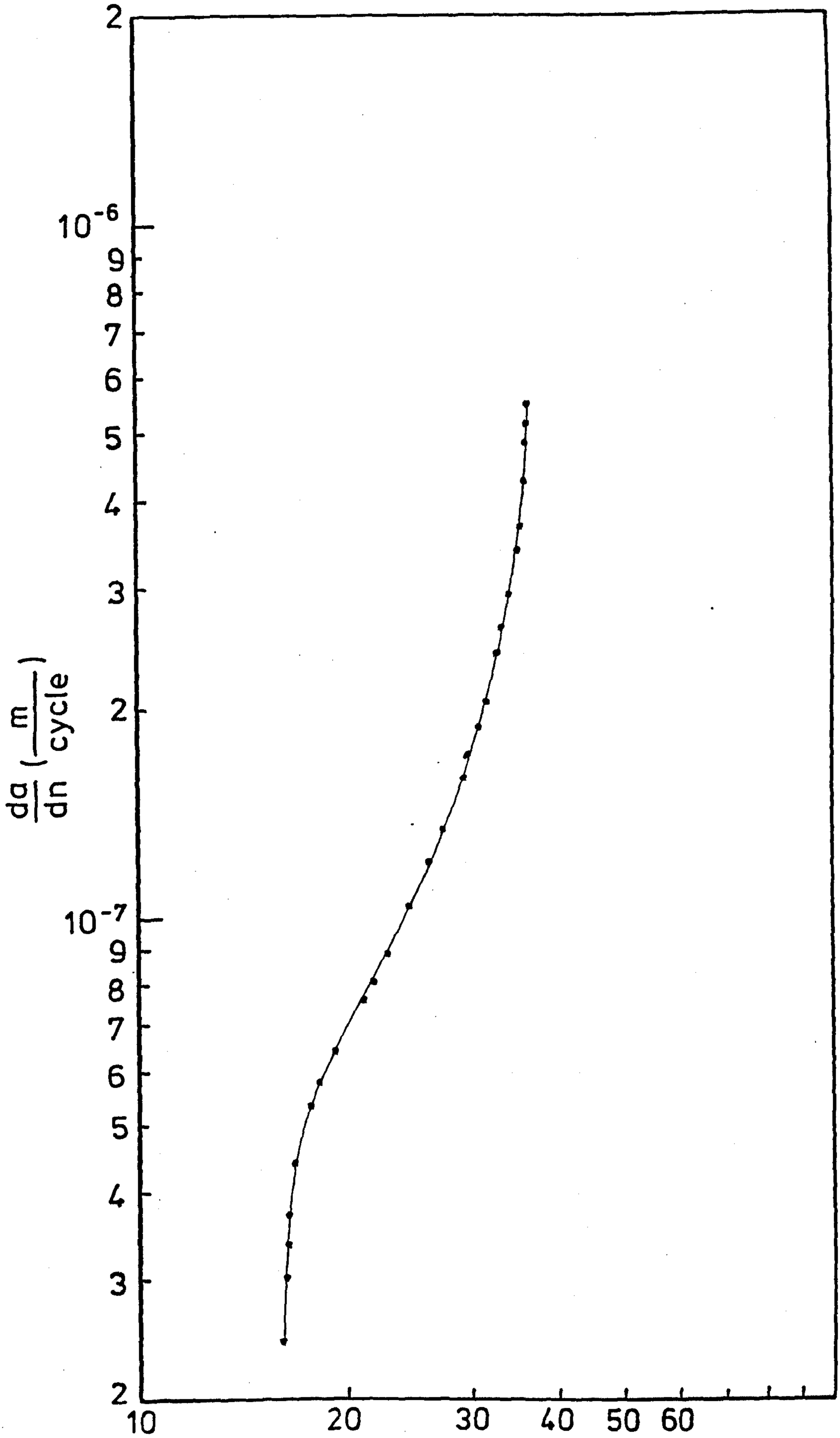

Figure 53. Actual da/dN vs ΔK data calculated from test No.17 showing minimal scatter

4.5 Hardness survey

Before undertaking a metallographic examination of the material, a hardness survey of both the parent plate and the welded specimens was carried out. The survey was performed using a standard Vickers Hardness Testing Machine, modified by the addition of a micro-hardness machine precision vice and turntable. All results were produced using a 5 Kg load (HV5) at intervals of 0.75 mm. For the parent plate material in the longitudinal direction the result was reasonably consistent at a value of 260 ± 10 Hv, which is well within the accepted scatter bands of approximately 15%.

In the case of the welded material, the specimen was first polished to one micron then etched in 10% Nital. The hardness survey took the form of three lines of indentations spanning the parent plate, H.A.Z. and weld metal. The results are shown in figure 54. As can be seen, the hardness was considerably higher in the H.A.Z. than in the parent plate. The most startling aspect of this hardness profile is the fact that the value for the H.A.Z., especially in the last weld pass, can reach a maximum value of 435 Hv. In the H.A.Z. of the other weld runs the hardness was considerably lower, due to the tempering effect of the following passes. In all three hardness surveys the value for the weld metal was lower than that recorded for the parent plate.

It is worth looking more closely at the high H.A.Z. hardness value as it may prove to be more important than is at first realised. It is widely acknowledged that problems associated with stress corrosion cracking, hydrogen induced cold cracking and underbead cracking occur with hardness values over 350 Hv. The problem is such that pipeline welders in the field put a top limit of 238 Hv in order to stop stress corrosion cracking and hydrogen induced cold cracking (Ref 100). As discussed in the literature survey, hardness values can be related to yield stress. Using the correlation outlined by Hart (Ref 66) in conjunction with the hardness values found in the hardness survey of the H.A.Z., it seems not unreasonable to suggest that the yield strength of the material can reach over 1100 N/mm^2. This is well over the 900 N/mm^2 value quoted by Hockenhull (Ref 5) for a pre-cracked specimen above which stress corrosion cracking may become a problem, especially in the context of this project where significant quantities of hydrogen are produced under severe overprotection conditions.

A hardness survey of the heat treated material produced a consistent reading of 380 ± 8 Hv, again indicating that the material yield strength should be in the region of 1000 N/mm^2.

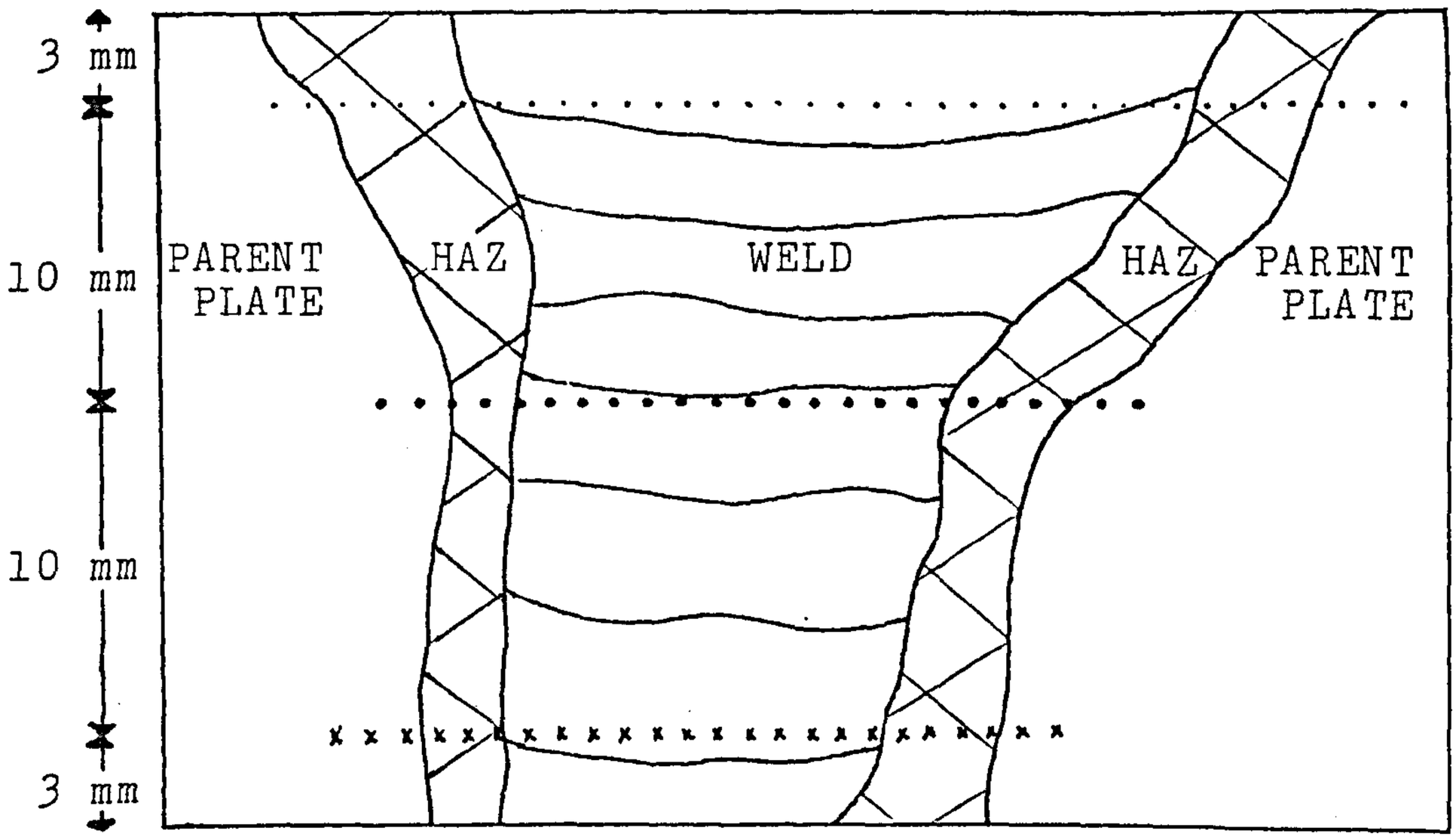

Schematic of weld

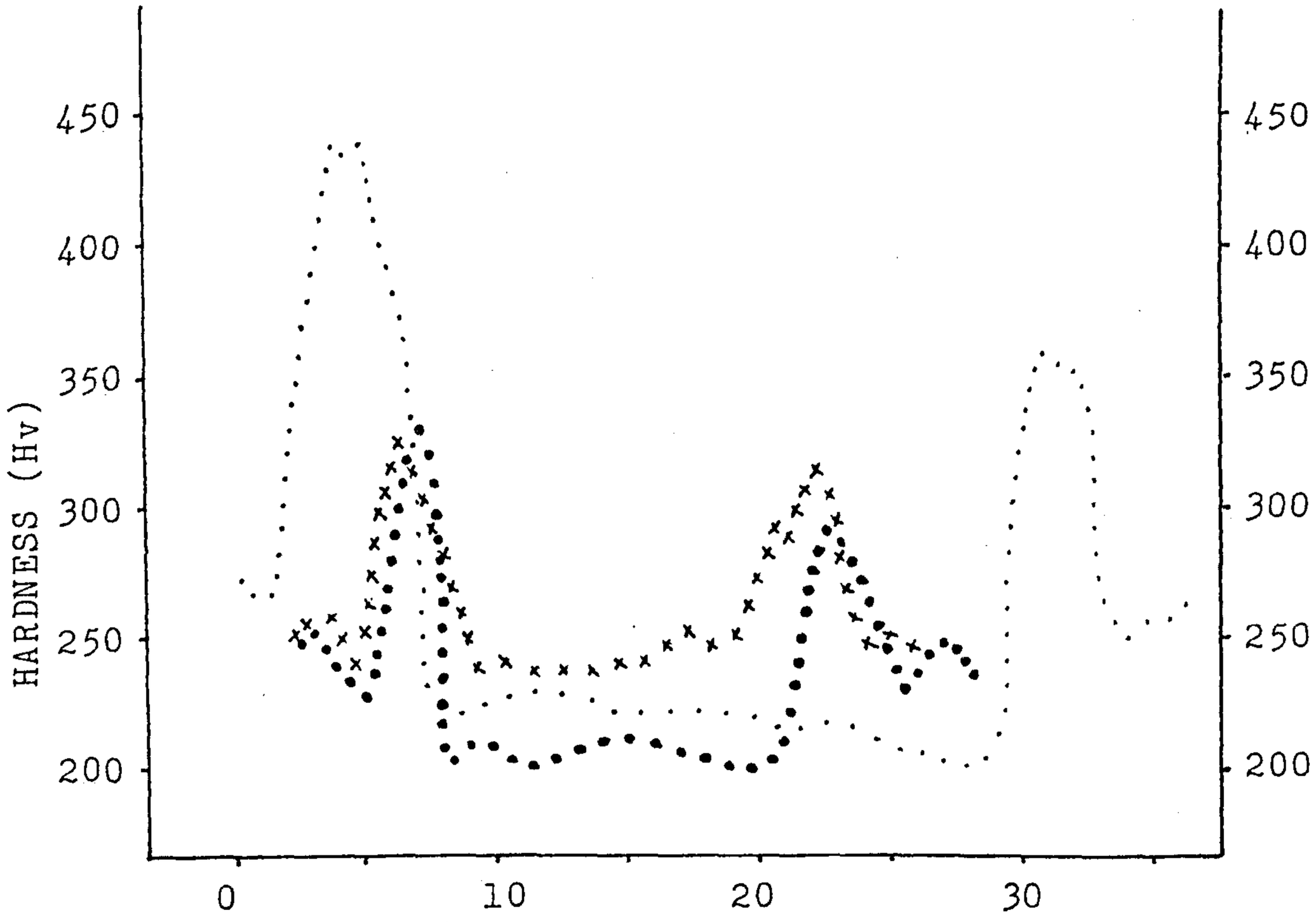

Figure 54. Hardness survey of parent plate, H.A.Z. and weld metal

4.6 Material metallography

During the course of the project work, extensive metallographic examinations were carried out on both the parent plate specimens and the welded specimens in both the etched and unetched conditions. To facilitate this the material was polished to 1 micron then etched using 2% Nital. In the first instance this was done to study the distribution and morphology of inclusions and later to determine their effect and that of the base material microstructure on the fracture paths of corrosion fatigue cracks.

4.6.1 Inclusions

There were basically three main types of inclusions found in the parent plate samples of N-A-XTRA 70 examined. Surprisingly enough, manganese sulphide did not prove to be one of these. Normally with rolled steel specimens one would expect to find elongated type II manganese sulphide inclusions in the form of stringers parallel to the rolling direction. However, with this steel it was impossible to find large MnS stringers, the main reason being the low sulphur content of the material, i.e. 0.004%. The main inclusion types are shown by figure 55 and are discussed individually below.

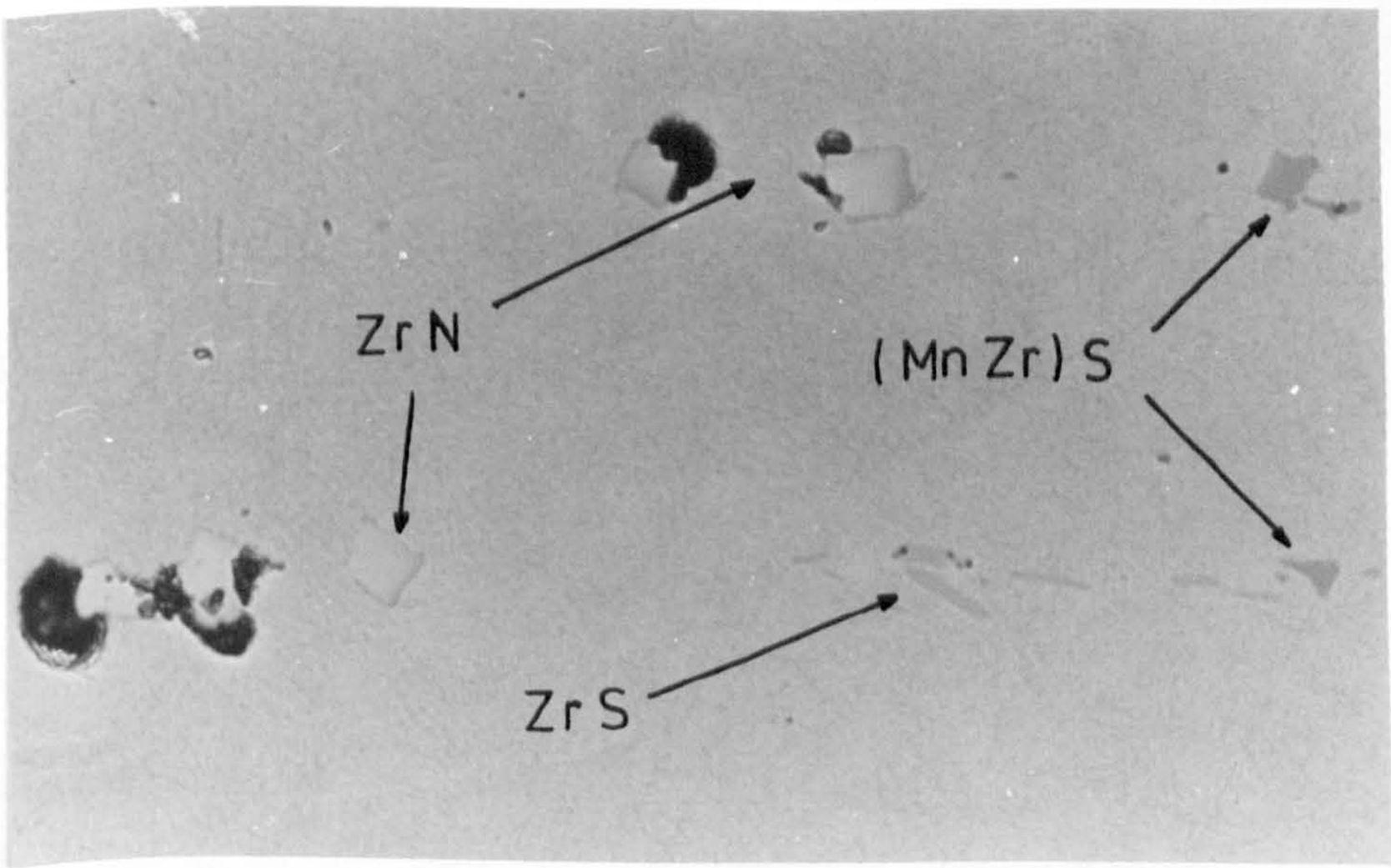

Figure 55. Types of inclusions found in parent plate N-A-XTRA 70 X 800

(a) Zirconium nitride

These inclusions were lemon yellow to orange in colour, approximately 8 microns in length along any side and varied in shape from square, rectangular, triangular, or trapezoidal to octagonal. Consultation with Dr.-Ing. B. Müsgen of Thyssen Aktiengesellschaft (Ref 109) revealed that the particles were indeed ZrN; the zirconium being added to the steel in order to bind free nitrogen and to control the sulphide morphology. Allmand (Ref 110) suggests that low zirconium contents give paler coloured and softer inclusions, whilst higher zirconium contents give darker colours and are much harder. Zirconium nitride is also difficult to eliminate from the steel because of its high specific gravity, and is generally found in the lower regions of the ingot. It is not malleable at steel working temperatures, which would explain why the particles had not been deformed by rolling. The dark material attached to the ZrN particle shown in figure 55 is zirconium silicate.

(b) Zirconium sulphide

These inclusions were in the form of bluish grey (low zirconium content) to yellowish tan (higher zirconium content) stringers, average length approximately 8 microns. In cast material the inclusions are globular but at steel working temperatures those with less zirconium deform easily. Those richer in zirconium deform less readily. In most instances the colour of the particles is more or less the same as manganese sulphide and the two sulphides are almost indistinguishable in ordinary light. There is probably a great deal of MnS in solid solution with ZrS. Not surprisingly, given the low sulphur content, there was very little ZrS found in the steel.

(c) Mixed manganese / zirconium sulphide

The third type of inclusions found were less angular and regular than the zirconium nitride particles. The colour was darker than that of the zirconium sulphide, being a darker orange/yellow. The 'rounded prismatic' shape of these inclusions was due to their limited plasticity at steel working temperatures.

Of all the inclusions found in the steel, the more prismatic zirconium nitride was the most frequently observed. From a purely microscopic standpoint it is difficult to say what effect these particles would have on an advancing corrosion fatigue crack. Figure 56, which was produced using a plastic replica technique on N-A-XTRA 70 by Callister (Ref 111), shows quite clearly how the fatigue crack has avoided the ZrN particle. However, it must be remembered that this situation occurred for a fatigue crack in air and

Figure 56. Pre-fatigue crack avoiding ZrN particle X 400

at 0.5 Hz. For a more relevant situation figure 57 shows how the corrosion fatigue crack has run through a cluster of ZrN particles. Figure 58 shows how the crack has encountered a ZrS stringer, propagated along part of the stringer, then continued through the parent material, and figure 59 shows how a corrosion fatigue crack has completely split a ZrN particle.

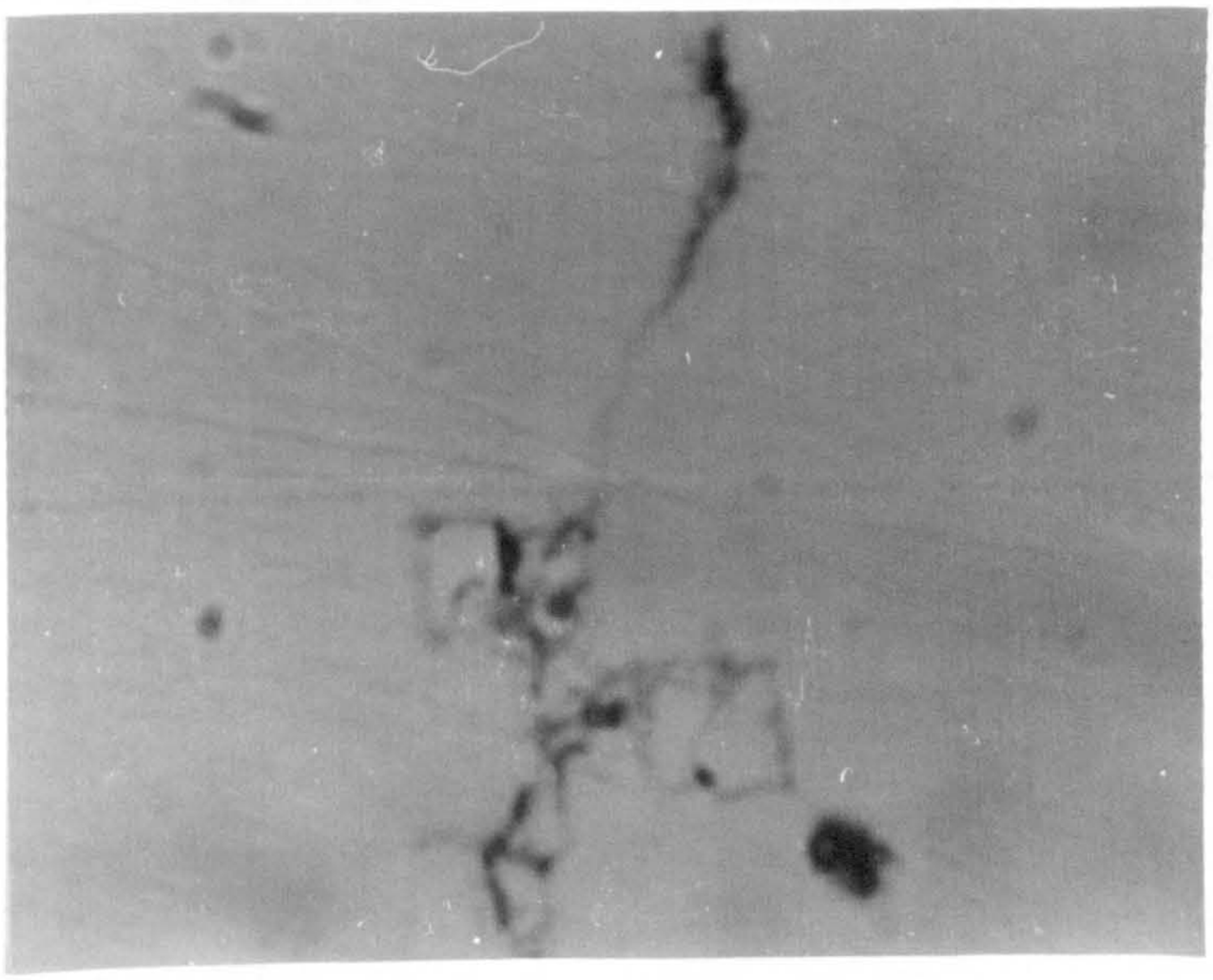

Figure 57. Corrosion fatigue crack running through ZrN cluster X 2500

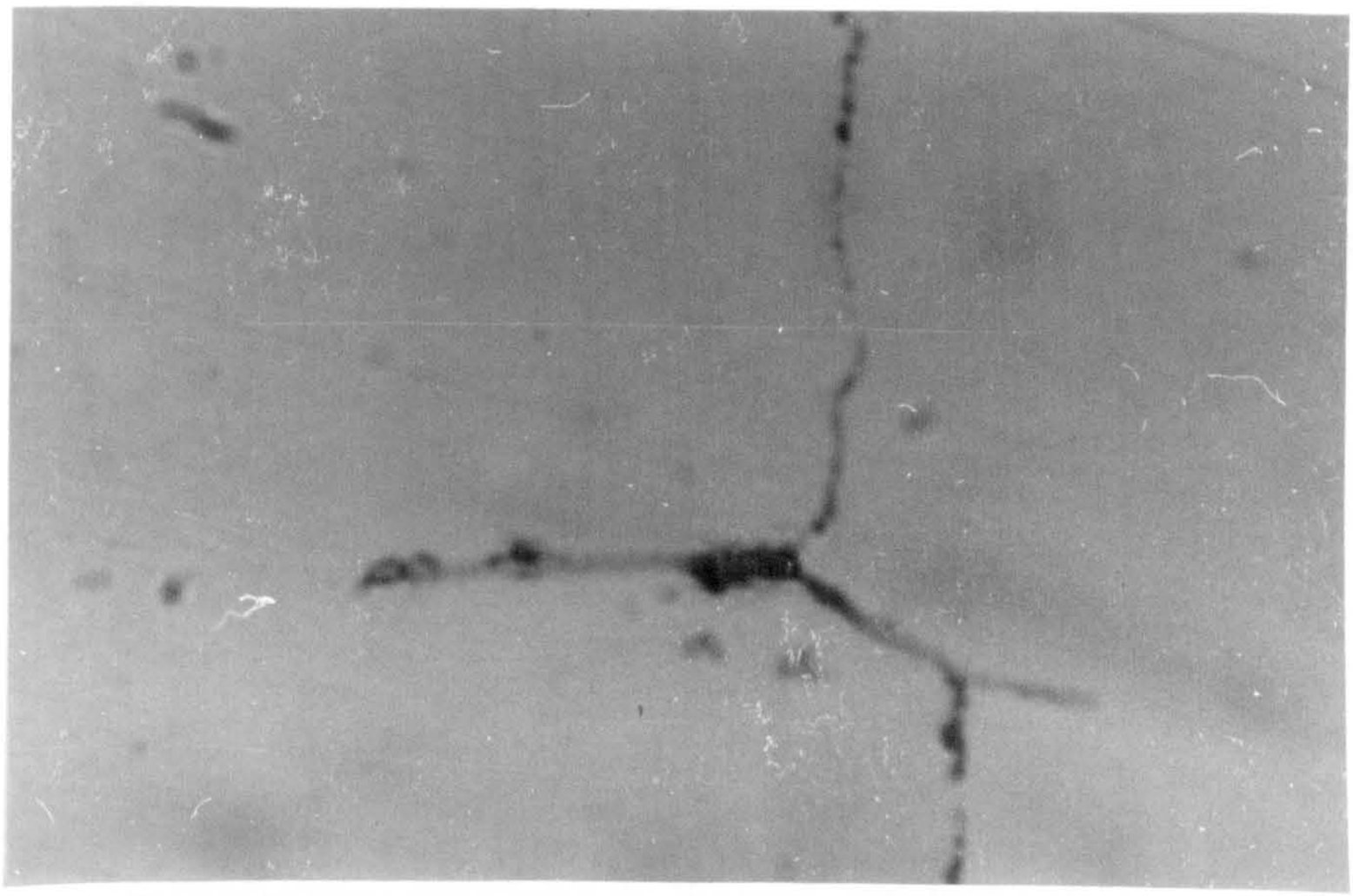

Figure 58. Corrosion fatigue crack running along ZrS stringer X2500

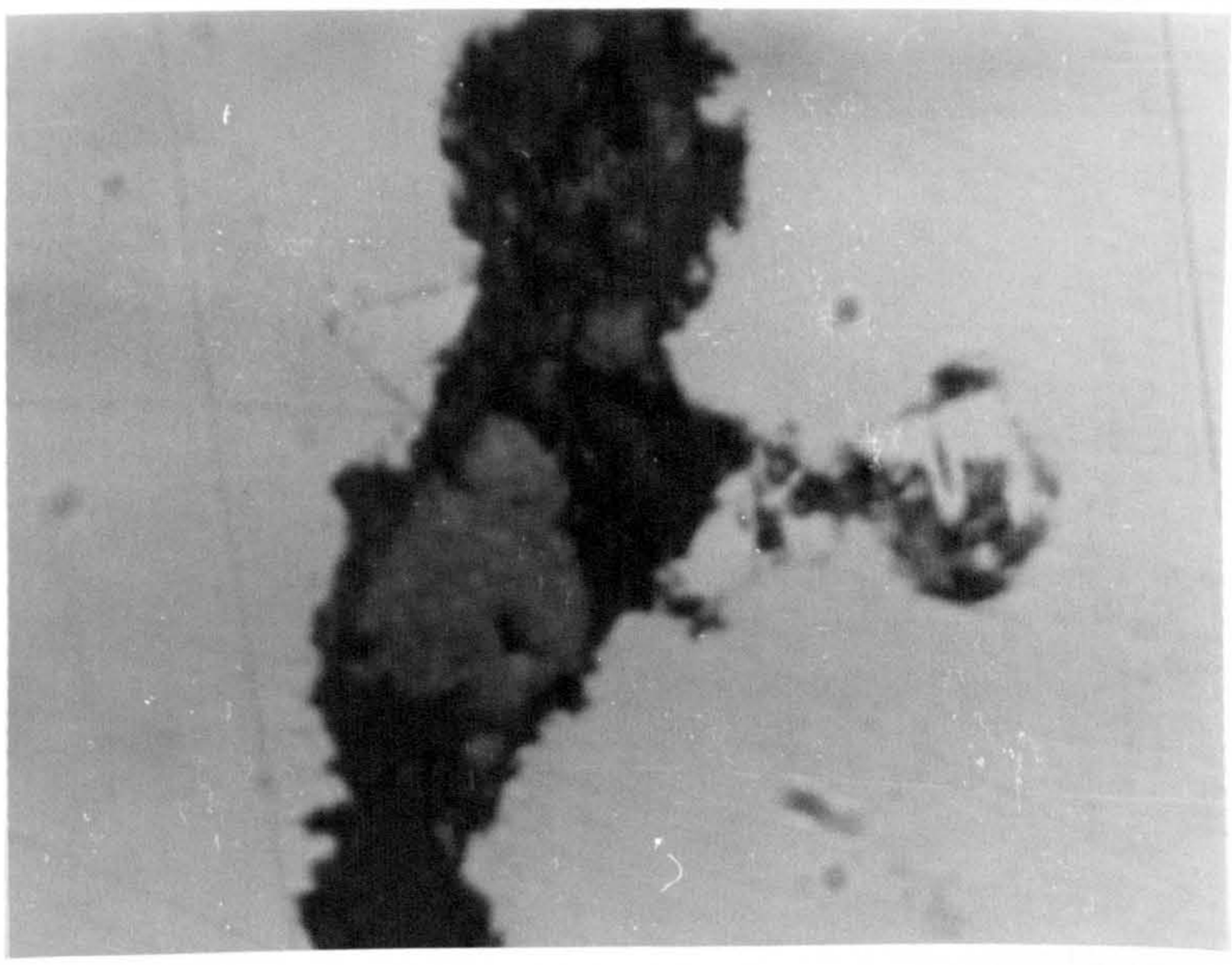

Figure 59. Corrosion fatigue crack splitting ZrN particle X 2500

One comment that must be made regarding all these photos showing fatigue and corrosion fatigue cracks interacting with inclusions, is that they are taken at the surface of the specimen where the particles and the crack are under plane stress conditions. This may not be a true representation of what actually happens under plane strain conditions encountered in the bulk of the material, therefore, any conclusions drawn must be tempered with this knowledge in mind.

4.6.2 Microstructures

Figure 60 shows the typical etched microstructure of the parent plate material. An extremely fine ferrite substructure with well distributed fine carbide and nitride precipitates can be seen.

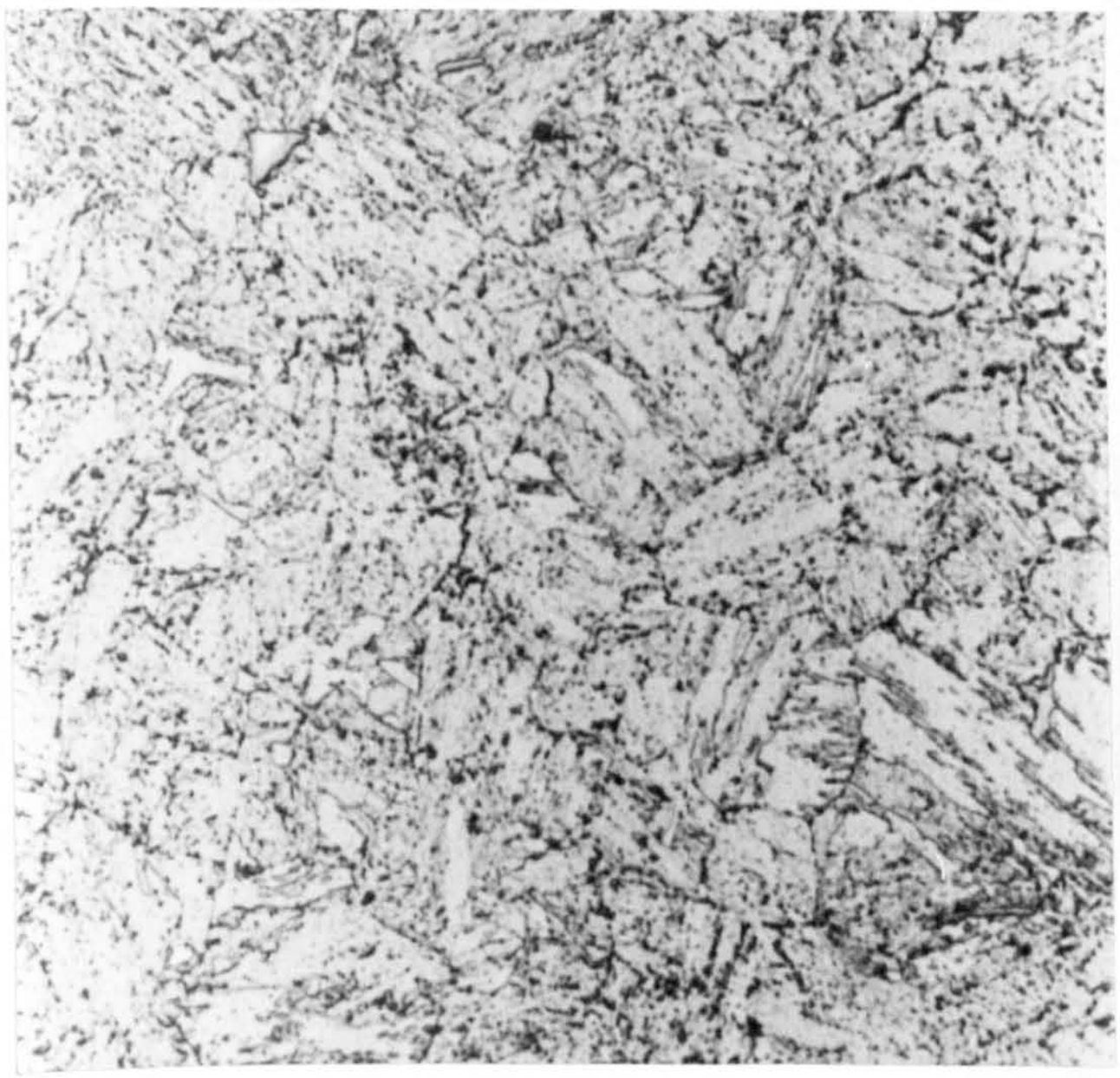

Figure 60. Parent plate microstructure X 800

It is this combination which accounts for the high strength and toughness of the material.

The as-deposited weld metal shown in figure 61 is completely different to that of the parent plate. The acicular ferrite structure obtained was due to the lower carbon content of the weld metal (0.07% as opposed to 0.16% in the parent plate), and to the high cooling rate of the low (3 KJ/mm) heat input during welding.

The heat affected zone, because of the range of heating and cooling rates, was seen to exhibit quite a wide variation in microstructural profiles. The H.A.Z. itself can be broken down into two distinct regions (shown in figure 62)- Region A, which is closest to the parent plate and is the cooler area, and Region B, which because of its closer proximity to the weld metal will be much warmer.

Figure 63 shows the transition from the parent plate material into the cooler region A of the H.A.Z. The most salient feature of this micrograph is the dark precipitate around the prior austenite grain boundaries. In this area

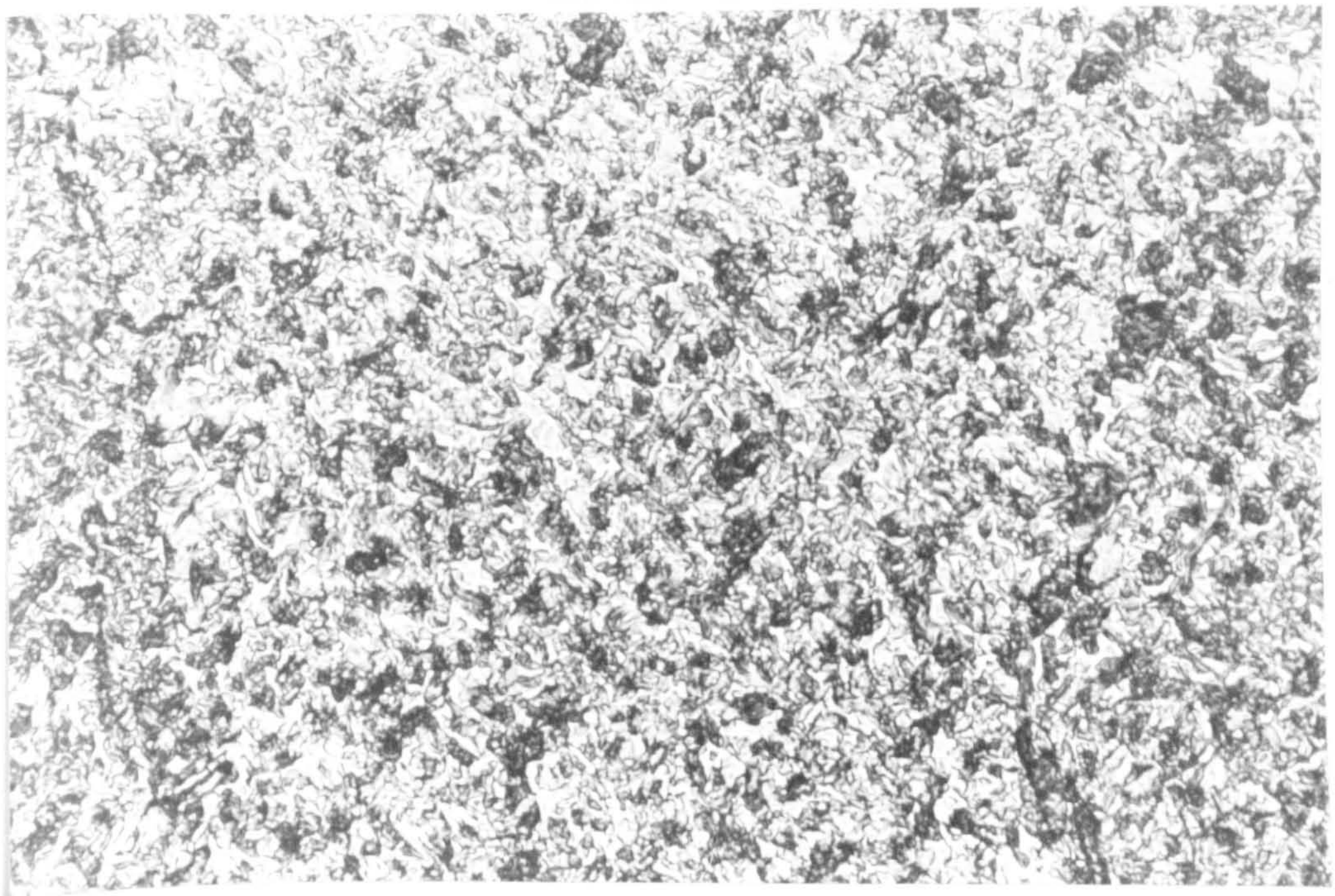

Figure 61. As-deposited weld metal X 650

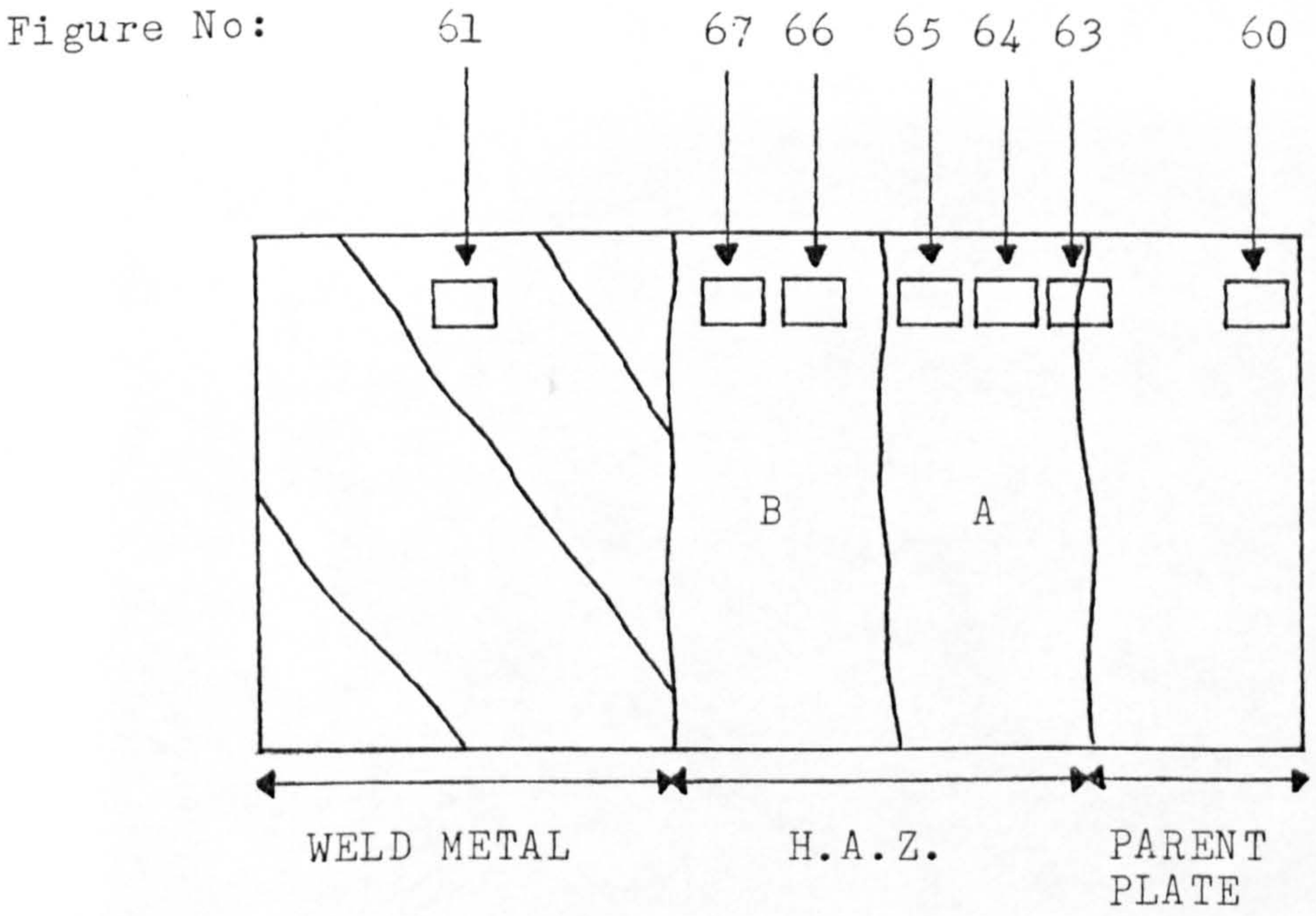

Figure 62. Position of microstructure photographs

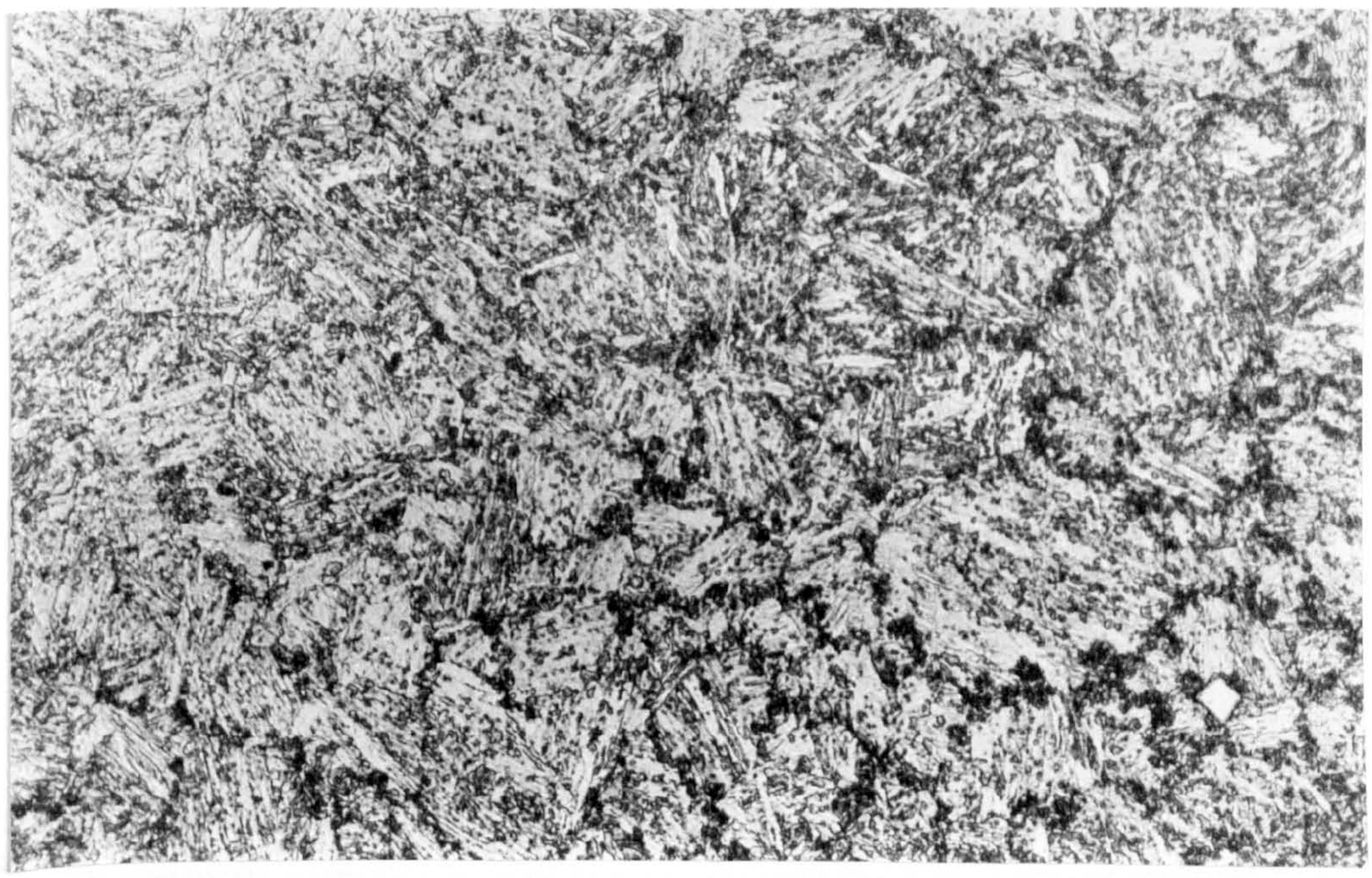

Figure 63. Transition from parent plate to H.A.Z. region A X 500

the temperature reached an estimated 800°C and the subsequent cooling rate was quite low. This would have enabled dissolved carbides to precipitate at the grain boundaries, which seems to be the case.

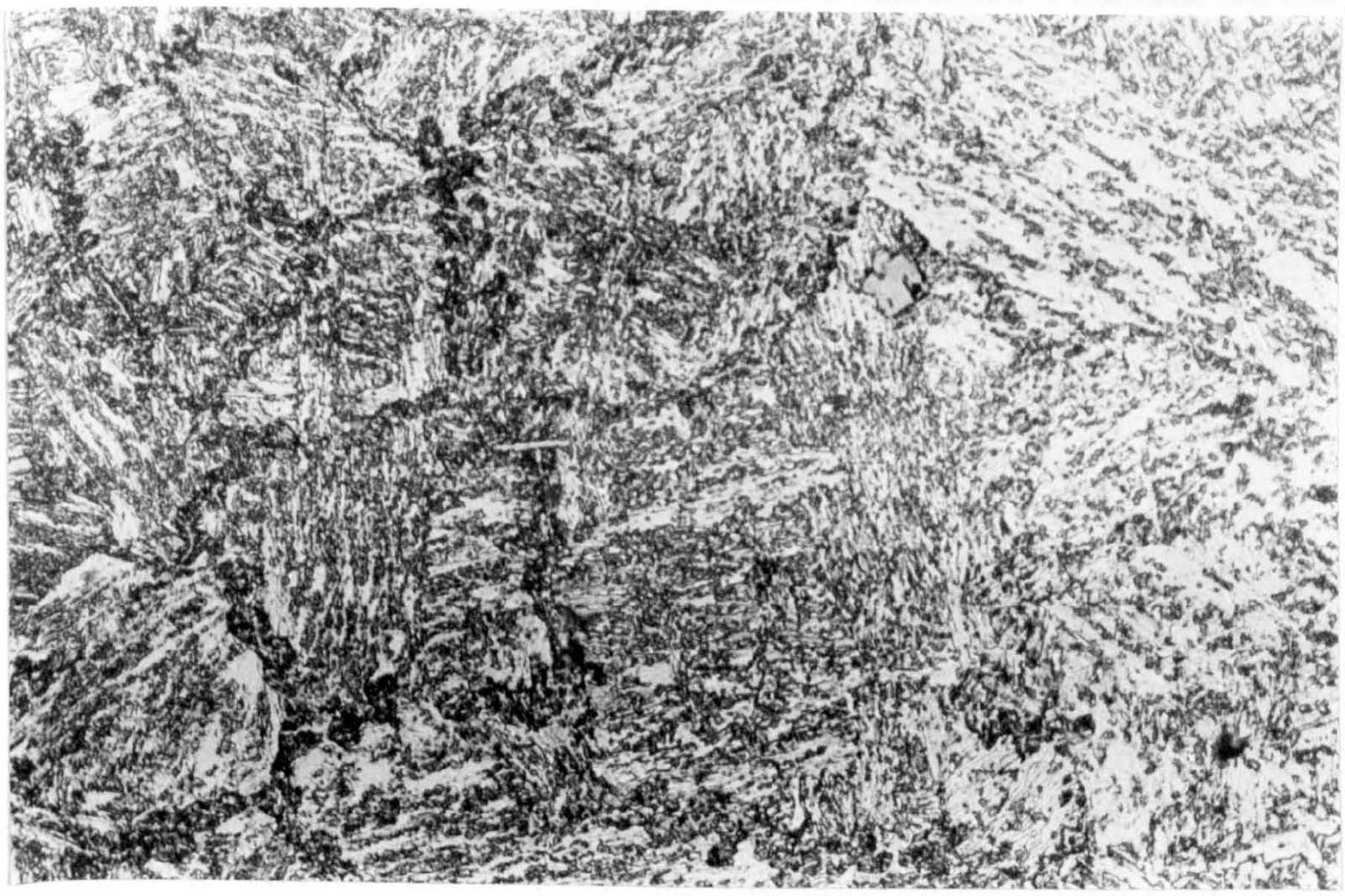

Figure 64. Transition of lower temperature H.A.Z region X 500

Figure 64 shows the transition to the grain refined area of the cooler H.A.Z. region. This area was noticeable for it's uniform distribution of carbides, produced by the grain refining action of several weld runs. Figure 65 shows the centre of this region.

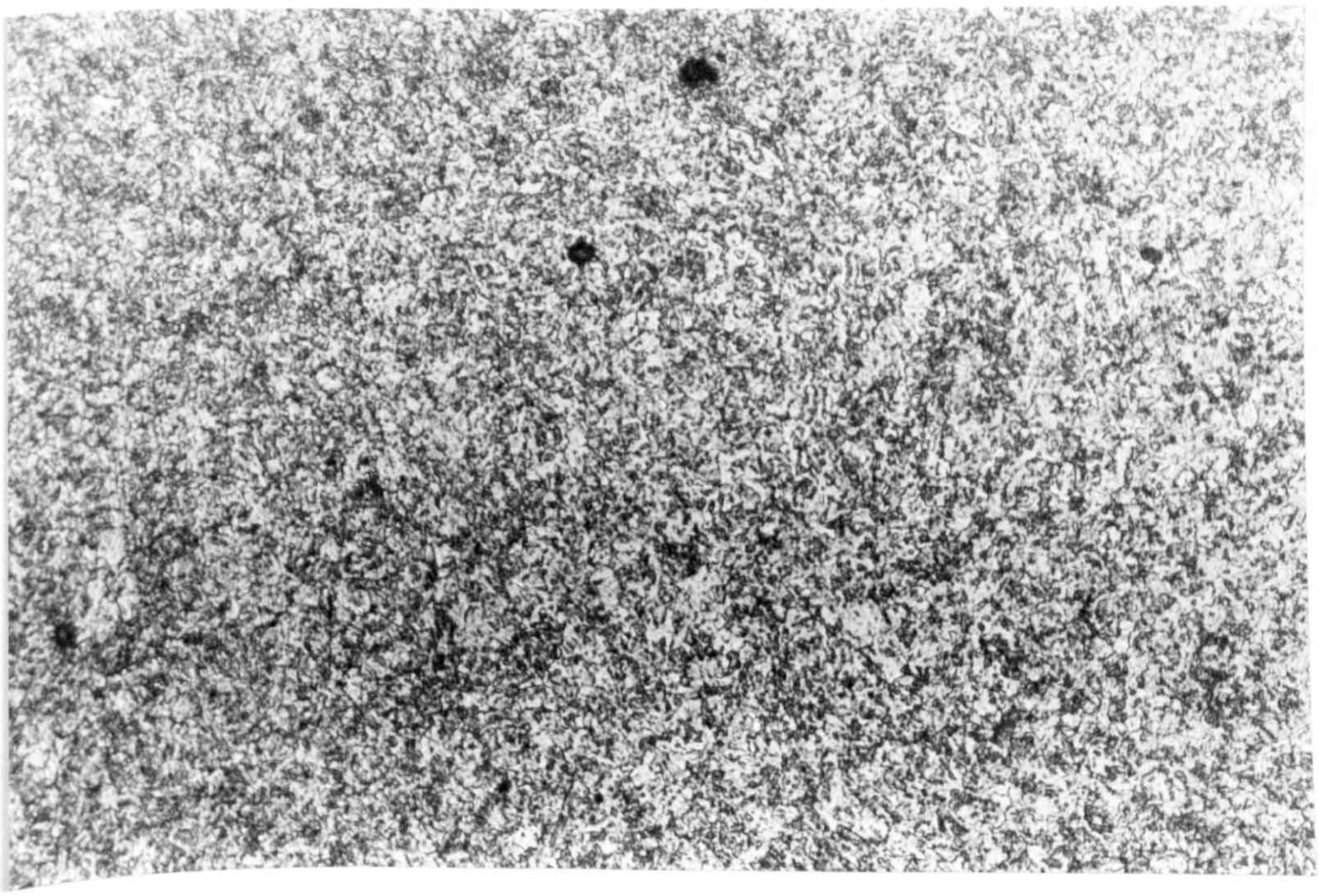

Figure 65. Grain refined area of H.A.Z. X 500

In the hotter region of the H.A.Z. the microstructure is very similar in appearance to the parent plate. However, in this area the temperature will have reached between 1300° and 1500°C, which is enough to cause rapid grain coarsening. This can be seen quite graphically in figure 66 where the grain size has increased dramatically in a relatively short distance. This increase in grain size continues until at the weld metal interface the grain size is quite large, as can be seen from figure 67.

For the heat treated material, metallographic examination shows that the structure resembles that of the original parent plate material (figure 68). However, the prior austenite grain size has increased, thus making the microstructure resemble that of the grain coarsened region in the H.A.Z.

In the final analysis of the material used in this project it must be said that the microstructures were similar for both the parent plate and the H.A.Z. material. Apart from one area of the H.A.Z., where the carbides had dissolved and re-precipitated on the grain boundaries, the only real difference was the prior austenite grain size and

Figure 66. Grain coarsening in H.A.Z. material X 120

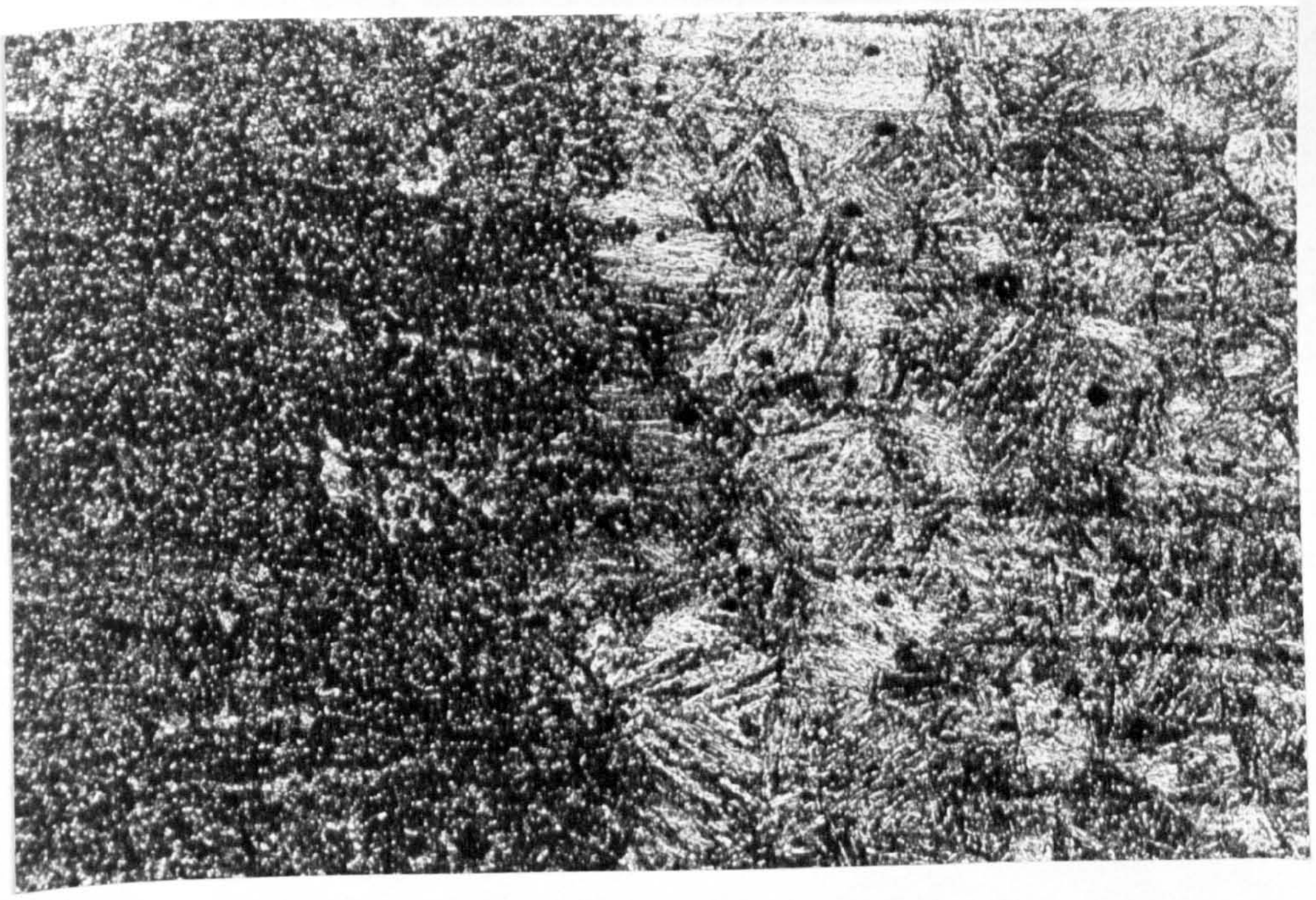

Figure 67. H.A.Z./weld metal interface X 120

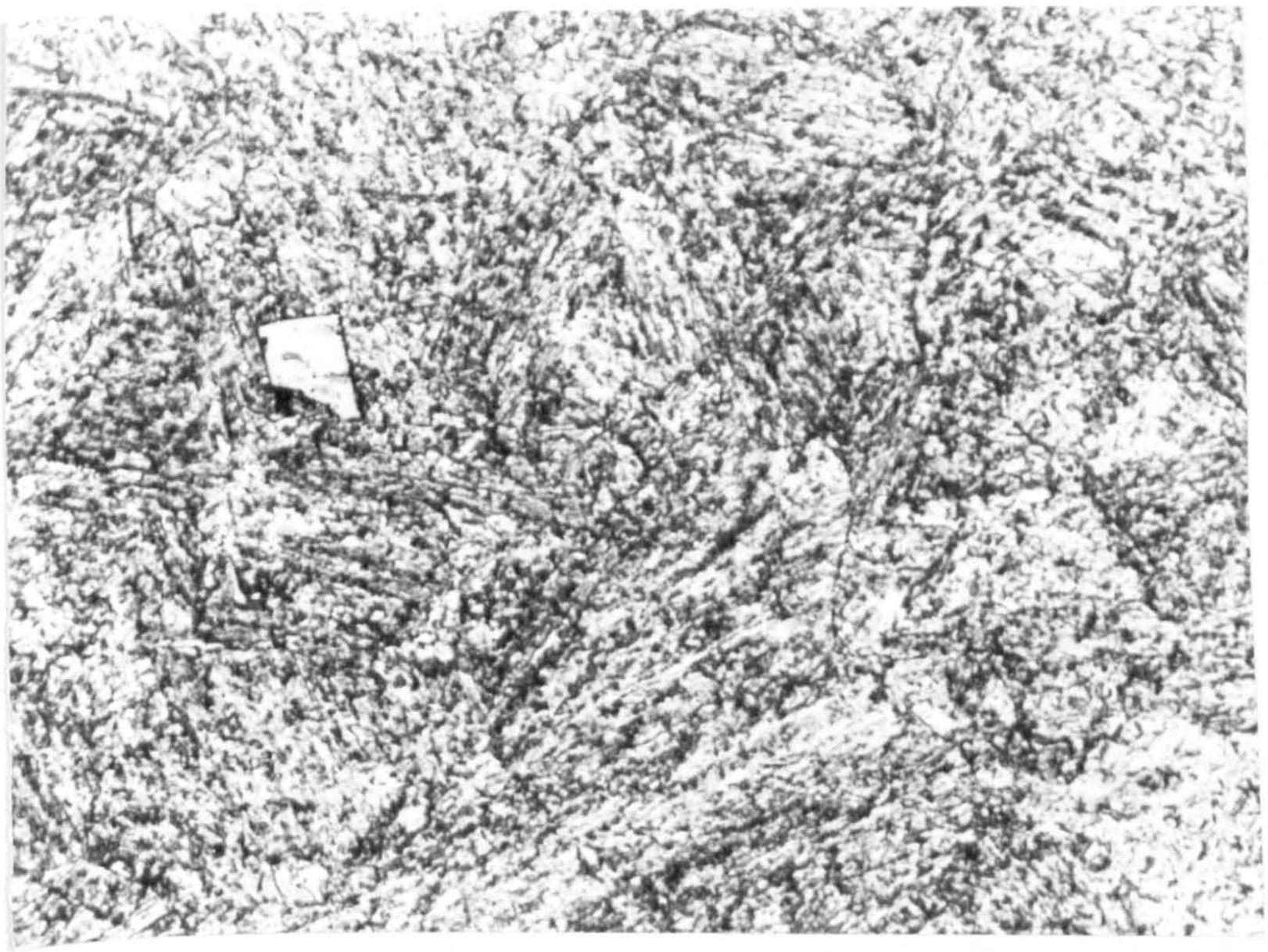

Figure 68. Heat treated material microstructure X 650

recrystallised grain size. The underlying structure was still basically a fine distribution of carbide particles in a ferrite background. Obviously the weld metal was a different microstructure, but as it is widely believed that corrosion fatigue cracks propagate predominantly in the heat affected zone region, no corrosion fatigue testing was carried out in the weld metal.

4.7 Inclusion survey of fracture surfaces

When the corrosion fatigue fracture surfaces were analysed in the scanning electron microscope (S.E.M.), a salient feature observed regularly was the zirconium based inclusions discussed earlier. The most frequent kind were the cuboid type judged to be zirconium nitride. Figure 69 shows two groups of these particles; on the left hand side of the photograph, and more clearly within a deep crack in the centre. Figure 70 shows these central inclusions at a higher magnification.

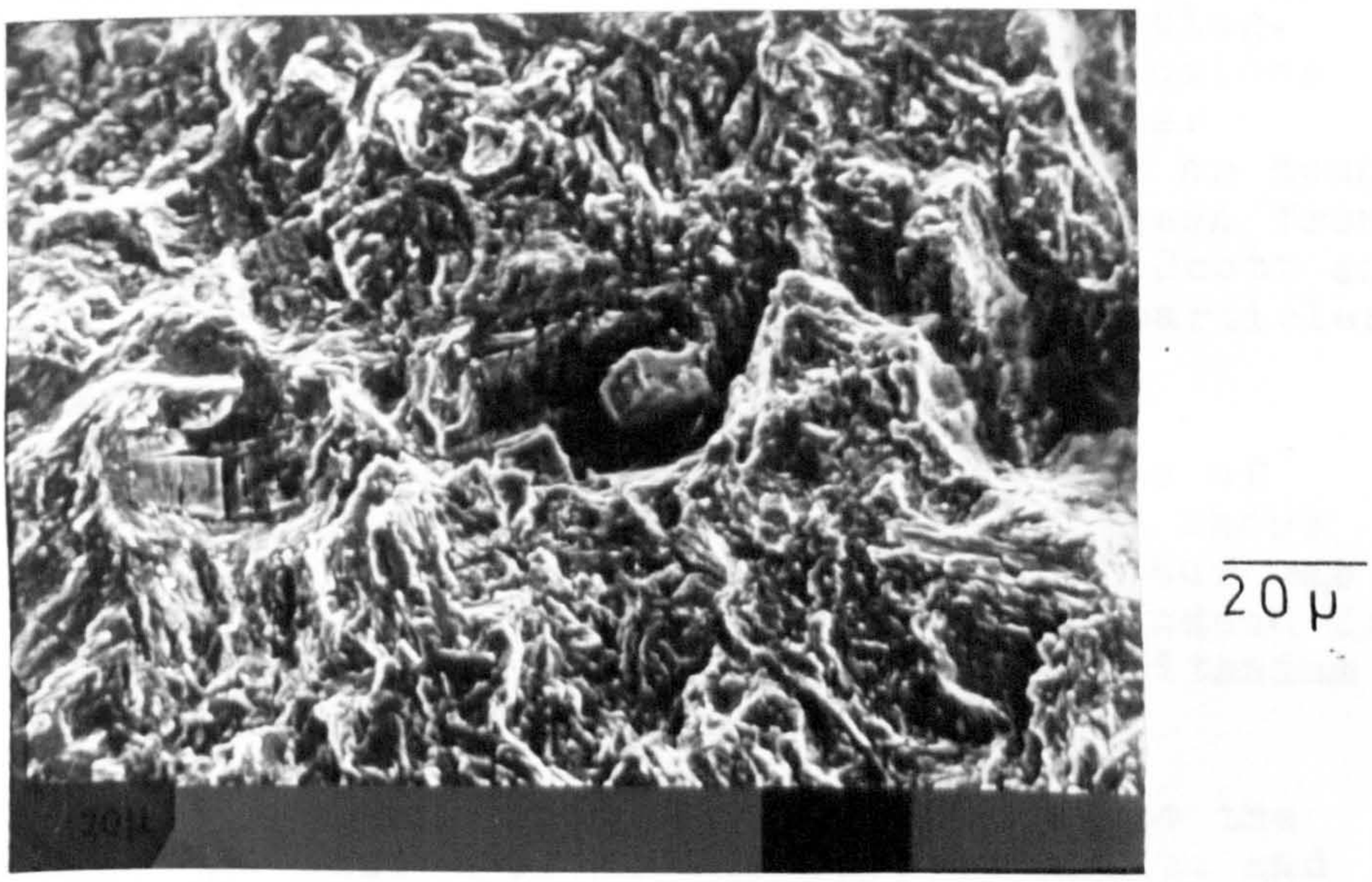

Figure 69. Fracture surface with ZrN particles (parent plate)

Figure 70. Higher magnification of central portion of figure 69

Figures 69 and 70 were taken from a parent plate specimen under free corrosion conditions and represent the fracture surface at an intermediate stress intensity range $\Delta K = 26 MPa\sqrt{m}$. These figures quite clearly illustrate the two main situations in which the particles appear:

a) bonded to the matrix quite solidly; and
b) separated from the matrix on most sides.

It is interesting to compare figure 70 with figure 71, which is a micrograph of a similar specimen at a similar ΔK value under similar environmental conditions only viewed 'side on' using an optical microscope. Two ZrN particles can be seen at the bottom of two corrosion pits. In the upper pit the steel matrix seems to have been corroded away leaving the particle hanging, whereas in the lower pit the particle seems to have stopped the pit from advancing. Such observations appear to suggest that the inclusions are cathodic with respect to the steel matrix under conditions of free corrosion. It is, however, by no means certain that this is always the case, as can be seen from figure 74. In addition, evidence put forward by Scott and Silvester (Ref 50) suggests that zirconium rich particles may dissolve in the corrosion fatigue process.

Figure 72 is a characteristic analysis of the type of inclusions shown in figure 70. The spot analysis shows Fe, Zr and Ti to be the major peaks. As no sulphur was found it is safe to assume that the particle is indeed ZrN or a zirconium-titanium nitride with a very low titanium content.

Analysis of the H.A.Z. under similar conditions to the above exhibited the same type of particle formation and distribution, as can be seen from figure 73. Figure 74 shows a 'side on' view of the fracture surface using the S.E.M. This shows quite clearly how the particle has fractured, while still remaining well bonded to the matrix. It was quite common to find ZrN particles shattered in such a way at all levels of stress intensity on both H.A.Z. and parent plate fracture surfaces. Some exhibited clean rectilinear fractures whilst others were badly smashed, as shown in figure 75 (which was taken from a parent plate specimen at $\Delta K = 28 MPa\sqrt{m}$, protected cathodically at -700 mV S.C.E.).

Figure 76 shows the final failure section of a parent plate specimen. It quite clearly exhibits the classic ductile dimple and particle configuration, with the ZrN inclusions most certainly being the sites of initiation of the micro-voids which link up to form dimples.

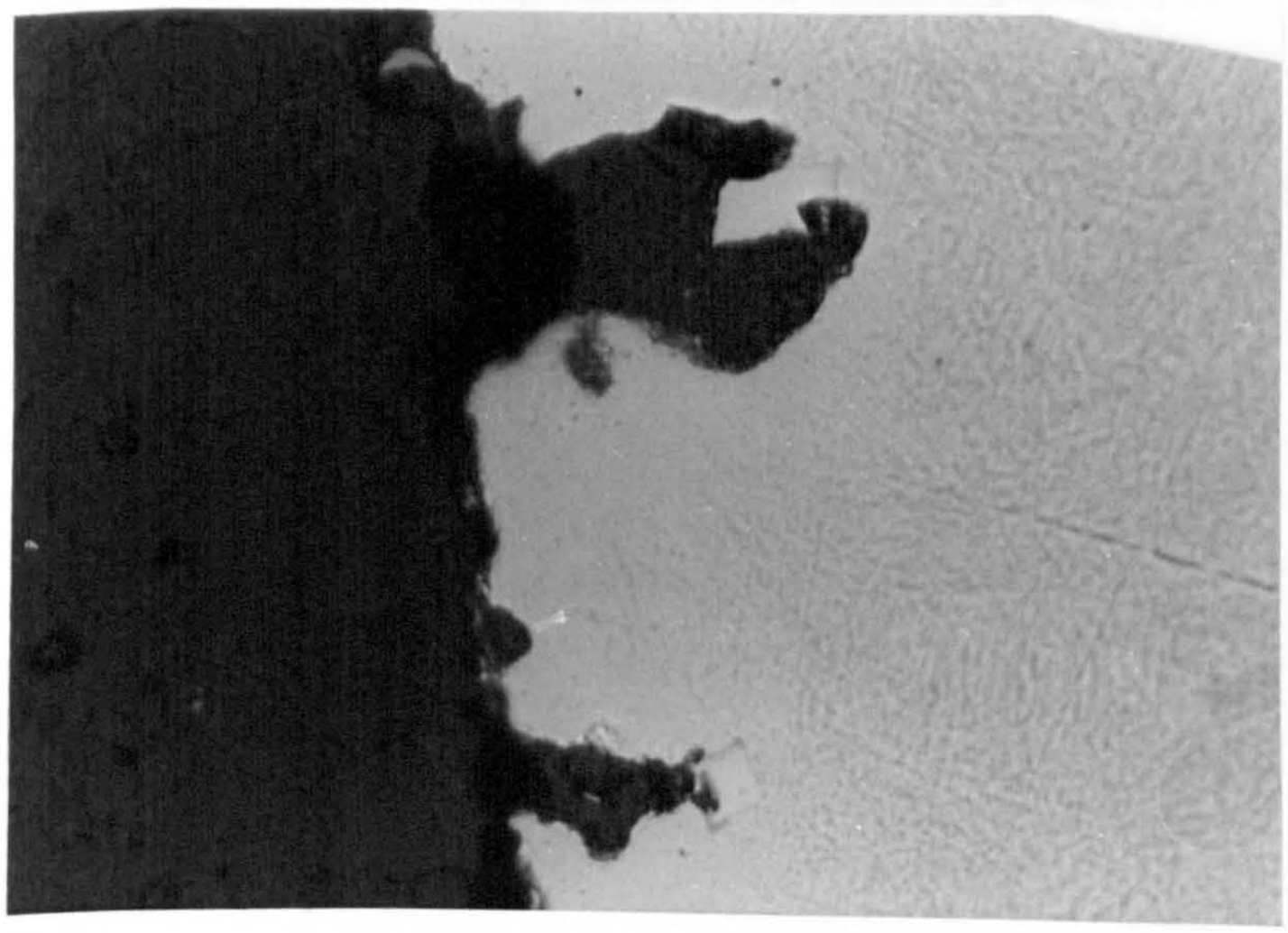

Figure 71. Edge of corrosion fatigue surface X 650
(parent plate)

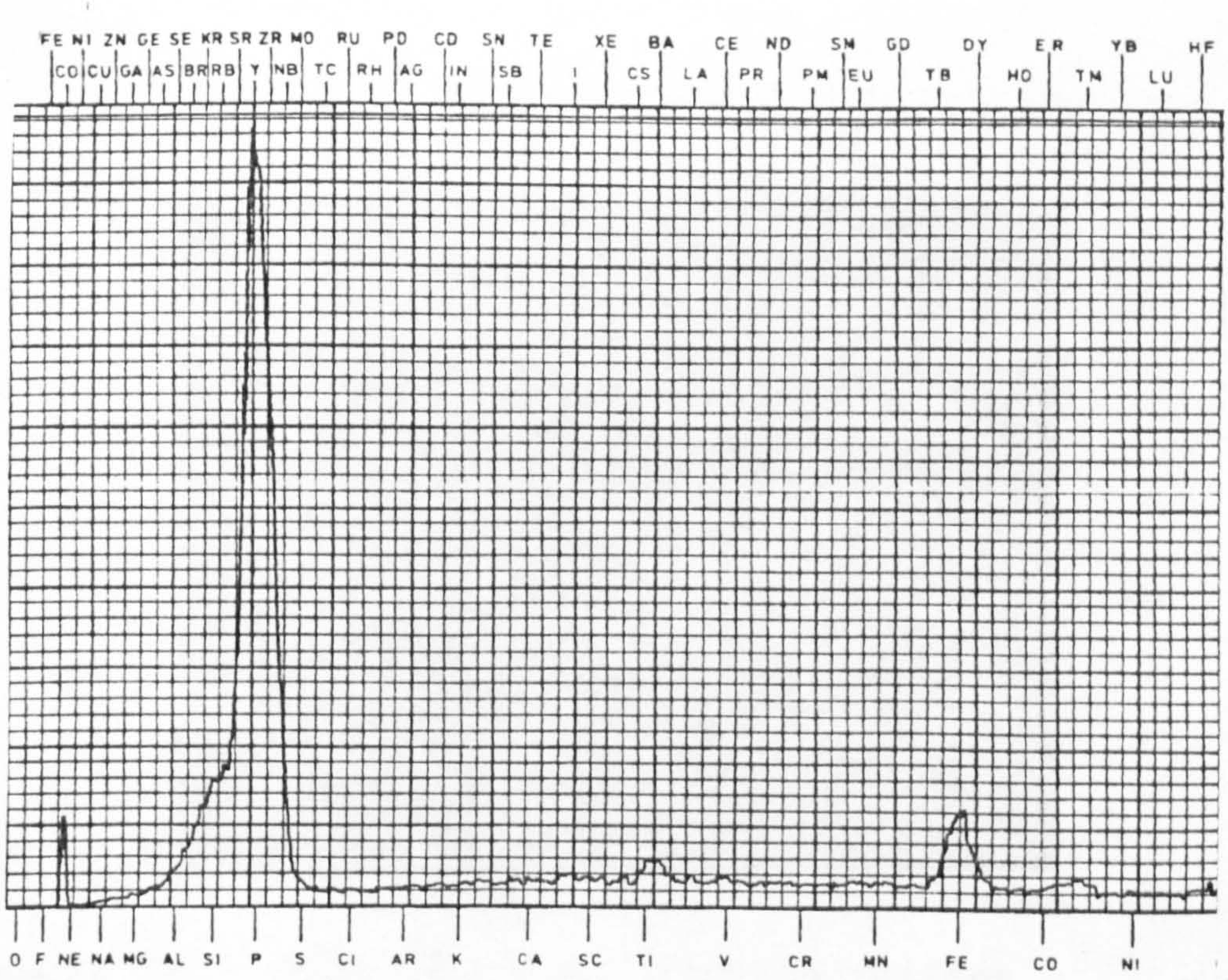

Figure 72. Characteristic analysis of ZrN inclusion

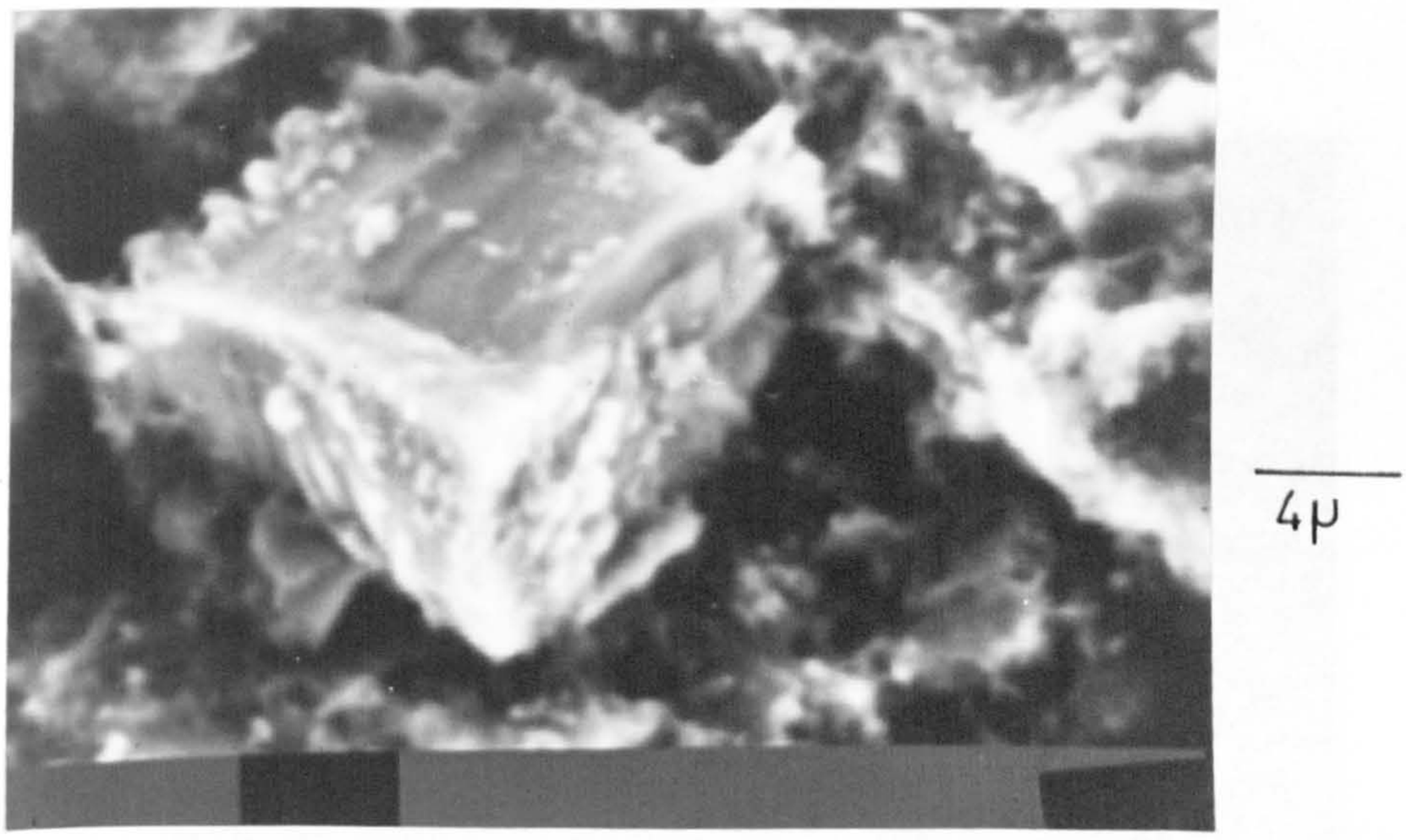

Figure 73. ZrN particle on H.A.Z. fracture surface

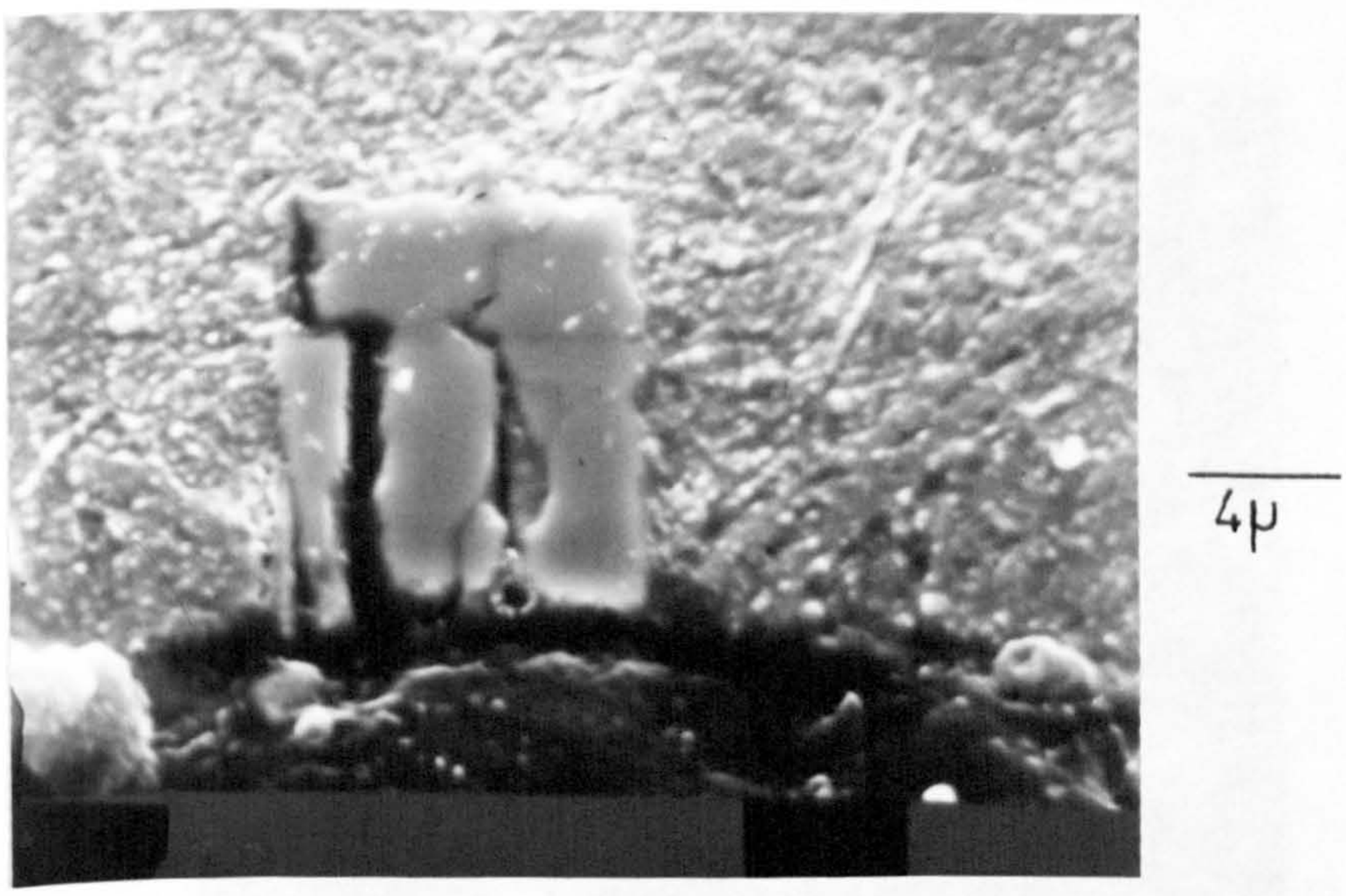

Figure 74. Edge of H.A.Z. fracture surface

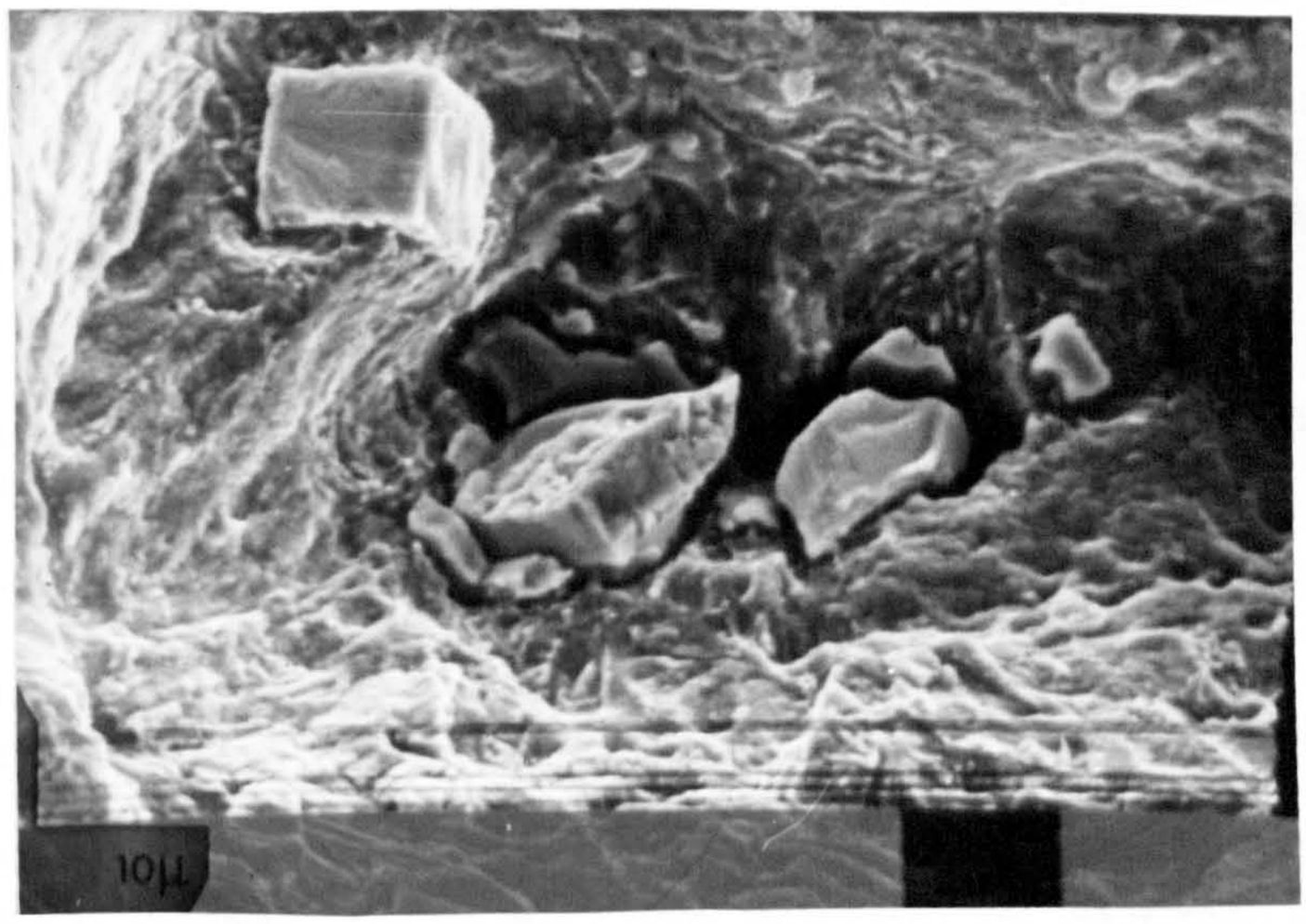

Figure 75. Fracture surface of parent plate showing fragmented inclusions

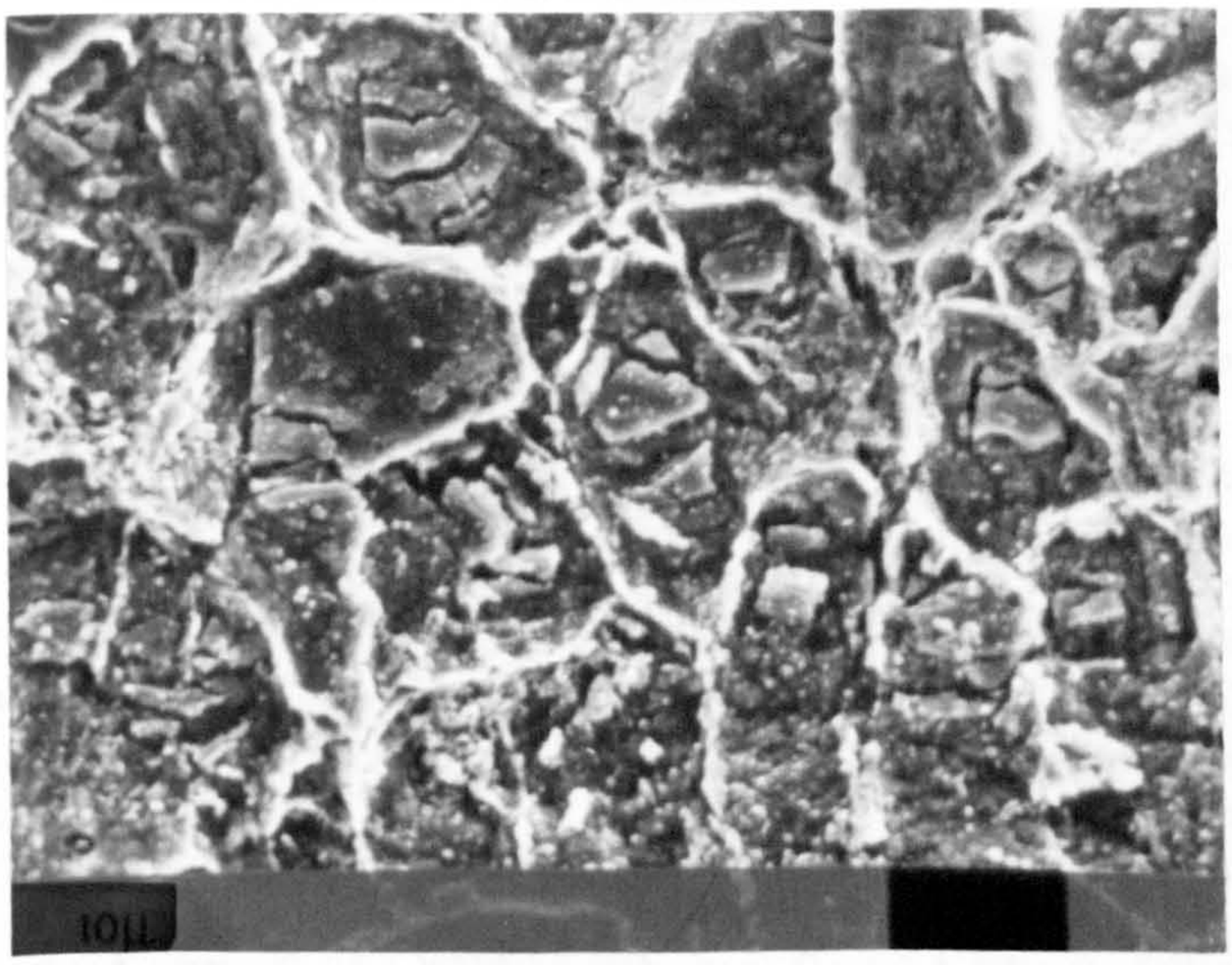

Figure 76. ZrN particles at the bottom of ductile dimples

Since the zirconium rich particles behaved in a similar way for both H.A.Z. and parent plate material under the whole spectrum of environmental and potential conditions in operation during this project, it is very difficult to say how they affect the path of the advancing corrosion fatigue crack.

Laird (Ref 112), in his discussion on the influence of metallurgical structure on the mechanisms of fatigue crack propagation, suggests that for high strain fatigue, micro-structures containing second phase particles may have their fatigue crack propagation rates affected by:

1) the strength of the particles in relation to that of the matrix,

2) the size of the particles,

3) the nature of the bond between the second phase and the matrix.

Large second phase particles, stronger than and well bonded to their matrix, should have little effect on crack propagation since any crack would seek out the easiest path through the matrix. On the other hand, with a distribution of hard particles in a softer matrix (a situation observed in N-A-XTRA 70) the crack front may advance with sporadic increases in crack propagation rate as the more brittle inclusions are fractured. This would however be a localised effect which may or may not be significant to the overall crack propagation rate, depending on the amount of second phase particles present.

As can be seen from the photographs, several things can occur; the particles can remain well bonded to the matrix in either the shattered or unshattered condition, or they can remain unshattered and disbond almost completely. As no shattered particles were found in unfatigued material, it seems reasonable to suggest that the advancing crack front has caused the inclusion to shatter. It may be possible that the particles hold up the advancing crack front until the stress level is high enough to fracture them, allowing the crack to progress. Thus the particles may act as crack stoppers. However, the alternatives are that the particles have no appreciable effect on the local crack propagation rate, or in the case where the particles have disbonded almost completely, then decohesion may lead to a localised increase in the crack propagation rate.

In work carried out on N-A-XTRA 70 by Callister (Ref 142), comparison between the amount of ZrN found on the fracture surface of fatigue specimens and that found on a polished surface plane parallel to the fracture surface, showed a significantly higher fracture surface occurrence. It was further noted that inclusions exposed on the fracture surface, although frequently cracked, did on the whole

appear to be complete and standing proud of the fracture surface. It was suggested that debonding between matrix and inclusion was the main process of fatigue crack propagation on encountering an inclusion. With reference to the present work, two points must be raised: firstly, Callister's fatigue experiments were conducted in air so there will have been no electrochemical interaction between the particles and the matrix; and secondly, for this project comparison between the density of ZrN particles exposed on the fracture surface and on a polished surface plane parallel to the fracture surface, showed no great difference in particle density under various cathodic protection potentials. The major reason why there is this difference between the results for corrosion fatigue experiments and in-air experiments may be the nature of the corrosion fatigue process. In the fatigue in-air condition the crack front will encounter numerous small areas of weakened material associated with the zirconium inclusions. In the corrosion fatigue condition, however, the advancing crack front will not need to seek out the weakened inclusion areas since the processes of hydrogen embrittlement and anodic dissolution will have in effect reduced the strength of the whole matrix ahead of the much faster advancing crack front.

Whatever the definitive effect of the zirconium rich inclusions, it is the author's belief that they play very little part in affecting the overall performance, in terms of corrosion fatigue crack propagation, of N-A-XTRA 70. This is because, although small and brittle, they are so widely dispersed that the percentage of the inclusions interacting with the propagating crack at any one time would be very small.

4.8 Surface deposits

Surface deposits were found on all specimens except those tested in air. In the case of the freely corroding specimens and those protected at -700 mV (S.C.E.), a greenish deposit formed on the specimen surface within several hours of immersion. Initially it formed near to the notch and on parts of the specimen that were in contact with the rollers and it gradually increased until, by the end of the experiment, nearly all of the specimen was covered with the deposit. As the experiment progressed the deposit changed colour from it's initial green to a darker green to brown/red. This deposit was analysed using X-ray spectroscopy equipment and was shown to consist of mainly iron oxide. It is almost certain that the deposit was ferrous hydroxide in the first instance, which oxidised to form hydrated ferric oxide, as shown by equation 5 (page 7). During the corrosion fatigue test the deposit was easily removed by gentle brushing, whereas brushing in flowing water and ultrasonic cleaning was needed to remove it from the fracture surface. Figure 77 shows the fracture surfaces of specimens fatigued under conditions of free corrosion, in air, and under cathodic protection.

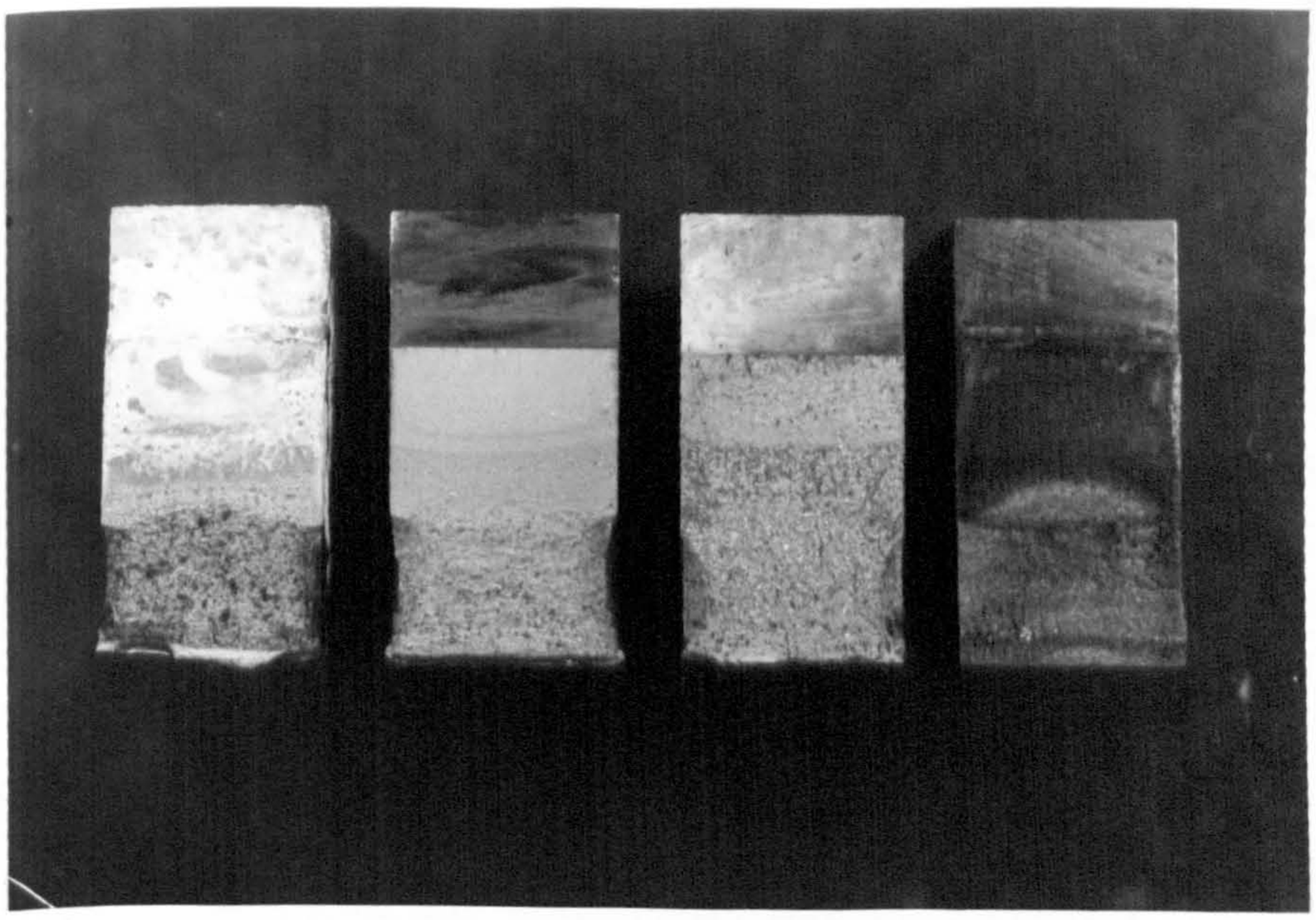

A = severe overprotection of heat treated specimen
B = in-air
C = overprotection
D = free corrosion

Figure 77. Fracture surfaces of specimens fatigued under various environmental conditions

In the case of all other cathodically protected specimens, the fracture surfaces showed varying degrees of calcareous deposit formations. These ranged from a very fine deposit, almost undetectable by eye, on the 'correctly' protected (-780 mV S.C.E.) specimens to a quite thick covering on those specimens at -1300 mV S.C.E. The morphology of the deposits is shown schematically in figure 78.

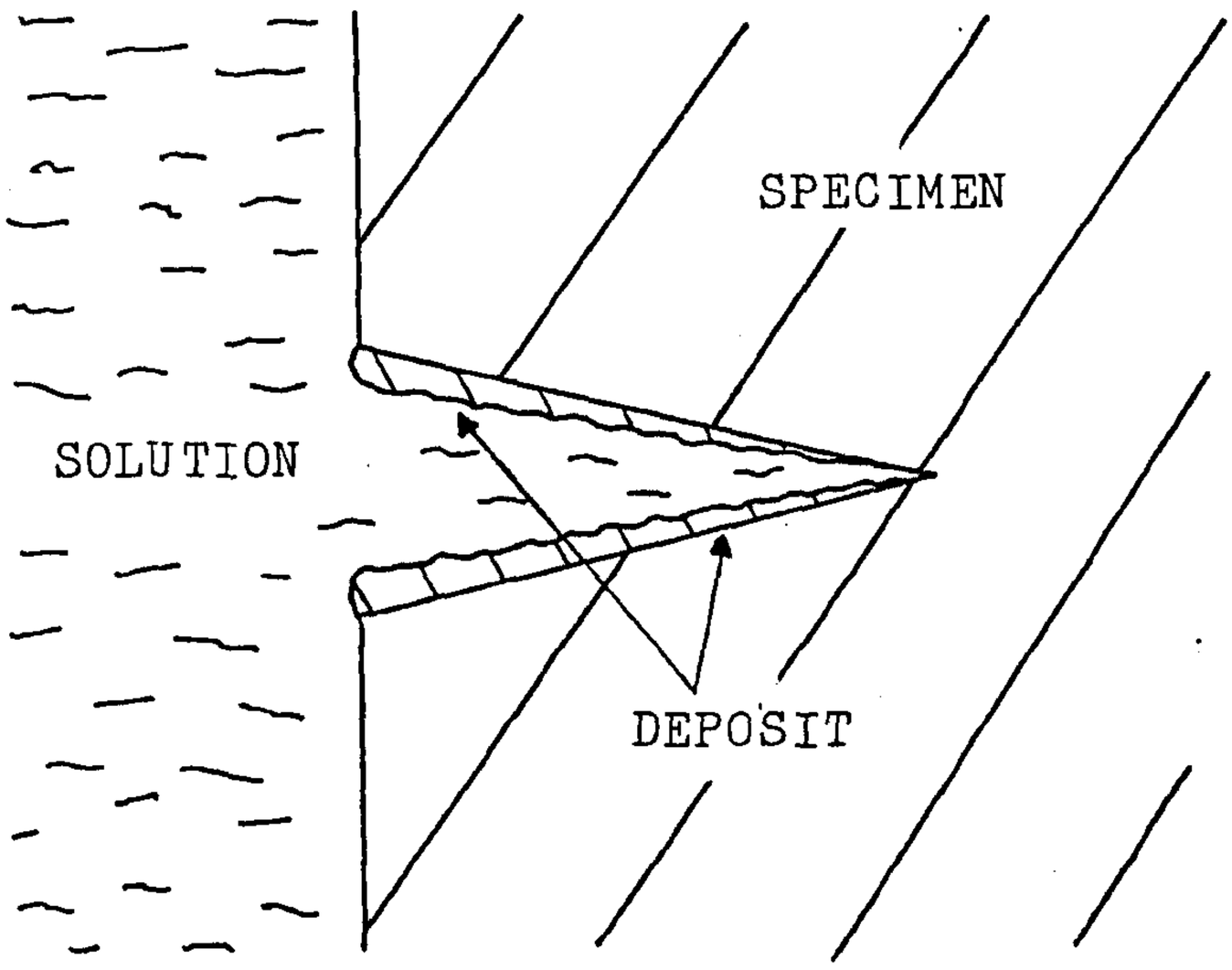

Figure 78. Schematic of calcareous deposit morphology

This generalized behaviour can be explained purely by the time involved to form the deposit in terms of the rate of crack advance. Obviously the longer the fracture surface is in contact with the sea water environment then the thicker the deposit will be. Therefore it is not surprising that the thickest deposits were found on the pre-fatigue fracture surface, whereas virtually no deposit was encountered at the crack tip region where fresh material had only just been exposed.

Photographs obtained using a scanning electron microscope show this more clearly. Figure 79 shows calcareous deposits formed in the middle of the prefatigue surface at two different magnifications. The coral/honeycomb type structure can clearly be seen in figure 80. Figure 81 shows the final fatigue surface and how the level of calcareous deposit has been greatly reduced.

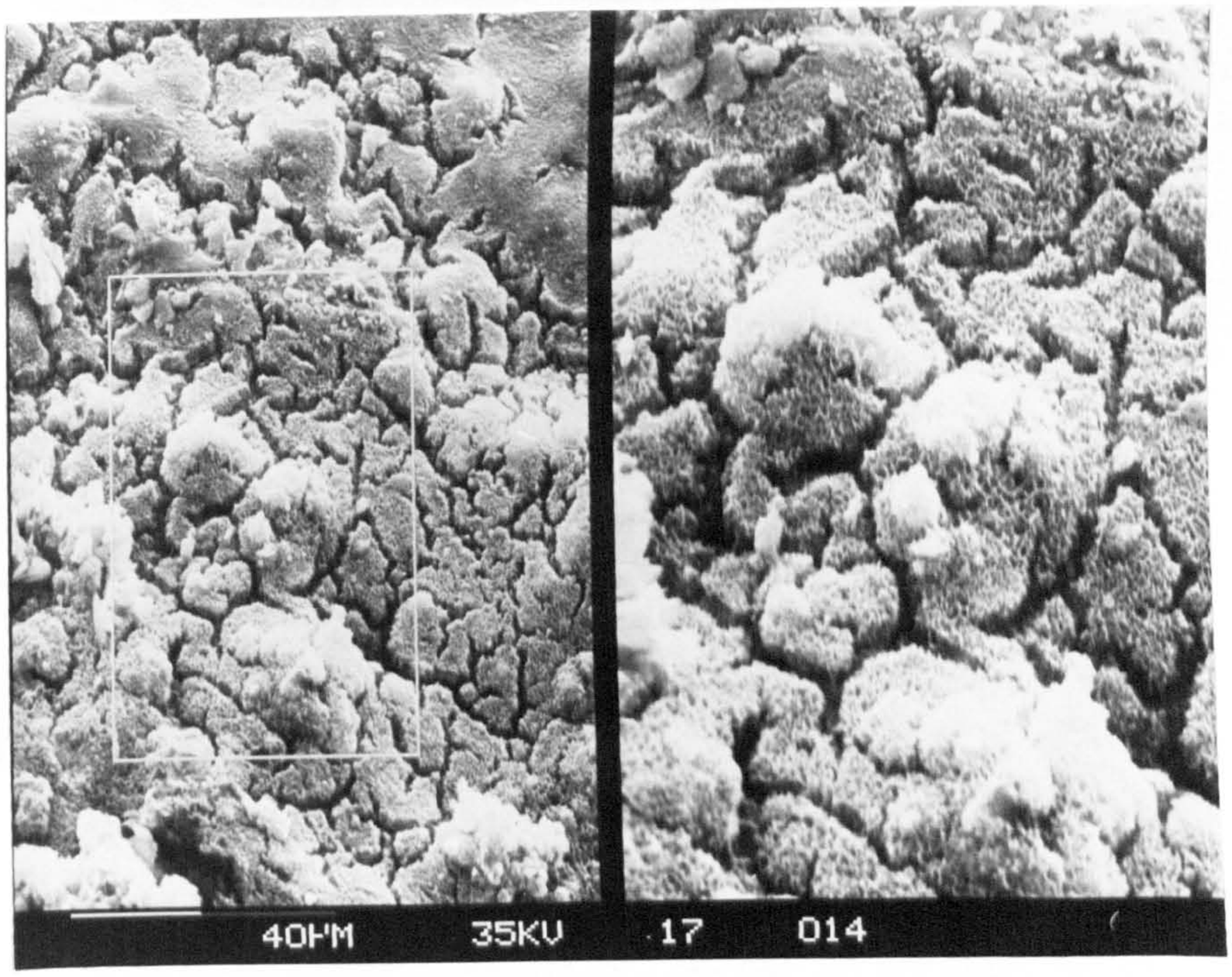

Figure 79. Deposit formed on prefatigue fracture surface

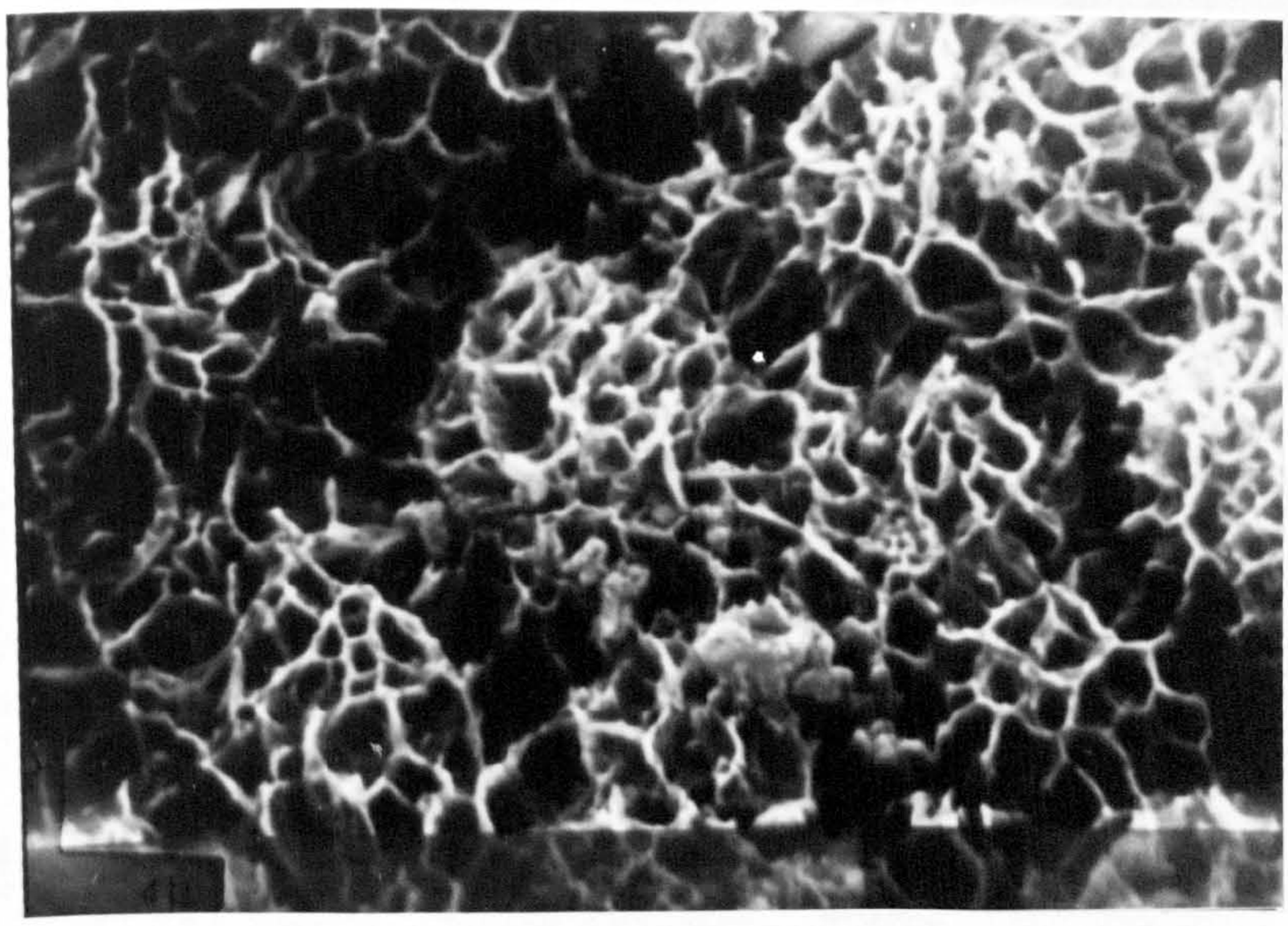

Figure 80. As figure 79 at higher magnification

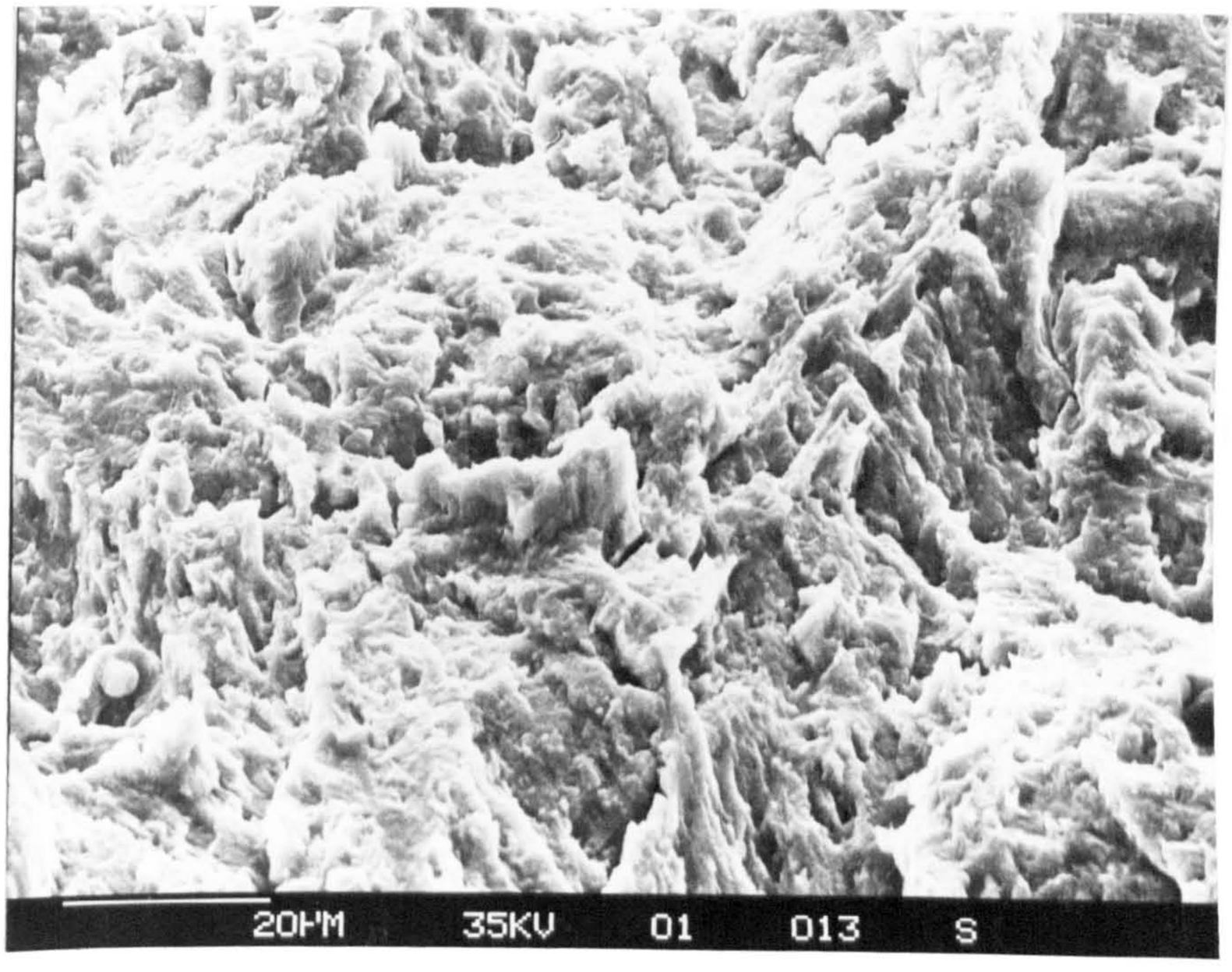

Figure 81. Deposit on final fatigue fracture surface

With this situation in mind it is worth discussing the effect of calcareous deposits on crack closure.

It is generally believed that calcareous deposits cause a wedging action which reduces the effective stress intensity range at the crack tip and reduces closure. It is the author's belief that in this project this did not occur, the reasons being that with an R ratio of 0.6 the crack faces would not come in contact with each other throughout the course of the test and also in the cases of severe overprotection when the deposit formation rate was at its highest, the crack propagation rate was also at its highest due to hydrogen embrittlement. As intimated previously, this means that the crack front would be advancing too fast for any deposits formed to have any significant effect. It is also the author's belief that any proposed effects for laboratory specimens cannot readily be translated to offshore structures where size effects, crack geometry, tidal forces and marine growths will affect the deposition and integrity of the deposits.

Fracture surfaces were analysed using the dispersive analysis attachement on the S.E.M. Figure 82 shows part of the prefatigue surface of a parent plate specimen cathodically protected at -1300 mV (S.C.E.).

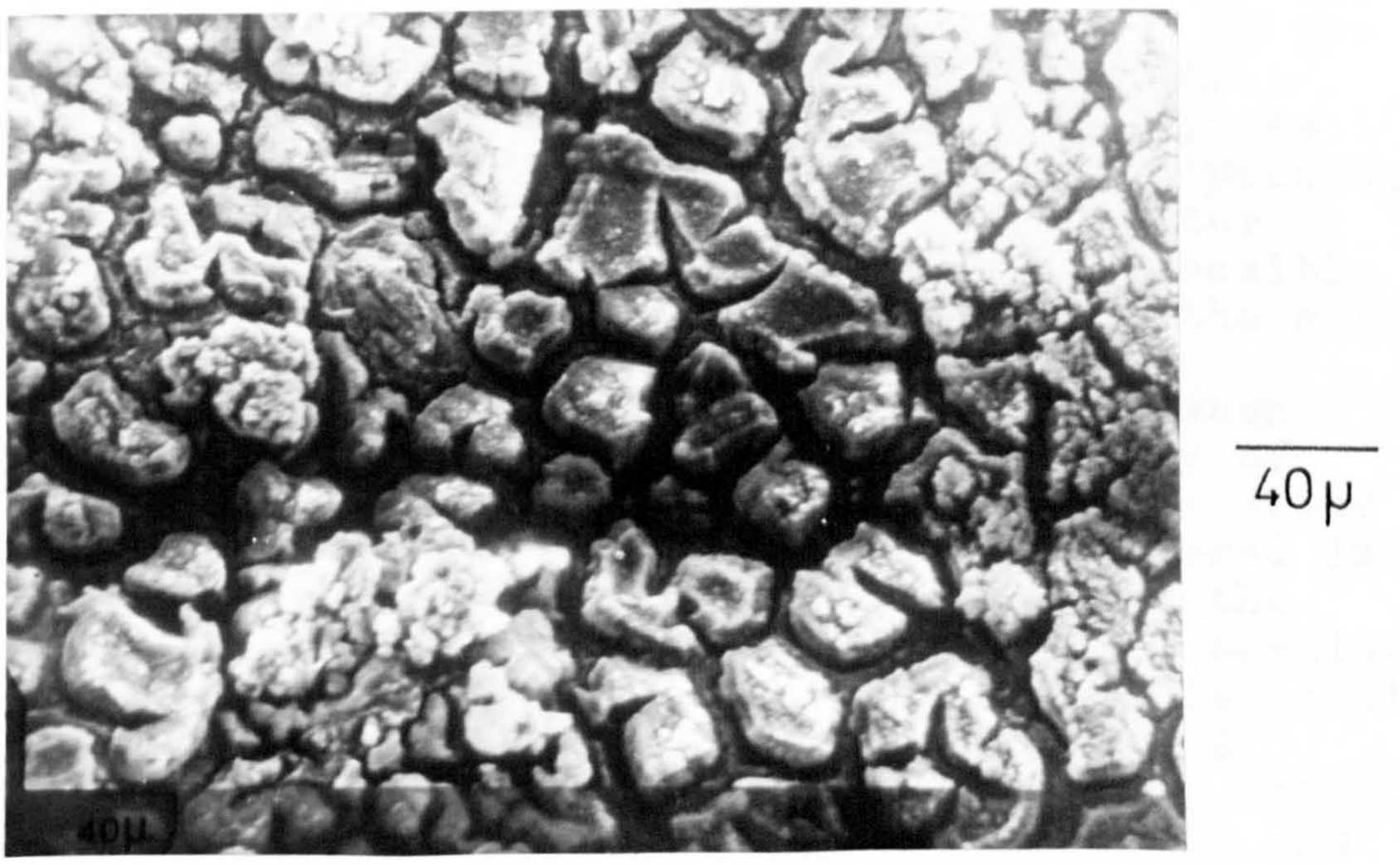

Figure 82. Calcareous deposits on prefatigue surface at -1300 mV (S.C.E.)

The left hand side of figure 82 is closest to the outside of the specimen and shows a relatively flat deposit surface broken up by quite wide shrinkage cracks. The right hand side is towards the middle of the crack and is characterised by a more even dispersion of deposit. Figure 83 is a higher magnification of an area in the middle of figure 82.

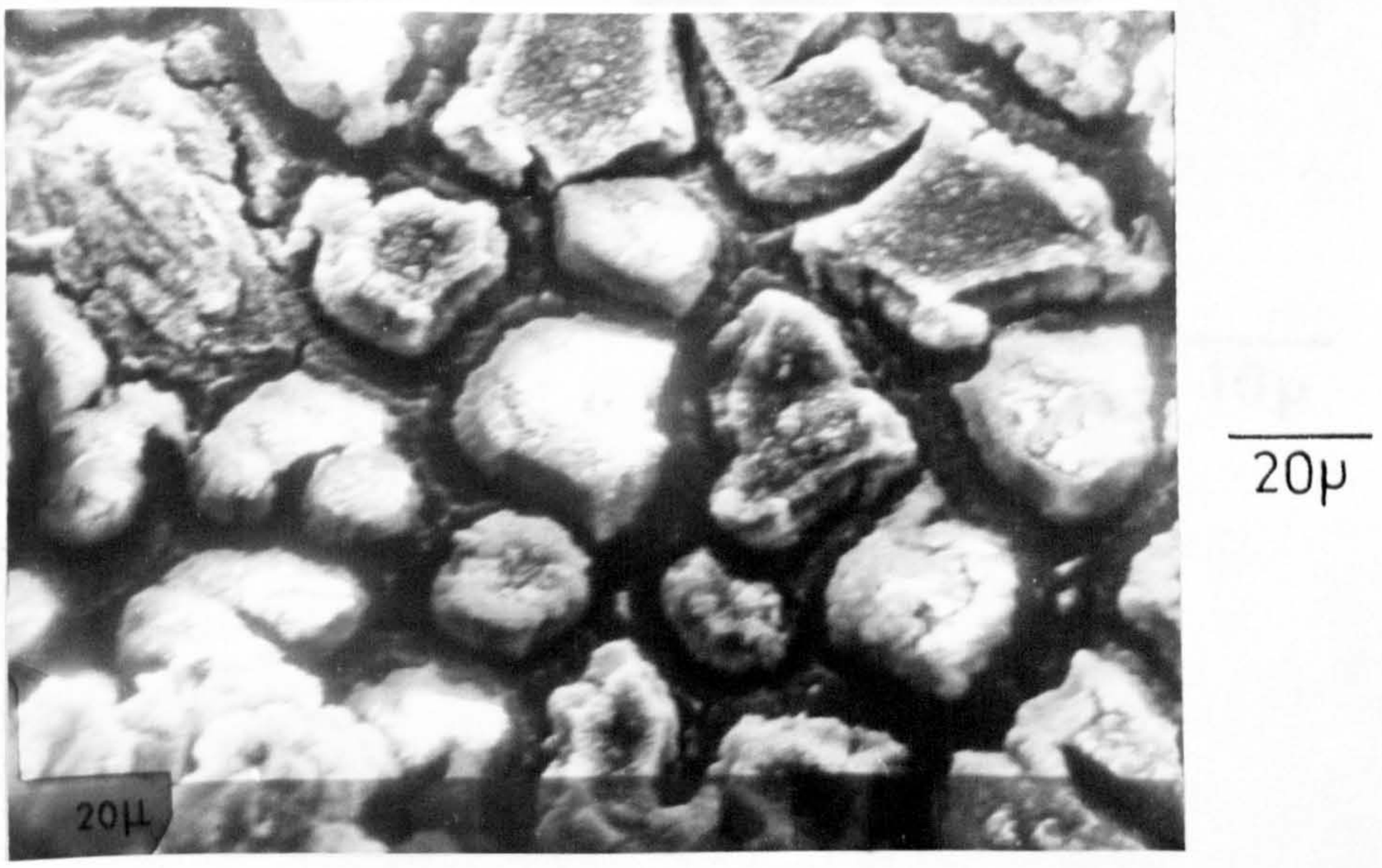

Figure 83. Higher magnification of central area in figure 82.

One reason for the change in morphology of the deposit formation may be to do with the pumping action of the crack and the turbulence/sea water velocity at the edges of the crack. As discussed in the literature survey, it is believed that the thickness and integrity of deposit is reduced with increasing water velocity, and as the pumping action and water turbulence is expected to be greater at the outside of the fatigue crack, it is quite feasible for the deposit to be more 'broken' and thinner at the edges.

One fact which seems to be ignored by researchers when discussing calcareous deposits is that the majority of investigations are carried out when the deposit has dried out, so it is not in the same form as that encountered in the wet state (hence the shrinkage cracks found in the deposits). It is the author's experience that any specimens removed at the completion of a corrosion fatigue test felt 'slimy' and the deposit came away on the fingertips. This is in complete contrast to the 'hard' deposits that would be expected in conjunction with crack blocking and wedging. This reaffirms the author's belief that there is the possibility of the deposit being squeezed out of the crack at the edges instead of mechanically interfering and wedging the crack open.

The form of the deposits found in this project have been shown in the preceding figures. From the observations carried out it seems that the deposits form evenly over the surface and gradually increase in thickness. This can be seen in figure 84 which shows the fatigue fracture surface (of a parent plate specimen cathodically protected at -1400 mV S.C.E.) close to the final fracture where the metal had not been exposed to the sea water solution for very long.

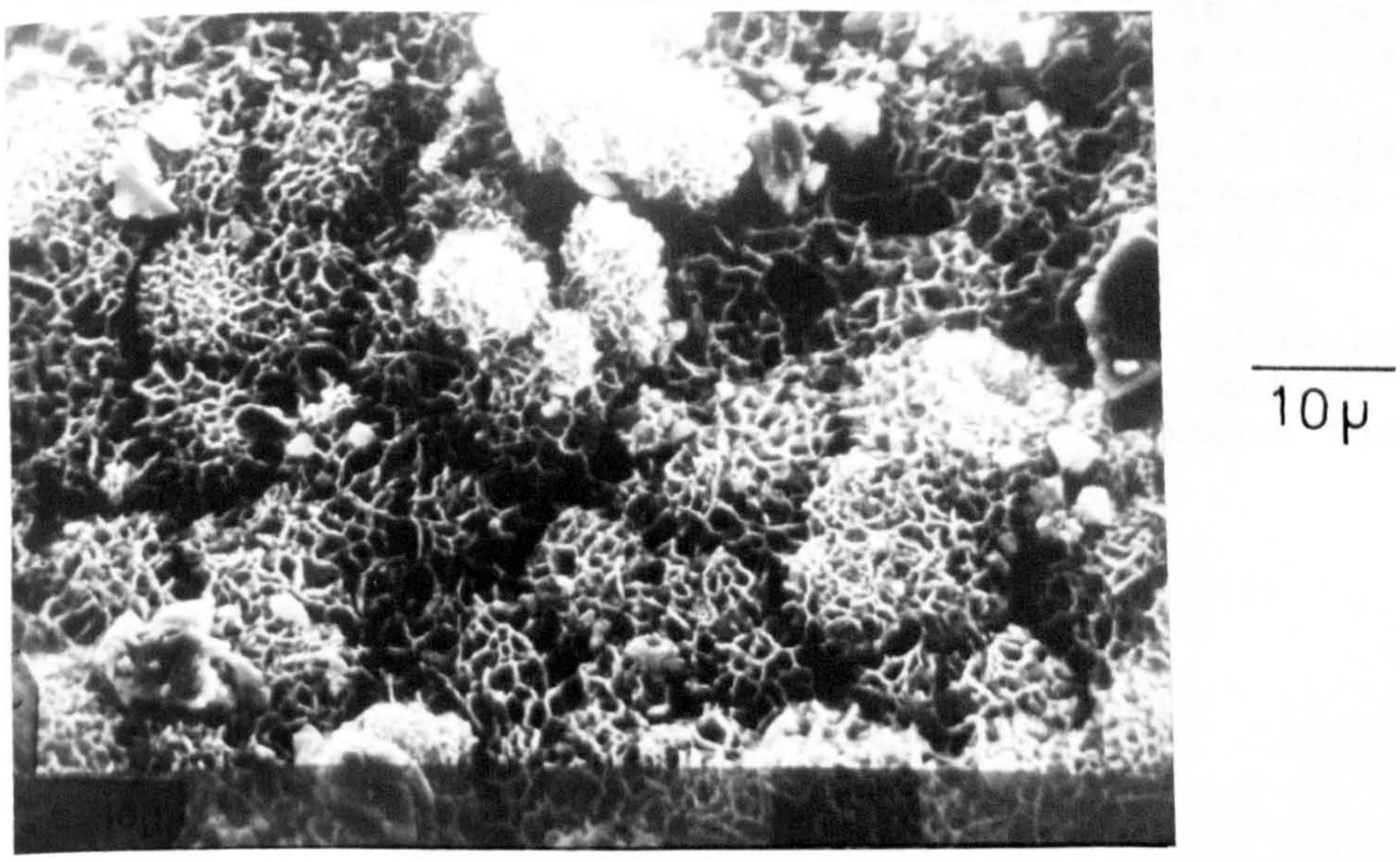

Figure 84. Early formation of deposits

Moving further down the fracture surface towards the pre-fatigue area, the deposit is seen to change and 'grow' outward in fibrous bundles (figure 85). With increasing deposit thickness, this coral/honeycombe structure changes to the flatter,'cake icing' type of structure as was shown in figure 83.

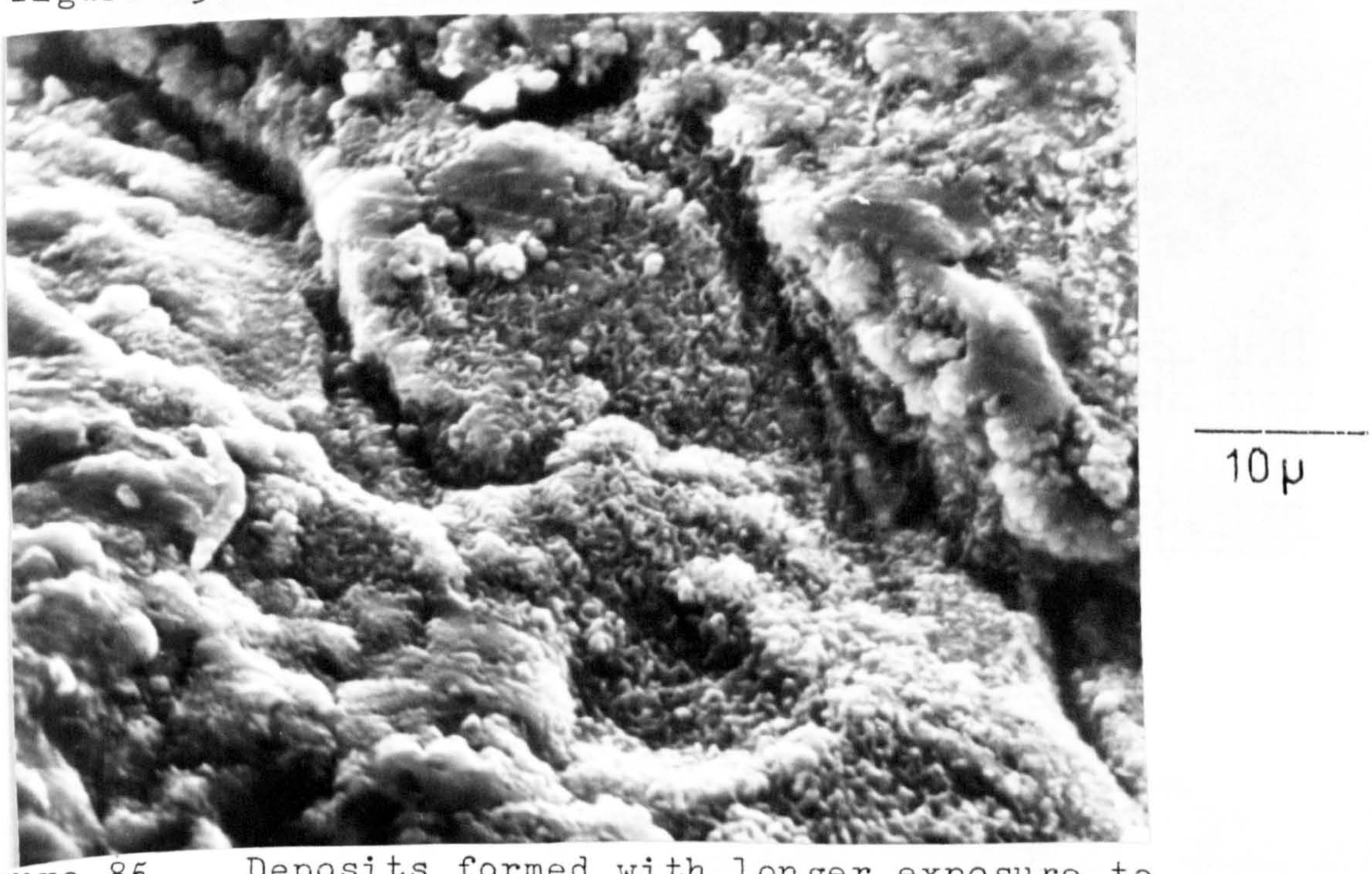

Figure 85. Deposits formed with longer exposure to the environment

The deposits were analysed using the energy dispersive analyser attached to the S.E.M. As can be seen in figure 86, magnesium is the most abundant element. This may be explained by the fact that in artificial sea water the Mg^{++}/Ca^{++} ratio is approximately 5/1. Since very little calcium was shown up by the analysis it may be inferred that the deposit consists mainly of $Mg(OH)_2$ and $MgCO_3$. Work by Ulanovsky (Ref 113) and Berner (Ref 114) has suggested that a pH of 8.3 is necessary to form $CaCO_3$ and a pH of 9.3 is necessary to precipitate $Mg(OH)_2$, while Philipponneau, Dagbert and Galland (Ref 115) comment that $CaCO_3$ precipitation is slower than $Mg(OH)_2$.

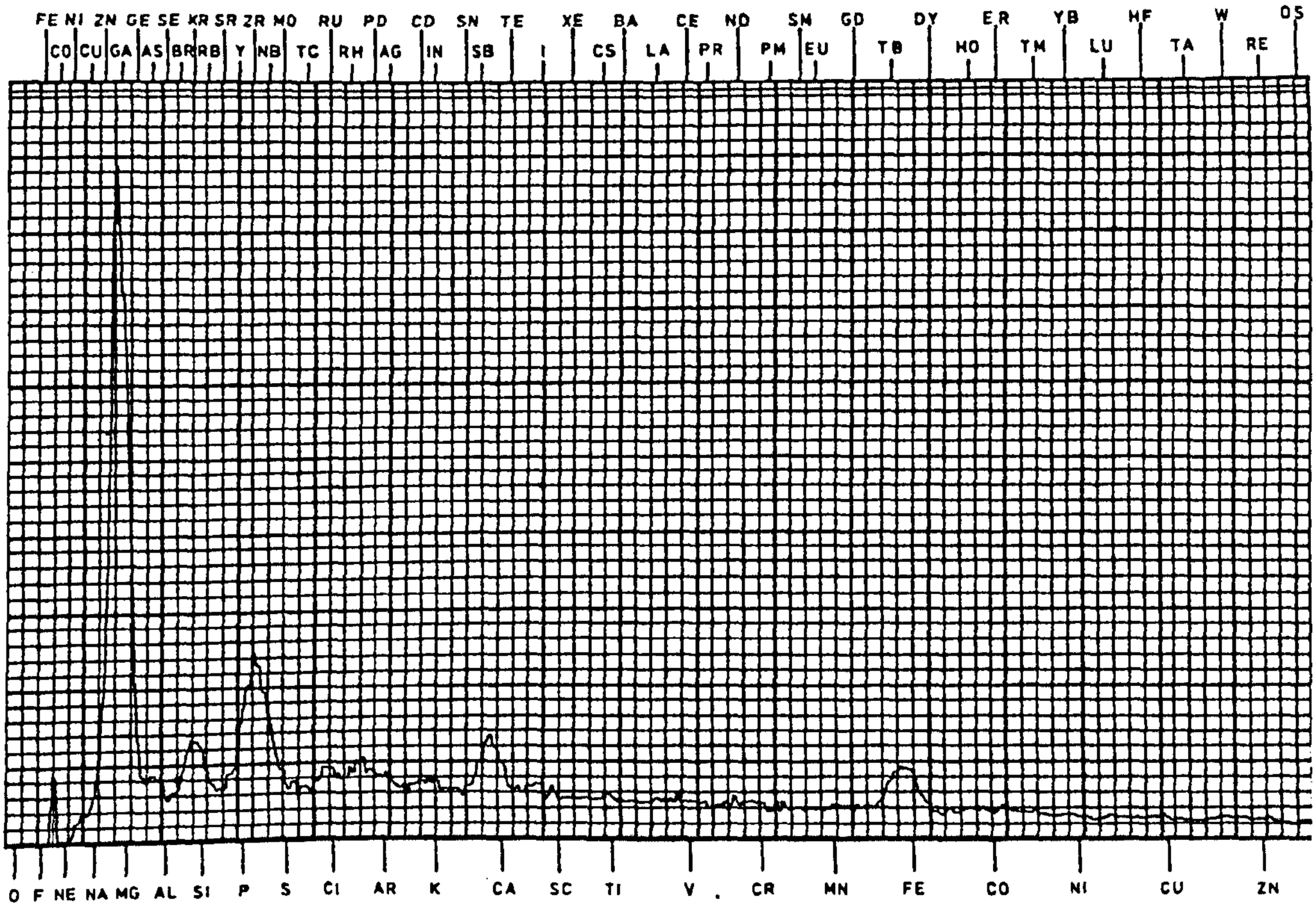

Figure 86. Analysis of calcareous deposits

It has already been noted that the deposit morphology changed with increasing cathodic protection (decreasing potential). Although it can be generally said that the deposit thickness and tenacity increased with increasing cathodic protection, this did not continue indefinately. At potentials of -1400 mV S.C.E. the deposits had become more porous and less adherent to the metal surface. Large flakes of deposit were seen to break off from the surface and float away. This usually happened when a hydrogen gas bubble also broke away from the surface, and it is believed that it is hydrogen which accounts for this porosity of deposit (Refs 116, 117). It is also probable that as the cathodic protection potential is decreased, a pH drop may be encountered due to the formation of hydrochloric acid, resulting from the breakdown of sodium chloride. As mentioned before, a minimum pH of 8.3 is necessary for calcareous deposit formation, therefore any reduction in pH, localised or in the solution bulk, would have an effect on the deposit morphology.

Under normal cathodic protection the calcareous deposits grow thicker and denser and in doing so reduce the current density required to achieve the protection potential. The deposits also effectively restrict the access of oxygen to the metal's surface to a diffusion limited rate, such that hydrogen production becomes the most important cathodic reaction. This raises the question of just how beneficial are calcareous deposits, and what exactly is a 'correct' cathodic protection potential in an offshore situation?

If a calcareous scale is required to reduce the current density used to protect the structure, then obviously the quicker the deposit is generated the better, in economic terms. This is infact the case for certain platforms, where it is common practice to apply considerable excess current when a platform is first installed (Ref 118). This may not, however, be such a good idea as it first seems due to the fact that along with calcareous deposits ionic hydrogen will also be generated bringing associated problems of hydrogen embrittlement. As will be seen from this project, the generation of hydrogen by overprotection has a serious detrimental effect on the corrosion fatigue performance of a high strength steel which far outweighs any beneficial effect that may be caused by calcareous deposits. Besides, as already mentioned, on an offshore structure it is probable that calcareous deposit formation will not be uniform or consistent over the whole of the protected surface. Also, it is not known exactly how calcareous deposits react to alterations in current density, or whether deposit properties are dependant on factors such as total charge passed, magnitude of charge, time at a certain charge, etc.

4.9 Discussion of corrosion fatigue results

4.9.1 Fatigue crack propagation behaviour for parent plate material in air

Although this project deals primarily with the corrosion fatigue of a high strength steel in sea water, several parent plate specimens were fatigued in air in order that the data generated might act as a base line for comparison with corrosion fatigue data. It must be pointed out here that fatigue in air is also a form of corrosion fatigue. As early as 1935 it had been demonstrated by Gough and Sopwith (Ref 119) that air decreased the fatigue strength relative to tests in vacuo. However, as the in-air condition will be as close to 'in vacuo' as any offshore operational steel is likely to come, air will for this project be classed, to all intents and purposes, as a non corrosion fatigue medium.

Before continuing with the discussion of results, several points must be made clear. As mentioned earlier only the intermediate region of crack growth can be successfully described by the Paris equation, therefore statements about the material's overall performance must be viewed with this in mind. It must also be explained what is meant by resistance to fatigue cracking or increased fatigue life in the context of this report. For the Paris part of the curve, resistance will be assessed by the level of da/dN achieved at a given value of ΔK. The lower the value of da/dN, the greater will be the resistance to fatigue and hence the better the fatigue performance.

Fatigue crack propagation rate data for the in-air condition is presented graphically in the form log da/dN against log ΔK in figures 87, 88 and 91. The principal features of this data are considered to be:-

(1) The crack propagation rate of the in-air parent plate specimens proved to be lower than that for any other specimen / environmental condition combination. This was true at all values of ΔK.

(2) Unlike other specimen / environmental condition combinations, there did not appear to be easily definable transition points between the initiation stage, the steady state crack growth stage and the final failure stage.

(3) Figure 91 shows that for a ΔK value of 20 MPa$\sqrt{m}$, the crack propagation rate for in-air is almost an order of magnitude lower than that for a parent plate specimen fatigued at -1400 mV (S.C.E.).

As mentioned earlier, it is widely accepted that the Paris equation $da/dN = C\Delta K^m$ is only applicable to the intermediate crack growth region. As a test of this relationship's ability to describe fatigue crack growth behaviour, the values obtained for C and m from the experimental data were used to integrate the Paris equation. Representative values of C and m for all the experimental classes are given in table 19. This table also shows the percentage difference between the calculated number of cycles taken to grow a certain crack length and the actual number of cycles taken (as measured by a mechanical counter attached to the fatigue rig). It is clearly shown that the C and m values used in the integrated Paris equation produce a calculated N that is only 1.4% different from the actual N. Since both results are very close it is apparent that, for the intermediate range of crack growth, the in-air fatigue crack propagation rate data obeys a Paris type relationship of the form $da/dN = C\Delta K^m$.

The values of C and m presented in table 19 can only be regarded as being representative of the average fatigue crack propagation rate behaviour. This is because for all the fatigue and corrosion fatigue testing the mechanical test perameters such as frequency, load amplitude and stress ratio were fixed. In addition, the values of C and m were calculated using data obtained from what was believed to be the intermediate region of crack growth.

From an examination of the fracture surfaces of the in-air specimens (examples of which are shown in figures 106 and 107), several prominent features were found:-

(1) There was an apparent lack of striations on any part of the fracture surface.

(2) The condition of the fracture surface increased in roughness from a relatively smooth prefatigue and low ΔK fatigue area to a much rougher and more jagged, higher ΔK fatigue area.

(3) In the low ΔK region the fracture surface was characterised by many small secondary cracks. In the higher ΔK region there were more secondary cracks apparent, some of which were relatively large and deep.

(4) The secondary cracking in the low ΔK region consisted of more single fronted cracks rather than the highly branched cracking found at higher ΔK values.

Since crack branching causes a reduction in the effective level of stress concentration at the main crack front, microstructural factors and their influence on crack branching may significantly influence fatigue life according to whether they impede or enhance the possibility of the

MATERIAL	CONDITION	COVERED	C	m	ΔN actual	ΔN calc.	Δ%
Parent plate	-700	No	3.87×10^{-10}	1.85	20440	19039	-6.9
Parent plate	-700	Yes	4.03×10^{-10}	1.76	21379	22195	+3.8
Parent plate	free corr.	No	4.71×10^{-11}	2.65	5956	6408	+7.6
Parent plate	-1200	Yes	2.61×10^{-10}	2.26	5190	5670	+9.2
Parent plate	-1300	No	1.78×10^{-9}	1.75	4252	4493	+5.7
Parent plate	-1300	Yes	1.95×10^{-8}	0.97	2740	2943	+7.4
Parent plate	-1400	No	1.14×10^{-7}	0.46	3529	3843	+8.9
Parent plate	-1400	Yes	1.12×10^{-8}	1.13	3266	3544	+8.5
Parent plate	in air	No	5.34×10^{-8}	3.05	31597	32026	+1.4
H.A.Z.	-700	No	3.21×10^{-9}	1.16	18850	18862	+0.1
H.A.Z.	-700	Yes	1.54×10^{-8}	0.79	13700	12920	-5.7
H.A.Z.	-1400	No	2.61×10^{-7}	0.34	1600	1785	+11.6
H.A.Z.	-1400	Yes	1.44×10^{-7}	0.54	2997	3188	+6.3
H.A.Z.	free corr.	No	4.12×10^{-9}	1.27	13020	13998	+7.5
Heat treated	-1300	Yes	2.88×10^{-7}	0.31	2887	2773	-3.8
Heat treated	-1400	No	5.53×10^{-7}	0.25	1024	1060	+3.5
Heat treated	-1400	Yes	6.18×10^{-7}	0.25	1402	1485	+5.9
Heat treated	free corr.	Yes	3.27×10^{-8}	0.50	6770	7573	+11.9

Table 19. Paris constants for all microstructures

Figure 106. Fracture surface of early stages of fatigue in-air ($\Delta K \simeq 23$ MPa$\sqrt{m}$)

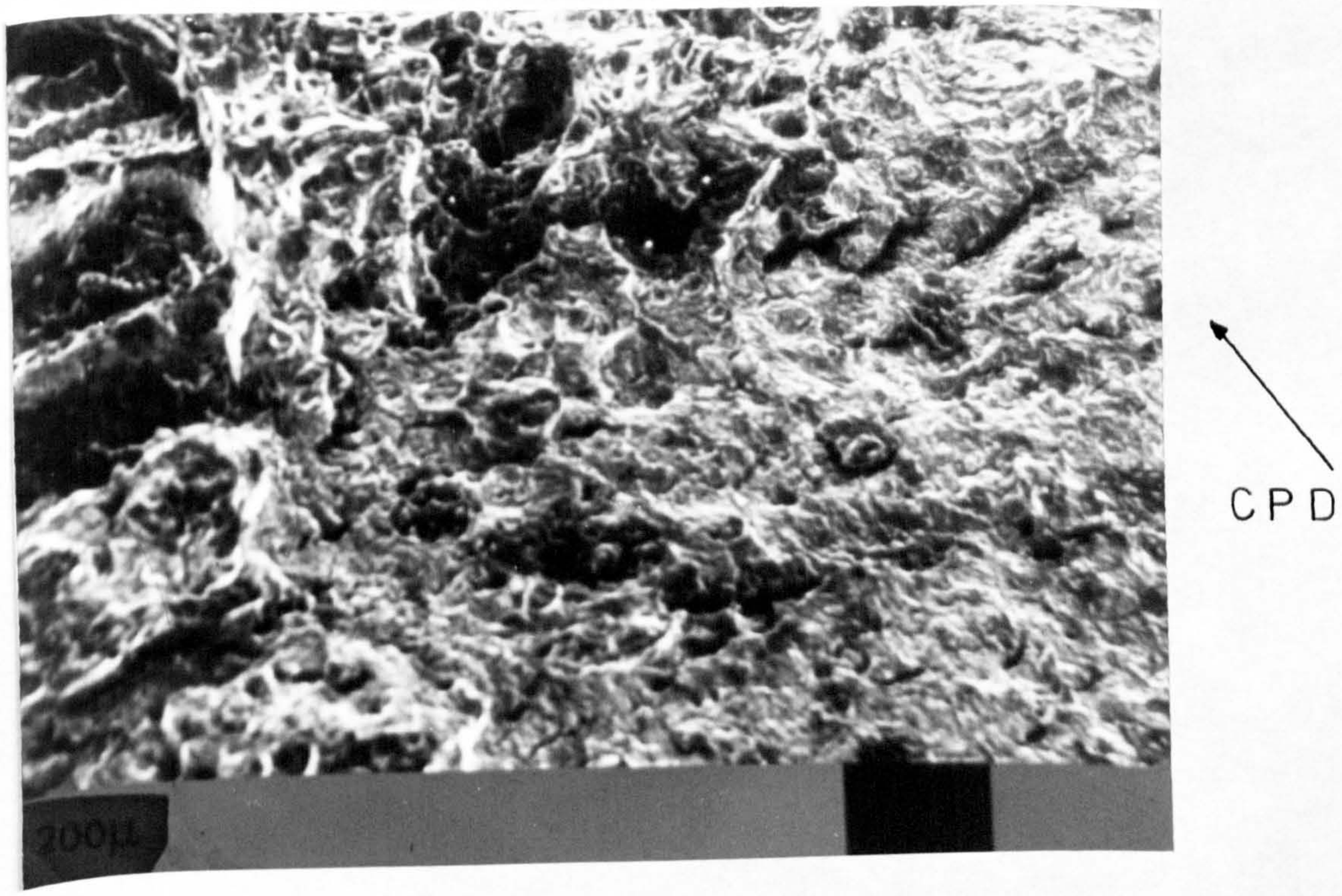

Figure 107. Fracture surface of final fatigue region in-air ($\Delta K \geq 37$ MPa$\sqrt{m}$)

crack front advancing or being attenuated. Several researchers observed (Refs 121,122,123) the beneficial role of microstructure in attenuating the fatigue crack process by means of increasing the deflection and branching of the advancing fatigue crack. Such repeated crack branching would be expected to dissipate a portion of the strain energy at the tip of the propagating crack and lead to a slower propagation rate. For example, it is generally considered that the pearlite phase acts as a reinforcement within the bulk ferrite matrix and locally provides a mechanical barrier to crack advance. Indeed, Thompson (Ref 120) shows quite clearly how the fatigue crack in BS 4360:50D was found to detour around a pearlite colony. This avoidance or degree of mechanical interference was shown to depend on the orientation of the carbide platelets within a given pearlite colony. For N-A-XTRA 70 no such microstructural effect was found. This was mainly due to the homogeneous nature of the material, which consisted of a fine carbide dispersion in a ferrite matrix. The only major discontinuity in the microstructure was the relatively large ZrN particles found intermittently throughout the material. However, as discussed in the inclusion section (4.4.1)these particles were considered to have very little effect on the overall fatigue crack propagation rate, although they may locally interfere with the growing crack front.

As already mentioned, there was no evidence of striation formation during the microscopic examination of the fracture surfaces. This was true for all classes of specimen / environmental conditions and not just the in-air fatigue. For the corrosion fatigue tests it was at first thought that general corrosion and surface deposits either destroyed or disguised the striations but even the in-air fatigue surfaces seemed to be devoid of them. One reason for this may have been that the striations were just too small to be seen. It can be calculated that in the intermediate region for in-air fatigue the striation spacing should be around 0.02 μm. The only seemingly regular striation type markings were parallel microcracks occasionally found on the fracture surface. These usually had a spacing in the region of 1 μm.

As pointed out by Tomkins (Ref 124), striations are simply a reflection of the localized crack tip plastic deformation rather than a representation of the amount of new crack surface created during each cycle. In this case the calculated figure of 0.02 μm for striation spacing may not be a true representation. However, even a striation spacing of ten times the above figure would still mean that they were quite difficult to distinguish.

4.9.2 Corrosion fatigue crack propagation behaviour of N-A-XTRA 70 parent plate material

Corrosion fatigue tests were carried out on N-A-XTRA 70 parent plate specimens under the following conditions:- free corrosion, cathodic protection potentials of -700 mV (S.C.E.), -780 mV (S.C.E.), -1200 mV (S.C.E.), -1300 mV (S.C.E.), -1400 mV (S.C.E.), initial protection of -780 mV (S.C.E.) then overprotection of -1300 mV (S.C.E.) for approximately 2800 cycles then back to -780 mV (S.C.E.). In all cases, except free corrosion and -1200 mV (S.C.E.), specimens with and without their crack sides covered were tested. The corrosion fatigue crack propagation rate data is presented in the form of graphs of log da/dN against log ΔK in figures 87, 88, 89, 90, 91 and 97. The major features of these graphical data are considered to be:

1) For a cathodic protection potential of -700 mV (S.C.E.) the corrosion fatigue crack propagation rate of specimens which did not have their crack sides covered was higher than for those specimens which did.

2) In the case of specimens where the crack sides were not covered, the corrosion fatigue crack propagation rate associated with a protection potential of -780 mV (S.C.E.) was the closest to that generated by the in-air fatigue.

3) Specimens in which the crack sides were covered and protected to a potential of -700 mV (S.C.E.) gave a corrosion fatigue crack propagation rate which was even closer to the in-air fatigue rate than that of specimens which were cathodically protected to -780 mV (S.C.E.) and did not have their crack sides covered.

4) For a cathodic protection potential of -1300 mV (S.C.E.) the corrosion fatigue crack propagation rate of specimens which did have their crack sides covered was higher than for specimens which did not.

5) Above a ΔK value of approximately 27 MPa$\sqrt{m}$ the corrosion fatigue crack propagation rate associated with a protection potential of -1300 mV (S.C.E.) for specimens with their crack sides covered was greater than that associated with a protection potential of -1400 mV (S.C.E.) for specimens without their crack sides covered.

6) For a ΔK value of approximately 20 MPa$\sqrt{m}$, the corrosion fatigue crack propagation rate for a cathodic protection potential of -1400 mV (S.C.E.) was almost an order of magnitude greater than the rate associated with in-air fatigue. This was true for both covered and uncovered specimens.

7) Above a ΔK value of approximately 26 MPa$\sqrt{m}$, the corrosion fatigue crack propagation rate associated with a protection potential of -1400 mV (S.C.E.) for specimens which had their crack sides covered was greater than that for specimens which did not have their crack sides covered.

8) The general trend of the data seems to suggest that for parent plate material, covering the crack sides at low levels of cathodic protection (-700 mV S.C.E.) reduces the fatigue crack propagation rate. However the reverse is true at higher levels of cathodic protection (-1300, -1400 mV S.C.E.), when the specimens with their crack sides covered exhibited less corrosion fatigue resistance than those without their crack sides covered.

9) For more electronegative protection potentials (-1300, -1400 mV S.C.E.), the Paris curves have a shape which is characteristic of stress corrosion controlled crack propagation behaviour.

In an attempt to show the consequences of different environmental conditions more clearly, a crack propagation rate (C.P.R.) enhancement index was devised. This is defined as (Ref 144):-

$$\frac{da/dN_{(env)}}{da/dN_{(air)}}$$

Since the C.P.R. enhancement index for air will be unity it should be quite easy to assess the influence of different environmental conditions on the corrosion fatigue performance - the closer to unity, the better the performance; the further from unity, the worse the performance.

Plots of C.P.R. enhancement index against ΔK for parent plate specimens are shown in figure 99. In order to maintain compatibility with the Paris plots already described, a ΔK range of approximately 20 to 30 MPa$\sqrt{m}$ was chosen. Values within this range should lie within the intermediate crack growth area for all specimens and be directly comparable with the Paris plots, remembering that for the regions of threshold and final fatigue the Paris equation is not strictly valid.

The significant features of the data presented in figure 99 are:

1) For specimens without their crack sides covered, it can be said that overall a 'correct' cathodic protection potential of -780 mV (S.C.E.) gave a C.P.R. enhancement index closest to that of in-air fatigue. Next closest was underprotection at -700 mV (S.C.E.), then free corrosion, then overprotection. As could be expected for the overprotected specimens, the C.P.R. enhancement index increased with the increase in electronegativity of the protection potential.

2) For specimens with their crack sides covered, it can be said that overall a protection potential of -700 mV (S.C.E.) gave a C.P.R. enhancement index that was closest to unity (even closer than that of -780 mV S.C.E. for specimens without their crack sides covered). Of the overprotected specimens, the C.P.R. enhancement index for -1400 mV (S.C.E.) was worse than that for -1300 mV (S.C.E.).

3) Above a ΔK value of approximately 27 MPa$\sqrt{m}$, a protection potential of -1300 mV (S.C.E.) for specimens with their crack sides covered gave a C.P.R. enhancement index that was slightly further from unity than that of -1400 mV (S.C.E.) for specimens without their crack sides covered.

A major consideration to be gleaned from the data presented in terms of Paris curves and C.P.R. enhancement indices is that cathodic protection potentials that are equal to and more electronegative than -1200 mV (S.C.E.) produce fatigue crack propagation behaviour which is considerably worse than that associated with a purely free corrosion situation. This fact raises a worrying aspect of offshore cathodic protection behaviour, namely the use of overprotection potentials in the wake of storm damage. In this situation the protection potential is 'turned up' in order to repolarize the platform quickly. However, as can be seen from the above results, this may actually be doing more harm than good.

As discussed in the literature survey, the main causes of reduced fatigue life under the influence of cathodic overprotection are considered to be hydrogen embrittlement and anodic dissolution. It is widely accepted that only steels with yield strengths in excess of about 550 N/mm^2 (Ref 50) are sensitive to hydrogen embrittlement at constant stress, therefore N-A-XTRA 70, the steel used in this work which has a yield strength in excess of 700 N/mm^2, can be regarded as sensitive even in the absence of adverse hydrogen charging situations.

In order to fully understand the corrosion fatigue mechanisms active in this project, the fracture surfaces of all specimens were analysed using a scanning electron microscope. Two types of specimens were examined - those in which the calcareous scales and surface deposits were removed; and those fresh from the test environment. The latter set has already been discussed with a view to the influence of calcareous deposits. Of the former group, the most common feature found on the fracture surfaces of overprotected specimens was quasi-cleavage facets of the type shown in figures 108, 109 and 110. The fracture surfaces of the severe overprotection specimens were characterised as having an angular, brittle, quasi-cleavage type appearance with a substantial amount of fine secondary cracking. The length and depth of the secondary cracks was found to increase towards higher ΔK regions.

It was noticeable on the fracture surfaces of the severely overprotected specimens that the ZrN particles did not exhibit the same amount of shatter damage associated with free corrosion and protection potentials of -700 and -780 mV (S.C.E.). Figure 111 shows how a ZrN particle has lost matrix material on almost all sides. It was proposed in the section on inclusions that under 'normal' corrosion fatigue the particle may act as a localised crack stopper until a stress build-up shatters the particle and enables the crack front to move on. This may not be the case for severe overprotection; the embrittled matrix at potentials of -1300 and -1400 mV (S.C.E.) may allow secondary cracking at the particle/matrix interface to disbond the particle and thus allow the crack front to quickly bypass it.

Figures 112, 113, 114 and 115 are views of a fracture surface seen side-on. They show how the corrosion fatigue crack profile changes over the whole length of the crack. The depth and degree of opening of the secondary cracks increase as the major fatigue crack progresses from the prefatigue/fatigue initiation region through the intermediate Paris region until the final failure zone is reached.

In contrast with the fracture surfaces produced by severe overprotection potentials, the fracture surfaces observed at near theoretically correct protection potentials and free corrosion showed substantially less quasi-cleavage. The predominant feature of these surfaces was the abundance of corrosion pits and although the secondary cracks were more numerous, they appeared smaller in length and were not as deep. Figures 116 and 117 are typical of a free corrosion fracture surface.

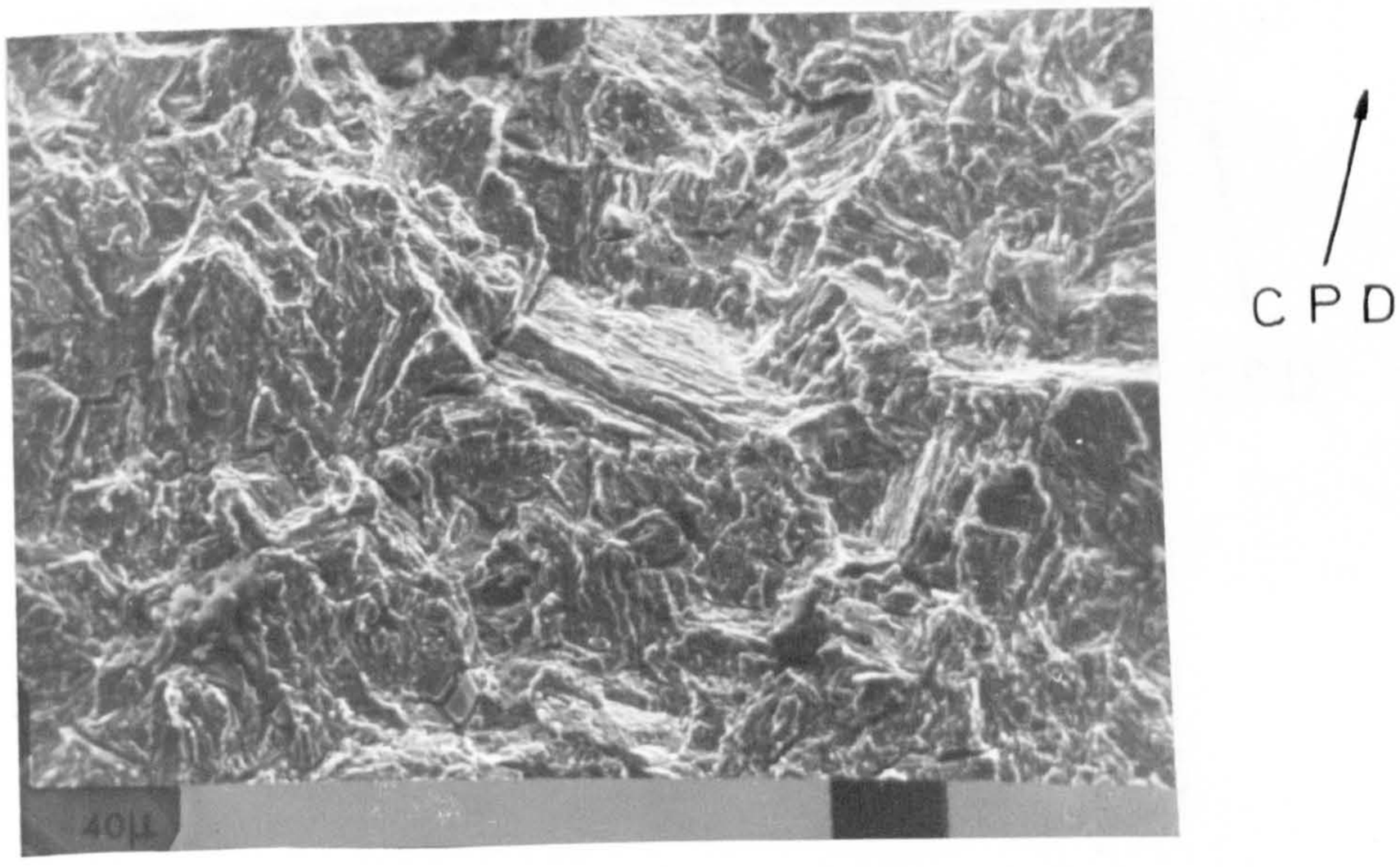

Figure 108. Fracture surface of parent plate specimen, -1400 mV (S.C.E), crack side covered (ΔK = 24.5 MPa$\sqrt{m}$)

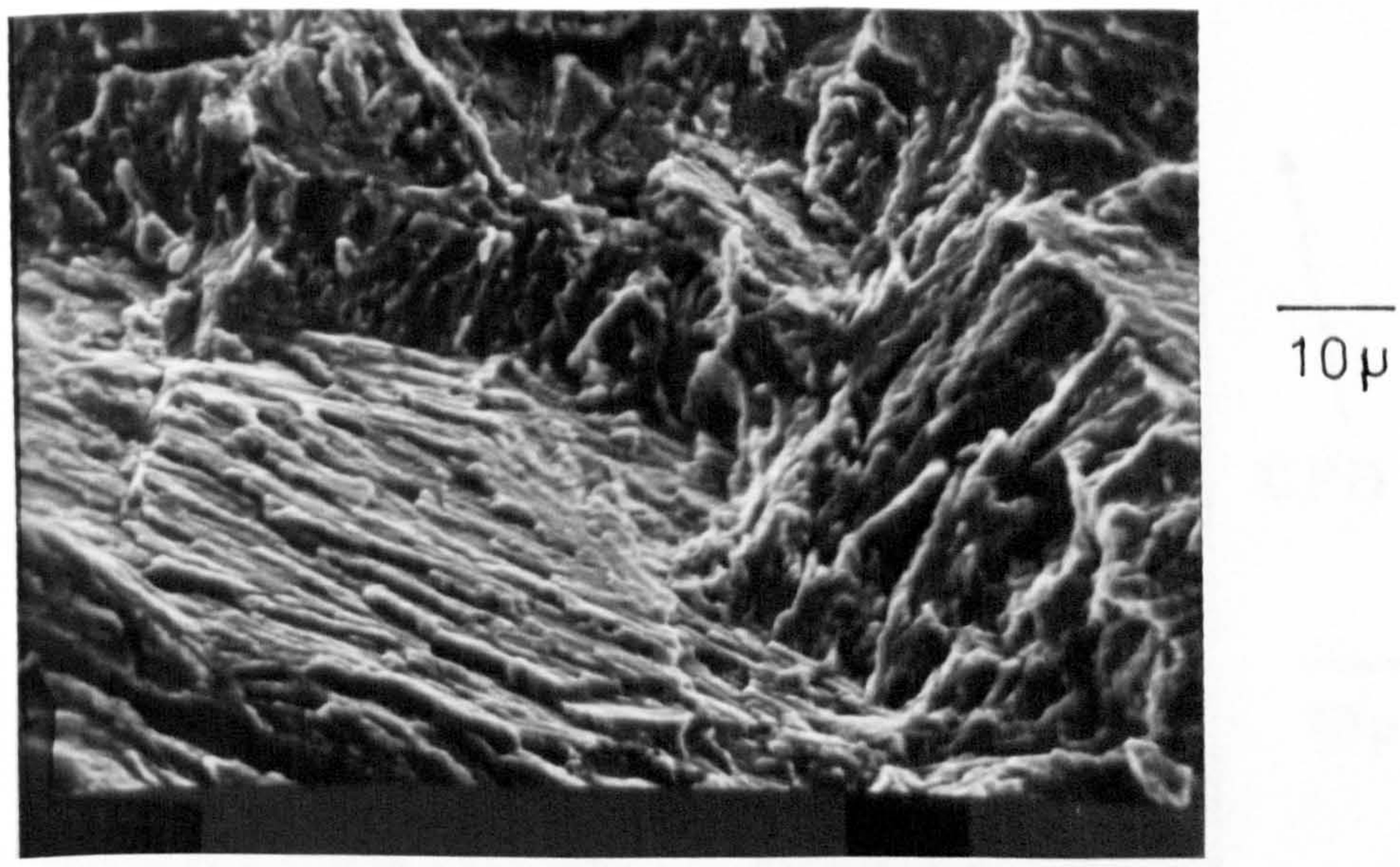

Figure 109. Magnification of central area of figure 108.

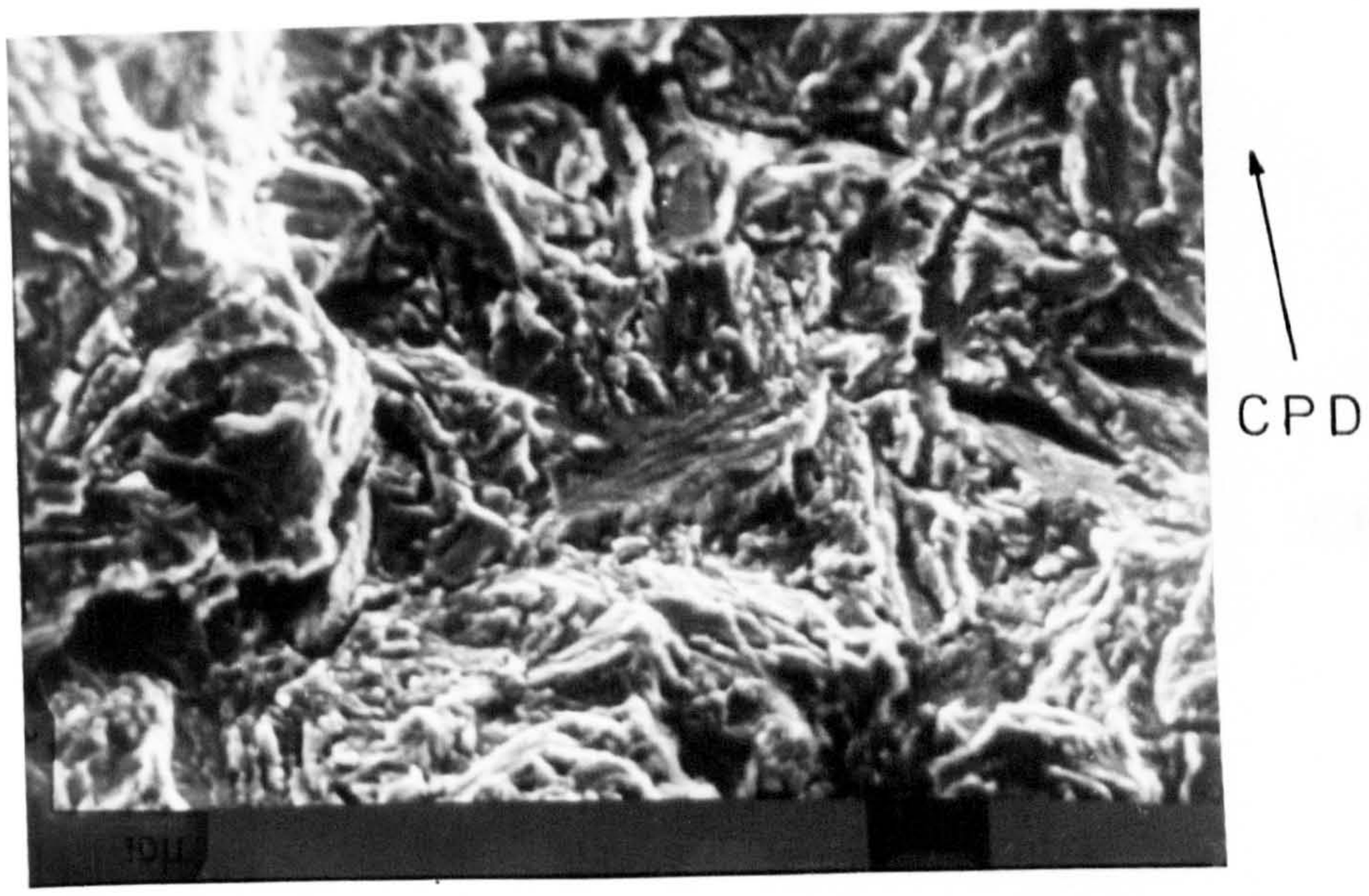

Figure 110. Fracture surface of parent plate specimen, -1400 mV (S.C.E), crack side covered (ΔK = 30 MPa$\sqrt{m}$)

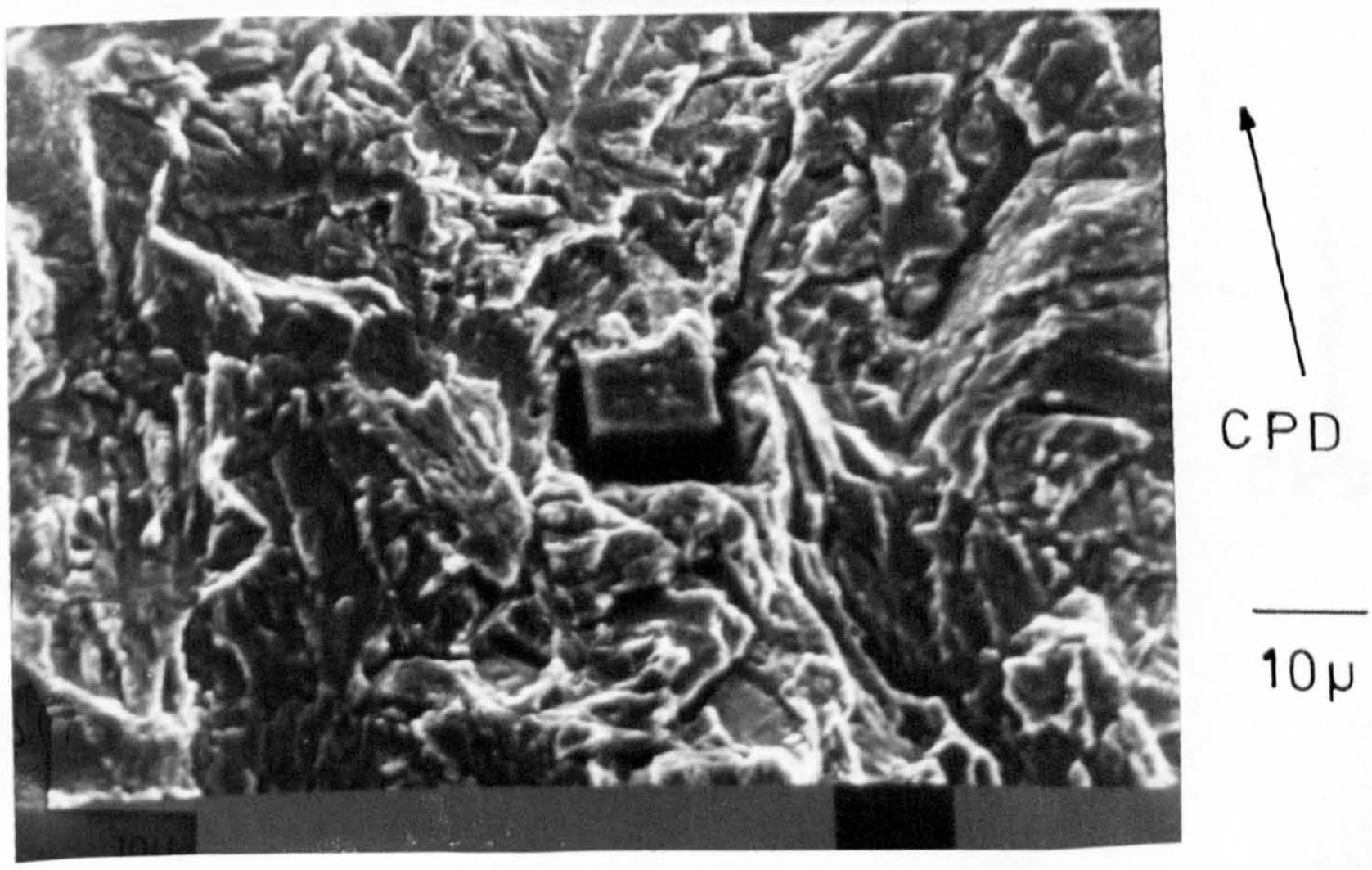

Figure 111. Fracture surface of parent plate specimen, -1400 mV (S.C.E), crack side not covered (ΔK = 28 MPa$\sqrt{m}$)

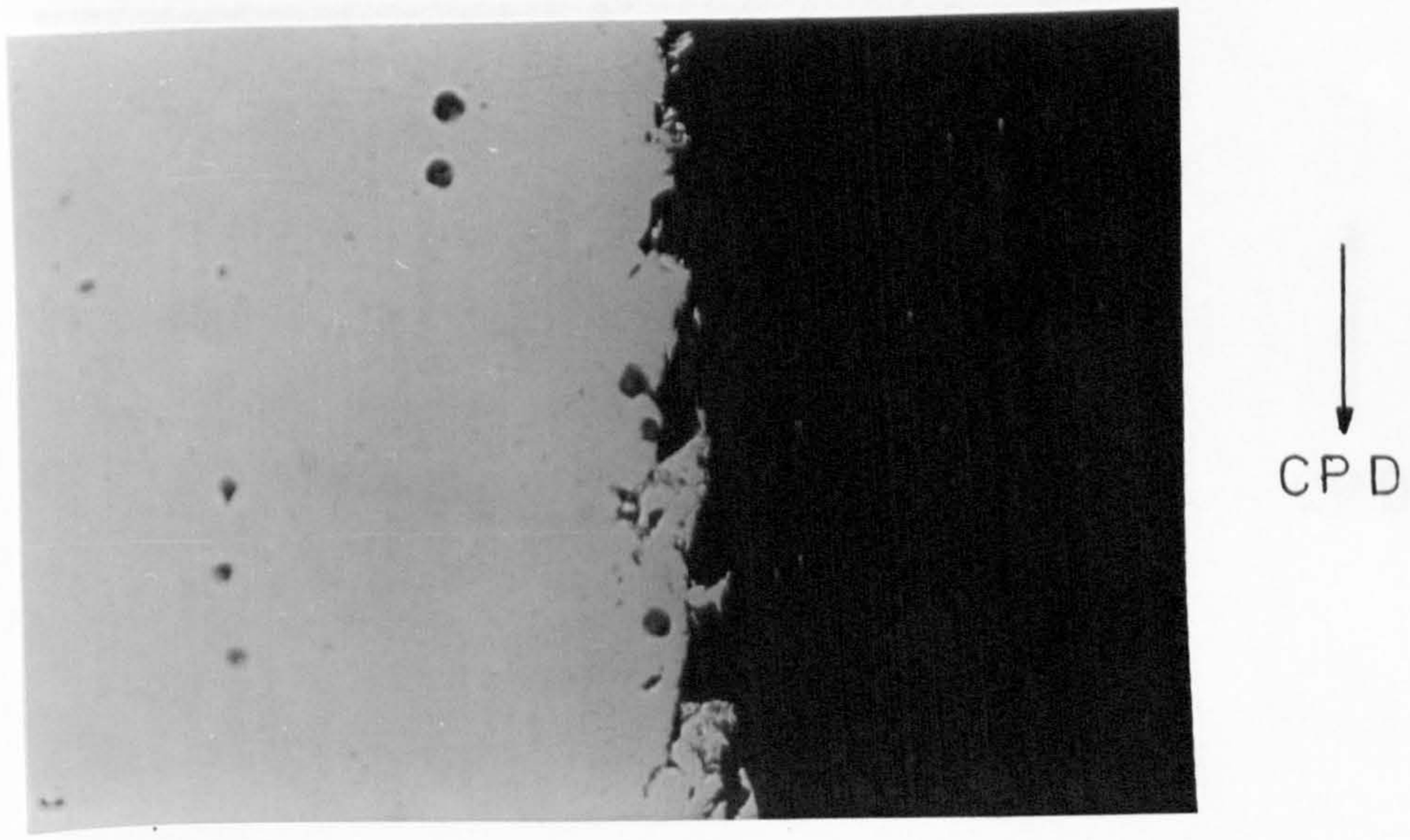

Figure 112. Profile of fracture surface at prefatigue/ fatigue initiation region, -1400 mV (S.C.E.), crack sides not covered X 450

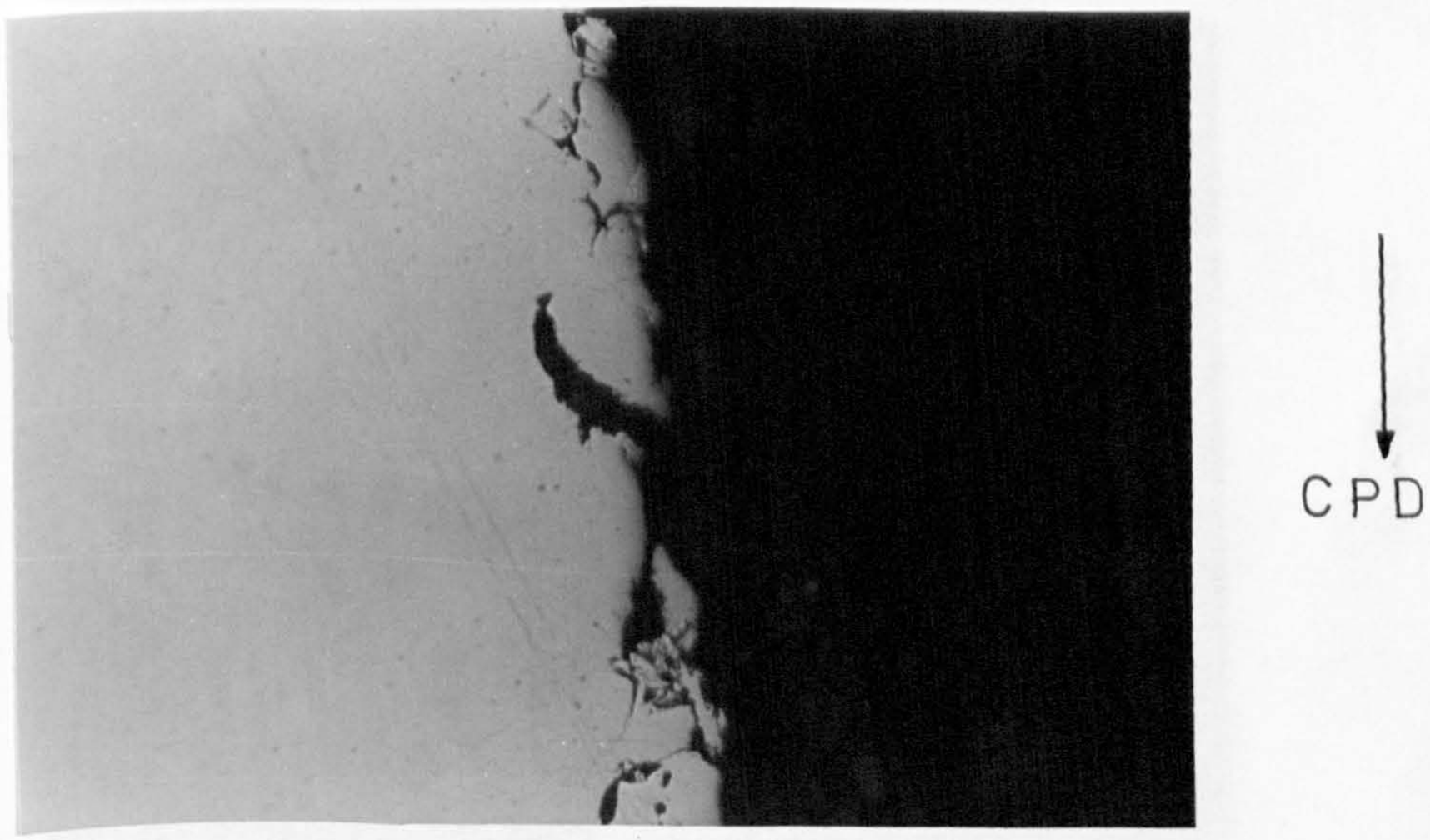

Figure 113. Profile of fracture surface at low ΔK intermediate cracking region, -1400 mV (S.C.E.), crack sides not covered X 450

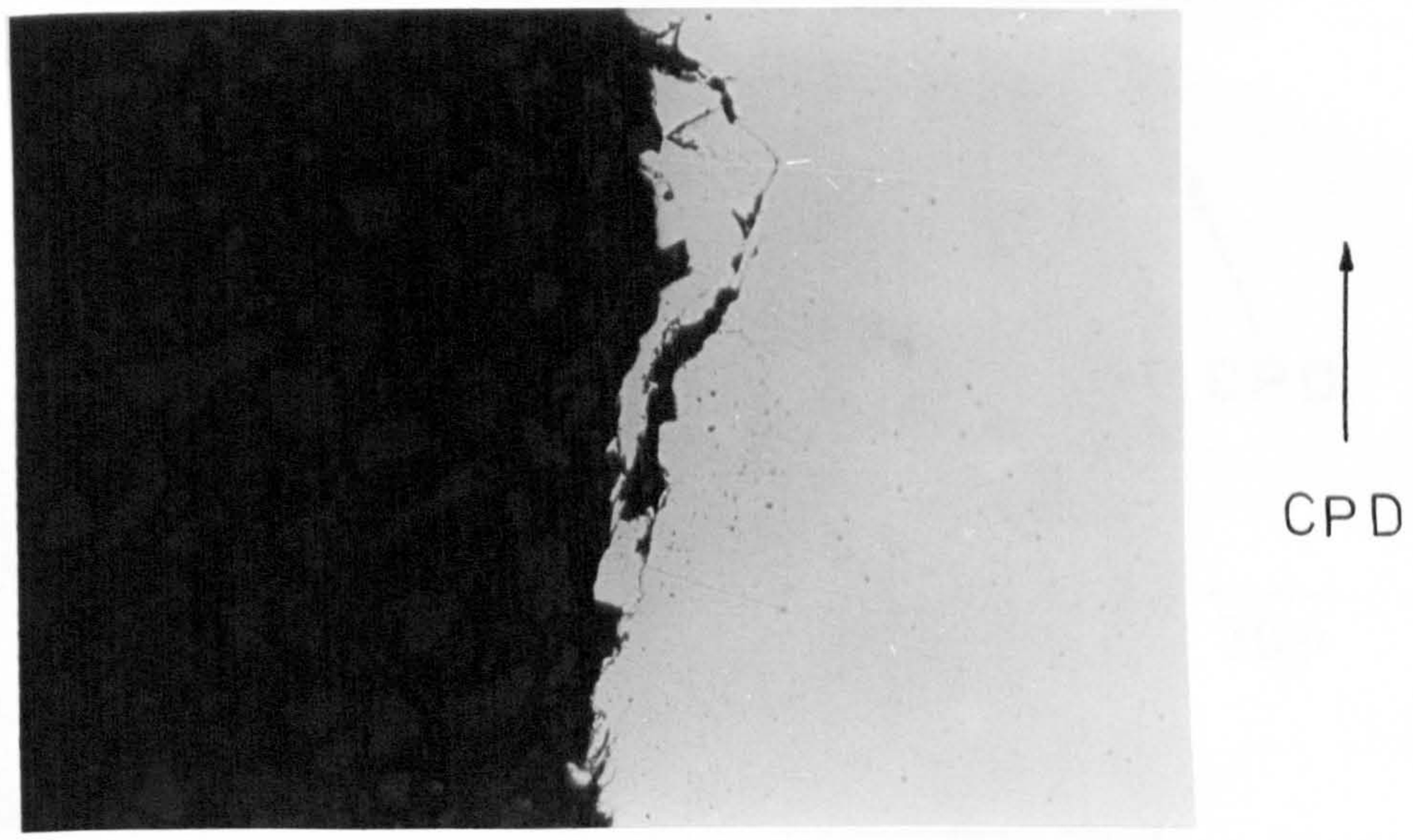

Figure 114. Profile of fracture surface at high ΔK intermediate cracking region, -1400 mV (S.C.E.), crack sides not covered X 450

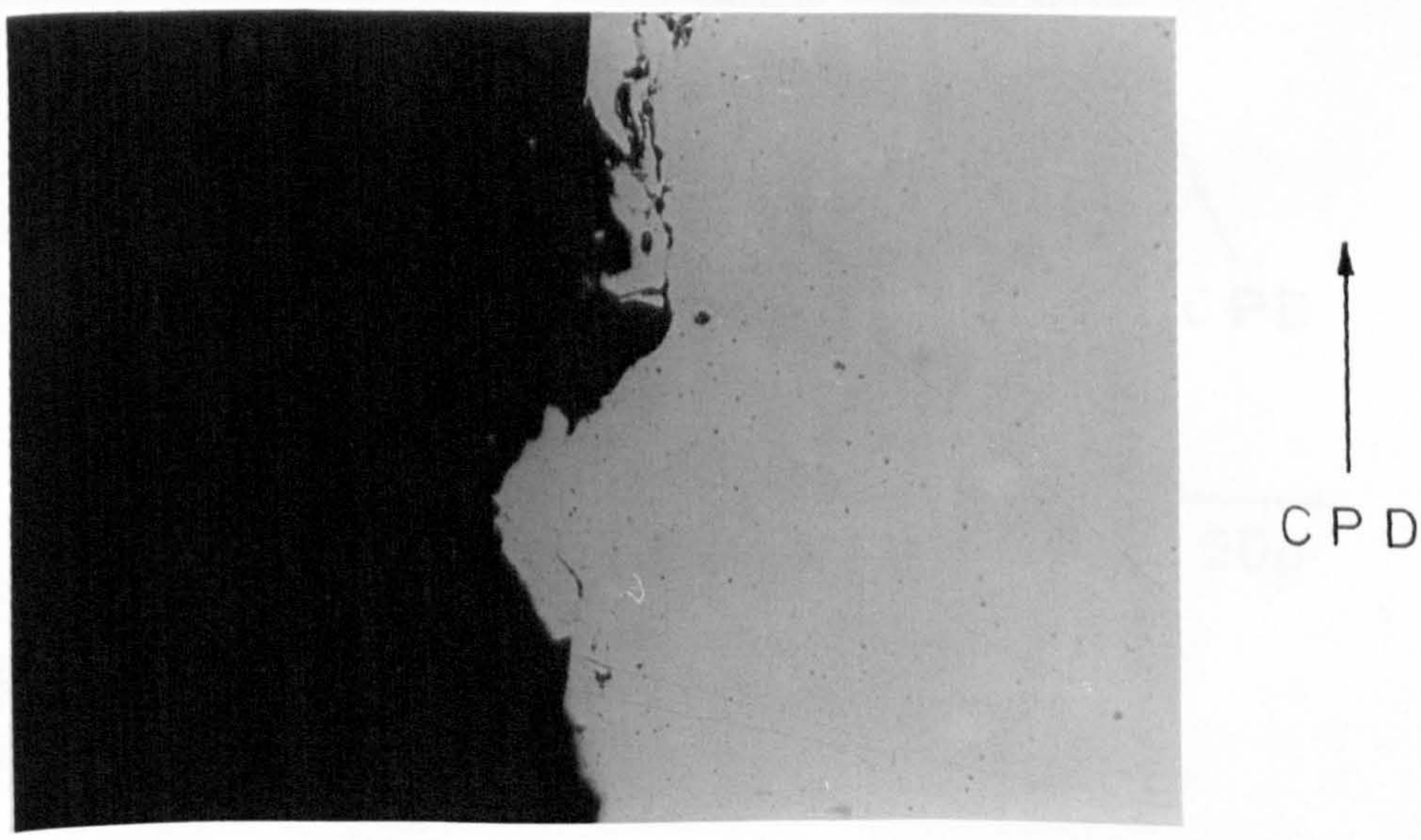

Figure 115. Profile of fracture surface at final failure region, -1400 mV (S.C.E.), crack sides not covered X 450

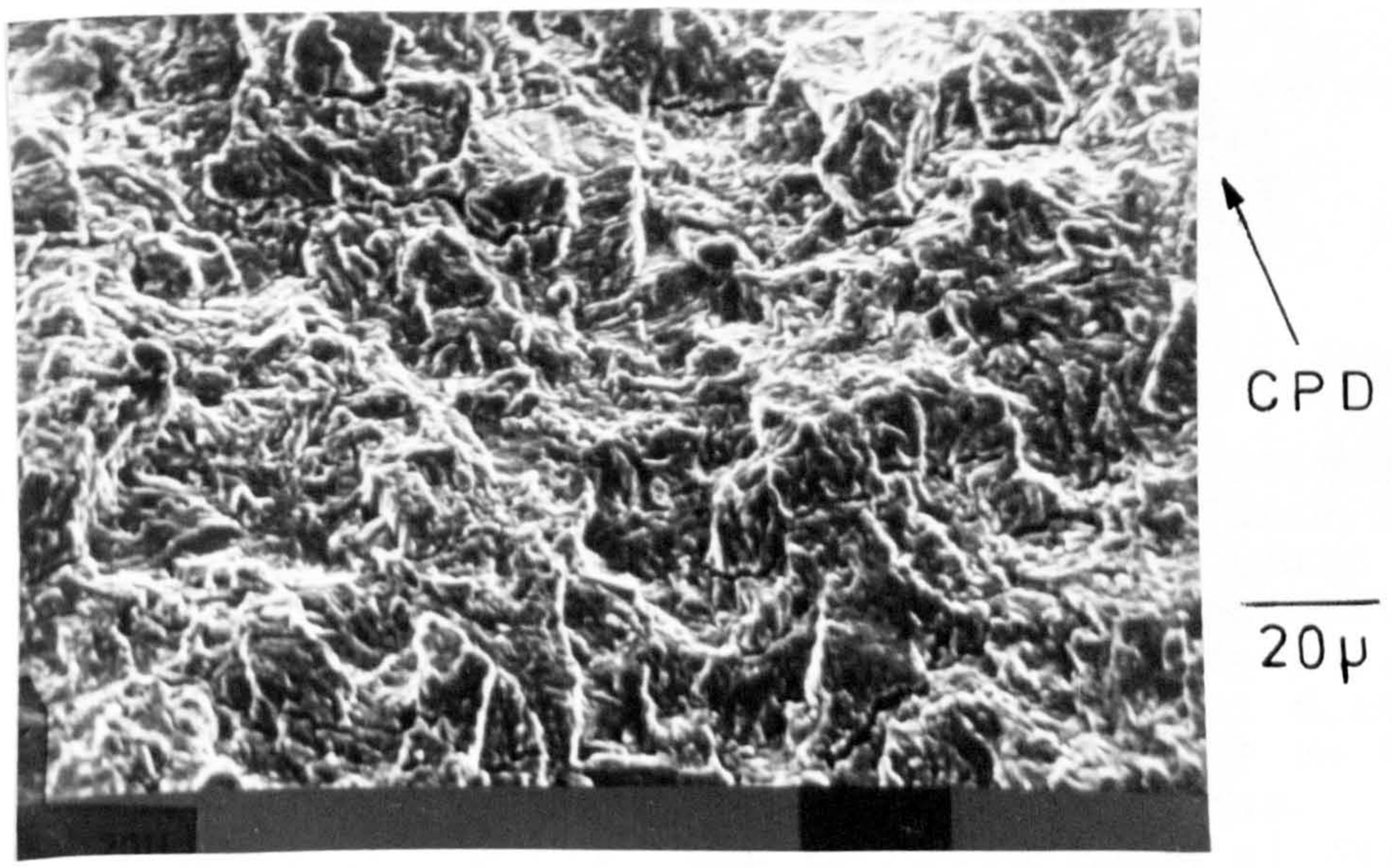

Figure 116. Fracture surface of free corrosion specimen, crack sides not covered (ΔK = 19 MPa$\sqrt{m}$)

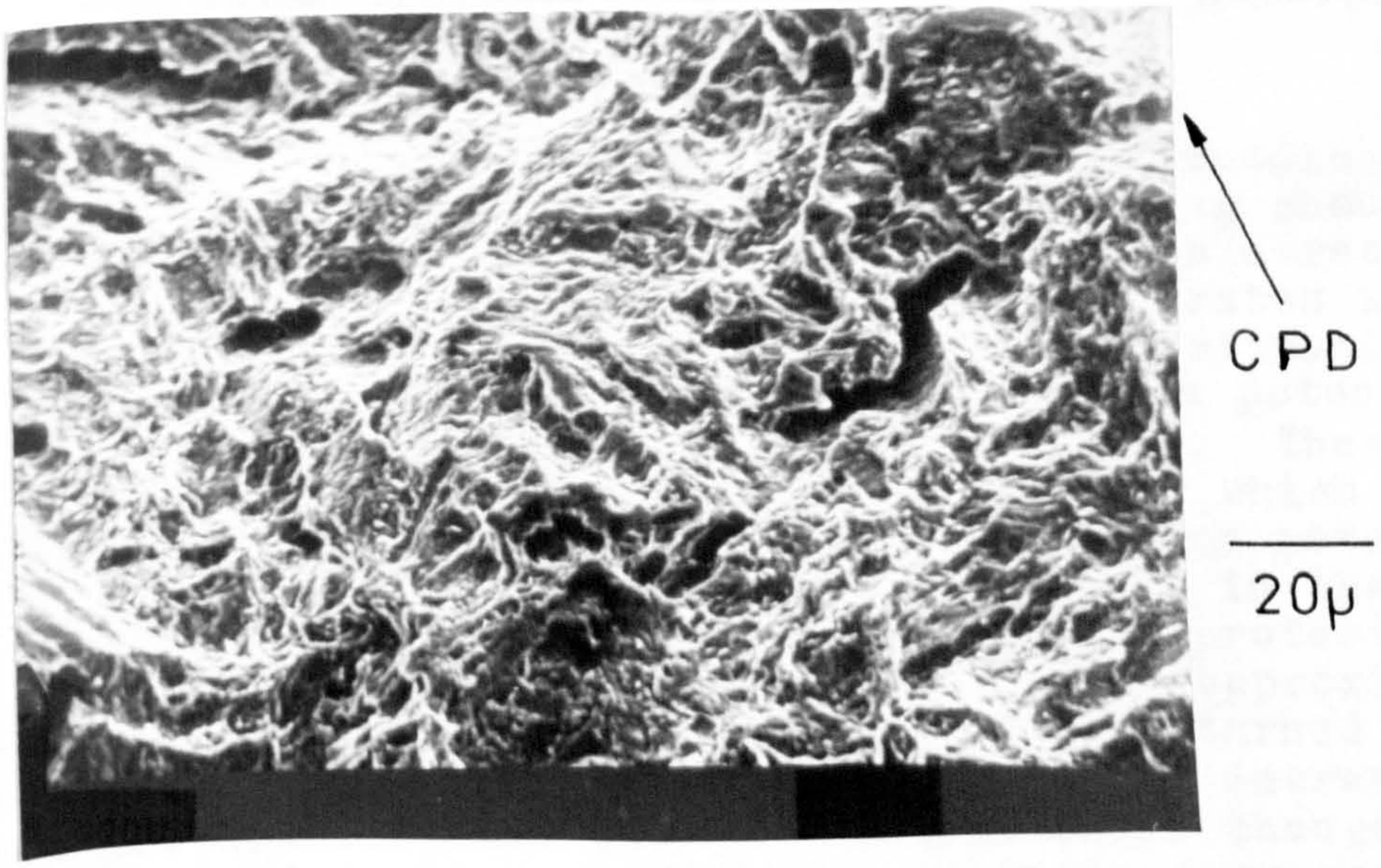

Figure 117. Fracture surface of free corrosion specimen, crack sides not covered (ΔK = 26 MPa$\sqrt{m}$)

In the case of free corrosion a corrosion cell is set up in the vicinity of the fatigue crack (see figure 118). This corrosion cell is caused by the differential aeration of the solution within the crack. Oxygen will be used up by the cathodic reaction. As this happens and the oxygen supply is depleted, the metal within the crack can become anodic whilst the cathodic reduction reaction can proceed uninterrupted outside the crack. As the metal ion concentration increases locally within the crack, Cl^- diffuses into the pit to maintain charge neutrality. As the Cl^- concentration increases, so the reaction

$$FeCl_2 + 2H_2O \rightleftharpoons Fe(OH)_2 + 2HCl \qquad - (42)$$

proceeds to the right hand side of the equation, producing acid and $Fe(OH)_2$. If the pit is occluded (i.e. there is no influence from the environment outside the crack apart from diffusion of Cl^-) this reaction will continue until it reaches equilibrium and the pH reaches a steady value, usually at a relatively low pH. In the absence of dissolved oxygen the cathodic reaction within the crack will be the reduction of hydrogen. The amount of hydrogen ions produced is dependent on the rate of dissolution of ferrous ions. As the metal atoms ionize and pass into solution they leave their electrons within the metal. These electrons are then available for the cathodic reaction. Since there can be no net accumulation of electrical charge during steady state corrosion, the total hydrogen evolution rate must equal the total metal dissolution rate. This last reaction is dependent on the amount of freshly formed crack surface per fatigue cycle. It can be seen, therefore, that under conditions of free corrosion, along with the anodic dissolution process, a certain amount of natural hydrogen charging will be present.

Under severe cathodic polarization conditions, anodic dissolution and any consequent crack tip blunting should be suppressed and hydrogen uptake increased. As a result of this forced hydrogen charging, crack growth rates will be increased above those of the free corrosion situation. The effect of decreasing the cathodic protection potential is graphically illustrated in figure 97 (page198). These data were produced from a set of experiments in which the specimen was fatigued under a cathodic protection potential of -780 mV (S.C.E.) until it was believed to be in the intermediate growth region. At this stage the protection potential was changed to -1300 mV (S.C.E.) for approximately 2800 cycles, after which period it was again returned to -780 mV (S.C.E.). Figure 97 shows the dramatic increase in crack propagation rate when the potential is changed to -1300 mV (S.C.E.) and a similar dramatic decrease in crack propagation rate when the potential is returned to -780 mV (S.C.E.). These changes are reflected in the fracture surfaces of the specimens, as can be seen in figures 119, 120 and 121.

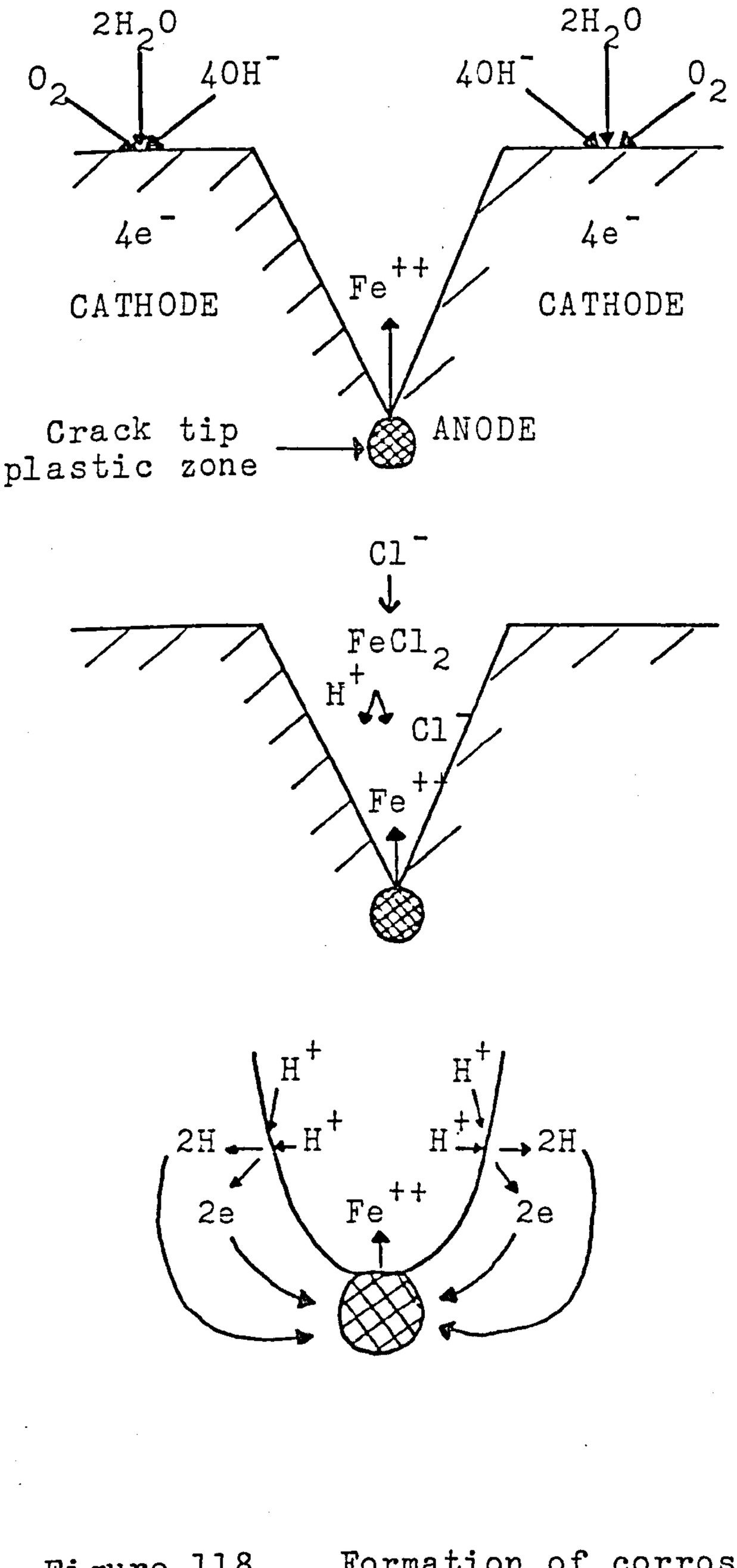

STAGE I

Primary electrochemical reactions occurring during fatigue in sea water

STAGE II

Migration of Cl^- ions from sea water into crack causing formation of $FeCl_2$ which is hydrolysed and forms H^+ and Cl^-

STAGE III

Hydrogen embrittlement caused by formation of H from H^+ ions which are formed in Stage II

Figure 118. Formation of corrosion cell in fatigue crack (Ref 99)

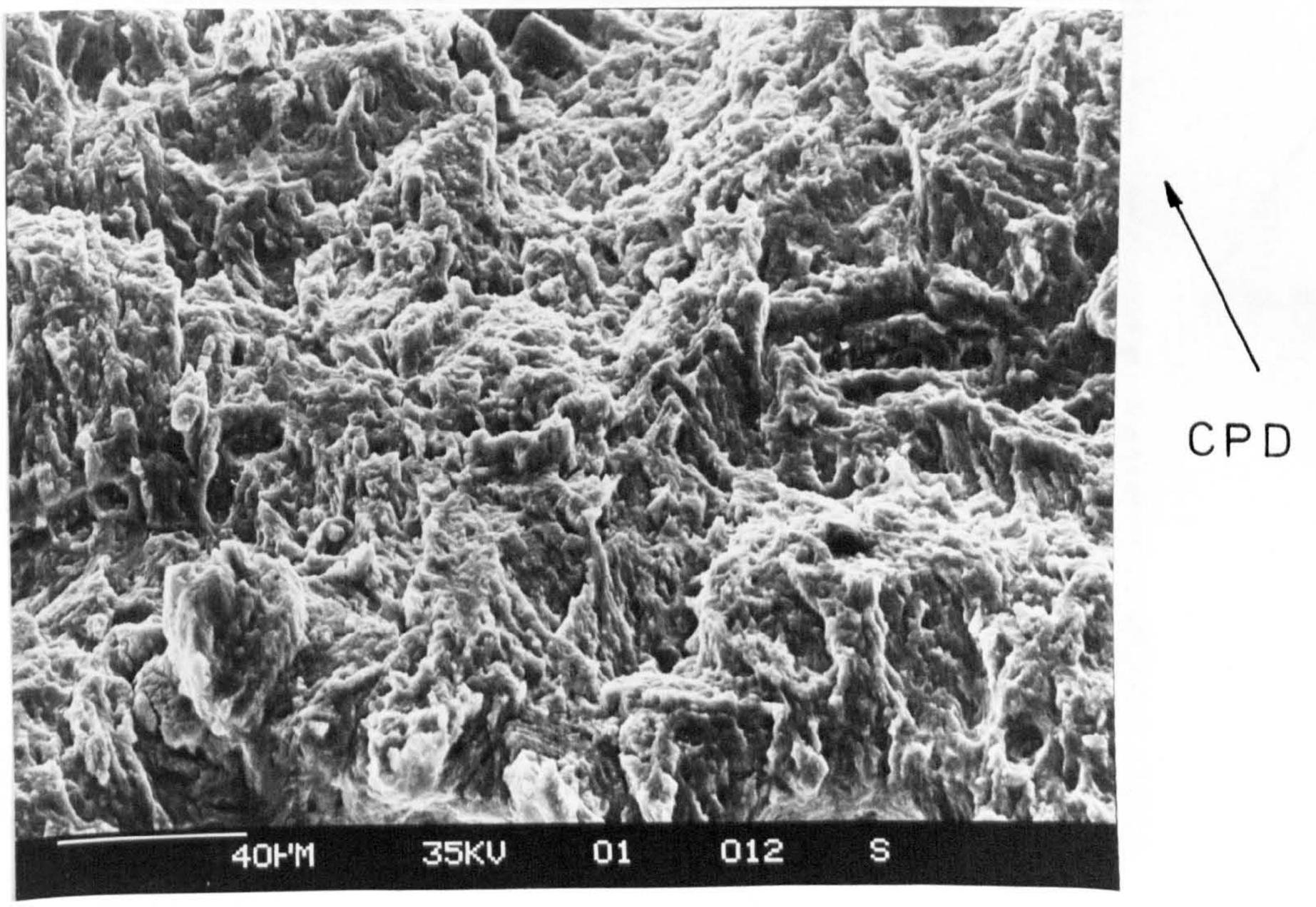

Figure 119. Parent plate specimen protected at -780 mV (S.C.E.), crack sides covered (ΔK = 20 MPa$\sqrt{m}$)

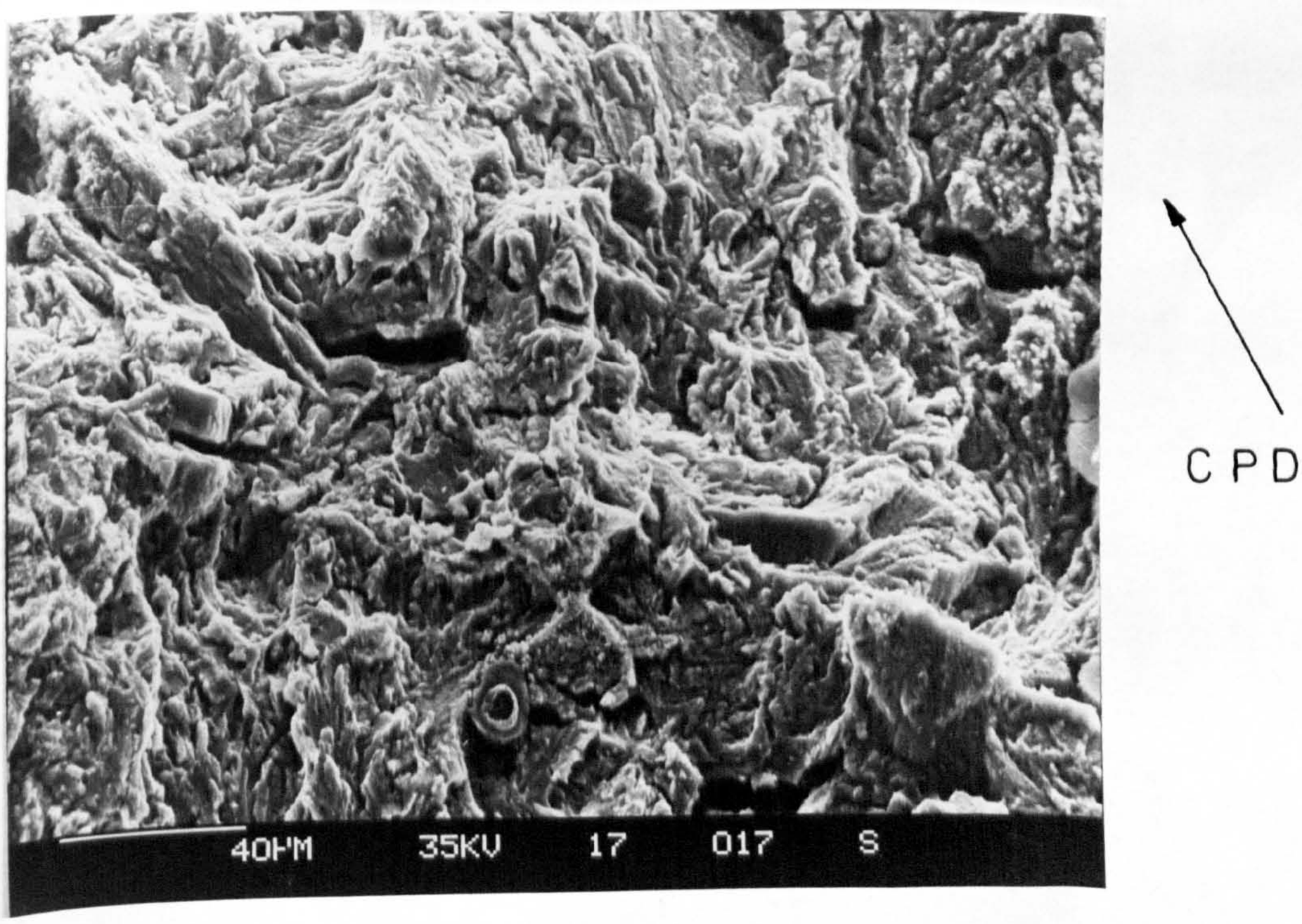

Figure 120. Parent plate specimen protected at -1300 mV (S.C.E.), crack sides covered (ΔK = 29 MPa$\sqrt{m}$

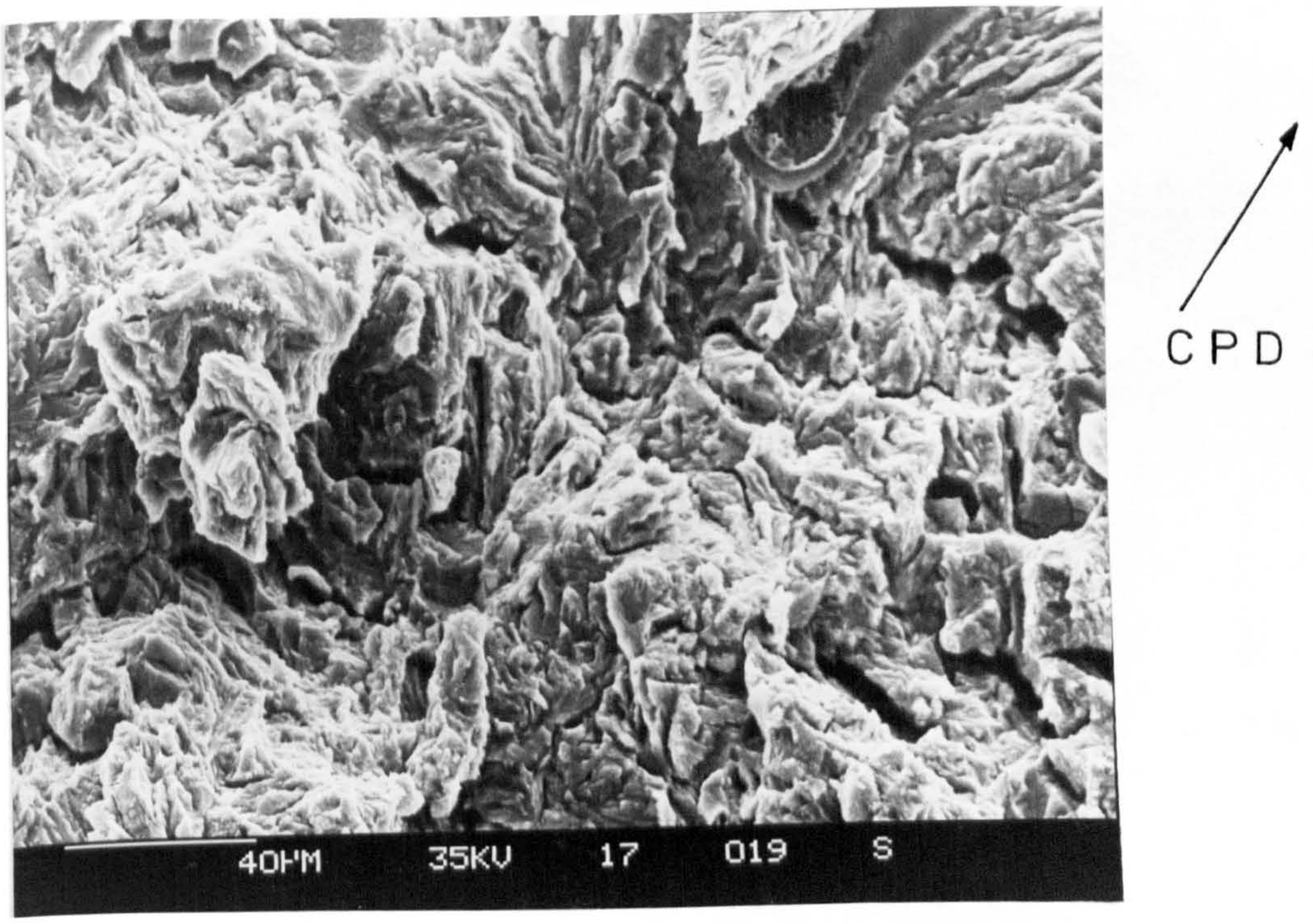

Figure 121. Parent plate specimen protected at -780 mV (S.C.E.), crack sides covered (ΔK = 30 MPa$\sqrt{m}$)

Figure 119 shows the relatively even and finer fracture surface associated with low ΔK and a protection potential of -780 mV (S.C.E.). In figure 120 the potential has been decreased to -1300 mV (S.C.E.) and the fracture surface has subsequently taken on a more brittle appearance and developed large and quite deep secondary cracks. In figure 121 the protection potential has been reduced to the original -780 mV (S.C.E.); the fracture surface however has retained it's brittle appearance. This will be due to the fact that although the forced hydrogen charging will be reduced due to discontinuing the severe overprotection potential, there will be a residual hydrogen content ahead of the crack tip. Although this may start to diffuse away when the potential is returned to normal, the microstructure for a finite distance ahead of the crack tip will remain embrittled due to the hydrogen which had diffused ahead of the crack tip during severe overprotection.

The effect of hydrogen on the corrosion fatigue crack path can be gauged from the following set of figures. These are similar to figures 119, 120 and 121 in that they are of a specimen which was fatigued under a cathodic protection potential initially of -780mV (S.C.E.) then -1300 mV (S.C.E.) then finally -780 mV (S.C.E.) again. They differ, however, in that they depict the crack side-on.

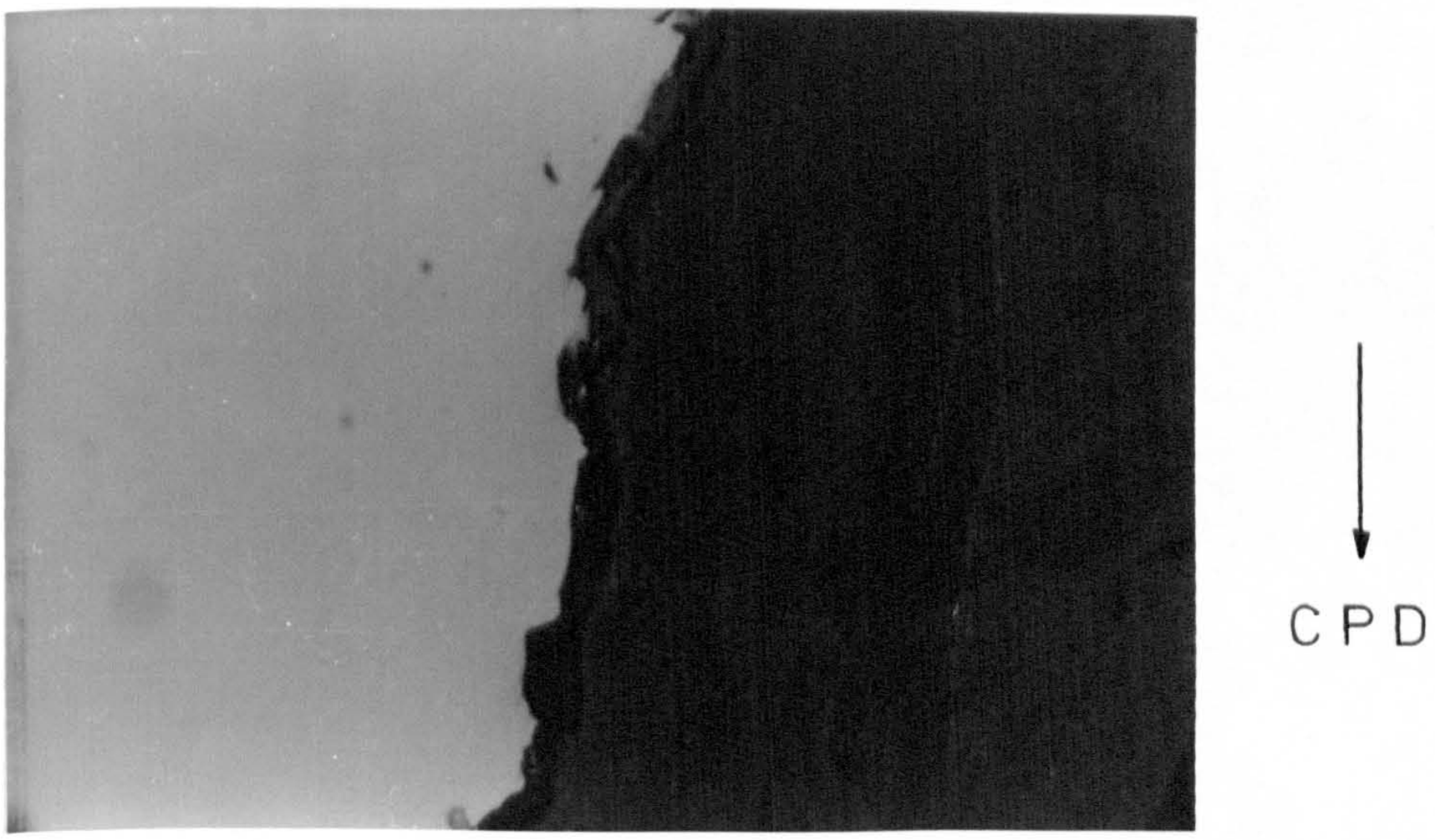

Figure 122. Profile of fracture surface, -780 mV (S.C.E.), crack sides not covered (ΔK = 22 MPa$\sqrt{m}$) X 450

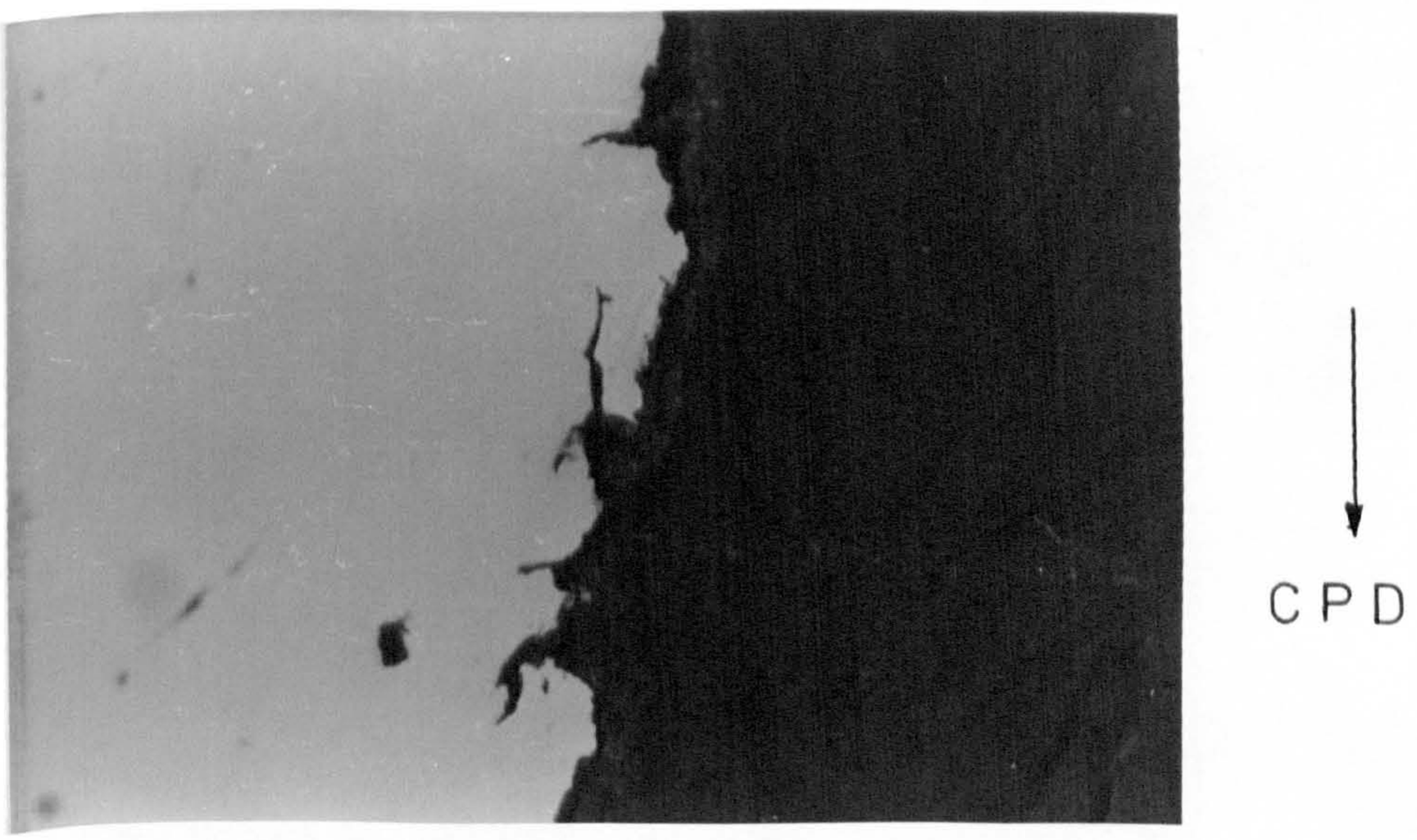

Figure 123. Profile of fracture surface, -1300 mV (S.C.E.), crack sides not covered (ΔK = 25 MPa$\sqrt{m}$) X450

Comparison of figure 122 with figure 112 reveals the difference in corrosion fatigue crack profile for a near theoretically correct cathodic protection potential of -780 mV (S.C.E.) and a severe overprotection potential of -1400 mV (S.C.E.). Figure 122 shows a very much smoother and flatter crack profile, the perturbations being more rounded in nature than the jagged brittle appearance of figure 112. This would be very much in keeping with the anodic dissolution mechanism expected at a potential of -780 mV (S.C.E.).

In figure 123 the protection potential has been changed to -1300 mV (S.C.E.) and the effect on the corrosion fatigue crack profile has been quite dramatic. The length and frequency of secondary cracks has increased considerably and the overall appearance is reminiscent of the hydrogen embrittlement type profile first seen in figures 112, 113, 114 and 115.

Figure 124 shows the region of crack where the protection potential has been changed back to the initial setting of -780 mV (S.C.E.). It can be seen quite clearly that the crack profile has become less jagged than that apparent in figure 123. The depth and frequency of secondary cracking has reduced and the nature of the crack profile seems to be returning more or less to that seen in figure 122. Once again the mode of propagation appears to be anodic dissolution dominated now that the forced hydrogen charging regime has been discontinued and the embrittled material region has been passed.

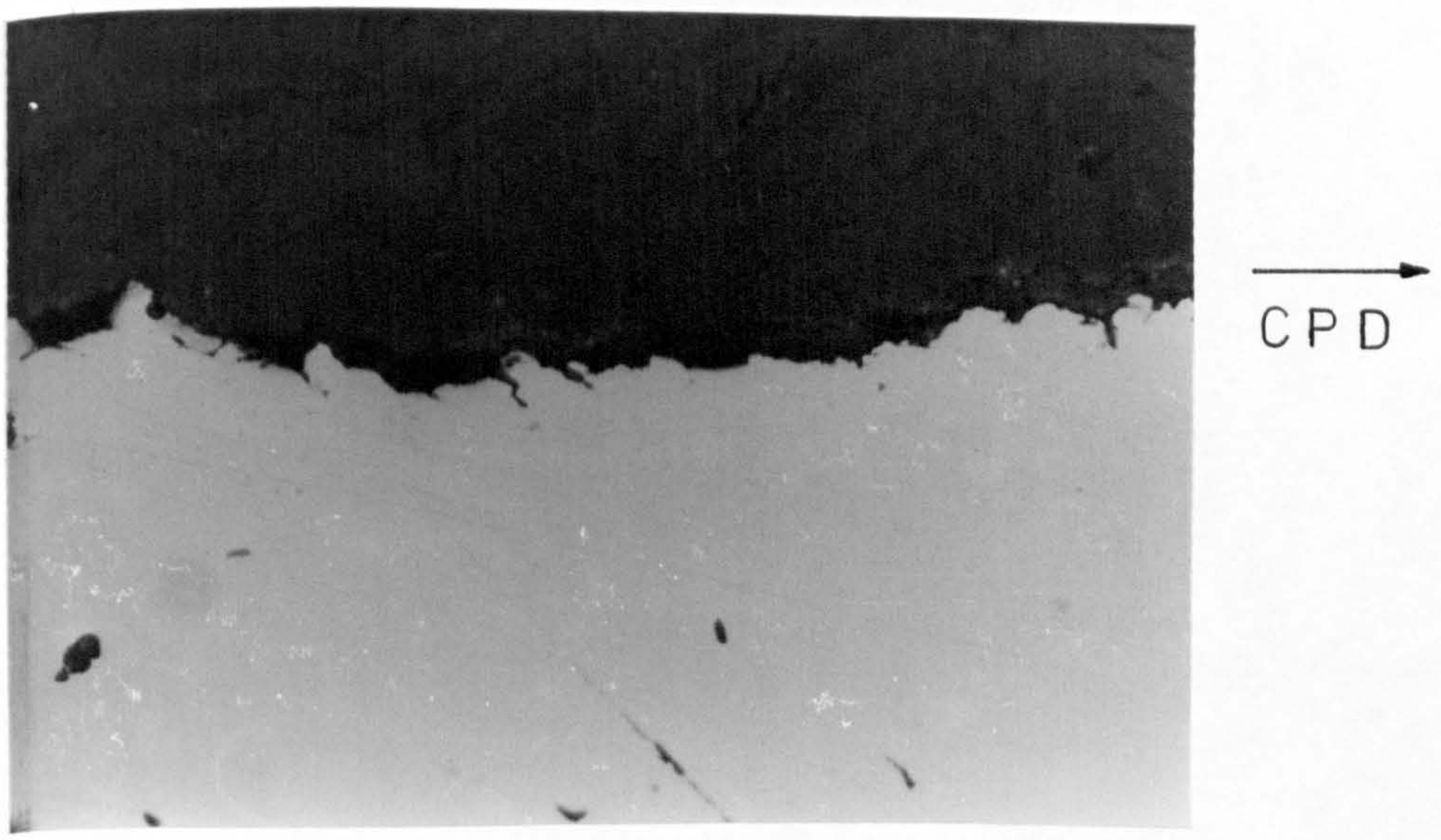

Figure 124. Profile of fracture surface, -780 mV (S.C.E.), crack sides covered (ΔK = 34.5 MPa$\sqrt{m}$) X 450

When comparing figure 124 to figure 121 it can be seen that in this case the fracture profile became less jagged when the overprotection potential was removed, whereas in figure 121 it did not. This can be explained by the fact that the position where the photo was taken in figure 121 was still within the embrittled zone, whereas in figure 124 it was not.

This raises interesting questions on just how overprotection and forced hydrogen charging affect corrosion fatigue crack propagation. Is any damage done to the microstructure permanent? Will hydrogen that has been charged into the steel during overprotection remain there or diffuse away once the overprotection potential has been removed? In order to attempt to clarify the position we must look at how hydrogen is believed to affect steel.

Hydrogen is unique among the elements in it's great mobility in steel, even at ambient temperatures. The small hydrogen atoms can diffuse very rapidly and are believed to concentrate in regions of high triaxial stress in front of the crack, usually considered to be at the elastic/plastic interface of the plastic zone. As discussed in the literature survey, the zone ahead of the crack tip is believed to be affected by hydrogen in several ways :-

(1) Hydrogen can affect the interatomic forces between atoms and in particular, reduce the cohesive force at or near the crack tip. A key component of this theory is the accumulation of excess hydrogen at the regions of maximum triaxail stresses mentioned above, or it may be possible that accumulations could occur preferentially at grain or carbide boundaries.

(2) Adsorbed hydrogen at the crack tip lowers the surface energy of the material, thereby lowering the fracture stress and thus facilitating crack propagation (Ref 127), according to the equation:

$$\sigma_{FR} = (E\gamma/b)^{\frac{1}{2}}$$

where b = interatomic spacing
E = Youngs modulus
γ = surface energy
σ_{FR} = fracture stress

In this process hydrogen may be adsorbed preferentially on an interface or boundary, causing interfacial separation when sufficient amounts are present. Although this could come about from a decreased cohesive strength or surface energy in the manner mentioned above, it is unlikely that these are the only possibilities. For example, particle/matrix bonding may be affected (as already mentioned this may occur for ZrN particles under conditions of severe overprotection); hydrogen may react or interact with other adsorbed species forming local brittle regions; or the strain for coherency loss could be affected.

(3) A third proposed mechanism is the pressure theory. This approach is based on the early proposal by Zapffe (Ref 68) that embrittlement of steels results from high internal pressures produced by the formation of molecular hydrogen within voids or fissures. It is possible that such high pressures can be generated under certain conditions, e.g. cathodic charging, and may assist the externally applied stress, but the model does not address the basic question of how the normally ductile metal undergoes brittle failure rather than deforming plastically or failing by local ductile rupture. In high strength steels, the observation that cracking occurs in dry molecular hydrogen at low pressures has in effect eliminated the pressure model since it is accepted that it is not possible to produce large internal pressures under these conditions (Ref 126).

It seems fitting that just as atomic hydrogen is extremely nimble and elusive in steel, the definitive rationalisation of the cause of hydrogen embrittlement has proven to be just as evasive. So far up to nine different mechanisms have been proposed for hydrogen assisted cracking at the atomic or lattice level (Ref 143). Any examination of these and their associated experimental constraints does not provide unequivocal support for one over the other. In fact, the predictions or test results are not truly exclusive to one mechanism, if indeed exclusivity does exist. It is not difficult to imagine a scenario where an internal flaw, pressurized by recombined hydrogen gas, whose interface is weakened by adsorbed hydrogen, sits in a surrounding lattice, the atomic bonds of which are weakened by dissolved hydrogen. This is probably an extreme speculation but it does, however, make the point that the form of the hydrogen may dictate how failure is promoted. The unique characteristics of hydrogen (in the iron lattice) of a high diffusivity, a limited equilibrium solubility, a large partial molar volume, a high reactivity with most elements, an ability to recombine to molecular hydrogen with a large associated pressure change, a tendency to modify local electron distributions, and a positive but varying interaction with internal heterogeneities, control it's effect on fracture processes. It seems logical to suggest therefore that the apparent mechanism of crack propagation and subsequent failure will depend on which of these characteristics dominate.

Returning to the question of what happens when the over-protection potential is removed, several other questions must also be raised. Will the hydrogen in the zone of embrittled material ahead of the crack front remain there or will it now diffuse to the lower concentration areas, i.e. further into the bulk or back to the surface? It is more than likely that if the hydrogen is in it's recombined gaseous form at a metal/secondary particle interface, then the chances of it going anywhere quickly are very small. However, it is much harder to say what will happen if the

hydrogen is in the form of dissociated atoms which can move about the lattice much more freely. Further, if the crack propagation rate is increased because of some lowering of the cohesive force between atoms at the crack tip, will this effect remain if the hydrogen diffuses away, or is the effect temporary and localised to the region near to the hydrogen species?

In an attempt to answer these questions and to understand exactly what happens once the cathodic overprotection potential is reduced from -1400 to -780 mV (S.C.E.), we must consider the diffusion of hydrogen. The mathematical treatment put forward below is simplistic in nature because a more advanced understanding involves complex mathematics which is beyond the scope of this project (Ref 146).

Let us assume that at a time, t_0, when the overprotection potential is returned to the original setting of -780 mV (S.C.E.), the concentration of hydrogen in the region just ahead of the crack tip (Zone A) is C_0. A further assumption will be made which involves the hydrogen diffusing away such that in another region, Zone B, the concentration will be C_x after a time t. The centre of Zone B will be the distance x from the centre of Zone A.

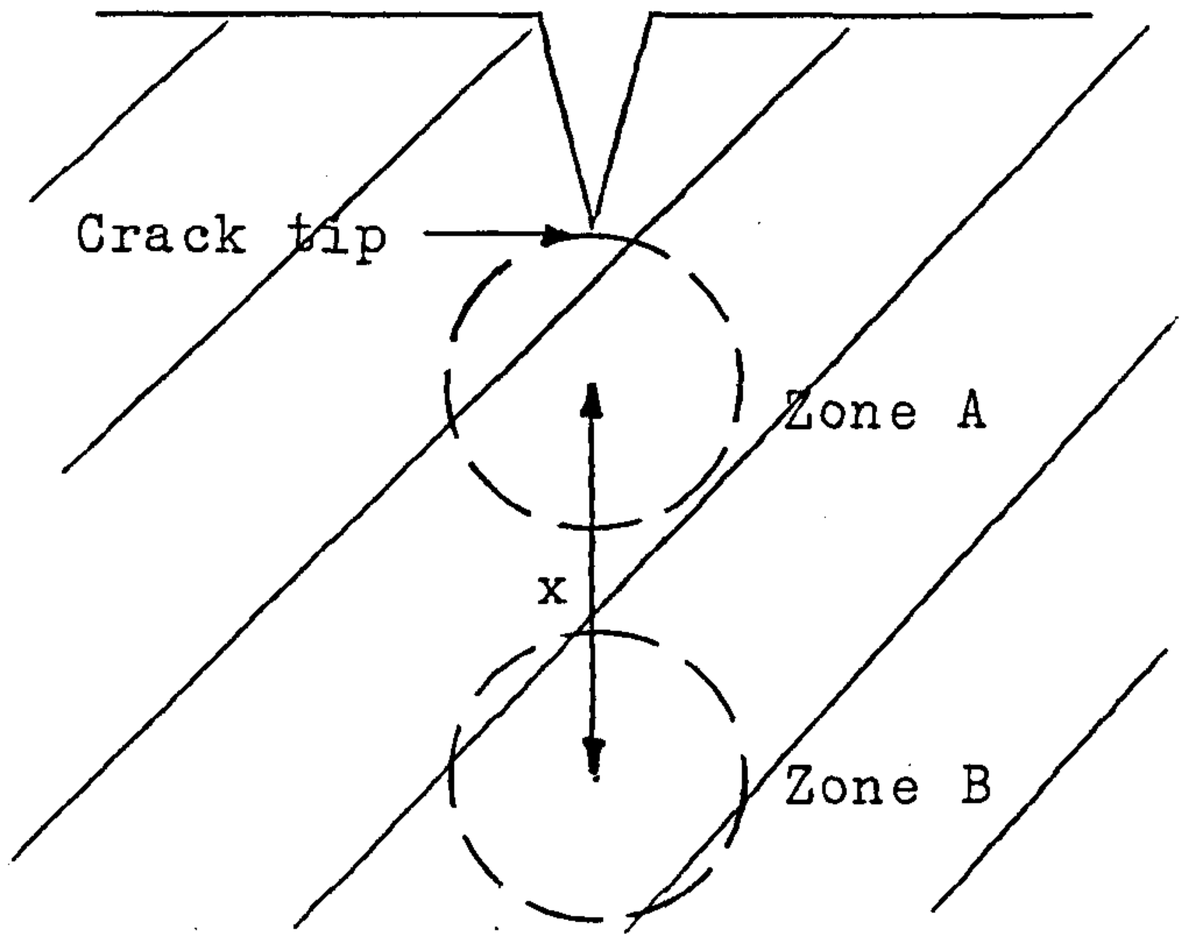

From the solution to Fick's second law (Ref 147):

$$\omega = x/2\sqrt{Dt}$$

where ω is associated with the Gaussian error function
D = diffusion coefficient of hydrogen in iron at $20^0C = 1.5 \times 10^{-3} mm^2/s$
t = time
x = distance from centre of Zone A to centre of Zone B.

If we let t = 300 seconds and x = 0.5 mm purely arbitarily, then:

$$\omega^2 = \frac{0.25}{4 \times 1.5 \times 10^{-3} \times 300}$$

$$\therefore \omega = 0.372677$$

From standard erf ω tables, erf ω = 0.3433

If we now substitute this value into the solution of Fick's second law:

$$C_x = \frac{C_0}{2} (1\text{-erf } \omega)$$

this gives $C_x = 0.328\ C_0$.

From this simple calculation it can be seen that even after a relatively short period of time following the removal of the overprotection potential, hydrogen concentration in the region ahead of the crack tip will be substantially reduced. If we assume that the matrix does not suffer permanent damage from the presence of hydrogen, then it is reasonable to assume that as the hydrogen diffuses away the degree of embrittlement will reduce. This last assumption seems to be substantiated by figures 97 and 98. It can be clearly seen that almost immediately after the cathodic protection potential was reduced to -780 mV (S.C.E.) the crack propagation rate for both parent plate and heat affected zone material dropped significantly.

Since this is a purely theoretical model and several assumptions have been made, it is worth mentioning the validity of these assumptions. The proposal that the hydrogen diffuses away from the crack tip once the overprotection potential is removed may not be strictly correct in all situations. If the hydrogen is in the gaseous phase then the probability is that it will remain where it is. This is because the N-A-XTRA 70 microstructure consists of a dispersion of carbides in a ferrite matrix and it has been shown that carbide interfaces are strong traps for hydrogen, so strong infact, that once saturated with hydrogen they should never desorb at room temperature (Ref 143).

The assumption that the iron matrix does not suffer permanent damage from the presence of hydrogen may not be true. Certainly gaseous hydrogen may distort the lattice; the phenomenon clearly seen in the case of surface blistering. However, whether ionic hydrogen will permanently effect atomic bond strength is rather difficult to ascertain. As already mentioned, the only evidence from this project seems to suggest that once the hydrogen concentration is reduced the embrittlement effect is reduced also.

The only certain comment to be made in answer to the above questions is that whatever process occurs it will be time dependant. Therefore, after the overprotection potential is removed, a finite amount of material in front of the crack tip will still be affected by the hydrogen and as such will experience increased crack propagation rates even when the specimen is once again correctly protected. However, due to the extreme mobility of the hydrogen atom, this may not last for any great length of time.

Due to the nature of corrosion fatigue and the reactions taking place within the crack, modification of the solution within the crack is expected to be an important factor when considering the crack propagation rate. The alternate opening and closing of the corrosion fatigue crack results in pumping of the electrolyte into and out of the crack on each cycle. It does not seem unreasonable to suggest that this should promote mixing of the bulk and crack solutions such that no modifications of the crack electrolyte take place. Table 20 (Ref 145) presents a summary of those factors which are projected as potentially important with regard to crack solution - bulk solution mixing during corrosion fatigue. In the light of these, however, the above assumption may not be strictly correct. Leaving aside diffusion for the moment, Turnbull (Ref 125) postulates that the position of maximum ingress of fresh solution during loading for a wedge-shaped crack can be given by :-

$$\frac{X_{tr}}{L} \simeq \sqrt{R} \qquad - (30)$$

where X_{tr} = position of maximum ingress of fresh solution (measured from the crack tip)
L = crack length
R = Ratio of minimum to maximum load

In the absence of diffusion this analysis indicates that fresh solution would never reach the crack tip if $R>0$. Similarly, a particle initially at the crack tip would move towards the crack mouth during unloading but would never reach it ($R>0$) before flow reversal caused it to move back towards the tip.

If the diffusion process is now considered, a much simpler situation arises. Increasing the overall depth of the crack will simply lead to a greater diffusion distance, hence the longer path for diffusion should tend to give a greater departure from the bulk concentration. The whole situation is further complicated when crack closure effects are considered. In practice, crack closure effects could result in greater replenishment of crack tip solution but details of the extent of closure across the crack front at varying distances from the crack tip for different R values

Fatigue Variable	Influence upon Modification or Mixing
Frequency	mixing is projected to increase linearly with increasing frequency
Crack length	mixing is projected to increase with the cube of crack length
Temperature	mixing is projected to increase with increasing temperature
Stress wave form	mixing is projected to increase the more rapid the crack opening and closing (constant frequency)
Specimen geometry and test method	fatigue test procedures which enhance relative motion between the crack and bulk electrolyte are projected to enhance mixing
Applied current density	modification of the crack electrolyte is projected to be more likely the greater the applied current density (either anodic or cathodic)

Table 20. Listing of fatigue variables and the projected influence of each upon crack electrolyte modification or mixing with the bulk solution

are not well known. There is some evidence (Refs 148, 149) that, at least in the mid ΔK region, crack closure is predominantly a surface, i.e. plane stress, phenomenon. However, due to the complex nature of the phenomenon and the experimental difficulties with closure detection and interpretation of results, the effect of crack closure on the pumping action within corrosion fatigue cracks is not absolutely clear.

The problem with the above discussion in the context of this project is that S.E.N. specimens were used throughout, therefore during each test, although the crack length did increase it only affected diffusion and fluid flow from the crack tip to the crack mouth. As the crack was open to the solution on each side, the diffusion and fluid flow from the crack tip to the sides should have remained relatively constant over the whole of the crack length. Since the R ratio used in this project was 0.6, the crack would never have fully closed, therefore, in comparison to a fully opening and closing crack (R = 1), the pumping action would be reduced. An additional factor of importance in relation to pumping action of corrosion fatigue cracks is that with increasing crack length goes increasing crack mouth opening displacement, and hence the mean crack opening, or volume of solution/metal area ratio, increases.

It may also be argued that due to the surface roughness of the fatigue fracture surface and the build up of calcareous deposits, the overall amount of solution volume in the crack affected by the pumping action should be less than for a theoretically smooth sided wedge-shaped crack. One other major factor not yet discussed is the use of plastic covers to seal off the sides of the crack and simulate a 'real' thumbnail type crack.

As can be seen from the results already presented, covering the crack sides does have a significant effect on the corrosion fatigue crack propagation rates of different microstructures and under different environmental conditions. The general conclusion seems to be that for cathodic protection potentials associated with severe overprotection (-1300, -1400 mV S.C.E.), covering the crack sides produced an increased crack propagation rate regardless of microstructure. This was also true of heat affected zone microstructure for potentials close to the theoretical correct protection potential. Parent plate, however, exhibited a reduced crack propagation rate when the crack sides were covered at near correct cathodic protection potentials. The major question to be answered here is why does covering the crack sides have such a marked effect on the corrosion fatigue crack propagation rate?

A major effect of covering the crack sides is likely to be a reduction in the effectiveness of the pumping action of the crack to expel and replace the solution within it. This can result in a reduction of the oxygen replenishment rate and a reduction in replenishment of fresh solution. As mentioned before, increasing the R ratio decreases the pumping action and it is believed (Ref 150) that increasing the R ratio from 0.1 to 0.7 could lead to a 100 fold decrease in concentration of oxygen. A reduction in the pumping action can have several consequences. As well as reducing the amount of dissolved oxygen in the crack it may also lower the amount of calcareous deposit produced on the crack walls, since unless the solution is replaced, the concentration of calcium and magnesium salts in solution will fall locally as they are deposited. If this was indeed the case it was not noticeable from purely visual inspection after each test run. It must be remembered here that calcareous deposits will themselves reduce the pumping action due to the roughness of their profile interfering with fluid flow and due to their volume reducing the fluid volume in the crack. If the calcium and magnesium salts are not replenished because the effect of the pumping action has been reduced, then there will be less and less calcareous deposits produced on the crack faces as the crack length increases. This could possibly cause a reduction in any crack wedging effect. Moreover, since calcareous deposits cause a reduced current density demand at a given potential, this would also be affected locally. Returning to the effect of reducing the level of oxygen in the crack, it can be seen that oxygen depletion from

solution is likely to transfer the cathodic reaction to that of hydrogen formation. If the hydrogen ions produced by the decomposition of water cannot be removed as hydrogen gas bubbles, then there will be a decrease in the pH of the solution at the crack tip region. Since it is believed that calcareous deposits form at a pH greater than 8.3 (Ref 91), then a lowering of the solution pH within the crack should dissolve any deposits present. The observation of calcareous scales on specimens which had their crack sides covered, at all levels of cathodic protection, clearly shows that large shifts in pH in the acidic direction are unlikely to have taken place. Of course, to balance any oxygen depletion it must be remembered that as the crack length increases the crack mouth enlarges and the pumping action, and hence renewal of solution, will also increase.

At higher overprotection potentials the covered crack sides should stop hydrogen from diffusing away into the bulk solution. It was quite noticeable how hydrogen bubbles formed on and became attached to the plastic covers until quite large volumes were attained. The hydrogen bubbles in themselves would not have presented a great problem since it is not the gas molecule which is absorbed into the matrix but atomic hydrogen. However, with the increase in hydrogen bubbles resident near to the specimen, the probability of dissociation of the molecular hydrogen and absorption of the resultant hydrogen ions must increase.

At this point the consequence of a reduction in the oxygen content within the crack must be considered due to the importance of the oxygen-hydrogen interrelationship. It is known (Ref 151) that oxygen absorbs preferentially to hydrogen, but hydrogen promotes subcritical fracture whereas oxygen prevents it. It is also known that hydrogen readily diffuses in steel whereas oxygen does not. The results of hydrogen permeation studies on steel in NaCl solutions by Barth and Troiano (Ref 127) clearly reveal that the presence of oxgyen sharply inhibited hydrogen permeation and hence it's absorption at low to moderate cathodic overvoltages. It was shown that at -900 mV (S.C.E.) the permeability of hydrogen under aerated solution exposure was at least one order of magnitude less than when the same solution was de-aerated. From this it seems clear that oxygen inhibits pick up in the potential range of cathodic protection while the removal of oxygen allowed hydrogen to enter and permeate the steel at the same potentials. Other researchers (Refs 128,129) have shown that even in cases where increased hydrogen evolution under cathodic protection potentials has occured, it does not necessarily follow that hydrogen absorption will occur. Strongly adsorbed molecules or ions (oxygen or oxygen complexes), even on cathodic surfaces, may cause hydrogen ions to be discharged not on the metal surface, but rather at some distance on the surface of the adsorbed layer, with negligible penetration of this layer.

For parent plate specimens tested it was found that covering the crack sides at a cathodic protection potential of -700 mV (S.C.E.) reduced the corrosion fatigue crack propagation rate, whereas for severe overprotection potentials the propagation rate was increased. These results are similar to those produced by Scott and Silvester (Ref 50) for BS 4360:50D steel in sea water. Their results show that at a free corrosion potential (-650 mV (silver/silver chloride)) reducing the oxygen concentration from the normal 7 to 8 mg/l to 1 mg/l significantly reduced the crack growth rates, whereas for protection potentials of -800 and -1000 mV this was not the case. Indeed, at -1000 mV the crack growth rate was enhanced.

The results obtained for the parent plate specimens in this project begin to make a bit more sense if we consider the fact that covering the crack sides should limit the amount of fresh oxygen entering the crack. If this is correct then the cathodic reduction reaction:

$$O_2 + 2H_2O + 4e^- \rightarrow 4OH^-$$

will become retarded. This may also affect the pH either through reduced production of hydroxyl ions or through a reduced level of oxidation of metal ions. Assuming that the anodic dissolution mechanism is more prevalent than hydrogen embrittlement at low cathodic protection potentials, then any reduction in the cathodic reaction will cause a reduction in the crack growth rate. Under conditions of severe overprotection the situation will be quite different. The anodic dissolution mechanism will be suppressed in favour of the hydrogen embrittlement process and in this situation, as discussed above, the absence of oxygen is definately deleterious to the corrosion fatigue resistance of the material. With only limited amounts of oxygen blocking hydrogen adsorption and hence absorption, it can be seen that enhanced embrittlement should follow.

It is interesting to note that covering the crack sides of the specimens and cathodically protecting them to -700 mV (S.C.E.) gave a better corrosion fatigue resistance than specimens which did not have their crack sides covered and were protected to the theoretically correct protection potential. The reasoning why a supposedly underprotected specimen should outperform a supposedly correctly protected specimen may fall into two regimes:

(a) The covered crack is behaving in the way discussed above and the reduced oxygen content is slowing down the dominant anodic dissolution mechanism.

(b) A potential of -780 mV (S.C.E.) under normal experimental conditions may not infact be the correct protection potential. It could perhaps be that it is slightly too high and a situation has arisen where limited forced hydrogen charging is occurring.

4.9.3 Corrosion fatigue crack propagation behaviour of N-A-XTRA 70 heat affected zone material

Tests were carried out on welded N-A-XTRA 70 specimens in which the corrosion fatigue cracks were grown through the heat affected zone material under the following conditions: free corrosion, cathodic protection potentials of -700 mV (S.C.E.), -1400 mV (S.C.E.), initial protection of -780 mV (S.C.E.) then overprotection of -1300 mV (S.C.E.) for approximately 2800 cycles then back to -780 mV (S.C.E.). In all cases except free corrosion, specimens with and without their crack sides covered were tested. The corrosion fatigue crack propagation rate data is presented graphically in the form of log da/dN against log ΔK in figures 92, 93 and 98. The significant features are considered to be:-

(1) For a cathodic protection potential of -700 mV (S.C.E.) the specimens with their crack sides covered exhibited, over the whole ΔK range, a corrosion fatigue crack propagation rate which was greater than that for specimens without their crack sides covered. This is in direct contrast to the results obtained at this potential for parent plate specimens.

(2) For a cathodic protection potential of -1400 mV (S.C.E.) the specimens with their crack sides covered exhibited a corrosion fatigue crack propagation rate which was greater than that for specimens without their crack sides covered, over the whole of the ΔK range. This was in contrast to the parent plate specimens where the crack covered specimens exhibited a greater corrosion fatigue crack propagation rate only above a ΔK level of approximately 26 MPa$\sqrt{m}$.

(3) The general trend of the data seems to suggest that for welded N-A-XTRA 70 material in which the corrosion fatigue crack is grown through the heat affected zone, covering the crack sides increases the corrosion fatigue crack propagation rate.

(4) For cathodic protection potentials of -1400 mV (S.C.E.) the shape of the Paris curve is characteristic of stress corrosion dominated crack propagation behaviour.

As discussed in the parent plate material section, crack propagation rate enhancement index data was plotted against ΔK for each of the different specimen - cathodic protection potential conditions. These results are shown in figure 100 (page 201). The significant features of the data are considered to be :-

(1) For specimens with their crack sides covered a cathodic protection potential of -700 mV (S.C.E.) exhibits a crack propagation rate enhancement index closest to unity, and hence offers the best corrosion fatigue performance.

(2) For both covered and uncovered specimens, a cathodic protection potential of -1400 mV (S.C.E.) exhibits a C.P.R. enhancement index which is the furthest removed from unity, being significantly worse than that generated by freely corroding specimens.

(3) All specimens with their crack sides covered showed greater C.P.R. enhancement indices than their non-covered counterparts for all levels of cathodic protection potential tested.

Examination of the results for corrosion fatigue crack growth through the heat affected zone shows that at cathodic protection potentials of -1400 mV (S.C.E.), covering the crack sides increased the crack growth rate. This is similar to the situation encountered for parent plate specimens and, as discussed in that section, can be attributed to the plastic covers reducing the amount of oxygen within the crack enclave. For a protection potential of -700 mV (S.C.E.) however, the similarity with parent plate specimens ends. On this occasion welded specimens with their crack sides covered exhibited a corrosion fatigue crack propagation rate which was in excess of that for the non covered specimens. Since the testing conditions were similar for all specimens, whether parent plate, welded or heat treated, the effect must be material dependant.

In view of the proposal that the heat affected zone microstructure exhibits susceptibility to hydrogen embrittlement at protection potentials of -1400 mV (S.C.E.), it was expected that microscopic examination should show a similar quasi-cleavage fracture surface to that first seen in the parent plate photographs. Figures 125 and 126 confirm that this is indeed the case. The fracture surfaces show quasi-cleavage facets and substantial brittle secondary cracking.

A characteristic of the welded specimens was that their fracture surfaces were quite unlike those of the parent plate specimens when viewed at a low magnification, especially for cathodic protection potentials of -700 mV (S.C.E.). The first major difference noticeable is that overall the fracture surfaces appeared to be much more uneven and less regular than their parent plate counterparts. The second major difference, and perhaps the most intriguing, can be seen in figure 127. This shows lines of cracks running perpendicular to the crack propagation direction.

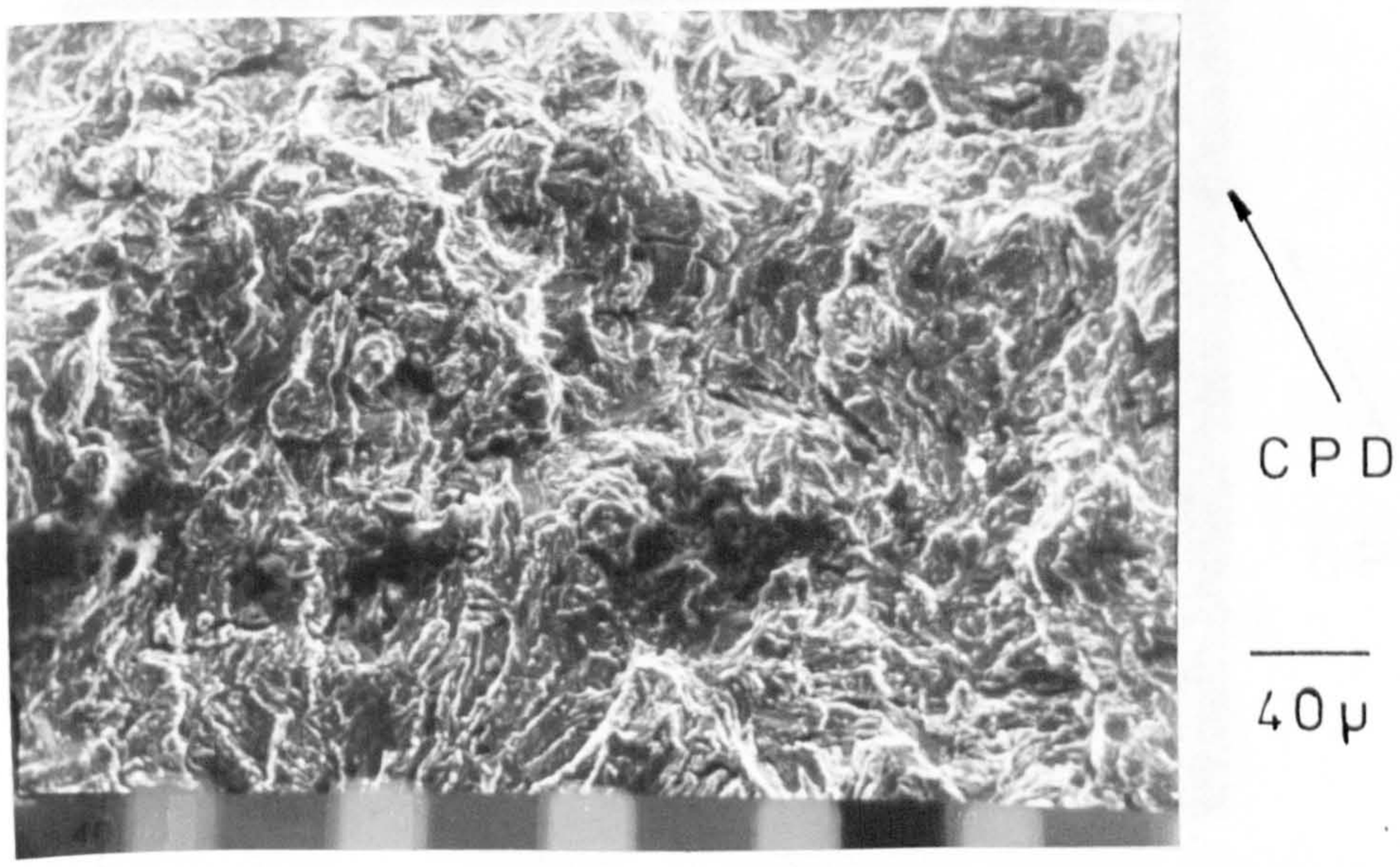

Figure 125. Fracture surface of heat affected zone, -1400 mV (S.C.E.), crack sides covered (ΔK = 34 MPa$\sqrt{m}$)

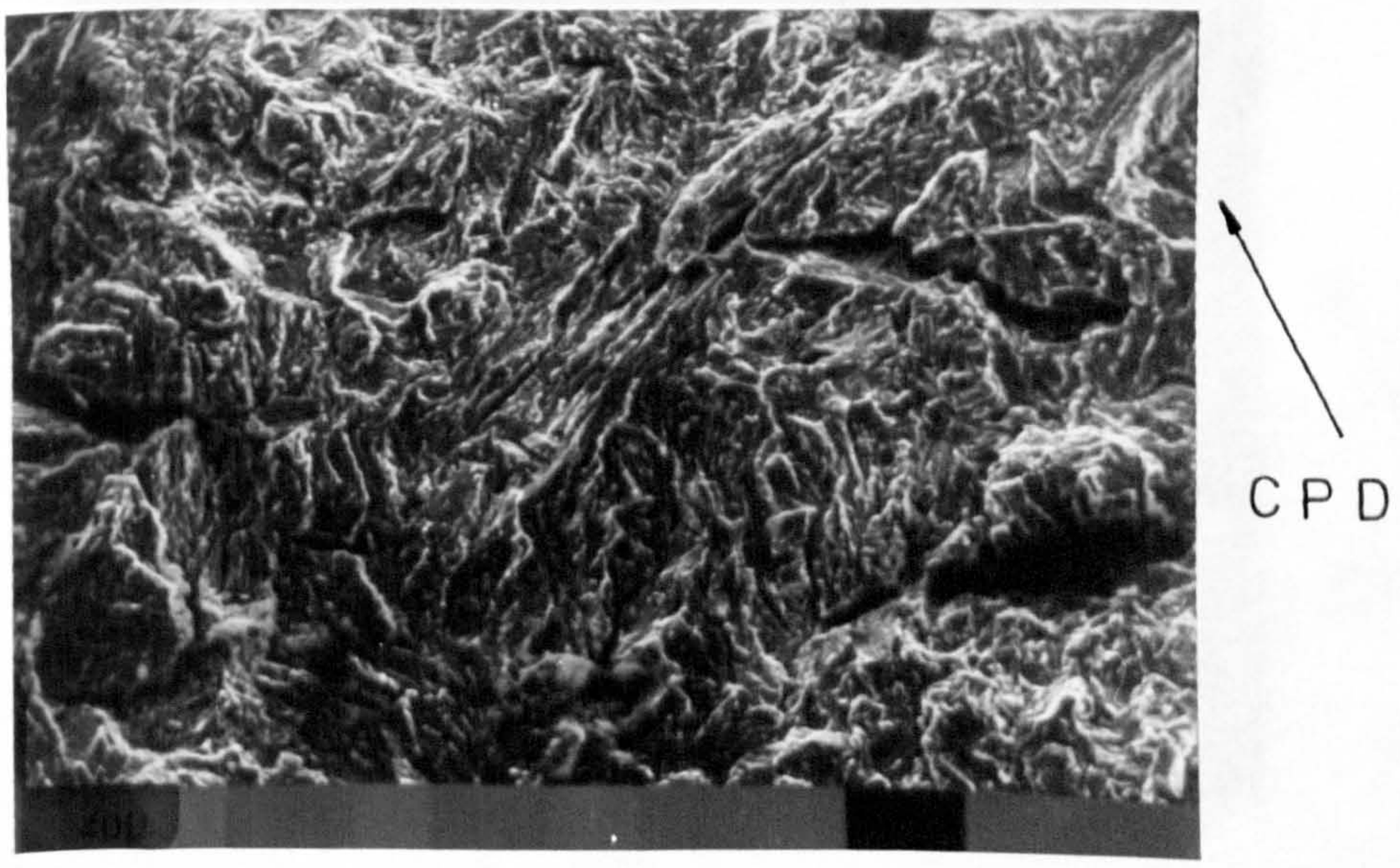

Figure 126. Fracture surface of heat affected zone, -1400 mV (S.C.E.), crack sides covered (ΔK = 37 MPa$\sqrt{m}$)

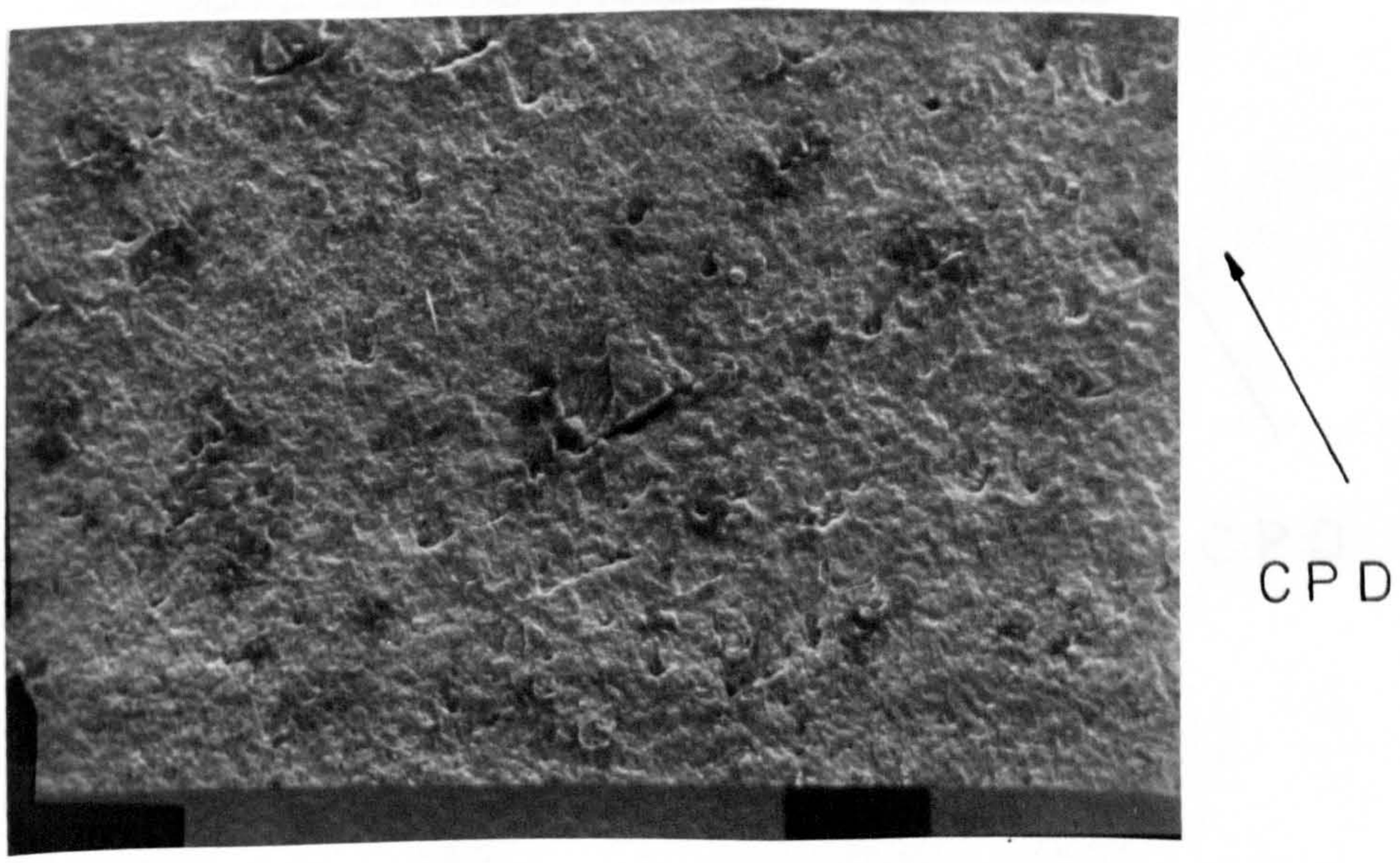

Figure 127. Fracture surface of heat affected zone, -700 mV (S.C.E.), crack sides not covered ($\Delta K \simeq$ 30 MPa$\sqrt{m}$)

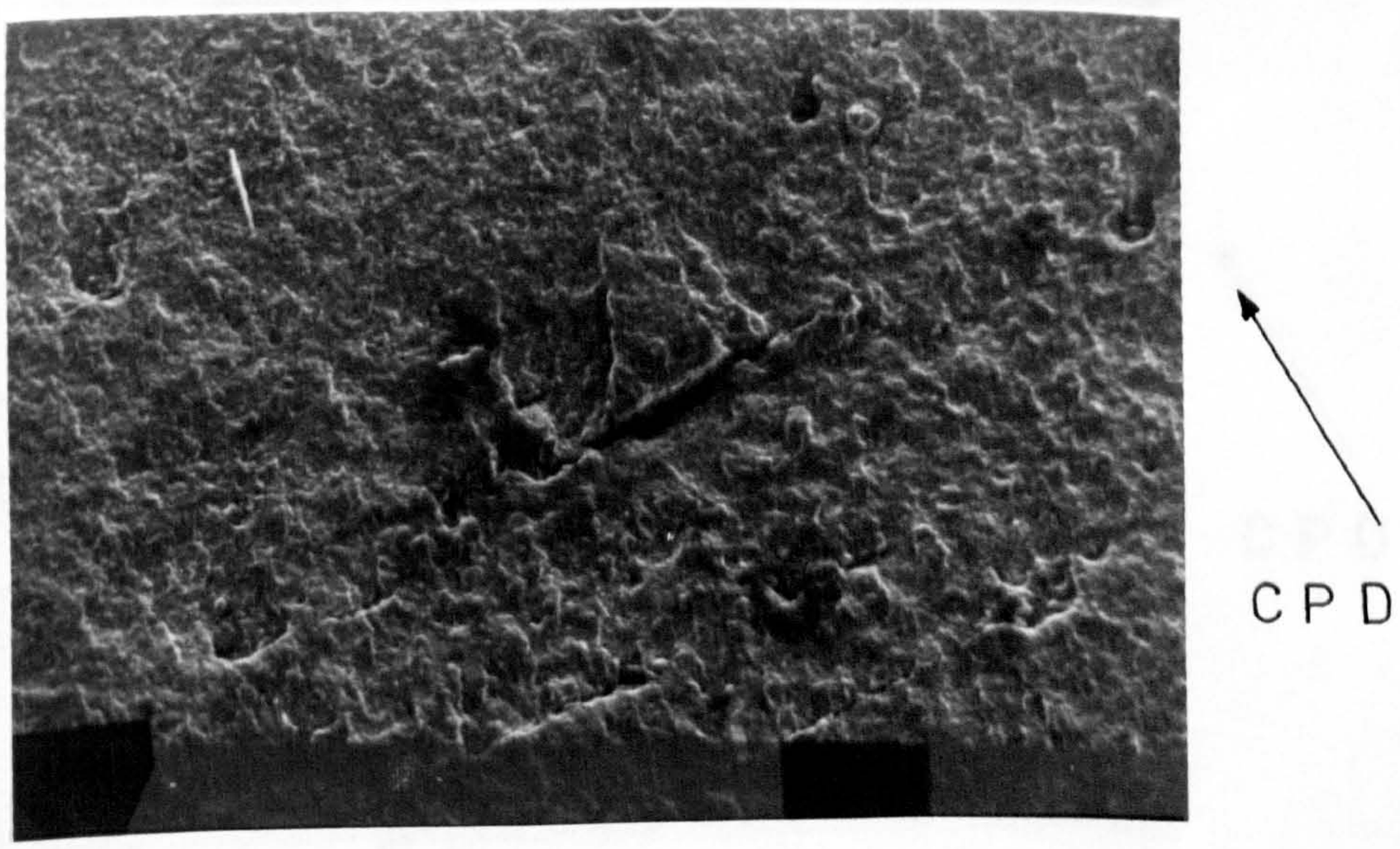

Figure 128. Figure 127 at a higher magnification

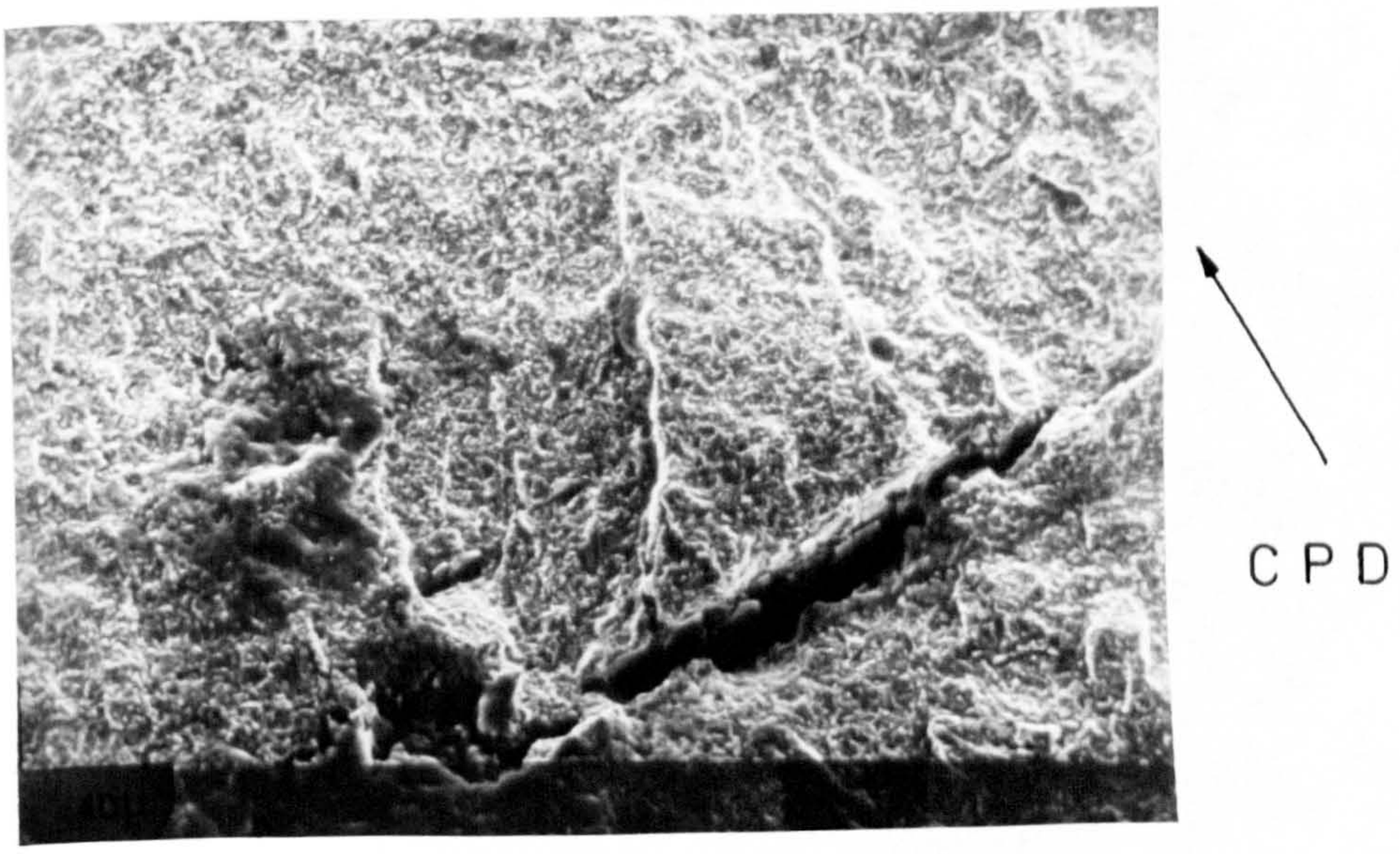

Figure 129. Plateau of material on fracture surface of heat affected zone material (magnification of figure 128)

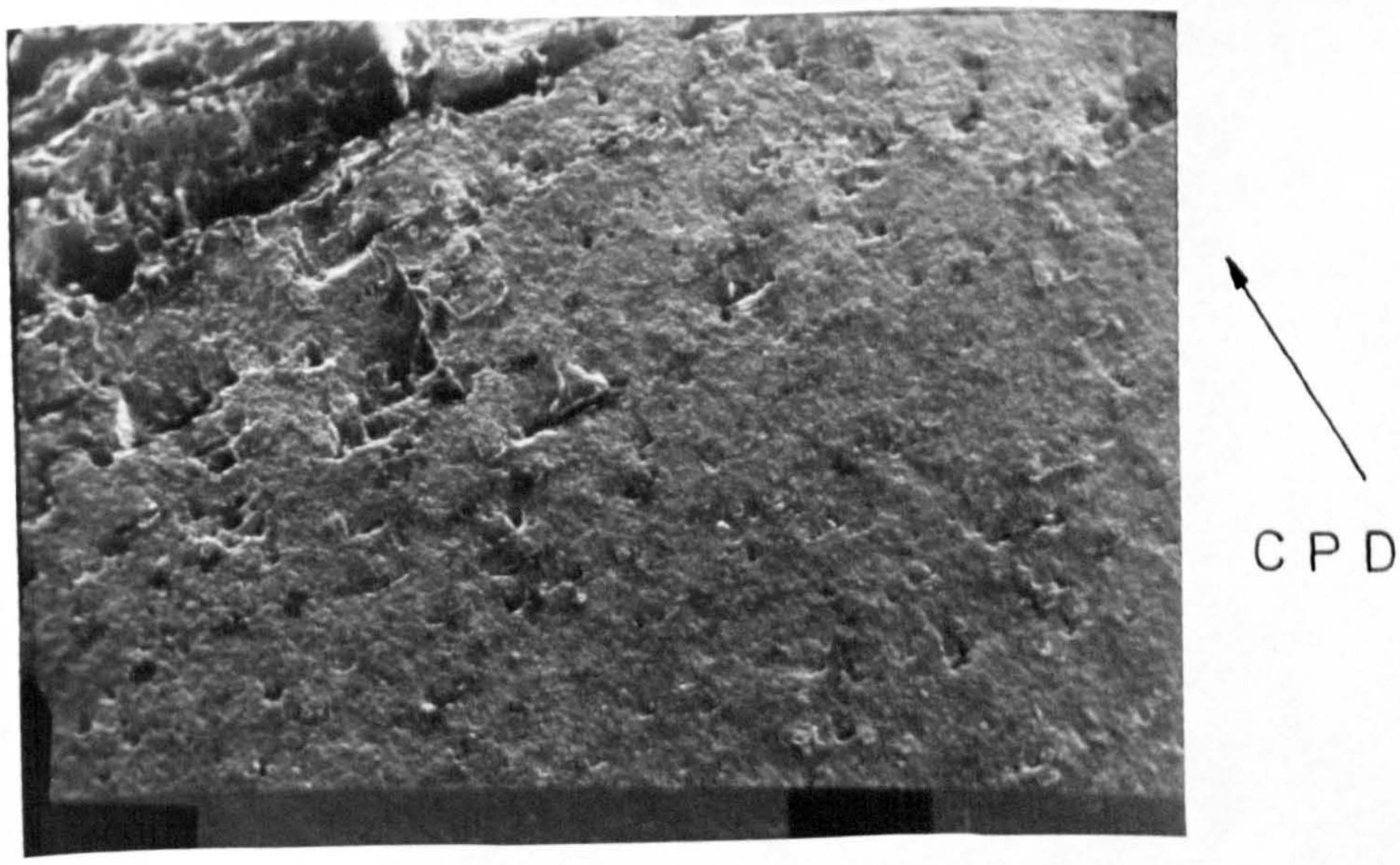

Figure 130. General fracture surface appearance of heat affected zone material

Figure 128 shows that these cracks are somewhat different from 'normal' secondary cracking in that a ridge or plateau of material is usually associated with each large secondary crack. This can be seen more clearly in figure 129, whilst figure 130 shows how the overall fracture surface exhibits an increase in density and size of these secondary cracks as higher ΔK values are reached.

Since the environmental and cathodic protection conditions were the same for both parent plate and welded specimens at -700 mV (S.C.E.), it must be a microstructural effect that is the cause of the difference in fracture surface appearance. As mentioned before, the hardness of the heat affected zone material is greater than that of the parent plate. This would lead to a greater susceptibility to hydrogen embrittlement, which is infact borne out by the enhanced corrosion fatigue crack propagation rates for a cathodic protection potential of -1400 mV (S.C.E.) shown in figure 96. At a potential of -700 mV (S.C.E.) the heat affected zone material was seen to exhibit a crack propagation rate approaching that of free corrosion whenever the cathodically protected specimens had their crack sides covered. This enhanced crack propagation rate is different to the reduced crack propagation rate at -700 mV (S.C.E.) produced by the parent plate specimens. Although it has been discussed that anodic dissolution is likely to be the dominant factor at such a protection potential and removal of oxygen may reduce the crack propagation rate for parent plate material, this may not be the case for the H.A.Z. material.

A crucial point seems to be that when oxygen access is difficult, electrochemical conditions may automatically allow hydrogen production according to the cathodic reaction:

$$2H^{+} + 2e^{-} \rightarrow 2H \rightarrow H_2\uparrow \text{ gas}$$

For the parent plate material such conditions of hydrogen formation may not be so harmful since the microstructure is not hydrogen sensitive and the reduction in the cathodic reaction:

$$O_2 + 2H_2O + 4e^{-} \rightarrow 4OH^{-}$$

will be the dominant factor.

For the heat affected zone material, however, the microstructure may have been sensitised enough so that any increase in hydrogen evolution at all will cause an increase in the corrosion fatigue crack propagation rate.

It is interesting to compare figures 95 and 96 with the above discussion in mind. It can be clearly seen from figure 96 that as the hardness of the microstructure, and

hence the yield strength, increases the corrosion fatigue crack propagation resistance of the material decreases when subjected to severe overprotection conditions. Under conditions of free corrosion the reverse is true. Figure 95 shows how the much stronger heat treated material exhibits a greater resistance to fatigue cracking than the weaker parent plate.

Having now discussed the effects of cathodic protection potentials and the influence of covering the crack sides, it is interesting to compare the Paris plots presented in figures 97 and 98 (pages 198 and 199). These plots were generated from specimens which were cathodically protected initially at -780 mV (S.C.E.) then -1300 mV (S.C.E.) for approximately 2800 cycles, then back to -780 mV (S.C.E.). Both figures show quite clearly how the specimens which had their crack sides covered exhibited corrosion fatigue crack propagation rates which were higher than for those specimens which had not. This was true for both parent plate and welded specimens. The hydrogen sensitive nature of the heat affected zone material is amply demonstrated in figure 98 once the protection potential has been changed to -1300 mV (S.C.E.). The crack propagation rate increases dramatically, the plot for crack sides covered showing the greater increase. Figure 97 shows how the parent plate microstructure is less sensitive to the increased hydrogen production at -1300 mV (S.C.E.), however once again the specimens which had their crack sides covered exhibited the greater increase in crack propagation rate.

Both of these figures aptly serve as a demonstration and a warning to the acceleration affect of overprotection on the corrosion fatigue crack propagation rate of a high strength low alloy steel. As can be seen from the heat affected zone material, a jump of almost an order of magnitude in the propagation rate can be expected if a severe overprotection potential is applied. It is the author's belief that great care should be taken when operating welded high strength steels under conditions of cathodic protection, especially since it is widely recognised that the initiation of fatigue cracks is almost rendered unnecessary by the high level of fatigue-susceptible welding defects present in fabricated components. A great deal of structural integrity and life may be lost in a very short period of overprotection.

Several points to be made about figures 97 and 98 are that the crack propagation rates for -1300 mV (S.C.E.) are average values due to the fact that the overprotection potential was maintained for a short period of time and hence did not have the time to stabilize. It can be argued that a certain amount of time is needed for the supply of hydrogen to the crack tip and the rate of crack advance to reach a new state of dynamic equilibrium. Further, it will

be noticed that once the overprotection potential was returned to -780 mV (S.C.E.) the corrosion fatigue crack propagation rate dropped very sharply for both the H.A.Z. and parent plate material, more so for the parent plate than the H.A.Z. This would once again indicate the H.A.Z. microstructure's sensitivity to the hydrogen remaining in the material and, in both cases, that the crack front either grows through the affected material quite quickly as it is slowing down or that the hydrogen diffuses away swiftly from the material ahead of the crack front.

As previously mentioned, under conditions of reduced oxygen in the crack enclave, the cathodic reaction is expected to change from the production of hydroxyl ions to the production of hydrogen. If electrons are supplied from an external power source, this cathodic reaction will increase and as a consequence the rate of hydrogen evolution will increase, which should in turn result in a lower pH value for the solution. It has already been discussed in this section how the corrosion fatigue crack propagation rate dramatically increases when the cathodic protection potential is reduced below -1000 mV (S.C.E.). This was attributed to hydrogen embrittlement. The results seem to fit the expected pattern for overprotection except that calcareous deposits were found on the crack faces. None should have occurred if the pH of the solution within the crack enclave had fallen into the acidic region (as would be expected for a cathodic overprotection/ deaeration situation).

There are several reasons why this seemingly anomalous calcareous deposition should occur:

(1) The pumping action of the fatigue crack promotes mixing of the bulk liquid and the solution within the crack, thus increasing the oxygen concentration and reducing any pH shift that may occur.

(2) Natural convection and solution agitation caused by the production and movement of hydrogen gas bubbles will promote a greater amount of stirring of solution within the crack enclave and increase the amount of mixing with the bulk solution. This will therefore reduce any pH shift caused by the decrease in the cathodic protection potential (Ref 152).

(3) It is possible that at the crack tip the pH will have been reduced to a value well below that needed for calcareous deposit formation. Therefore, initially the crack tip will be under a regime of low pH hydrogen embrittlement. However, as the crack grows and the pumping action increases, a situation described in point (1) above may occur. The pH in the region that was the crack tip will rise and calcareous deposits will form.

Since calcareous deposits were found on the crack faces of all overprotected specimens it is obvious that the pH within the crack was greater than 8.3, thus allowing deposit formation. However, as it was impossible to measure the pH at the crack tip it is impossible to say if any or all of the situations outlined above had occurred previously.

4.9.4 Corrosion fatigue crack propagation behaviour of heat treated N-A-XTRA 70 material

Corrosion fatigue crack propagation tests were carried out on heat treated N-A-XTRA 70 specimens under the following conditions:- free corrosion, -1300 mV (S.C.E.), -1400 mV (S.C.E.). For both the free corrosion condition and -1300 mV (S.C.E.) only specimens with their crack sides covered were tested. The corrosion fatigue crack propagation rate data is presented in the form of a graph of log da/dN against log ΔK in figure 94 (page 195). The significant features of this data are considered to be :-

(1) The shape of the Paris curve for cathodic protection potentials of -1300 and -1400 mV (S.C.E.) is very characteristic of stress corrosion dominated crack propagation behaviour.

(2) For a cathodic protection potential of -1400 mV (S.C.E.), specimens with their crack sides covered exhibited a higher corrosion fatigue crack propagation rate than those specimens which did not have their crack sides covered.

(3) For a ΔK value of approximately 25 MPa$\sqrt{m}$, specimens cathodically protected at a potential of -1400 mV (S.C.E.) exhibited a corrosion fatigue crack propagation rate which was almost an order of magnitude greater than that shown by freely corroding specimens.

As was the case for both the parent plate and the welded specimens, crack propagation rate enhancement index data was plotted against ΔK for each of the test conditions. The results are shown in figure 101 (page 202). The significant features of this data are considered to be :-

(1) C.P.R. enhancement indices for a cathodic protection potential of -1400 mV (S.C.E.) are approximately ten times those of freely corroding specimens.

(2) For a protection potential of -1400 mV (S.C.E.), the C.P.R. enhancement indices for covered specimens are higher than for non covered specimens, except for a very small region in the lower ΔK region.

From the graphs comparing C.P.R. enhancement indices for free corrosion and -1400 mV (S.C.E.), figures 102 and 103, the following significant features can be seen :-

(1) C.P.R. enhancement indices of heat treated specimens for a protection potential of -1400 mV (S.C.E.) are approximately double those of welded specimens and

approximately two and a half times those of parent plate specimens.

(2) C.P.R. enhancement indices of heat treated specimens under conditions of free corrosion are approximately half those of parent plate specimens and approximately two thirds those of the welded specimens.

In an attempt to discover why the heat treated material was so prone to accelerated corrosion fatigue crack propagation rates under conditions of cathodic overprotection, the fracture surfaces of several specimens were examined.

Examination by eye revealed the first major difference in the heat treated fracture surfaces over those of both parent plate and heat affected zone material. Instead of the more usual thumbnail-shaped crack front (figure 131a) found on all the parent plate and heat affected zone specimens, the crack front profile was that represented by figure 131b.

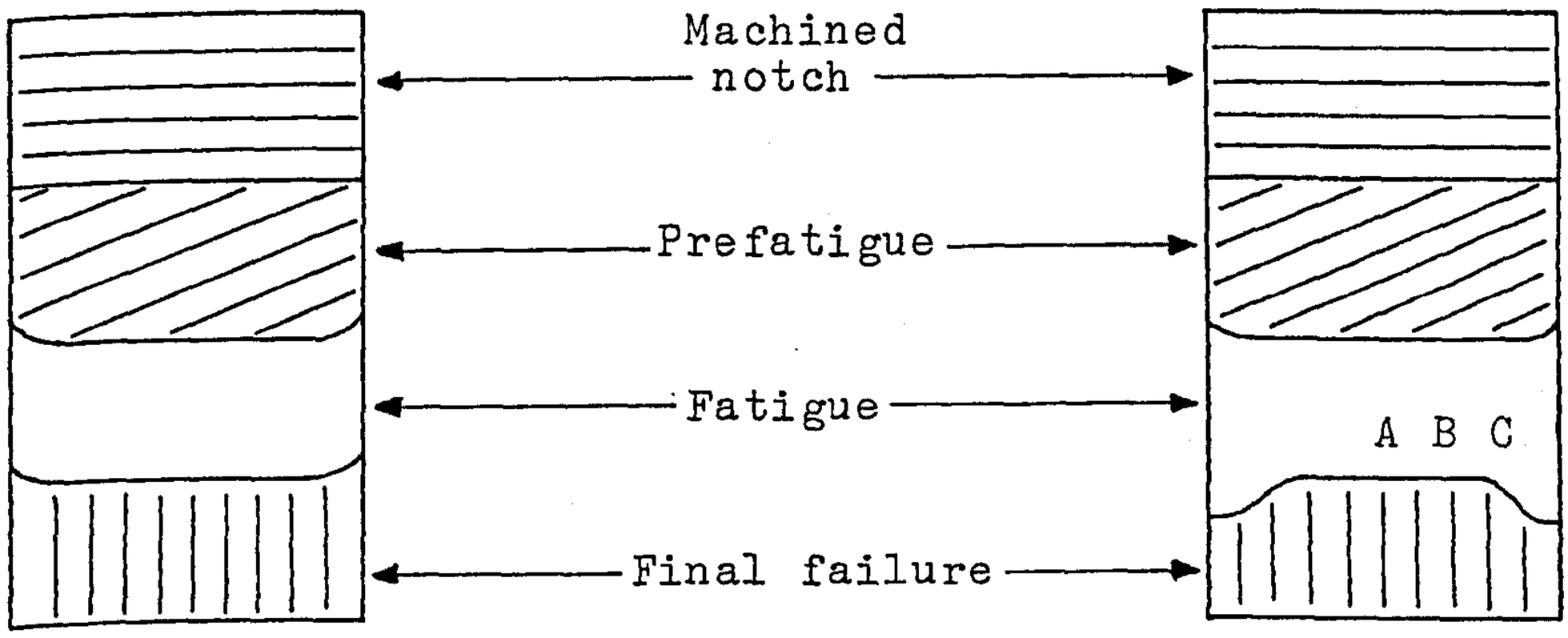

Figure 131. Comparison of heat treated and parent plate fracture surfaces

Actual photographic comparisons can be seen in figure 77 (page 128). It can be seen clearly that unlike other profiles where the fatigue crack has grown faster in the middle of the specimen, for the heat treated specimen the fatigue crack has grown faster on the outside edges.

Examination by a scanning electron microscope showed up further seemingly enigmatic features not found on the parent plate and heat affected zone material. Figure 132 shows an area of the fracture surface in the middle of the final fatigue area (position A in figure 131b). As this specimen was cathodically protected to a potential of -1400 mV (S.C.E.), the brittle quasi-cleavage facets seen in the centre of the photograph are not unexpected. However, towards the right hand side of the picture the fracture surface changes to a much smoother intergranular appearance.

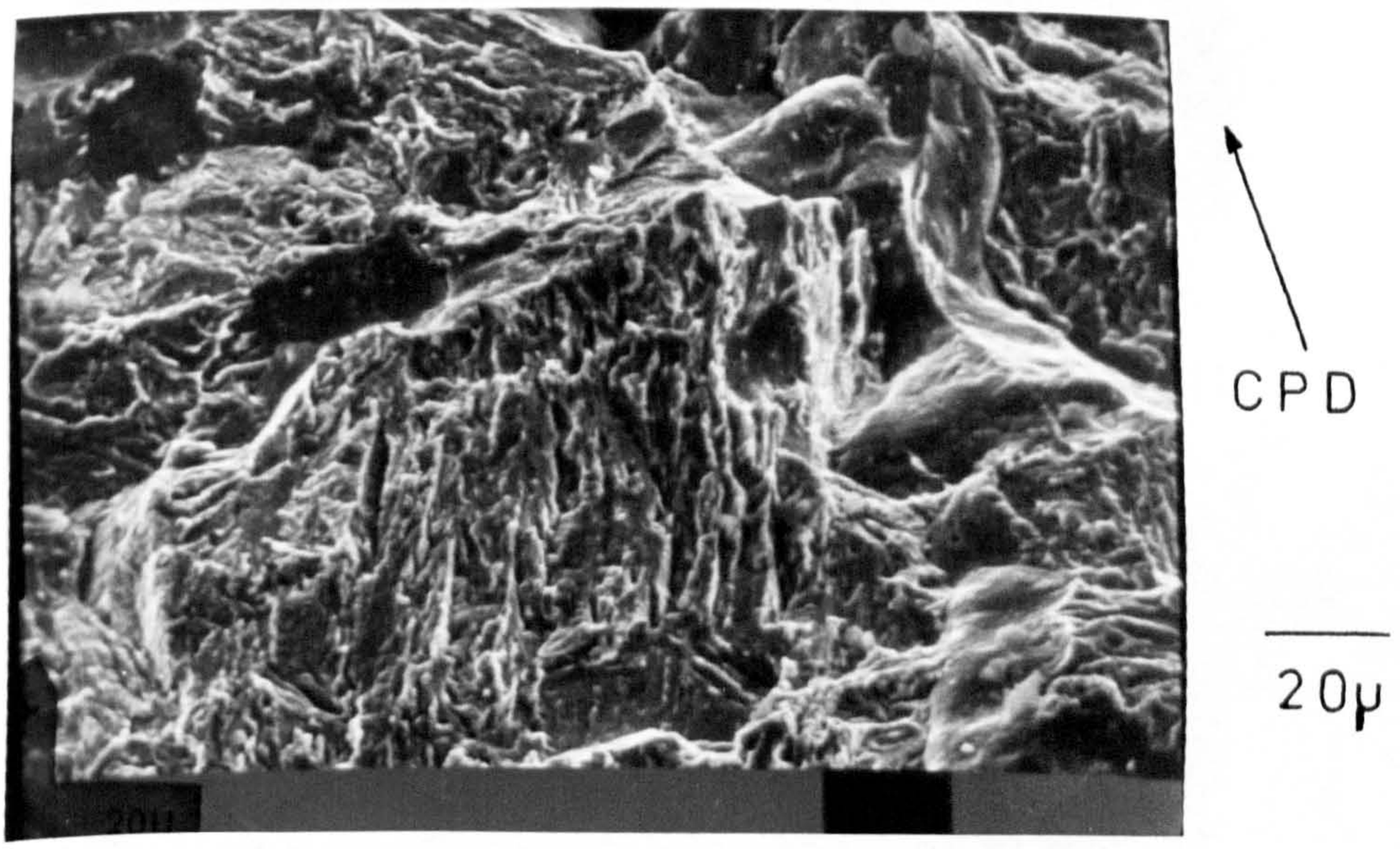

Figure 132. Fracture surface of heat treated material, -1400 mV (S.C.E.), crack side covered, central position (ΔK = 27 MPa$\sqrt{m}$)

Moving towards the edge of the fracture surface (position B in figure 131b), it can be seen from figure 133 how the fracture surface is becoming more intergranular in appearance with less quasi-cleavage until, as can be seen from figure 134, quite a substantial amount of the fracture surface is of an intergranular nature and exhibiting quite large secondary cracks (position C in figure 131b). As mentioned before, this type of fracture surface was unique to heat treated specimens.

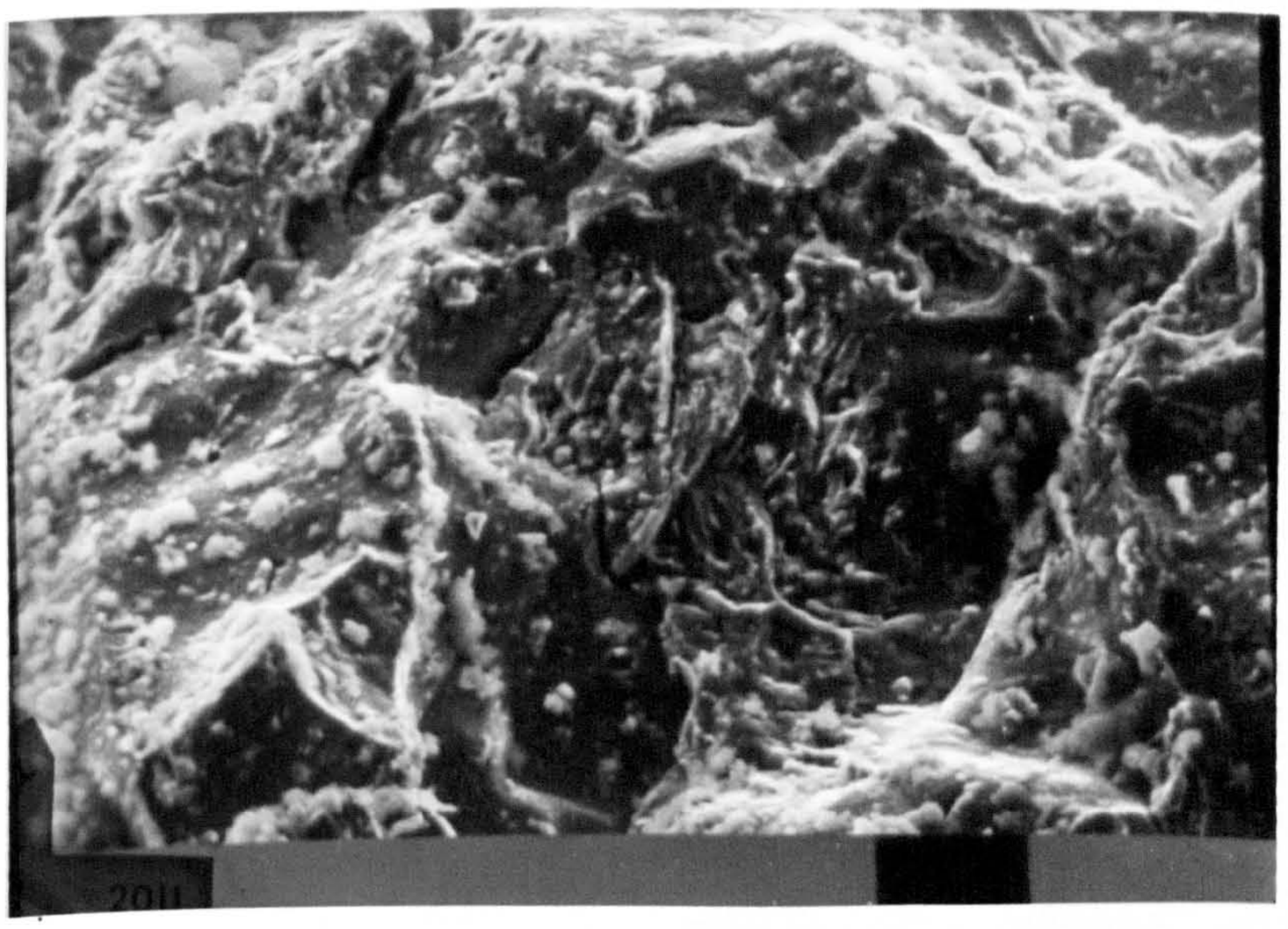

Figure 133. Towards the edge of fracture surface shown in figure 132

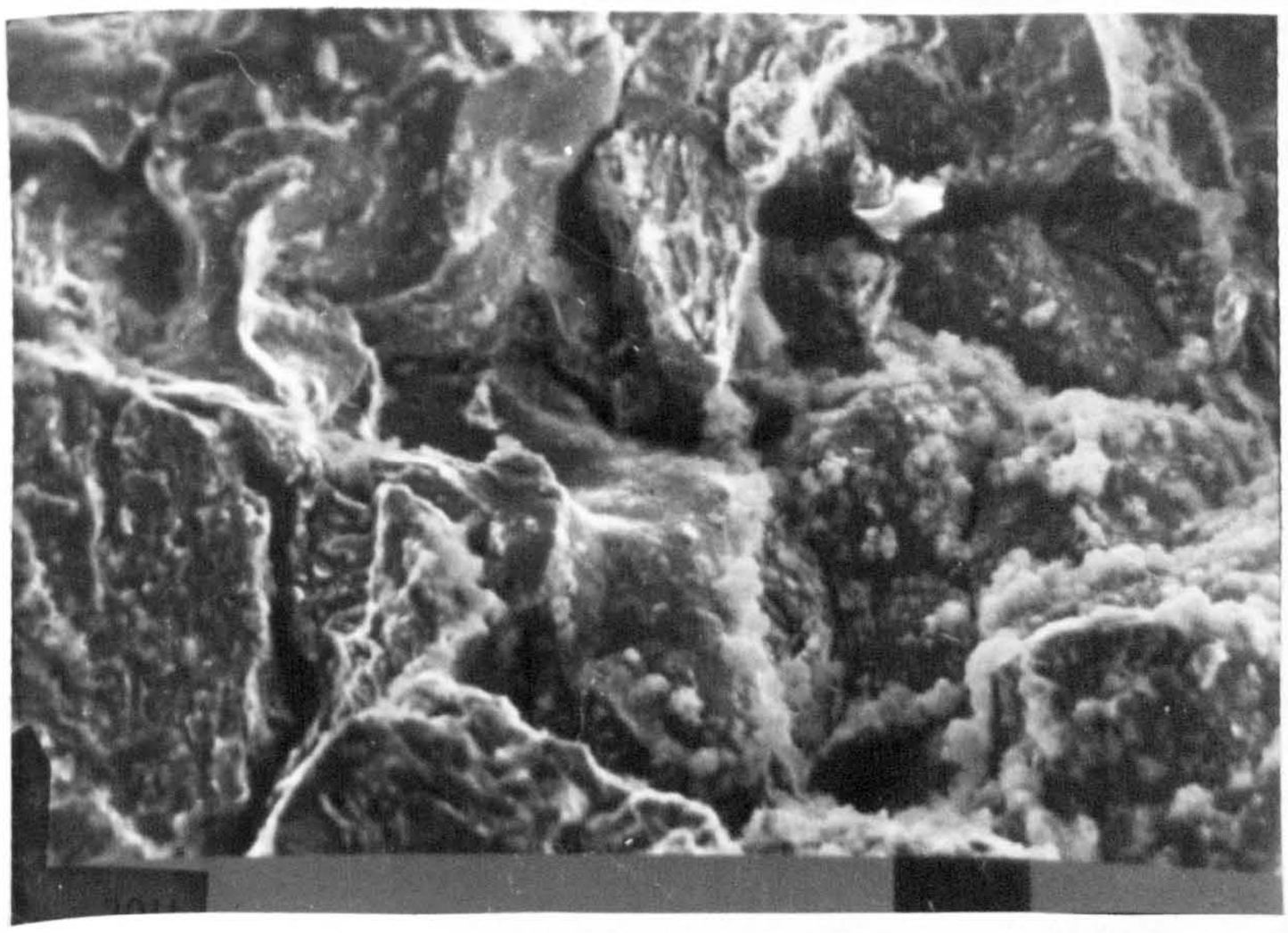

Figure 134. Edge of fracture surface shown in figure 132

Under normal corrosion fatigue situations for specimens with a rectangular cross section, the crack front proceeds faster at the centre than at the surface, hence the typical crack front profile as shown by figure 131a. One reason for this is that the centre of the specimen more nearly fulfills plane strain conditions; another reason is that towards the surface it is easier for diffusion and fluid flow to counteract any chemical or pH changes in the electrolyte at the crack tip. Since the environment, loading regime and frequency was the same for the heat treated specimens as it was for the welded and parent plate specimens, then it must be due to the difference in microstructure and/or mechanical properties of the heat treated material that the crack front profile and fracture surface was unlike that seen for the other two specimen types.

The two major factors affecting the corrosion fatigue crack propagation rate in the heat treated specimens discussed above must surely be the hydrogen produced by the cathodic protection potential of -1400 mV (S.C.E.) and the high hardness value produced by the thermal regime endured by the specimens prior to testing. This thermal treatment gave an overall hardness of 380 $\pm$ 8 Hv and resulted in a very fine tempered martensite/lower bainite structure reminiscent of the parent plate microstructure, the one difference being that the prior austenite grain size was bigger for the heat treated specimens. Although the hardness of the heat affected zone material was found to peak at 435 Hv in the area of the final weld pass, tests showed that in the region of the actual fatigue path the hardness never exceeded 307 Hv. Therefore the 380 Hv of the heat treated material was by far the highest for any of the microstructures subjected to corrosion fatigue under severe cathodic overprotection conditions. As discussed earlier, it is believed that this hardness value indicates a material yield strength in the region of 1000 N/mm^2. This puts the material firmly into the strength level bracket where stress corrosion cracking should be a problem under conditions of forced hydrogen charging. This proved to be exactly the case, as can be seen by the Paris plots obtained for the heat treated specimens. Figure 96 shows that apart from the initiation region the fatigue crack propagation rate was greater than 10^{-6} m/cycle and the overall shape of the Paris plot is typical of that produced by stress corrosion dominated crack propagation behaviour. Table 21 shows how much quicker the fatigue crack growth rate was in terms of cycles to failure for specimens with their crack sides covered.

Specimen	Average cycles to failure (-1400 mV S.C.E.)
Parent Plate	12800
H.A.Z.	8400
Heat Treated	4400

Table 21. Comparison of average cycles to failure (specimens with crack sides covered)

This comparatively quick time to failure was most likely the major reason why the fracture surfaces of the heat treated specimens cathodically protected at -1400 mV (S.C.E.) had so little calcareous deposit on them, since the thickness and density of deposit is not only potential dominated but also time dependent. This much reduced time from start of fatigue to final fracture may also give a clue as to why the crack front profile exhibited evidence of the crack growing faster at the edges of the specimen rather than in the middle. It has already been mentioned that the heat treated specimens are likely to show the greatest susceptibility to hydrogen embrittlement. It therefore seems likely that the areas which were subjected to the greatest amount of hydrogen will exhibit the fastest crack growth. From a purely logistical consideration it would be expected that for a cathodic protection potential of -1400 mV (S.C.E.), the surface of the specimen should see more hydrogen. This is because there will be an access restriction on the hydrogen generated at the surface stopping it from migrating to the interior of the crack. One other important factor, however, may hold the key and that is potential drop along a crack.

It is very interesting to consider results obtained for potential drop measurements on a medium-high strength steel (HY80) exposed to natural sea water by Congleton and Craig (Ref 130). In this work the potential drop down cracks of up to 13 mm in length were measured for control potentials in the range -1500 mV to 0 mV (S.C.E.). The results are summarized in table 22. It is worth considering these results due to the fact that 13 mm was approximately the start length of fatigue cracks in this project and also -1250 and -1500 mV (S.C.E.) are approaching the values of cathodic protection potentials used in this project. Turnbull and May (Ref 153) have also shown that at potentials between -700 and -1000 mV (S.C.E.) the potential drop is small. At potentials less than -1000 mV (S.C.E.) the potential drop increases markedly with increasing negative potentials and at a much greater rate than would be predicted from theoretical modelling. The

most likely explanation is that hydrogen bubbles, which can certainly be observed at potentials below -1000 mV (S.C.E.), create an additional restriction to mass transport and thus increase the potential drop (Refs 134, 135).

Bulk Applied Potential (mV S.C.E.)	Potential Drop (mV)	Specimen Potential at Crack Tip (mV S.C.E.)
-1500	+495	-1005
-1250	+560	-690
-950	+269	-681
-700	+37	-663
-500	-162	-662
-250	-360	-610
±0	-500	-500

Table 22. Specimen potential and potential drop for a 13mm long fatigue crack (Ref 130)

The basic cause of any variation in the potential of a metal or alloy with distance along the length of a crack can be attributed to the highly resistive path to current flow offered by the solution within the enclave. This highly resistive path to current flow causes the current density on the walls of the enclave to be significantly lower than on the outside exposed surfaces.

It can be seen therefore that under the conditions of severe overprotection and hydrogen sensitive material as encountered for the heat treated specimens, the formation of a crack front profile where the outside grows faster than the inside may not be as anomalous as it first seemed. It may indeed be the case in the results reported for this project that when the cathodic protection potential on the surface was -1400 mV (S.C.E.), it may have been considerably lower towards the middle of the crack front. This situation was not apparent for parent plate tests nor the heat affected zone tests. It was only when the very hydrogen embrittlement sensitive material of the heat treated specimens, coupled with the limited access situation (encountered by all specimens), was tested that the crack front profile changed. With hindsight it is easy to say that it would have been nice to compare the crack front profile for heat treated specimens which had not been so severely overprotected. However, the number of these specimens was limited and it was not possible to do so.

It is now possible to discuss table 19 (page 139) and figure 104 (page 205) in relation to all of the microstructures tested under the various conditions of corrosion fatigue. Yokobori (Ref 154) was the first to propose the existence of a relationship between the Paris exponent m and constant C of the form:

$$m = a\ln C + b$$

This relationship has been verified for many materials and is now generally accepted. Figure 104 has been produced from the C and m data found in table 19. Of the six data lines plotted, three are the results from this project and the other three are extrapolations from work by Bathias (Ref 131, fatigue of steel in air), Tanaka (Ref 132, fatigue of steel in air) and Thompson (Ref 120, corrosion fatigue of BS 4360:50D type steel in artificial sea water).

The results generated from this project are presented differently from the results of Thompson because it was found that the three microstructures tested, namely parent plate, heat affected zone, and heat treated material, produced three separate C against m plots as opposed to them all lying on one line.

Several major points can be gleaned from the data presented in figure 104. These are:-

(1) With regards to the results obtained in this study, it can be seen that each line follows the same general trend of aggressive environment (severe overprotection) characterised by low m, high C, and less aggressive environment (free corrosion/ near cathodic protection) characterised by high m, low C. This trend was further supported by the fact that values for parent plate in-air (arguably the least aggressive environment) exhibited the highest m and lowest C values of all specimens.

(2) As the hardness and strength of the microstructure increases there is a tendency for the m value to decrease. This trend is consistent with the suggestion by Maddox (Ref 133) that increasing the yield strength reduced the m value in the Paris equation. It must be noted here, however, that work by Tanaka (Ref 132) on various ductile steels in air has shown that the reduction in m with increasing yield strength is correct only for intermediate strength steels.

(3) When comparing C and m values in air for N-A-XTRA 70 and BS 4360:50D, the following values were obtained:

N-A-XTRA 70	$m = 3.05$,	$C = 5.34 \times 10^{-12}$
BS 4360:50D	$m = 2.53$,	$C = 5.32 \times 10^{-12}$

The figures for BS 4360:50D are mean data from U.K.O.S.R.P. (Ref 120).

(4) The figures present in point (3) show that as the material strength increased (N-A-XTRA 70 yield strength = 723 MN/m^2, BS 4360:50D yield strength = 338 MN/m^2), the value of the constant C remained almost static whereas the exponent m changed considerably. This would seem to agree with the general belief that m is material dependent.

(5) With reference to the parent plate line, it can be seen that the value of the constant C changed by almost 5 orders of magnitude when comparing the least aggressive (in-air) with the most aggressive (-1400 mV S.C.E.) environment. This would seem to agree with the general belief that C is environment dependent.

(6) As the hardness and strength of the microstructure increases, there is a tendency for the C against m line to shift towards lower m and higher C values. The overall length of the line was also found to reduce. This seems to suggest that the dependence of C on environment reduces as the material strength increases.

(7) The plot for parent plate specimens in this project is reasonably parallel to those of Bathias and Tanaka. However, for the heat affected zone and heat treated material the slopes of the lines decrease. This would seem to suggest that the parameters a and b in the relationship

$$m = a\ln C + b$$

are dependent on microstructure and strength of material. It has been shown by Bathias (Ref 131) that the coefficient b varies with Young's modulus.

4.10 Final assessment

It is finally worth commenting on how readily these results can be extrapolated to conditions experienced in the real world. As discussed previously some doubt has been raised as to how much faith can be placed in results generated at extremely high frequencies. The frequency of 0.1 Hz for this project was chosen in order to mimic the frequency of loading expected to be experienced by offshore structures. It is interesting to note results obtained by Atkinson and Lindley (Ref 144) for A533-B pressure vessel steel immersed in aerated 3% sodium chloride or distilled water. These results show that a definite peak occurred in growth rate as a function of cyclic frequency. The critical frequency at which maximum environmental enhancement of growth rate occurred was in the range 0.01 to 0.1 Hz. This can be seen in figure 135.

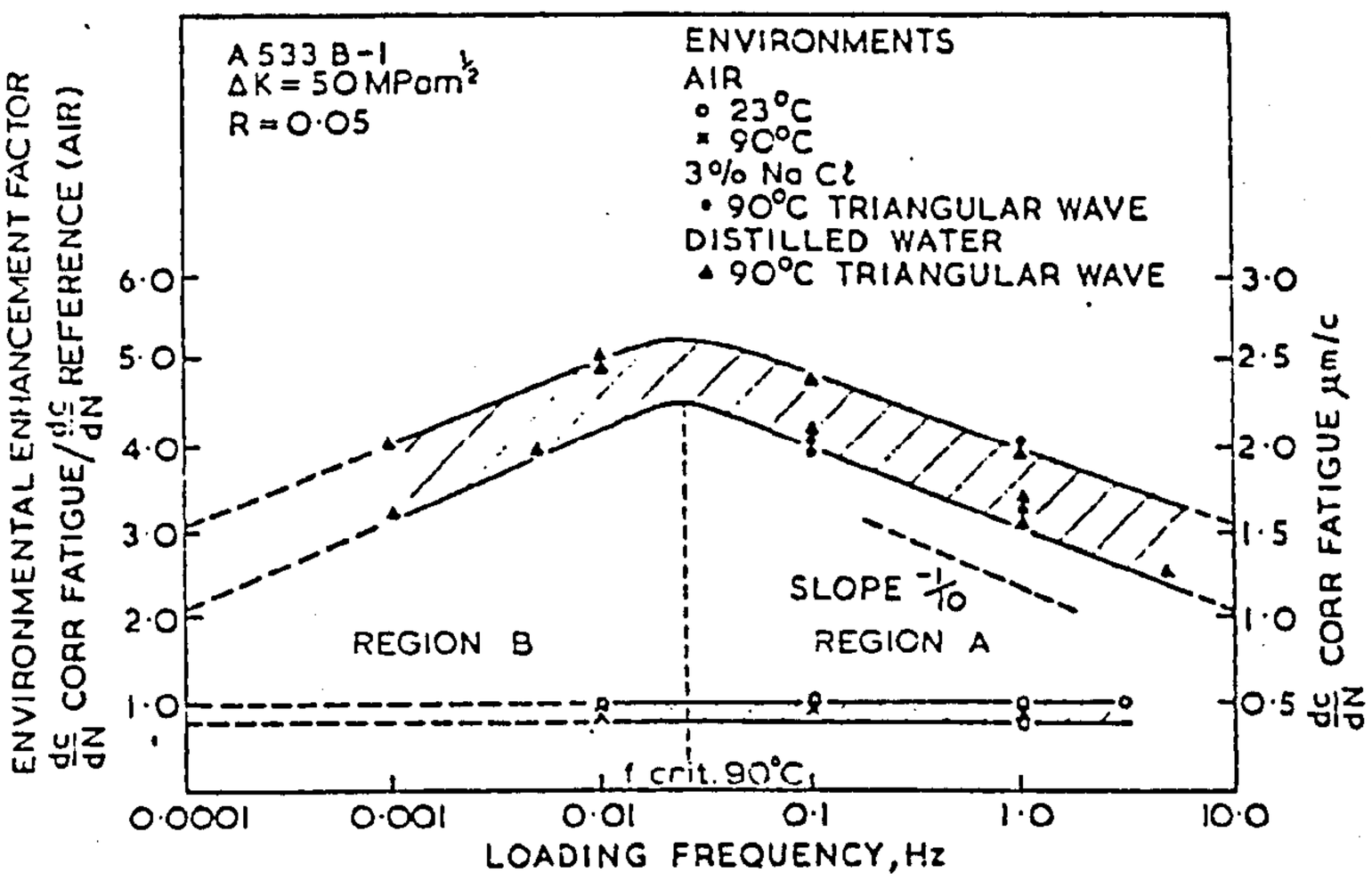

Figure 135. The effect of loading frequency on crack growth rates in A533-B steel (Ref 144)

Interesting as they are, the above results leave themselves open to critisism if they are to be used with reference to offshore structures. The fact that they were produced in 3% sodium chloride solution or distilled water means that they cannot be totally representative of what may happen in real sea water. For obvious reasons, any effects of calcareous deposits or submarine growths will not be present and it is therefore recommended that at least synthetic sea water should be used for corrosion fatigue experiments if real sea water is not available.

By using S.E.N. specimens which had their crack sides covered it was hoped to simulate the conditions found when a thumb-nail crack propagates under corrosion fatigue. If we are relating the results generated in this project to a typical offshore situation such as the failure of a tubular member due to corrosion fatigue, then it is worth commenting on the viability of the specimens used.

In the early stage of crack growth the crack profile will indeed be thumb-nail, as can be seen in figure 136(a), with sea water access only from the mouth of the crack.

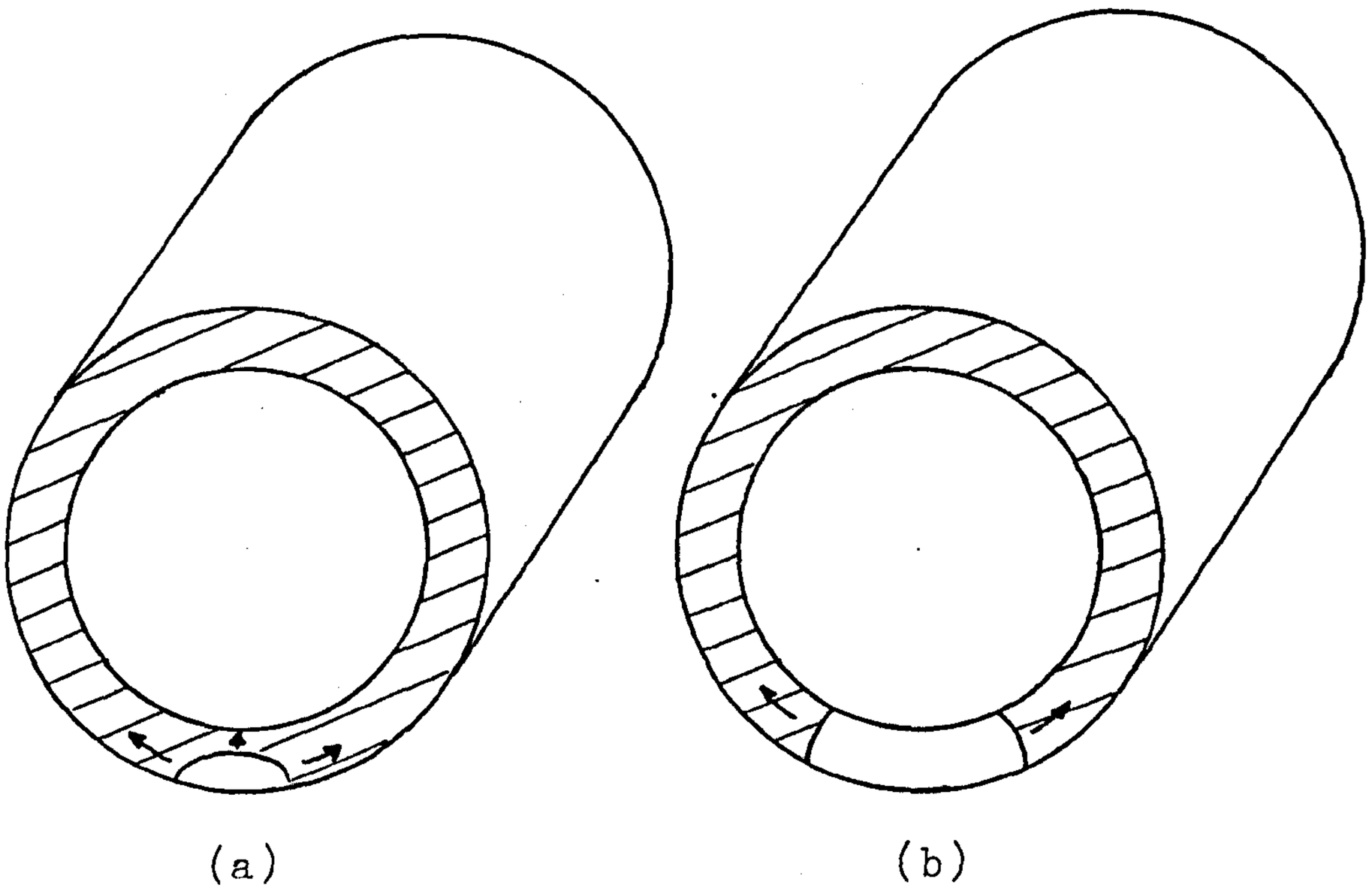

(a) (b)

Figure 136. Crack profile

However, after a certain time the crack will have grown completely through the thickness of the member. In this case the member will flood and will allow sea water ingress from both sides of the crack. This is similar to the standard S.E.N. specimen profile. If this argument is followed to the stage where the tubular member fails, it can be seen that the majority of the corrosion fatigue crack's life will be spent with the profile shown in figure 136(b).

It must be hoped, however, especially in the wake of the Alexander Kielland disaster, that all cracks on actual offshore structures would be detected and repaired, or at least monitored, whilst they were still in the thumb-nail stage.

From this project it was impossible to say how beneficial calcareous deposits were in terms of crack wedging. Since

the R ratio for all tests was 0.6 the crack would never fully close, thus wedging would not occur. It is also possible that the rate of crack advance driven by hydrogen embrittlement was greater than the rate of formation of deposit in the overprotected specimens and thus any calcareous wedge would never fully bridge the crack. Another possibility, and in the author's opinion a more likely one, is that Scott and Silvester's proposal for calcareous deposits mechanically interfering with crack closure and reducing the crack propagation rate (Ref 40) is somewhat optimistic. If infact wedging does take place for S.E.N. type specimens under laboratory conditions, then it is the author's opinion that the effect would be minimal on full-sized offshore structures, especially in relation to the thumb-nail type cracks discussed above.

Thanks largely to research projects such as the U.K.O.S.R.P. there is an abundance of information on the corrosion fatigue behaviour of standard constructional steels such as BS 4360:50D. The same situation, however, does not exist for high strength low alloy steels such as N-A-XTRA 70. In order to ascertain the usefulness of both the data produced by this project and the actual steel tested the results must be compared with those produced for a steel such as BS 4360:50D. To this end figure 105 (page 206) was produced. The plots of log da/dn against log Δk are taken from data produced by Scott and Silvester (Ref 50). The frequency used was 0.1 Hz and in the case of free corrosion the sea water temperature was 5^{0} C. Although the R ratio was approximately 0.1 it is considered that this will not significantly affect any comparison with the results for N-A-XTRA 70.

Considering the in-air lines first, it can be seen that over the whole range of Δk the N-A-XTRA 70 offers a better fatigue performance than BS 4360:50D. This finding is similar to that observed by Callister, Hockenhull and Billingham (Ref 142) in tests on the same materials. This situation changes dramatically, however, when the two steels are considered in a sea water environment. As can be seen from figure 105, there is a complete reversal in the corrosion fatigue performance, in terms of crack propagation rate, for the two steels under conditions of free corrosion. It is clear that the superior fatigue properties in-air of N-A-XTRA 70 disappear when subjected to a more realistic offshore situation. Although no direct comparison was found for cathodic overprotection potentials in the region of -1300 to -1400 mV (S.C.E.), it is the author's belief that N-A-XTRA 70 would exhibit a worse corrosion fatigue performance than BS 4360:50D at these lower potentials. This is due to the fact that the higher strength of N-A-XTRA 70 would render it more susceptible to damage by the hydrogen produced at these potentials.

The overprotection potentials just mentioned also have a bearing on the results for the heat affected zone and heat

treated specimens tested in this project. As the vast majority of offshore structures are fabricated using various welding techniques it is important to know how welded material behaves with regards to cathodic protection. From this project it can be seen that for a high strength low alloy steel the H.A.Z. and heat treated material perform badly when subjected to cathodic overprotection. This is worrying in the fact that the most common type of fatigue failures initiate from the defects which are a natural consequence of welding, the crack then propagating through the weld metal or the H.A.Z. and parent plate. As shown by the results from this project, if the H.A.Z. has incurred an increase in hardness and strength then for H.S.L.A. steels problems of severe hydrogen embrittlement and increased crack propagation rates may occur.

For offshore structures care is needed when cathodic protection is used. Overprotection is obviously harmful not only in terms of increased crack propagation rates but also the hydrogen produced may cause disbonding of paint films. Largely because of the adverse effects on crack growth rate of cathodic polarisation to below -800 mV (S.C.E.), use of a slightly higher potential around -720 mV (S.C.E.) has been considered beneficial (Ref 155). This view should be examined carefully, especially in the light of results obtained in this project, because it has been shown that such a potential may not fully suppress corrosion of the steel.Even though potentials of -700 mV (S.C.E.) produced corrosion fatigue crack growth rates close to that of the in-air specimens, on full size structures preferential attack at welds may occur in areas with inadequate levels of protection. It may also be true that in real life cathodic protection may not be beneficial at all times. If the assumption is made that corrosion during periods of calm (where there is no mechanical resharpening of the crack tip) will blunt the crack, then in cases where cathodic protection keeps the crack tip sharp by suppressing the anodic dissolution mechanism the next period of storms will continue the crack growth immediately rather than having to first resharpen the crack tip.

4.11 Graphical results

All the graphical results for this project will be found in the following pages.

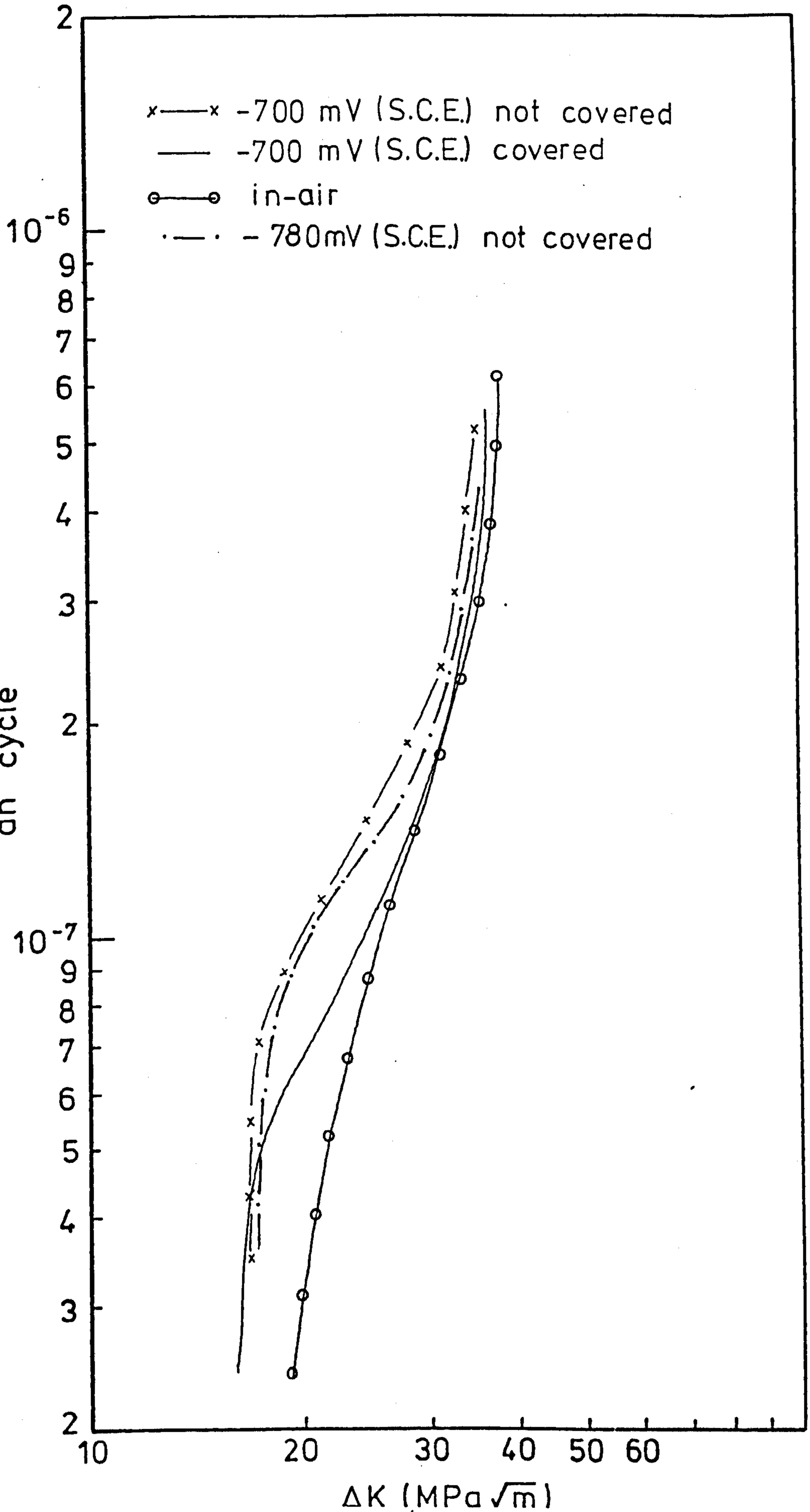

Figure 87. Graph of log da/dN against log ΔK for parent plate specimens (in-air, -700 mV S.C.E., -780 mV S.C.E.)

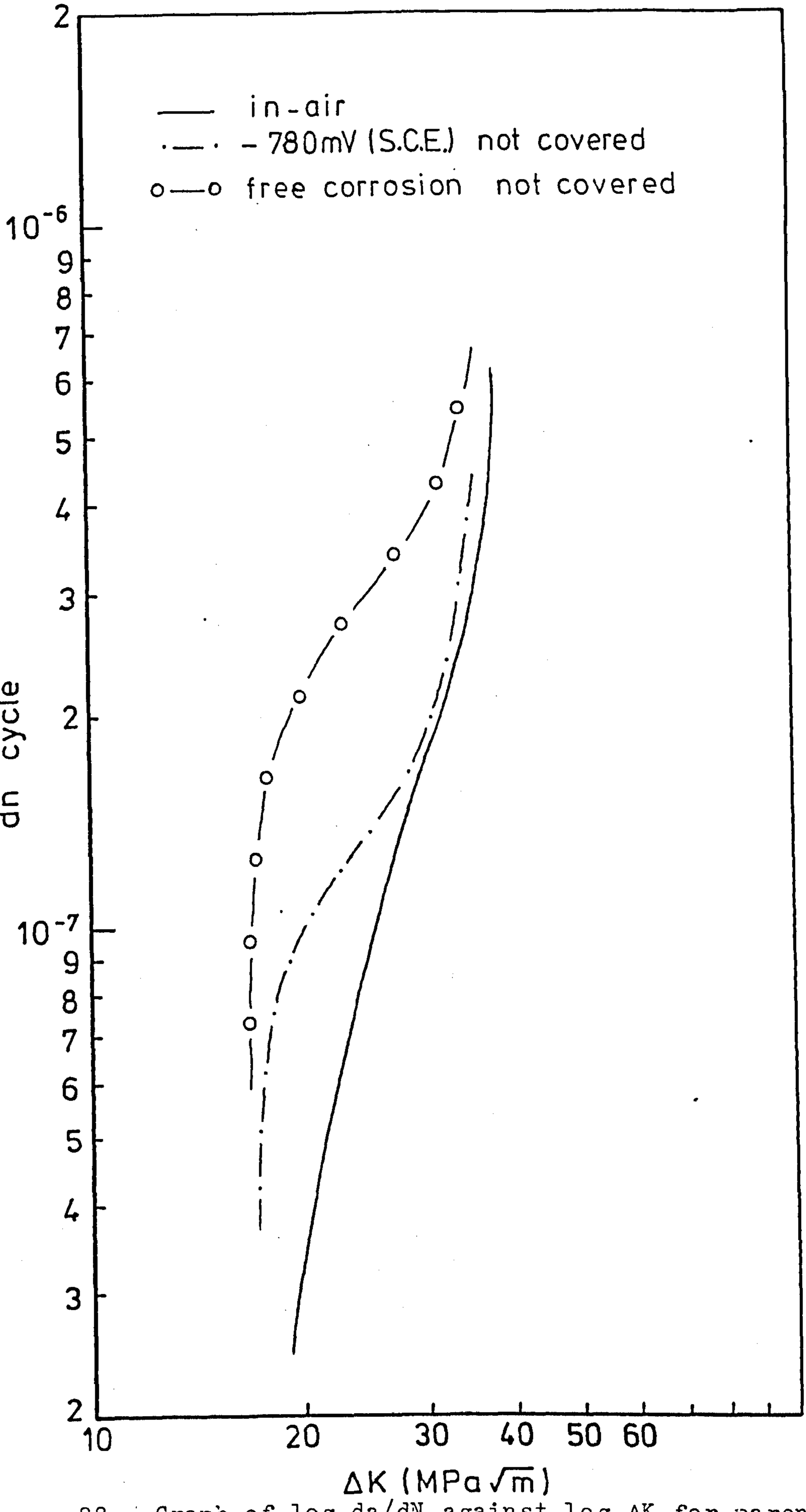

Figure 88. Graph of log da/dN against log ΔK for parent plate specimens (in-air, free corrosion, -780 mV S.C.E.)

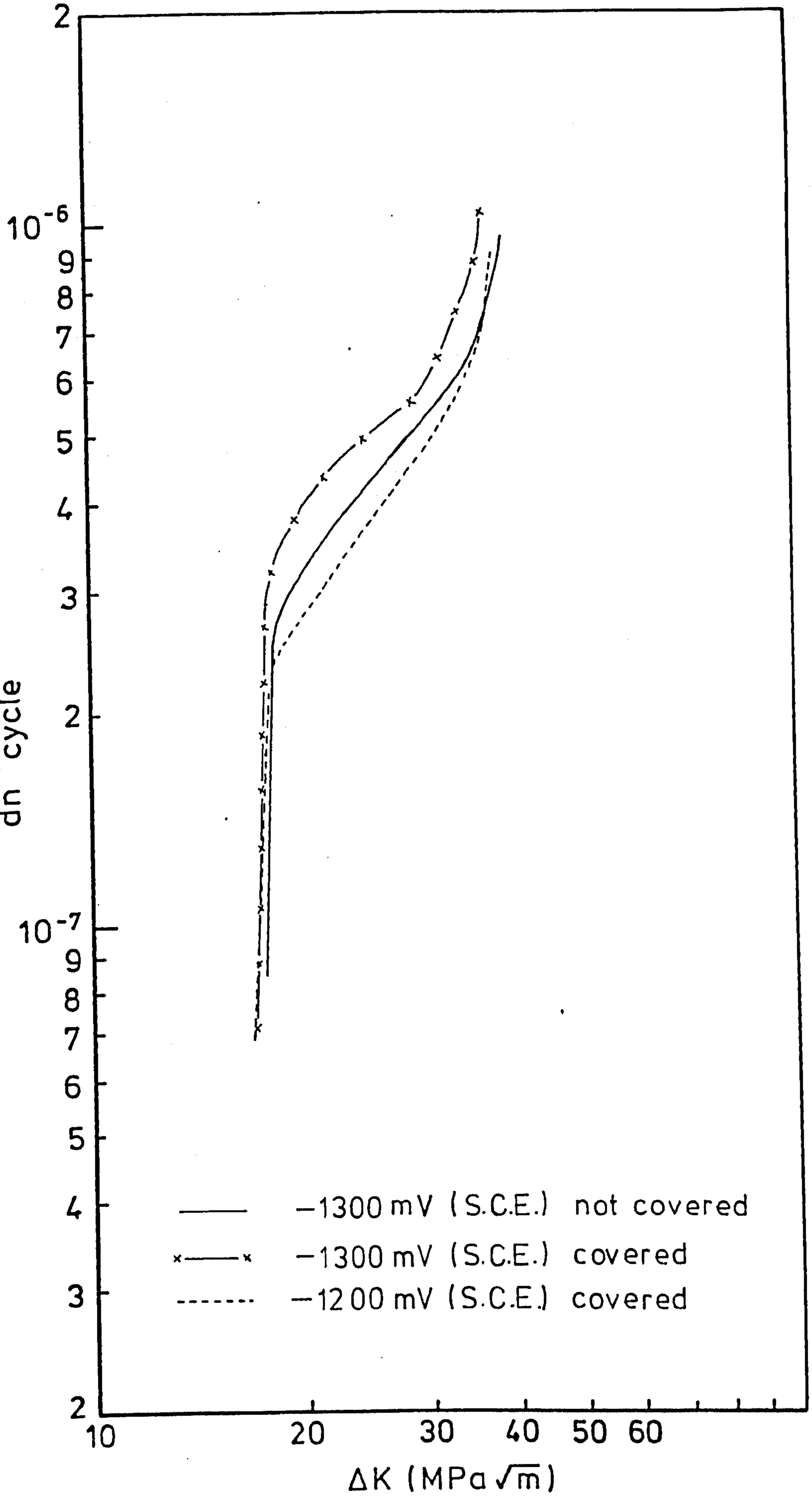

Figure 89. Graph of log da/dN against log ΔK for parent plate specimens (-1200 mV S.C.E., -1300 mV S.C.E.)

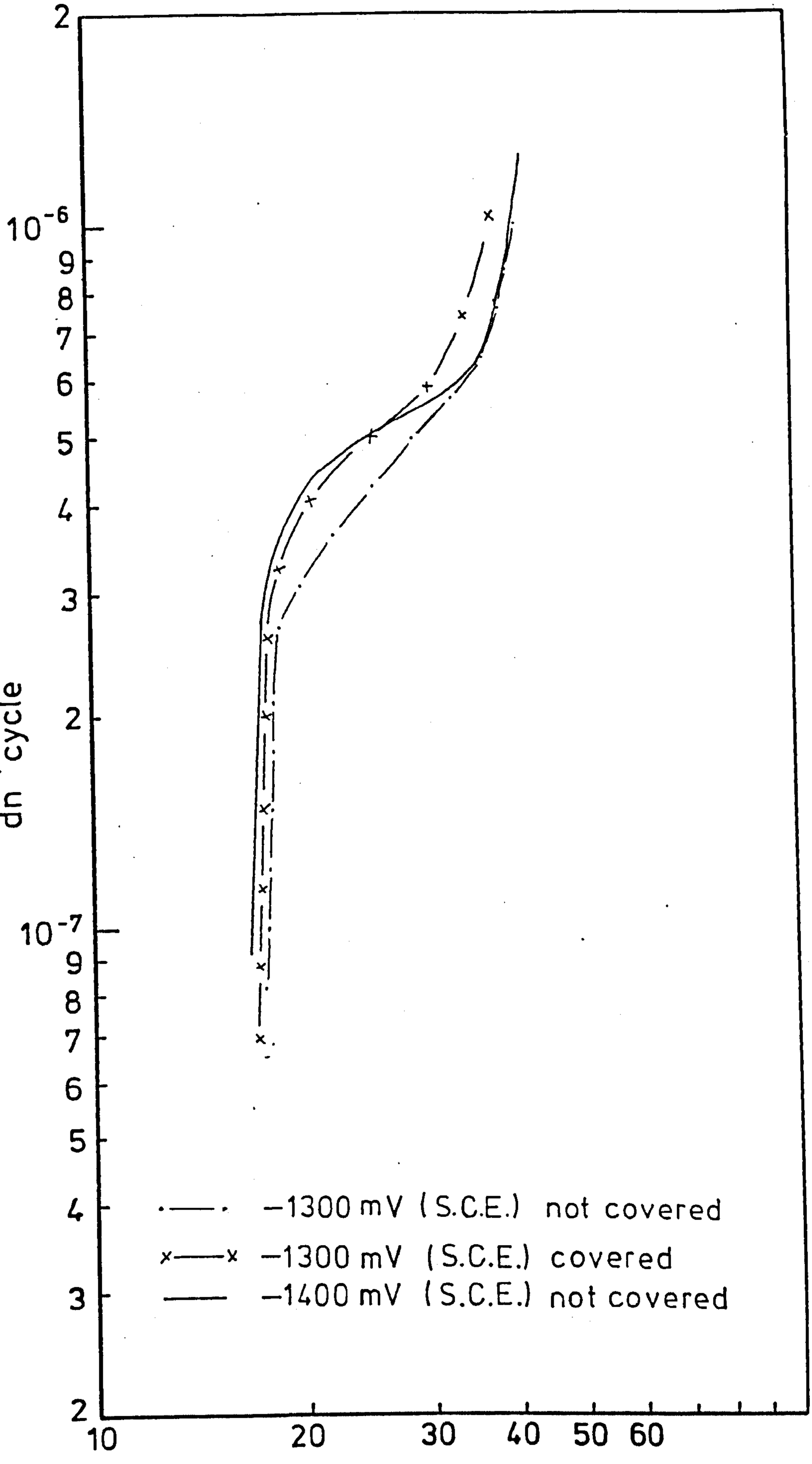

Figure 90. Graph of log da/dN against log ΔK for parent plate specimens (-1300 mV S.C.E., -1400 mV S.C.E.)

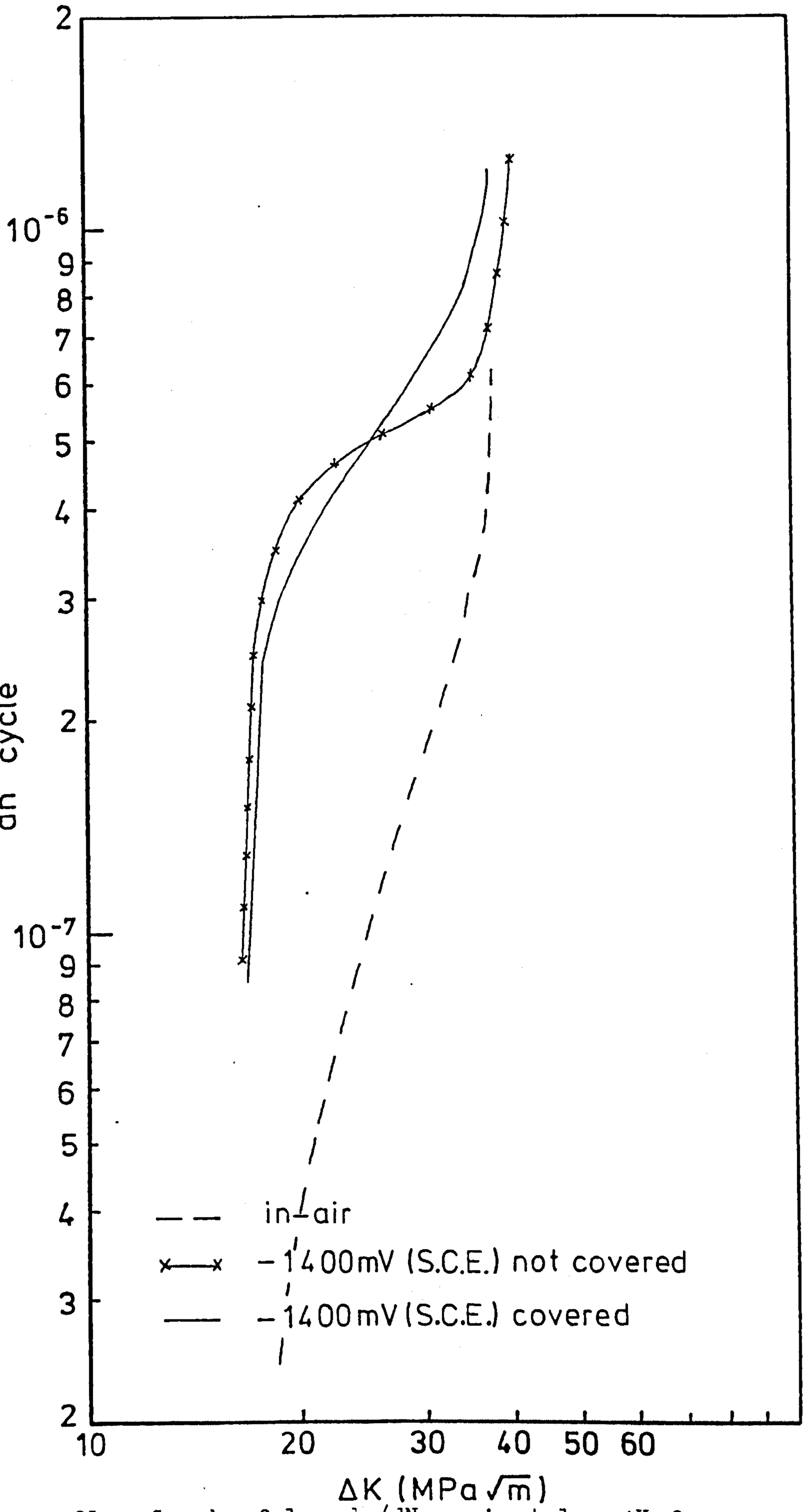

Figure 91. Graph of log da/dN against log ΔK for parent plate specimens (in-air, -1400 mV S.C.E.)

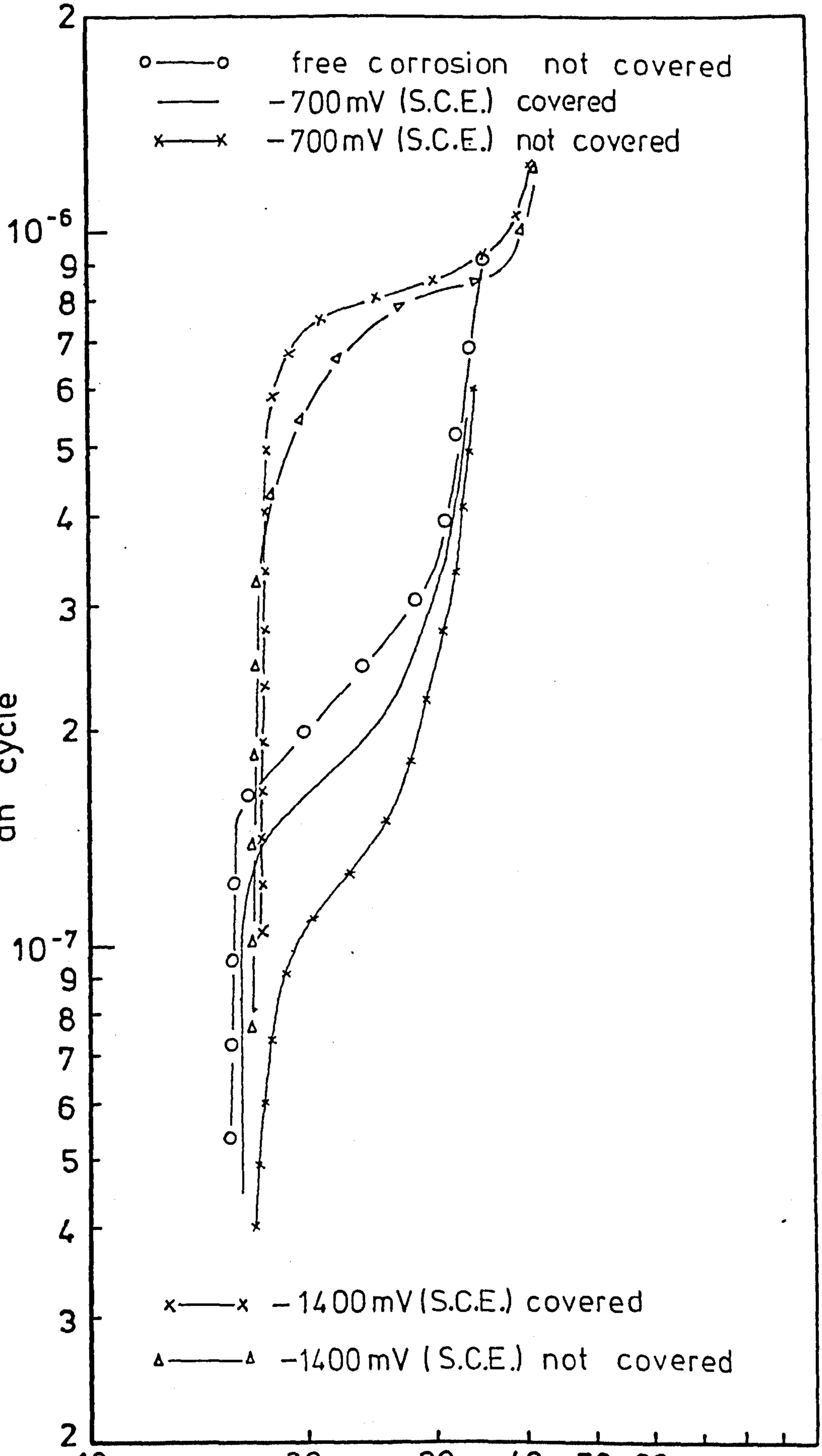

Figure 92. Graph of log da/dN against log ΔK for welded specimens (free corrosion, -700 mV S.C.E., -1400 mV S.C.E.)

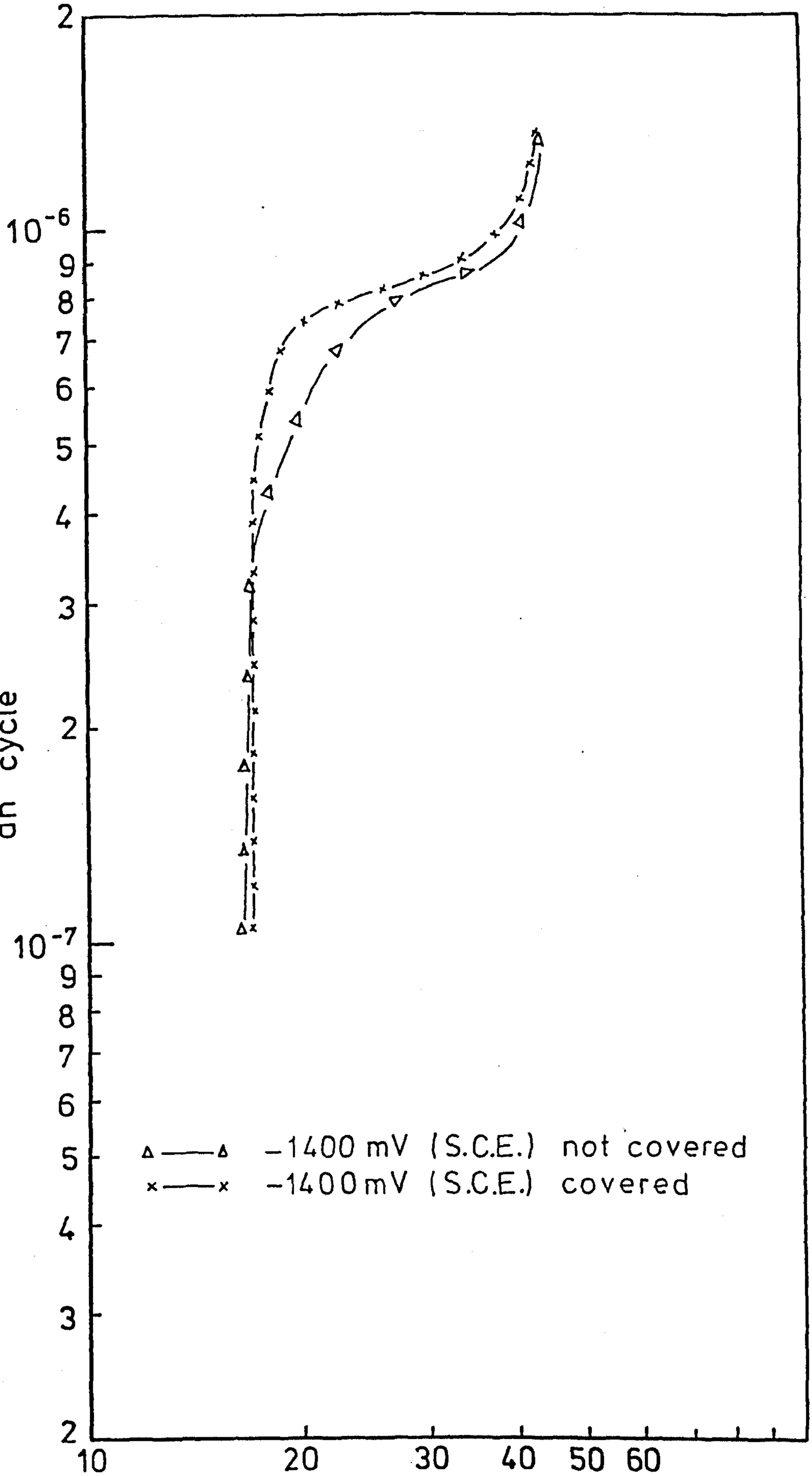

Figure 93. Graph of log da/dN against log ΔK for welded specimens (-1400 mV S.C.E.)

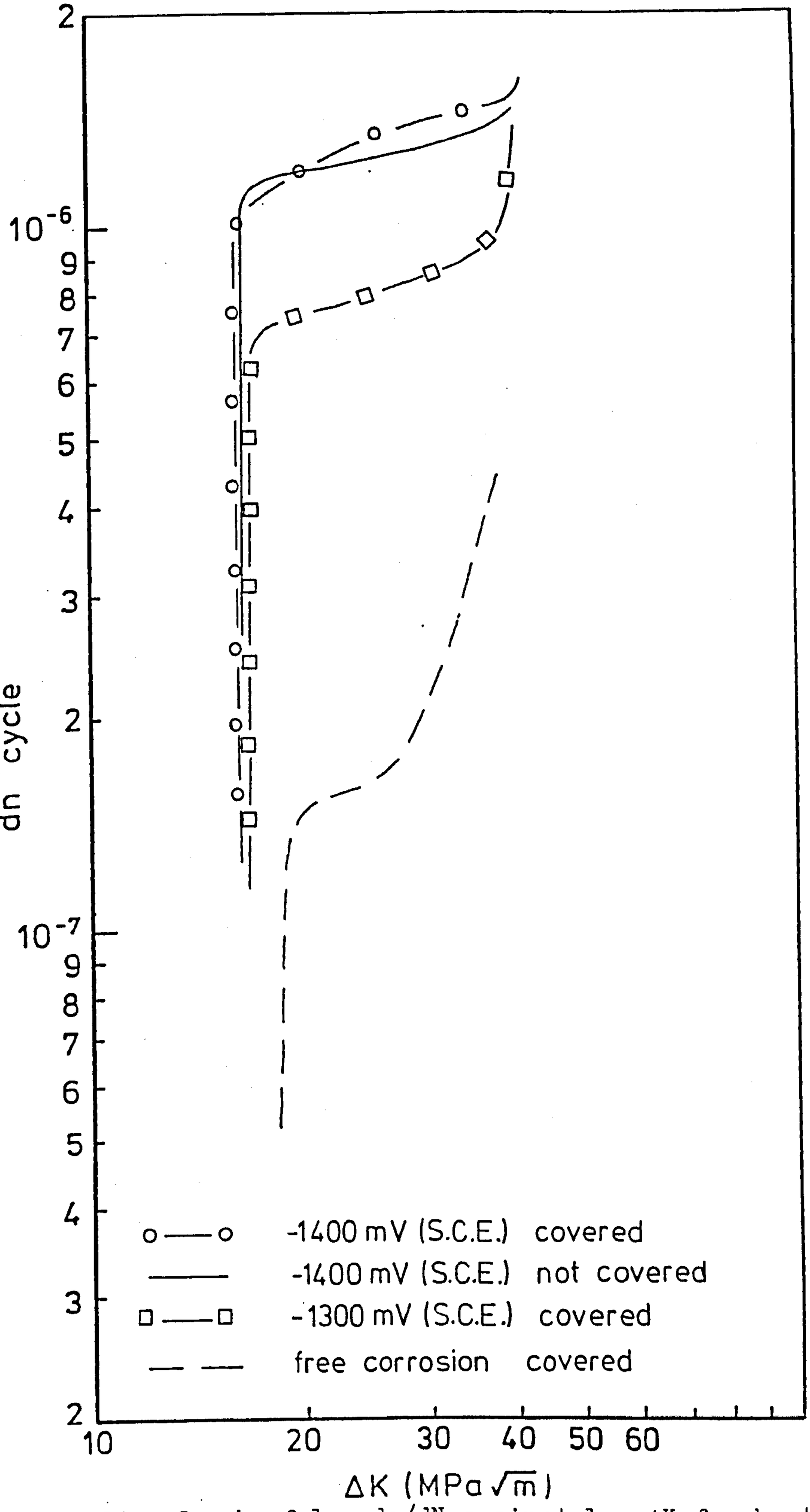

Figure 94. Graph of log da/dN against log ΔK for heat treated specimens (free corrosion, -1300 mV S.C.E., -1400 mV S.C.E.)

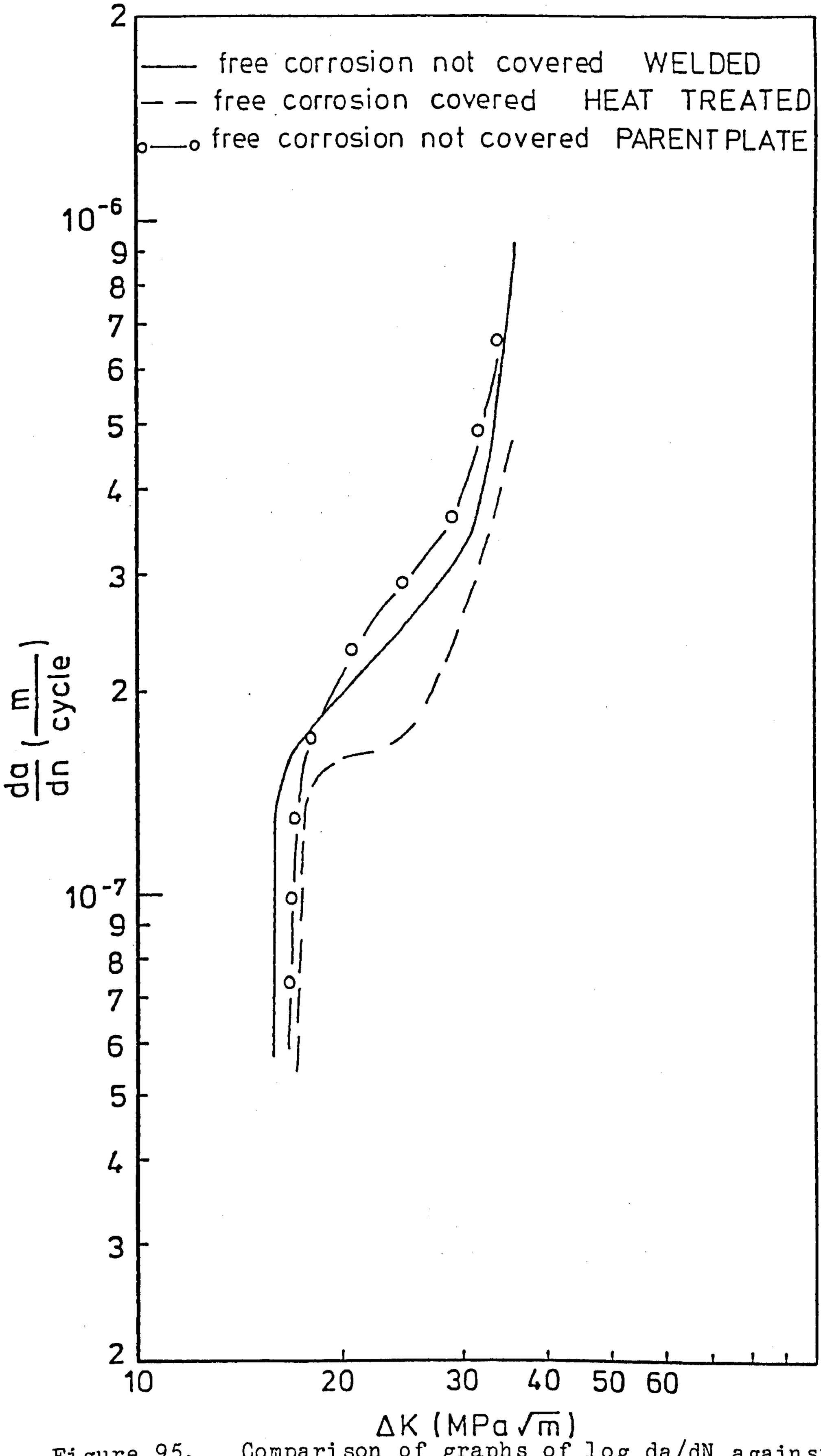

Figure 95. Comparison of graphs of log da/dN against log ΔK for different specimens (free corrosion)

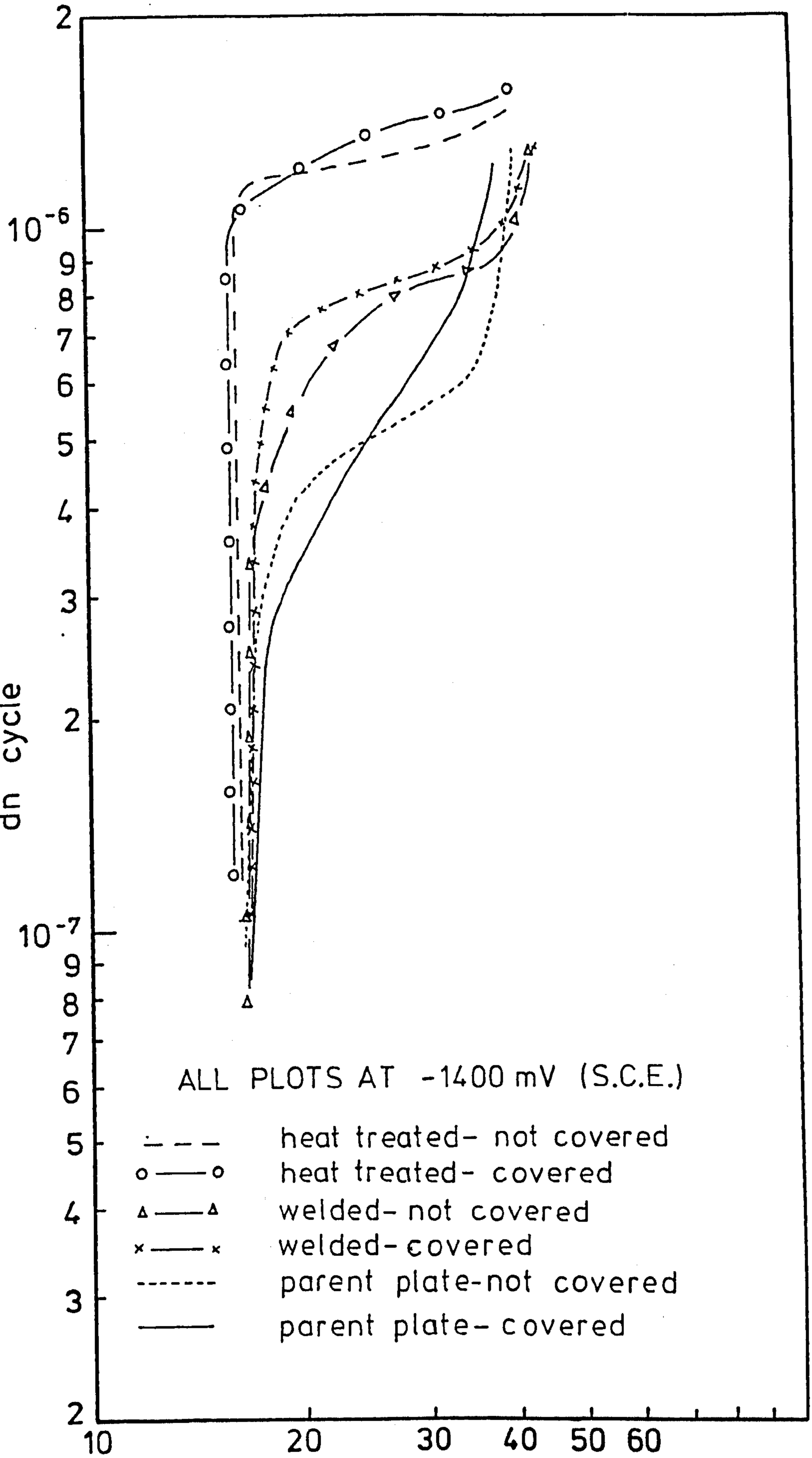

Figure 96. Comparison of graphs of log da/dN against log ΔK for different specimens (-1400 mV S.C.E.)

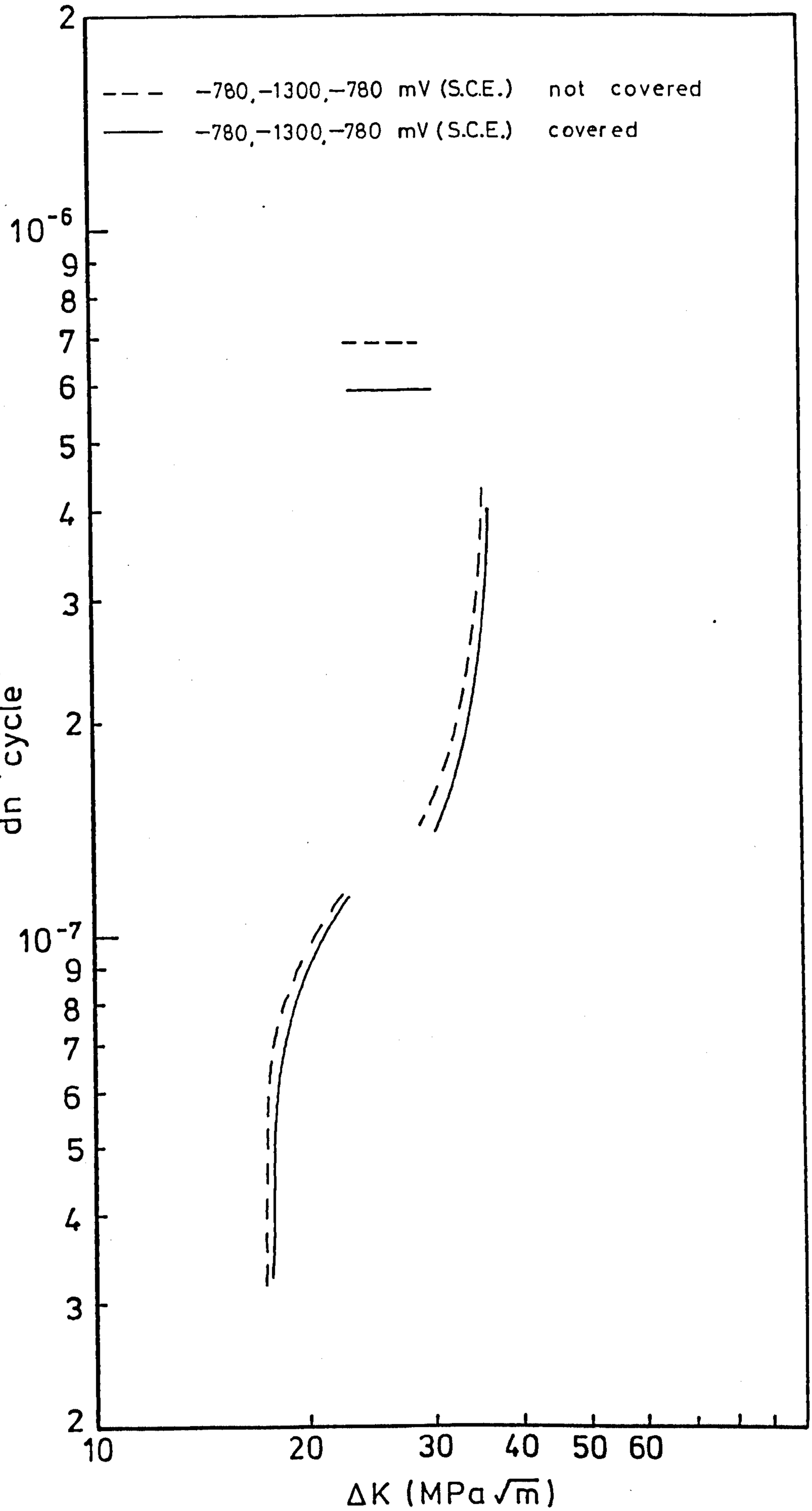

Figure 97. Graph of log da/dN against log ΔK for parent plate specimens (-780, -1300, -780 mV S.C.E.)

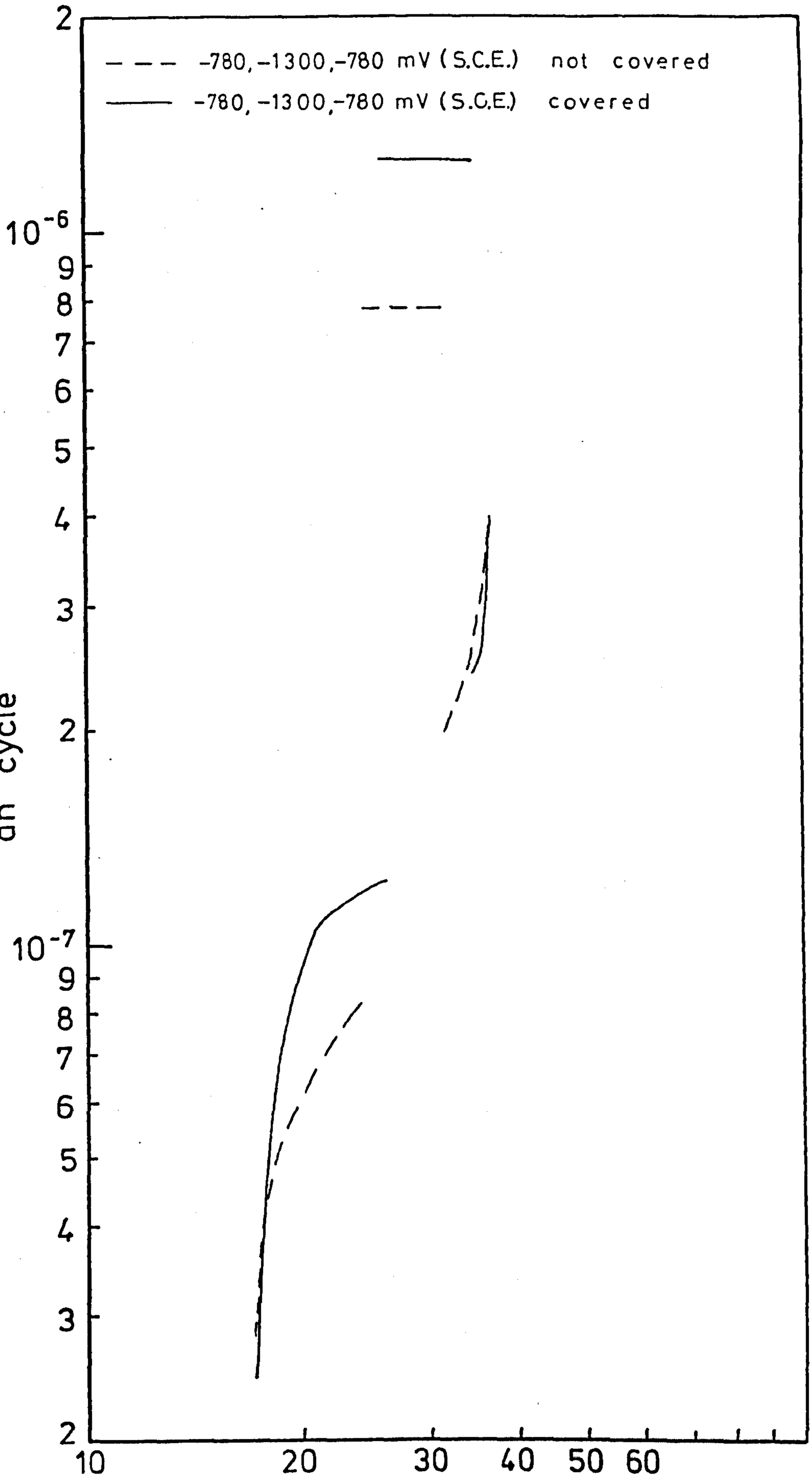

Figure 98. Graph of log da/dN against log ΔK for welded specimens (-780, -1300, -780 mV S.C.E.)

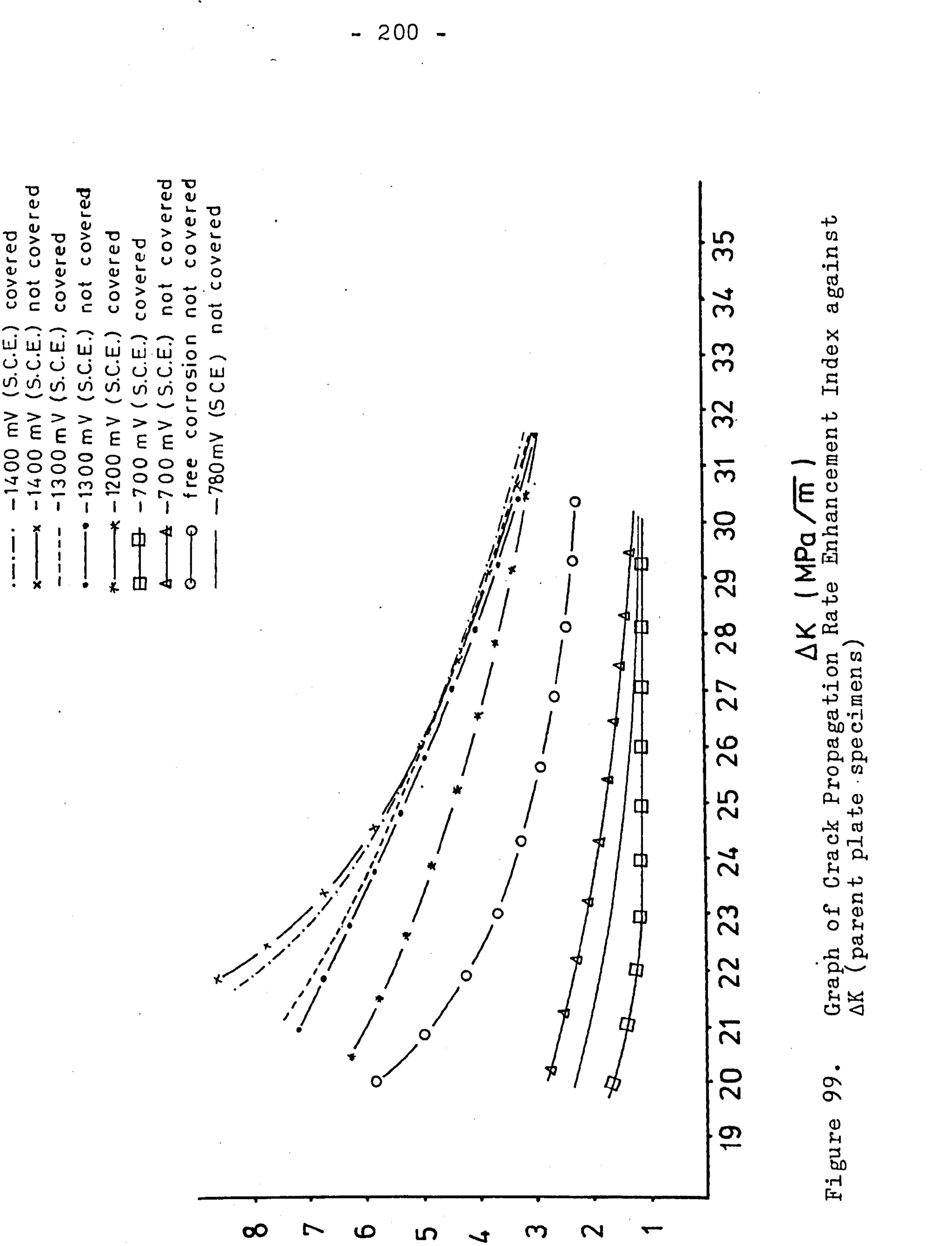

Figure 99. Graph of Crack Propagation Rate Enhancement Index against ΔK (parent plate specimens)

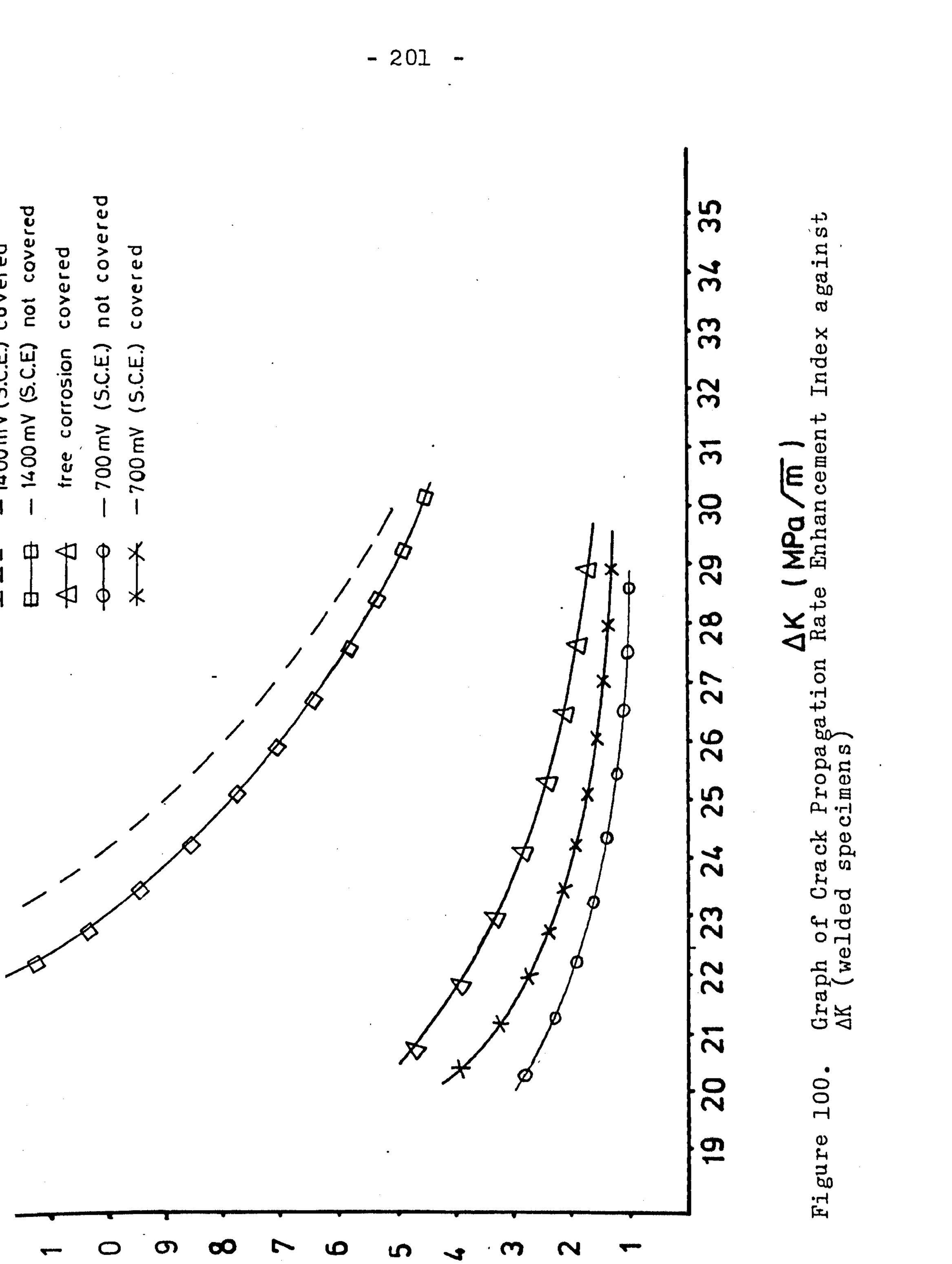

Figure 100. Graph of Crack Propagation Rate Enhancement Index against ΔK (welded specimens)

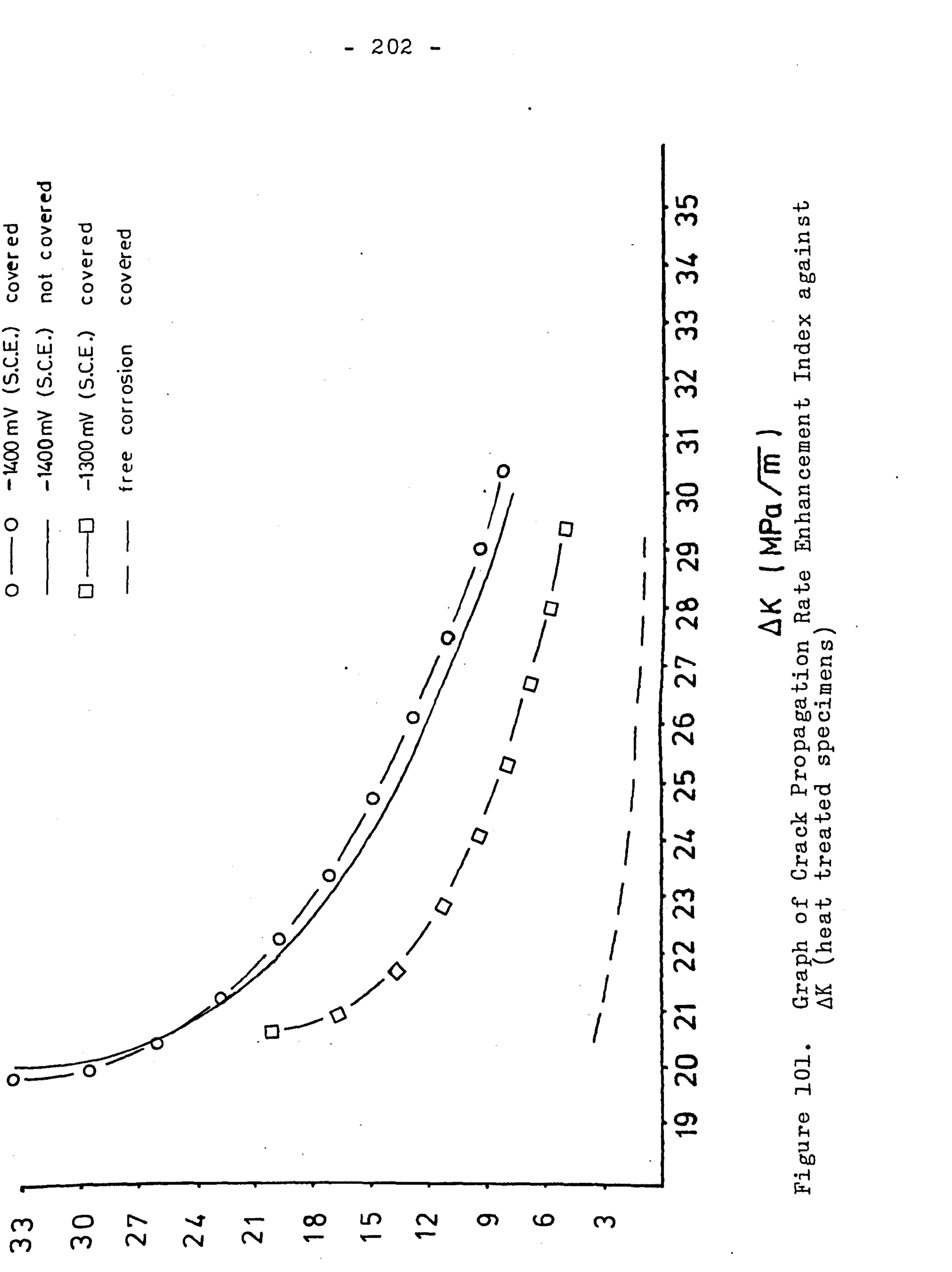

Figure 101. Graph of Crack Propagation Rate Enhancement Index against ΔK (heat treated specimens)

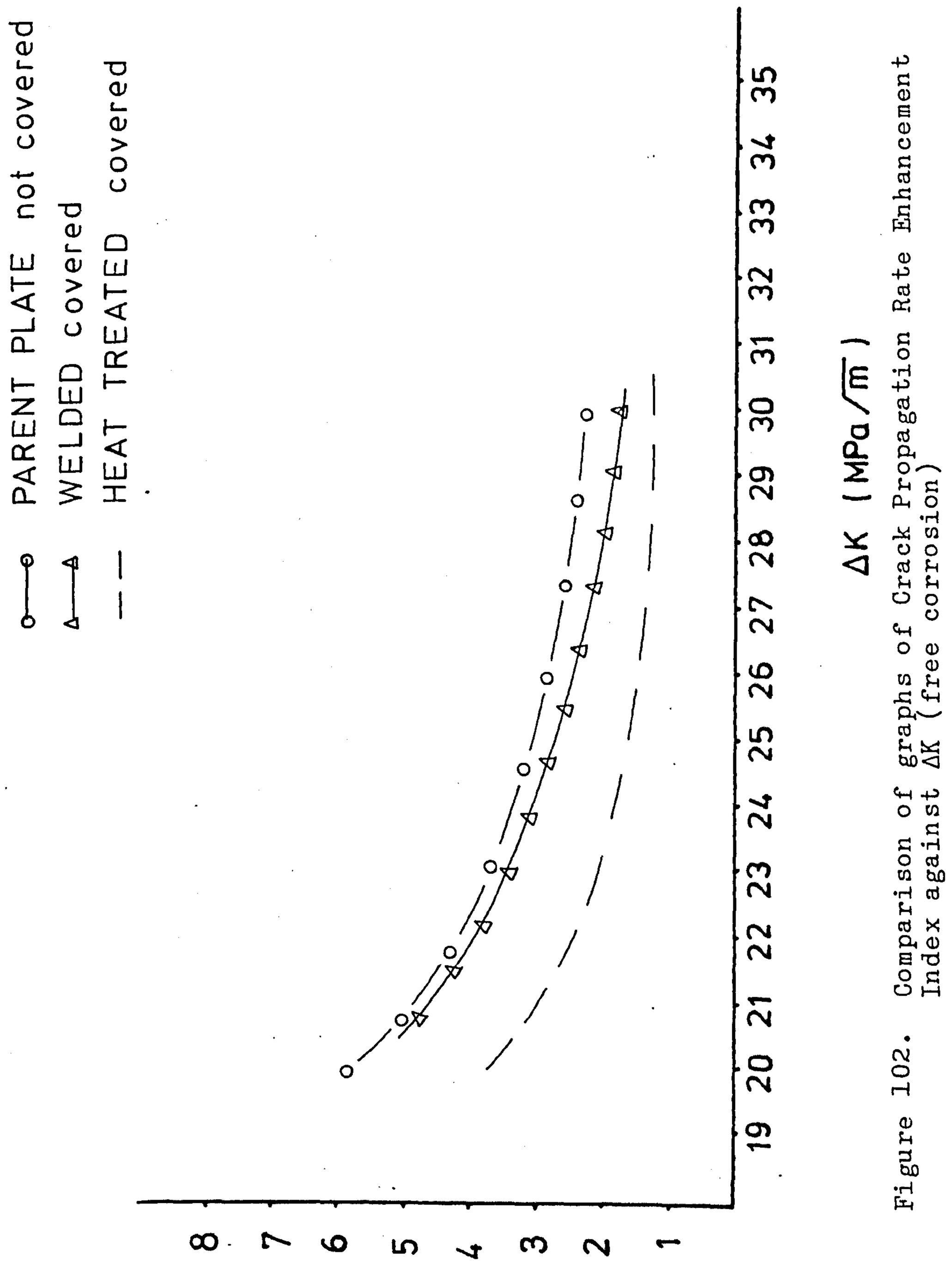

Figure 102. Comparison of graphs of Crack Propagation Rate Enhancement Index against ΔK (free corrosion)

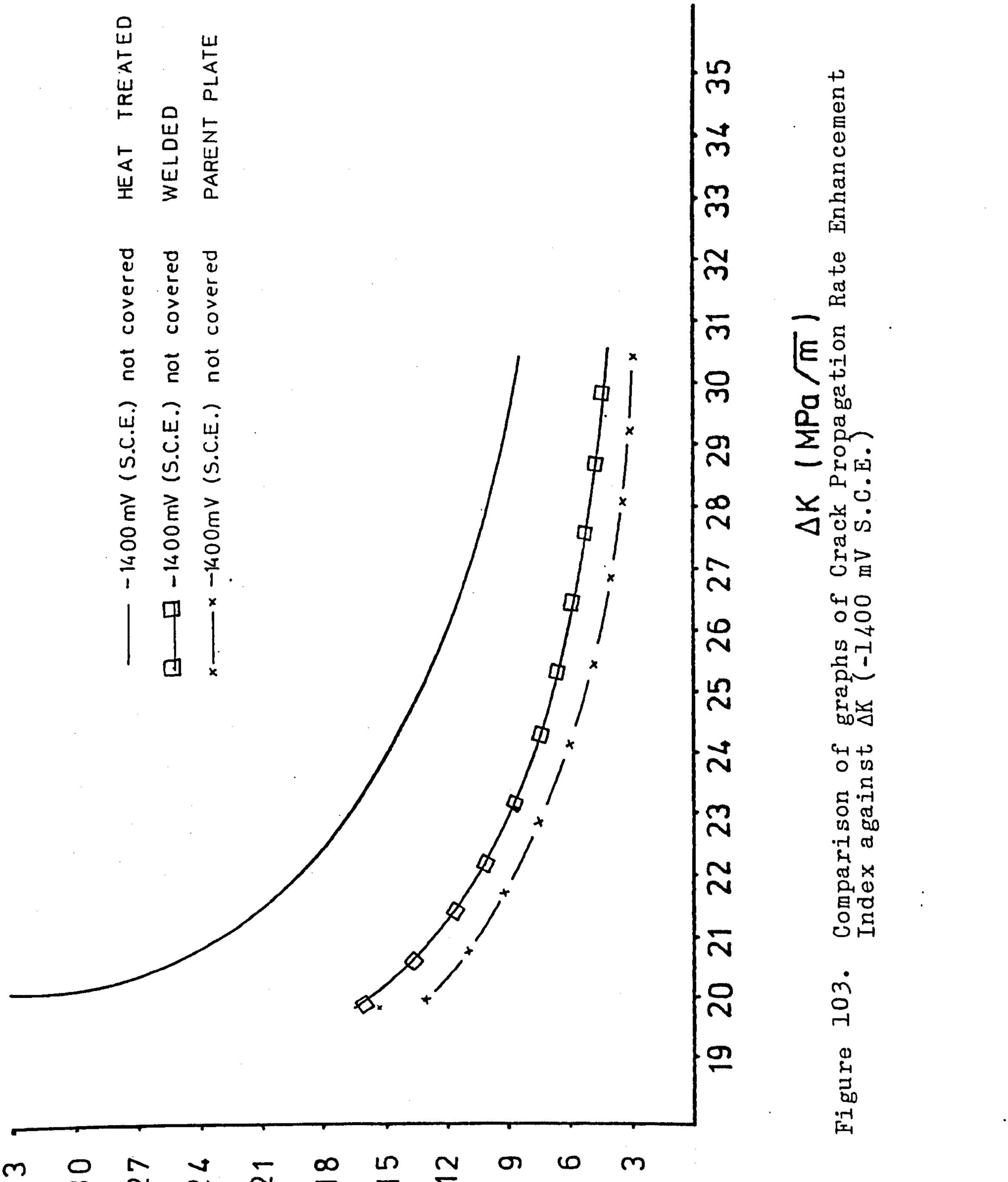

Figure 103. Comparison of graphs of Crack Propagation Rate Enhancement Index against ΔK (-1400 mV S.C.E.)

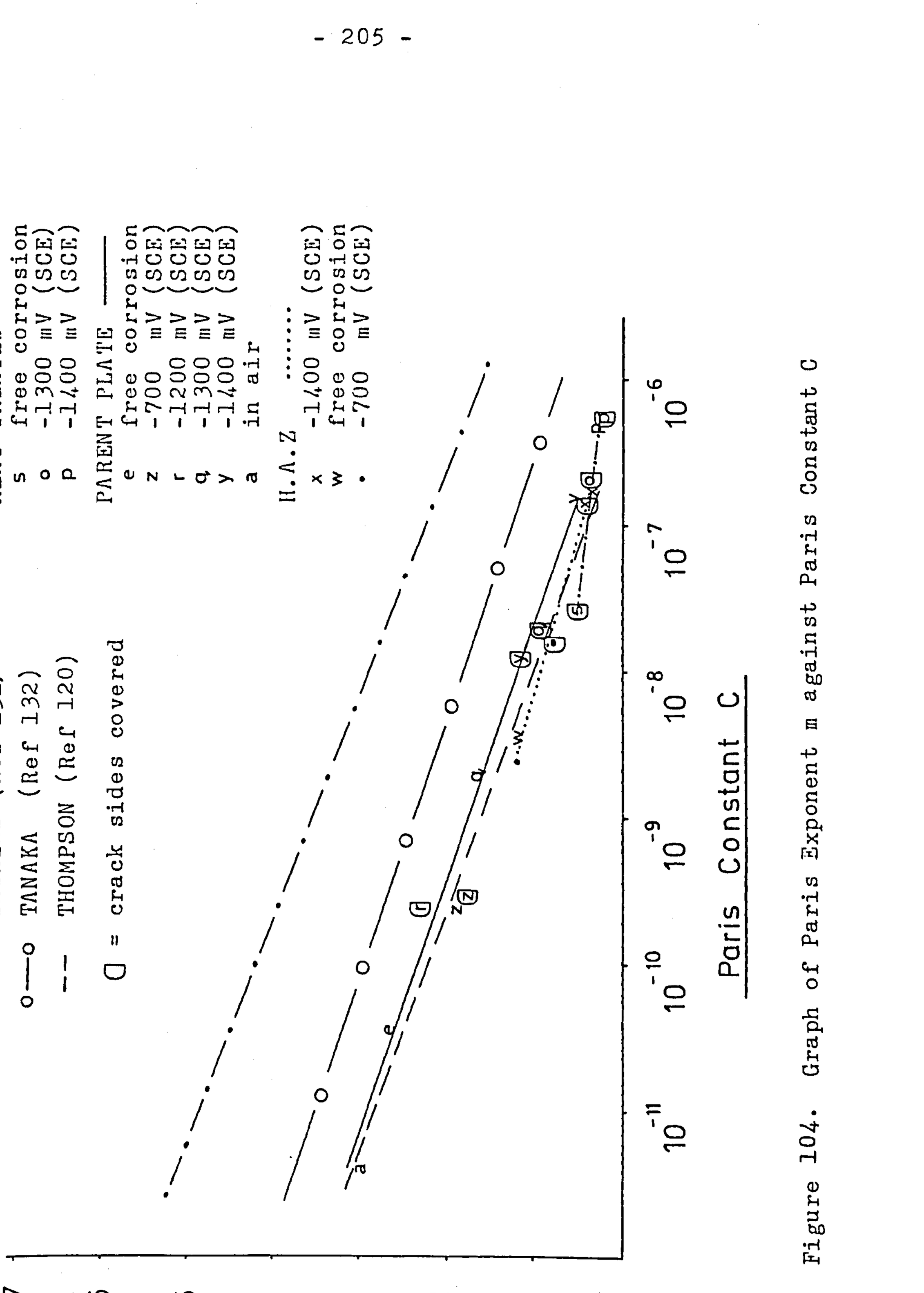

Figure 104. Graph of Paris Exponent m against Paris Constant C

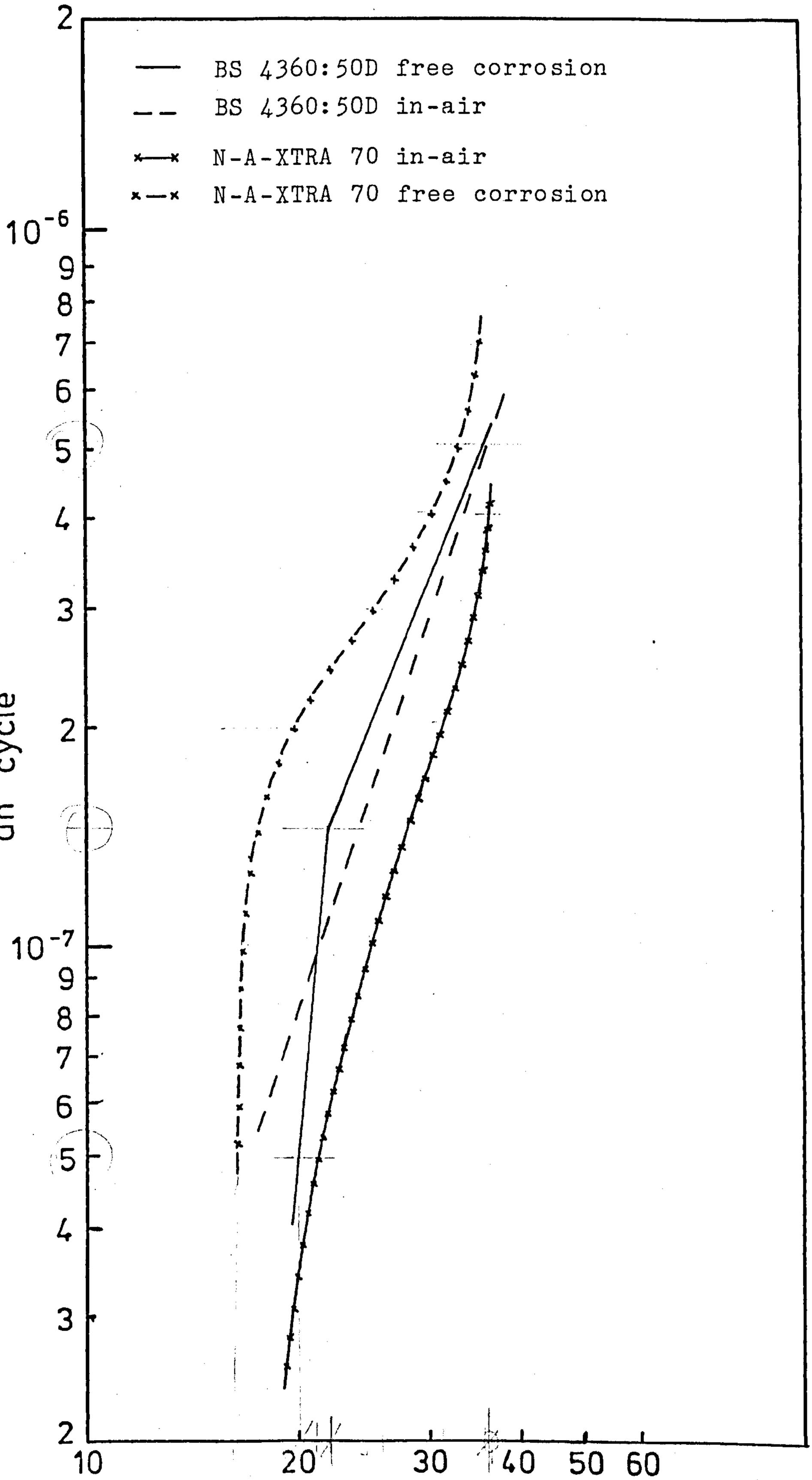

Figure 105. Comparison of corrosion fatigue crack propagation rates for N-A-XTRA 70 and BS 4360:50D

5. CONCLUSIONS AND FUTURE WORK

5.1 Conclusions

1) The optical method of crack growth measurement, involving the use of a travelling microscope, proved to be a very simple and effective means of obtaining crack extension data. Even under conditions of severe cathodic overprotection when the specimens became covered with calcareous deposits, no insurmountable problems were encountered which affected the accuracy of the readings or the ease of use of the equipment.

2) Except in the case of specimens fatigued in air, the computer analysis technique proved to be somewhat less than useful when it came to producing a reasonably accurate Paris plot. The least squares regression analysis program picked out the variability and scatter in the data points and accentuated them when working out the da/dN values. The computer method was, however, not the worst analysis technique. The secant method proved to be without peer in terms of failing to produce a recognizable Paris plot.

3) The graphical tangent to curve technique was found to be a simple, reliable and reasonably accurate method of obtaining corrosion fatigue crack growth rate data from experimental results of crack length against number of cycles. Even allowing for the problem of subjectivity, the technique was infinitely superior to either the computer or the secant method. Also, due to the reproducibility of results and the exceptionally low level of data scatter (especially when compared to the secant method), the technique generated a high degree of confidence in it as a dependable analysis tool.

4) The zirconium nitride particles found in the N-A-XTRA 70 microstructure, although they may interact with the advancing crack front locally, are not considered to have any great effect on the overall corrosion fatigue crack propagation rate.

5) The influence of cathodic protection potentials on parent plate N-A-XTRA 70 corrosion fatigue crack propagation rates is dependant on whether the specimens tested have their crack sides covered or not. As a general rule it can be stated that for small electronegative potentials (-700 mV S.C.E.),

specimens with their crack sides covered show a reduced corrosion fatigue crack propagation rate over specimens without their crack sides covered. For greater electronegative potentials (-1300, -1400 mV S.C.E.), specimens with their crack sides covered show an increased corrosion fatigue crack propagation rate over specimens without their crack sides covered. If specimens with their crack sides covered are taken to represent a typical thumb-nail crack, then the above results indicate that corrosion fatigue crack propagation data obtained from standard S.E.N. specimens are somewhat pessimistic for lower electronegative potentials and somewhat optimistic for higher electronegative potentials.

6) For all microstructural conditions tested, namely parent plate, heat affected zone, and heat treated material, the Paris curves generated for cathodic potentials of -1300 and -1400 mV (S.C.E.) were characteristic of stress corrosion dominated crack propagation behaviour. This was not totally unexpected given the strength of the steel used (723 MN/m^2), which is high enough to cause concern over stress corrosion cracking in the parent plate condition. For the H.A.Z. and heat treated material, where the strength levels may approach 1100 MN/m^2, it is expected that stress corrosion cracking behaviour would indeed occur, especially at severe cathodic overprotection potentials.

7) As a general rule it can be stated that for the three different microstructures tested under a cathodic protection potential of -1400 mV (S.C.E.), specimens without their crack sides covered exhibited better corrosion fatigue crack propagation behaviour than specimens with their crack sides covered.

8) Under conditions of severe overprotection (-1300, -1400 mV S.C.E.), heat treated material exhibited the worst corrosion fatigue crack propagation behaviour. Parent plate material proved to have the best behaviour, while the corrosion fatigue crack propagation behaviour of the heat affected zone was found to lie between that of the parent plate and the heat treated material. This general trend was true for both specimens with and without their crack sides covered.

9) Under conditions of free corrosion and for specimens without their crack sides covered, heat affected zone material exhibited better corrosion fatigue crack propagation behaviour than parent plate

material. This finding is in direct contrast to the situation observed in point 8. Heat treated specimens which had their crack sides covered proved to have a better corrosion fatigue crack propagation behaviour than either H.A.Z. or parent plate specimens which did not have their crack sides covered.

10) For a cathodic protection potential of -700 mV (S.C.E.), welded specimens with their crack sides covered exhibited higher corrosion fatigue crack propagation rates than welded specimens which did not have their crack sides covered. The reverse was found to be true for parent plate specimens.

11) For parent plate specimens with their crack sides covered, the corrosion fatigue crack propagation rate associated with a cathodic protection potential of -700 mV (S.C.E.) was closer to that generated by in-air fatigue than the rate produced by parent plate specimens cathodically protected to the theoretically correct potential of -780 mV (S.C.E.) without their crack sides covered.

12) For heat treated specimens under conditions of severe cathodic overprotection potentials (-1400 mV S.C.E.), the corrosion fatigue crack front was found to grow faster at the sides of the specimen than in the middle. This situation occurred for specimens with and without their crack sides covered. It is believed that the reason for this is due to the effect of greater hydrogen embrittlement on the outside of the specimen due to limited hydrogen access to the centre of the crack front and a potential drop situation. The high hardness associated with the heat treated specimens will result in the microstructure being more hydrogen sensitive.

13) Covering the crack sides of specimens is believed to cause a reduction in the pumping action of the crack and a reduction in the level of oxygen able to diffuse to the crack tip. It is anticipated that the lowering of the oxygen level causes the crack propagation rate of parent plate material to fall at low levels of cathodic protection by reducing the cathodic reaction. For high levels of cathodic overprotection and for material susceptible to hydrogen embrittlement, a reduction in oxygen increases the crack propagation rate by shifting the cathodic reaction to that of hydrogen production. There will also be less adsorbed oxygen on the material surface to interfere with hydrogen adsorption and hence absorption.

14) The reduction in the corrosion fatigue crack propagation rate at low levels of cathodic protection, arising from the reduction in the oxygen concentration implies that there is cathodic control (by reduction of O_2 to OH^-) of an anodic dissolution reaction at the crack tip. These results tentatively indicate that anodic dissolution is more important than hydrogen embrittlement at low levels of cathodic protection.

15) The Paris relationship, $da/dN = C\Delta K^m$, has shown itself to be a reliable tool in the analysis of corrosion fatigue crack propagation rate data for a high strength low alloy steel in the form of parent plate, H.A.Z. and heat treated S.E.N. specimens. It was found that several relationships of the form $m = a\ln C + b$ exist between the Paris exponent m and constant C, where a and b are dependant on material qualities. The constant C is influenced greatly by the effect of environment and cathodic protection, whereas the exponent m is influenced by the material microstructure.

16) Calcareous deposits formed on all specimens cathodically protected to potentials more electronegative than -700 mV (S.C.E.). The deposit morphology changed from a smooth, thin deposit at -780 mV (S.C.E.) to a thicker, more tenacious deposit at -1200 mV (S.C.E.). At -1400 mV (S.C.E.) the deposit was less well bonded to the specimen than at -1200 mV (S.C.E.), large flakes of deposit being dislodged from the specimen surface by hydrogen bubbles generated by the low potential.

17) The results from this project have shown that cathodic protection does not impart a corrosion fatigue crack propagation behaviour to N-A-XTRA 70 which is better than that produced by in-air fatigue. Only for parent plate specimens with their crack sides covered and subjected to a cathodic protection potential of -700 mV (S.C.E.), did crack propagation behaviour approach that of the in-air specimens.

18) When comparing the fatigue crack propagation rates of N-A-XTRA 70 and BS 4360:50D, it was found that for the in-air condition N-A-XTRA 70 exhibited a superior fatigue performance. For the free corrosion situation the reverse was true, with the higher strength material producing higher fatigue crack propagation rates than BS 4360:50D.

19) Overall the results of this project show that cathodic protection does have a profound influence on the corrosion fatigue crack propagation rates of parent plate, heat affected zone and heat treated material. Protection potentials of -700 and -780 mV (S.C.E.), whilst not reducing the crack propagation rate to that experienced in-air, did produce rates which were significantly better than those encountered for free corrosion. Severe overprotection was found to be very detrimental to all the microstructures tested, the effect increasing in severity with increasing microstructure hardness and strength.

20) Even though synthetic sea water has a composition similar to natural sea water, it does not contain the organic components of the latter, which might be important in corrosion fatigue. For this reason the present work should be viewed as a guide rather than a definitive study of the corrosion fatigue behaviour of N-A-XTRA 70 in sea water.

5.2 Recommendations for future work

1) In order to facilitate a direct comparison between the corrosion fatigue performance of a high strength steel such as N-A-XTRA 70 and BS 4360:50D, work should be carried out on the two materials using the same size specimens, same environment, same frequency, same loading regime and the same test rig if possible.

2) Painted specimens should be involved in a testing programme since painting plus cathodic protection is believed to be the optimum protection situation for an offshore structure.

3) No account was taken of variable loading during this project. It would therefore be useful to modify experimental techniques in future work to account for the effects of variable loading of the type expected to be encountered offshore.

4) Work should be carried out in the long transverse direction as opposed to the short transverse direction used for this project. This could be used to determine if the corrosion fatigue crack propagation behaviour of the material is different for cases when the fatigue crack has changed from the thumb-nail to the through-thickness condition.

REFERENCES

1. DEPT. OF ENERGY — Review of Information on the Fatigue of Tethering Systems for Tethered Buoyant Platforms, 1982.

2. ELIASSEN, S. & VALLAND, G. — Design rules for offshore cathodic protection systems. N.S.C. Conf., Inst. of Marine Engn., Vol. 91, 1979.

3. MADDOX, N.R. — Paper No. OTC 2051, Offshore Tech. Conf., Texas, 1974.

4. GURNEY, T.R. — Fatigue of Welded Structures. Cambridge Univ. Press, 1979.

5. HOCKENHULL, B.S. — Stress corrosion cracking and corrosion fatigue in offshore structures. Joint Offshore Conf., Feb 1976.

6. SANSONETTI, S.J. — To prevent corrosion at sea - think aluminium anodes! 1st Ann. Offshore Tech. Conf., Texas, May 1969, Paper No.OTC 1039.

7. SHRIER, L. — Corrosion, Vols. 1 & 2. Newnes Butterworth Ltd., London, 1975.

8. BILLINGHAM, J. — Introduction to corrosion in the marine environment. Short course notes: Inspection, Monitoring, Maintenance & Repair Offshore, Cranfield Inst. of Tech., 24 Nov-3 Dec 1982, p25.

9. STRUTT, J.E. — Introductory corrosion thoery. Short course notes: Materials in Offshore Engn., Cranfield Inst. of Tech., 1982.

10. LaQUE, F.L. — Corrosion Handbook (ed. by H. Uhlig), John Wiley, New York, 1948.

11. UHLIG, H.H. & WINSTON REVIE, R. — Corrosion and Corrosion Control. 3rd ed. John Wiley & Sons, 1985.

12. N.A.C.E. — Recommended practice - corrosion control on steel fixed offshore platforms associated with petroleum production. NACE Standard RP-01-76.

13. CHILTERN, J.P. — Principles of Metallic Corrosion. W. Heffer & Sons Ltd., 1968.

14. CHANDLER, K.A. — Marine and Offshore Corrosion. Butterworths, 1985.

15. ASKHEIM, N.E. — European Offshore Petroleum Conf., Paper 222, 1980.

16. HANSON, H.R. & HURST, D.C. — Corrosion control - Offshore platforms. Offshore Tech. Conf., Texas, Paper No. OTC 1042, 1969.

17. LEHMANN, J.A. — Cathodic protection of offshore structures 1st Ann. Offshore Tech. Conf., Texas, Paper No. OTC 1041, 1969.

18. HOCKENHULL, B.S. — Environmental effects. Course notes, Cranfield Inst. of Tech., 1983.

19. DET NORSK VERITAS — Technical note TNA 703, Review 1, 1981.

20. WYATT, B.S. — Offshore structures cathodic protection systems design procedures. Course notes, Cranfield Inst. of Tech., Oct 1982.

21. STRUTT, J.E., BILLINGHAM,J. & TURNER, W. — Techniques of the assessment and presentation of weld corrosion data. IRM 82, Edinburgh, Nov 1982.

22. BILLINGHAM, J. — Materials in the marine environment. Short course notes: Corrosion prevention offshore, Cranfield Inst. of Tech., Feb 1983.

23. COBURN, S.K. — Paper No. OTC 2139, 6th Offshore Tech. Conf., Texas, 1974.

24. MASUBUCHI, K. — Materials For Ocean Engineering. MIT Press, 1970.

25. SCHMITT, R.J. & PHELPS, E.H. — Corrosion performance of constructional steels in marine applications. Offshore Tech. Conf., Texas, Paper No. OTC 1047, 1969.

26. WEI, R.P. — On understanding environment enhanced fatigue crack growth - a fundamental approach. Fracture Mechanisms, Proc. ASTM-NSF Symposium, Kansas, 1978. ASTM STP 675, 1979.

27. RITCHIE, R.O. — Influence of microstructure on near threshold fatigue crack propagation in ultra high strength steel. Metal Science, Aug/Sept 1977.

28. KLESNIL, H. & LUKAS, P. — Influence of strength and stress history on growth and stabilisation of fracture cracks. Engn. Fract. Mech., Vol. 4, 1972, pp22-29.

29. LAIRD, C. & SMITH, G.C. — Crack propagation in high stress fatigue. Philosophical Magazine, Vol. 7, 1962, pp847-857.

30. TOMKINS, B. — Role of mechanics in corrosion fatigue. Metal Science, Vol. 13, 7, July 1979, pp387-395.

31. JOHNSON, R. & BRETHERTON, I. — Fatigue data from constant load amplitude tests on BS 4360:50D steel in air and seawater. UKOSRP Report 3/04, 1979.

32. ELBER, W. — Engn. Fract. Mech., Vol. 2, 1, July 1970, p37.

33. ELBER, W. — The significance of fatigue crack closure. Damage Tolerance in Aircraft Structures, ASTM STP 486, 1971, pp230-242.

34. LINDLEY, T.C. & RICHARDS, C.E. — The relevance of crack closure to fatigue crack propagation. CERL Lab. Report No. RD/L/N/198/73, 1973.

35. IRVING, P.E., ROBINSON, J.L. & BEEVERS, C.J. — Int. J. Fat., 11, 1975, pp1055-1056.

36. LINDLEY, T.C. & RICHARDS, C.E. — Fatigue crack growth at low stresses in steels. CERL Note No. RD/L/N/135/78, 1979.

37. STEWART, A.T. — Engn. Fract. Mech., Vol. 13, 1980.

38. WEI, R.P. & LANDES, J.D. — Correlation between sustained load and fatigue crack growth in high strength steels. Materials Research and Standards, ASTM 9, July 1969, p25.

39. AUSTEN, I.M. & WALKER, E.F. — Quantative understanding of the effects of mechanical and environmental variables on corrosion fatigue crack growth behaviour. Proc. Conf. on Influence of Environment on Fatigue, London, May 1977.

40. SCOTT, P.M. & SILVESTER, D.R.V. — UKOSRP, Report 3/02, 1977.

41. JASKE, C.E., PAYER, J.H. & BALINT, V.S. — Corrosion Fatigue of Metals in Marine Environments. Battelle Press.

42. ATKINSON, J.D. & LINDLEY, T.C. — The effect of frequency and temperature on environmentally assisted fatigue crack growth below K_{1scc} in steels. Inst. Mech. Eng./SEE Joint Conf. on Influence of Environment on Fatigue, London, 1977.

43. SIMMONS, G.W., PAO, P.S. & WEI, R.P. — Fracture mechanics and surface chemistry studies of subcritical crack growth in AISI 4340 steel. Met. Trans. A., Vol. 9A, 8, 1978, p1147.

44. ENDO, K., KOMAI, K. & IMASHIRO, N. — Environmental effects on initiation and propagation of fatigue cracks in high strength steel. Bulletin JSME, 20, 143, 1977, p513.

45. ISHIGURO, T. — Corrosion fatigue strength of steels for marine structures. Nippon Steel Technical Report 9, 1977, pp27-36.

46. MASUMOTO, I. & AKAISHI, T. — Study on corrosion fatigue of steel plates and welded joints in 3% NaCl aqueous solution - 2nd report: Effect of the grain size and cementite configuration of steels on the corrosion fatigue of steel. J. Japan Welding Soc., Vol.44, 9, 1975, p734.

47. AUSTEN, I.M. — Factors affecting corrosion fatigue crack growth in steels. Proc. of Offshore Steels Conf., Welding Inst., Nov 1978, p364.

48. BARSOM, J.M. — Corrosion fatigue crack propagation below K_{1scc}. Engn. Fract. Mech.,Vol. 3, July 1971, p15.

49. GALLAGHER, J.P. — Corrosion fatigue crack growth behaviour above and below K_{1scc}. Final Report NRL - 7064, AD708377, May 28, 1970.

50. SCOTT, P.M. & SILVESTER, D.R.V. — The influence of sea water on fatigue crack propagation rates in structural steel. UKOSRP Report 3/03, 1977.

51. POOK, L.P. & GREENAM, A.F. — Fatigue Testing and Design. Vol. 2, The Soc. of Environmental Engineers, London, 1976.

52. BARRETT, S.L. & TAYLOR, J.M.,Jr. — Cathodic protection experience in Cook inlet, Alaska. Offshore Technology Conf., Paper OTC 2700, 1976.

53. BOGAR, F.D. & CROOKER, T.W. — J. of Testing and Evaluation, Vol. 7, 3, 1979, p155.

54. VOSIKOVSKY, O. — J. of Testing and Evaluation, Vol. 6, 3, 1978, p175.

55. PETTIT, D.E., HOEPPNER, D.W. & HYLER, W.S. — Effects of environmental and complex load history on fatigue life. ASTM STP 462, 1970, p241.

56. HARTT, W.H. & HOOPER, W.C. — Corrosion, Vol. 7, 3, March 1980, p108.

57. IZDINSKY, D. — Welding Research Inst., 1971, p1.

58. TRUFYAKOV, V. — Br. Welding J., 1958, p491.

59. BOOTH, C.S. — The influence of simulated North Sea environmental conditions on the constant amplitude fatigue strength of welded joints. Proc. Offshore Tech. Conf., Vol. 1, 1979, p547.

60. VAESSEN, G.H.G. & DE BACK, J. — Fatigue behaviour of welded steel joints. Proc. Offshore Tech. Conf., Vol. 1, 1979, p555.

61. FORD, R.P. — Current understanding of the mechanisms of stress corrosion and corrosion fatigue. ASTM STP 821, 1984, p32.

62. BROWN, B.F. — Metallurgical Reviews, 1968, p171.

63. GALLAGHER, J.P. & WEI, R.P. — Corrosion fatigue crack propagation behaviour in steels. Int. Conf. on Corrosion Fatigue, Connecticut, 1971. Published NACE 2, Houston, 1972.

64. McMAHON, C. — J. of Engn. Mats. and Tech., 1973, p133.

65. JONES, C.H. — Symposium on Mats. for Underwater Tech., A.M.L., Paper 3, Poole, 1973.

66. HART, P.H.M. — Yield strength from hardness data. Welding Inst. Research Bulletin, June 1975, p176.

67. HOVLAND, I. — Stress corrosion behaviour of high strength steels in sea water under influence of cathodic protection/overprotection. Metallic Corrosion. Proc. 8th Int. Congress on Metallic Corrosion, Vol. 2, 1981, pp1321-1326.

68. ZAPFFE, C. & SIMS, C. — Trans. AIME, 145, 1941, p225.

69. DE KAZINSKY, F.J. — J. of Iron and Steel Inst., 177, 1954, p85.

70. GARAFOLO, F., CHOW, Y. & AMBEGAOKAR, R. — Acta Metallurgica, 8, 1960, p504.

71. BILBY, B.A. & HEWITT, J. — Acta Metallurgica, 10, 1962, p587.

72. TETELMAN, A.S. & ROBERTSON, W.D. — Trans. AIME, 224, 1962, p775.

73. TETELMAN, A.S. & ROBERTSON, W.D. — Acta Metallurgica, 11, 1963, p415.

74. TETELMAN, A.S. & McEVILY, A.J. — Fracture of Structural Materials. Wiley, New York, 1967.

75. PETCH, N.J. & STAPLES, J. — Nature, 169, 1952, p842.

76. BASTIEN, P. — Physical Metallurgy of Stress Corrosion Fracture. Interscience, New York, 1967.

77. TROIANO, A. — Trans. ASM, 52, 1960, p54.

78. ORIANI, R.A. & JOSEPHIC, P.H. — Acta Metallurgica, 1974, p1065.

79. STEIGERWALD, E.A., SCHALLER, F.W. & TROIANO, A.R. — Trans. Met. Soc. AIME, 218, 1960, p832.

80. GERBERICH, W.W. — Hydrogen in Metals. ASM, 1974, p115.

81. GERBERICH, W.W. & CHEN, Y.T. — Met. Trans., 6A, 1975, p271.

82. RAJ, R. & VARADAN, V.K. — The kinetics of hydrogen assisted crack growth. Mechanisms of Environment Sensitive Cracking of Materials, Met. Soc., London, 1977, p426.

83. McCRIGHT, R.D. — Effects of environmental species and metallurgical structure on the hydrogen entry into steel. Mechanisms of Environment Sensitive Cracking of Materials, Met. Soc., London, 1977, p306.

84. HUMBLE, R.A. — Corrosion, Vol. 4, 1948, p358.

85. LaQUE, F.L. — Corrosion, Vol. 6, 1950, p161.

86. DOREMUS, G.L. & DAVIS, J.G. — Materials Protection, Vol. 6, 1, 1967, p30.

87. COMPTON, K.G. — Cathodic protection of structures in sea water. Paper No. 13, Corrosion /75, Toronto, April 1975.

88. LaQUE, F.L. — Marine Corrosion: Causes and Prevention. J. Wiley and Sons, 1975.

89. ENDO, K., KOMAI, K. & SUZUKI, Y. — Influences of stress cycle frequency on propagation of corrosion fatigue cracks. ISME, Vol. 18, 115, Jan. 1975.

90. HUDSON, J.C. — The Corrosion of Iron and Steel. Van Nostrand Co. Inc., New York, 1940.

91. HARTT, W.H., CULBERSON, C.H. & SMITH, S.W. — Calcareous deposits on metal surfaces in sea water - a critical review. Corrosion, Vol. 40, 11, 1984, pp609-618.

92. WOLFSON, S.L. & HARTT, W.H. — Corrosion, Vol. 37, 2, 1981, p70.

93. GUILLEN, M.A. & FELIN, S. — Revista de Metallurgia, Vol. 2, 1966, p519.

94. SCOTT, P.M., THORPE, T.W. & SILVESTER, D.R.V. — Fundamental aspects of corrosion fatigue crack propagation in medium strength steels. Int. Conf. on Steel in Marine Structures, Paris, Oct. 1981.

95. WATSON, D.W. — Corrosion Fatigue Cracking in a 13% Cr - Stainless Steel in 3% Aqueous NaCl. M.Sc. Thesis, Cranfield Inst. of Tech., 1974.

96. PARKINS, R.N. — Some electrochemical aspects of the mechanisms of corrosion fatigue. Metal Science, Vol. 13, July 1979, pp381-386.

97. SHEPHERD, T. — Development of a Testing Procedure in Order to Investigate the Corrosion Fatigue Behaviour of a Structural Steel in a Marine Environment. M.Sc. Thesis, Cranfield Inst. of Tech., 1977.

98. THOMPSON, J.W.C. — The Effect of Cathodic Protection on Corrosion Fatigue Crack Propagation Behaviour of a Structural Steel in a Marine Environment. M.Sc. Thesis, Cranfield Inst. of Tech., 1980.

99. MILLAR, P.G. — Fatigue Crack Propagation Behaviour of a High Strength Low Alloy Steel in Sea Water. M.Sc. Thesis, Cranfield Inst. of Tech., 1983.

100. APPS, R.L. — Course notes. Cranfield Inst. of Tech., April 1983.

101. ANON. N-A-XTRA/X-A-R Quenched and Tempered High Strength and Wear Resistant Steels. July 1980, Thyssen, A.G.

102. ANON. Hochfeste Wasservergütete Sonderbaustähle N-A-XTRA und Ti. Aug. 1977, Thyssen, A.G.

103. DEGENKOLBE, J. & MÜSGEN, B. Hestellung, Verarbeitung und Anwendung Wasservergüteter Baustähle, in, Deutsche Forschungsgesellschaft für Blechverarbeitung und Oberflächenbehandlung. NR. 7, 1971, pp 136-145.

104. OERTLING. Manufacturers welding consumables specifications, 1977.

105. BRITISH STANDARD. BS 5762: 1979. Crack opening displacement (COD) testing.

106. B.D.H. CHEMICALS LTD. 'Sea Water Corrosion Test Mixture' Manufacturers chemical specification.

107. ARONSON, G.H. & RITCHIE, R.O. J. of Testing and Evaluation, Vol. 7, 4, 1979, p208.

108. GANGLOFF, R.P. Fatigue of Engineering Materials and Structures, Vol. 4, 1, 1981.

109. MÜSGEN, I.B. Private communication. Thyssen Stahl Akliengesellschaft, June 1983.

110. ALLMAND, T.R. Microscopic identification of inclusions in steel. British Iron and Steel Research Assoc., London

111. CALLISTER, D. Private communication. Cranfield Inst. of Tech., 1985.

112. LAIRD, C. The influence of metallurgical structure on the mechanisms of fatigue crack propagation. Fatigue Crack Propagation, ASTM STP 415, 1967, pp 131-168.

113. ULANOVSKY, I. J. of Applied Chemistry (USSR), 1955, p1143.

114. BERNER, R.A. Am. J. of Science, Vol. 276, June 1976, p713.

115. PHILIPPONNEAU, G., DAGBERT, J. & GALLAND, E. — Contribution to the study of magnesium/calcium deposits occuring during steel protection in sea water. Proc. 8th Conf. on Metallic Corrosion, Vol. 2, Germany, 6-11 Sept. 1981, p1327.

116. GRIGOREV, V.P. & POPOV, S.Y. — J. of Applied Chemistry (USSR), Vol. 35, 1962, p155.

117. GRIGOREV, V.P. — J. of Applied Chemistry (USSR), Vol. 34, 1961, p169.

118. HUDGINS, C.M., CASAD, B.M., SCHROEDER, R.L. & PATTON, C.C. — Effect of cathodic protection on the corrosion fatigue behaviour of carbon steel in synthetic sea water. J. of Petrol. Tech., Vol. 23, March 1971, p283.

119. GOUGH, H.J. & SOPWITH, D.G. — J. of Inst. Metals, Vol. 56, 1935, pp55-89.

120. THOMPSON, J. — Phenomenological investigation of the influence of cathodic protection on corrosion fatigue crack propagation behaviour in a BS 4360:50D type structural steel and associated weldment microstructures in a marine environment. PhD Thesis, Cranfield Inst. of Tech., June 1984.

121. JAMES, L.A. — J. of Testing and Evaluation, Vol. 1, 1, Jan. 1973, p52.

122. JAMES, L.A. — Welding J. Research Supplement, Vol. 52, 4, April 1973, p173.

123. TU, L.K.L. & SETH, B.B. — J. of Testing and Evaluation, Vol. 6, 1, Jan. 1978, p66.

124. TOMKINS, B. — Micromechanisms of fatigue crack growth at high stress. Metal Science, Aug.- Sept. 1980, pp408-417.

125. TURNBULL, A. — A theoretical analysis of the influence of crack dimensions and geometry on mass transport in corrosion fatigue cracks. N.P.L Report, DMA(A)69, July 1983.

126. HANCOCK, G.G. & JOHNSON, H.H. — Trans. AIME, 236, 1966, p513.

127. BARTH, C.F. & TROIANO, A.R. — Cathodic protection and hydrogen in stress corrosion cracking. Corrosion, Vol. 28, 7, July 1972, p259.

128. SMIALOWSKI, M. — Comptes Rendues du 2eme Symposium European Sur Les Inhibitions de Corrosion, Annal. Uni. Ferrara, N.S. Sec. v. Suppl. No. 4, 1966, pp203-222.

129. VETTER, K.J. — Electrochemical Kinetics. Academic Press, N.Y., 1967.

130. CONGLETON, J. & CRAIG, I.H. — Corrosion Processes. Ed. R.N. Parkins, Applied Science Publications Ltd., 1982, p209.

131. BATHIAS, C. & BAILON, J.P. — La fatigue des materiaux et des structures. Collection Université de Compiègne, p218.

132. TANAKA, K. — A correlation of ΔK_{th} value with the exponent, m, in the equation of fatigue crack growth for various steels. Int. J. of Fracture, 15, 1979, pp57-68.

133. MADDOX, S.J. — Welding Inst. Research Report E/48/72, 1972.

134. VERMILYEA, D.A. & TEDMAN, C.S. — J. Electrochem. Soc., Vol. 117, 1970, pp 437-439.

135. ATEYA, B.G. & PICKERING, H.W. — J. Electrochem. Soc., Vol. 122, 1975, pp 1018-1026.

136. CLARK, W.G.,Jr, & HUDAK, S.J.,Jr. — Variability in fatigue crack growth rate testing. J. Test. Eval., Vol. 3, 1975, pp 454-476.

137. DRAPER, H.R. & SMITH, H. — Applied Regression Analysis. Wiley, New York, 1966.

138. SCHEID, F. — Computers and Programming. Schaum's Outline Series, 1976.

139. ALCOCK, D. — Illustrating Basic. Cambridge Univ. Press, 1977.

140. CLARK, W.G.,Jr. & HUDAK, S.J.,Jr. — The analysis of fatigue crack growth rate data. Conf. on Appln. of Fract. Mech. to Design, Proc. 22nd Sagamore Army Mats. Res.

141. BUREAU VERITAS. Fatigue, crack propagation computer program. Computer Program Library, Bureau Veritas Marine Branch.

142. CALLISTER, D.R., BILLINGHAM, J. & HOCKENHULL, B.S. Improved fatigue performance in H.S.L.A. quenched and tempered steel. Offshore and Arctic Frontiers, 1986 O.M.A.E. Symposium.

143. HIRTH, J.P. Metallurgical Transactions, Vol. 11A, 6, 1980, pp 861-890.

144. ATKINSON, J.D. & LINDLEY, T.C. Proc. Conf. Influence of Environment on Fatigue, Inst. Mech. Eng., London, 1977, p65.

145. HARTT, W.H., TENNANT, J.S. & HOOPER, W.C. Solution chemistry modification within corrosion fatigue cracks. Corrosion Fatigue Tech., ASTM STP 642, 1978, pp 5-18.

146. DEVANATHAN, M.V. & STACHURSKI, Z. The adsorption and diffusion of electrolytic hydrogen in Palladium. Proc. Royal Soc., Vol. A 270, 1962, pp 90-102.

147. FAST, J.D. Gases in Metals. Unwin Bros. Ltd., 1976.

148. LINDLEY, T.C. & RICHARDS, C.E. Mats. Sci. Eng., Vol. 14, 1974, p 281.

149. McEVILY, A.J. Met. Sci., Vol. 11, 1977, p 274.

150. TURNBULL, A. Review of the electrochemical conditions in cracks with particular reference to corrosion fatigue of structural steels in sea water. Reviews in Coatings and Corrosion, Vol. 5, No. 1-4, 1982.

151. AUSTEN, I.M. & WALKER, E.F. The influence of environmental aggression on the corrosion fatigue behaviour of steels. Proc. Int. Conf. on Mechanisms of Environment Sensitive Cracking of Materials, Univ. of Surrey, April 1977, pp 334-347.

152. TURNBULL, A. Progress in the understanding of of the electrochemistry in cracks. Proc. Conf. on Localised Crack Chemistry and Mechanics in Environment Assisted Fracture, Philadelphia USA, Oct. 1983.

153. TURNBULL, A. & MAY, A.T. — Cathodic protection of crevices in BS 4360:50D steel in 3.5% NaCl in sea water. Mat. Perf., Vol. 22, 10, 1983, pp 34-38.

154. YOKOBORI, T., KAWADA, I. & HATA, H. — Proc. Inst. Strength and Fracture of Materials, Tohuku Univ., Sendai, Japan, Vol. 9, 35, 1973.

155. MORGAN, H.G. et al. — Proc. Int. Conf. on Steel in Marine Structures, CEC, Paris, 1981.

APPENDIX A

Electrochemical reactions of relevance to structural steels in chloride solution (Ref 150)

Anodic dissolution

$$Fe \rightarrow Fe^{2+} + 2e^-$$

$$3Fe + 4H_2O \rightarrow Fe_3O_4 + 8H^+ + 8e^-$$

Cathodic reduction

$$O_2 + 2H_2O + 4e^- \rightarrow 4OH^-$$

$$H^+ + e^- \rightarrow H$$

$$H_2O + e^- \rightarrow H + OH^-$$

$$Fe^{2+} + 2e^- \rightarrow Fe$$

Hydrolysis reactions

$$Fe^{2+} + H_2O = FeOH^+ + H^+$$

$$3Fe^{2+} + 4H_2O = Fe_3O_4 + 8H^+ + 2e^-$$

$$H_2O = H^+ + OH^-$$

Buffer reactions of sea water

$$H_2CO_3^* = H^+ + HCO_3^-$$

$$HCO_3^- = H^+ + CO_3^{2-}$$

where $[H_2CO_3^*] \equiv [H_2CO_3] + [CO_2(aq)]$

APPENDIX B

Least squares regression analysis program

```
 5 DIM N(100): DIM A(100)
10 POKE 23658,8
15 CLS : PRINT AT 3,2;"LEAST SQUARES CURVE FITTING"
 20 PRINT AT 5,7;"FOR FATIGUE DATA"
 25 PRINT AT 8,10; P MILLAR"
 30 PRINT AT 9,2;"_____________________________"
 35 PRINT AT 11,2;"ENTER YOUR SPECIMEN NUMBER"
 40 INPUT F$
 45 PRINT AT 13,8;"SPECIMEN  ";F$
 50 PRINT AT 16,0;"HOW MANY DATA POINTS HAVE YOU ?"
 55 INPUT V
 60 PRINT AT 18,12;"V = ";V
 65 PRINT AT 21,1;"PRESS ANY KEY THEN ENTER THE A AND N VALUES"
 70 PAUSE 0
 75 CLS
 80 PRINT  INK 2; FLASH 1;"   DO NOT ENTER 0 AS THE FIRST VALUE
 FOR EITHER N OR A      "
 85 INK 0: FLASH 0
 90 PRINT AT 2,6;"N","A": PRINT AT 2,6; OVER 1;"_","_"
 95 PRINT AT 2,0;"ROW": PRNT AT 2,0; OVER 1;"___"
100 PRINT
105 FOR I=1 TO V
110 INPUT N(I),A(I)
115 PRINT " ";I;" )   ";N(I),A(I)
120 NEXT I
125 PRINT
130 PRINT "IF YOU WISH TO ALTERANY VALUES PRESS Y"
135 INPUT H$: IF H$="Y" OR H$="y" OR H$="YES" OR H$="yes" THEN
 GO TO 145
140 GO TO 345
145 PRINT
150 PRINT "INPUT ROW "
155 PRINT
160 INPUT T: PRINT " ROW ";T
165 PRINT
170 IF T>V THEN  GO TO 150
175 IF T<1 THEN  GO TO 150
180 IF T-INT (T)<>0 THEN  GO TO 150
185 PRINT "IS IT AN N VALUE OR AN A VALUE ?"
190 PRINT
195 INPUT S$: PRINT "";S$;" VALUE"
200 IF S$<>"N" AND S$<>"n" AND S$<>"A" AND S$<>"a" THEN
 GO TO 185
205 IF S$="N" OR S$="n" THEN  GO TO 215
210 IF S$="A" OR S$="a" THEN  GO TO 280
215 PRINT
220 PRINT "ENTER NEW VALUE FOR ROW ";T;" COLUMN N"
```

```
225 PRINT
230 INPUT U: PRINT U
235 LET I=T: LET N(T)=U: LET N(I)=N(T)
240 CLS : PRINT AT 2,6;"N","A": PRINT AT 2,6; OVER 1;"_","_"
245 PRINT AT 2,0;"ROW": PRINT AT 2,0; OVER 1;"___"
250 PRINT
255 FOR I=1 TO V
260 PRINT " ";I;" )   ";N(I),A(I)
265 NEXT I
270 PRINT
275 GO TO 130
280 PRINT
285 PRINT "ENTER NEW VALUE FOR ROW ";T;" COLUMN A"
290 PRINT
295 INPUT U: PRINT U
300 LET I=T: LET A(T)=U: LET A(I)=A(T)
305 CLS : PRINT AT 2,6;"N","A": PRINT AT 2,6; OVER 1;"_","_"
310 PRINT AT 2,0;"ROW": PRINT AT 2,0; OVER 1;"___"
315 PRINT
320 FOR I=1 TO V
325 PRINT " ";I;" )   ";N(I),A(I)
330 NEXT I
335 PRINT
340 GO TO 130
345 DIM U(V): DIM H(V): LET E$="ERROR RETRY"
350 LET LN=0
355 INPUT "SELECT N AXIS UPPER LIMIT = ";HN
360 IF HN<=LN THEN  PRINT E$: GO TO 355
365 LET LA=0
370 INPUT "SELECT A AXIS UPPER LIMIT = ";HA
375 IF HA<=LA THEN  PRINT E$: GO TO 370
380 CLS : PLOT 31,16: DRAW 221,0
385 PLOT 31,16: DRAW 0,152
390 PRINT AT 21,8;"SPECIMEN  ";F$
395 PRINT AT 19,31; OVER 1;"¦";AT 0,4; OVER 1;"_"
400 PRINT AT 20,4;LN: PRINT AT 20,26;HN
405 PRINT AT 19,2;LA: PRINT AT 0,1;HA
410 PRINT AT 20,16;"N";AT 10,2;"A"
415 FOR I=1 TO V: LET G=221/HN
420 LET H(I)=N(I)*G: NEXT I
425 FOR I=1 TO V: LET W=152/HA
430 LET U(I)=A(I)*W: NEXT I
435 FOR I=1 TO V
440 PLOT (H(I)+24),((I)+14)
445 NEXT I
450 PRINT #0;"       FOR A COPY PRESS P"
455 IF INKEY$="" THEN  GO TO 455
460 IF INKEY$="P" OR INKEY$="p" THEN  COPY
465 CLS : PRINT AT 8,0;"INPUT Z=0 FOR A POWER FUNCTION"
470 PRINT AT 9,6;"Z=1 FOR AN EXPONENTIAL"
475 PRINT AT 12,1;"FOR A POLYNOMIAL, LET Z EQUAL"
480 PRINT AT 13,2;"THE NUMBER OF TERMS IN THE"
485 PRINT AT 14,9;"POLYNOMIAL"
490 INPUT Z
495 PRINT AT 17,11;"Z = ";Z
500 PAUSE 100
505 CLS
```

```
510 PRINT  FLASH 1'''  COMPUTING RESULTS          "
515 FLASH 0
520 IF Z>=2 THEN  GO TO 560
525 FOR I=1 TO V
530 LET A(I)=LN A(I)
535 NEXT I
540 IF Z=1 THEN  GO TO 560
545 FOR I=1 TO V
550 LET N(I)=LN N(I)
555 NEXT I
560 IF Z<=1 THEN  GO TO 580
565 FOR I=1 TO V
570 LET N(I)=N(I)/1000
575 NEXT I
580 LET N1=Z
585 IF N1>=2 THEN  GO TO 595
590 LET N1=2
595 DIM C(N1,N1)
600 LET C(N1,N1)=0
605 DIM D(N1)
610 LET D(N1)=0
615 FOR I=1 TO N1
620 FOR J=1 TO N1
625 IF I+J>2 THEN  GO TO 640
630 LET C(I,J)=V
635 GO TO 655
640 FOR K=1 TO V
645 LET C(I,J)=C(I,J)+N(K)^(I+J-2)
650 NEXT K
655 NEXT J
660 FOR K=1 TO V
665 IF I>1 THEN  GO TO 680
670 LET D(I)=D(I)+A(K)
675 GO TO 685
680 LET D(I)=D(I)+A(K)*N(K)^(I-1)
685 NEXT K
690 NEXT I
695 PRINT
700 FOR I=1 TO N1
705 NEXT I
710 DIM B(N1,N1)
715 LET B(N1,N1)=0
720 FOR R=1 TO N1
725 FOR C=1 TO N1
730 LET B(R,C)=1-ABS (SGN (R-C))
735 NEXT C: NEXT R
740 FOR R=1 TO N1-1
745 IF ABS (C(R,R))>0.00001 THEN  GO TO 760
750 CLS : PRINT AT 1,0;"CANT COPE WITH    ";C(R,R)
755 STOP
760 FOR C=R+1 TO N1
765 LET X=0
770 LET X=C(C,R)/C(R,R)
775 FOR K=1 TO N1
780 LET C(C,K)=C(C,K)-X*C(R,K)
785 LET B(C,K)=B(C,K)-X*B(R,K)
```

```
790 NEXT K: NEXT C: NEXT R
795 FOR R=N1 TO 1 STEP -1
800 FOR K=1 TO N1
805 IF R=N1 THEN  GO TO 825
810 FOR C=R+1 TO N1
815 LET B(R,K)=B(R,K)-C(R,C)*B(C,K)
820 NEXT C
825 LET B(R,K)=B(R,K)/C(R,R)
830 NEXT K: NEXT R
835 FOR I=1 TO N1
840 DIM Q(N1)
845 LET Q(I)=0
850 NEXT I
855 FOR J=1 TO N1
860 FOR K=1 TO N1
865 LET Q(J)=Q(J)+B(J,K)*D(K)
870 NEXT K
875 NEXT J
880 BEEP .1,.5
885 IF Z>1 THEN  GO TO 1075
890 LET Q(1)=EXP (Q(1))
895 IF Z=1 THEN  GO TO 995
900 CLS : PRINT " POWER FUNCTION"
905 PRINT "****************"
910 PRINT
915 PRINT "        A = Q(1) * N ^ Q(2)"
920 PRINT
925 PRINT "WHERE:"
930 PRINT
935 PRINT "Q(1) = ";Q(1)
940 PRINT
945 PRINT "Q(2) = ";Q(2)
950 FOR I=1 TO V
955 LET A(I)=EXP A(I)
960 NEXT I
965 FOR I=1 TO V
970 LET N(I)=EXP N(I)
975 NEXT I
980 PRINT #0;"FOR A COPY PRESS P": PAUSE 0
985 IF INKEY$="P" OR INKEY$="p" THEN  GO SUB 1695
990 GO TO 1185
995 CLS : PRINT "       EXPONENTIAL FUNCTION"
1000 PRINT "     **********************"
1005 PRINT
1010 PRINT "    A = Q(1) * EXP( Q(2) * N)"
1015 PRINT
1020 PRINT "WHERE:"
1025 PRINT
1030 PRINT "Q(1) = ";Q(1)
1035 PRINT
1040 PRINT "Q(2) = ";Q(2)
1045 FOR I=1 TO V
1050 LET A(I)=EXP A(I)
1055 NEXT I
1060 PRINT #0;"FOR A COPY PRESS P": PAUSE 0
1065 IF INKEY$="P" OR INKEY$="p" THEN  GO SUB 1725
```

```
1070 GO TO 1185
1075 CLS : PRINT "       POLYNOMIAL FUNCTION"
1080 PRINT "     **********************"
1085 PRINT
1090 PRINT "        A = Q(1) + Q(2) N"
1095 PRINT
1100 PRINT "WHERE:"
1105 PRINT ''"Q(1) = ";Q(1)
1110 PRINT ''"Q(2) = ";Q(2)
1115 IF Z=2 THEN  GO TO 1155
1120 FOR R=3 TO Z
1125 PRINT ''"            + Q(";R;") * N ^ ";R-1
1130 PRINT
1135 PRINT "WHERE:"
1140 PRINT
1145 PRINT "Q(";R;") = ";Q(R)
1150 NEXT R
1155 PRIN #0;"FOR A COPY PRESS P": PAUSE 0
1160 IF INKEY$="P" OR INKEY$="p" THEN  GO SUB 1845
1185 CLS : LET S=0
1190 LET A1=0
1195 PRINT ''TAB (2);"N";TAB 12;"A";TAB 22;"A CALC"
1200 PRINT "-----------------------------"
1205 FOR I=1 TO V
1210 IF Z>=2 THEN  GO TO 1240
1215 IF Z=1 THEN  GO TO 1230
1220 LET A1=Q(1)*N(I)^Q(2)
1225 GO TO 1260
1230 LET A1=Q(1)*EXP (Q(2)*N(I))
1235 GO TO 1260
1240 LET A1=Q(1)
1245 FOR R=2 TO Z
1250 LET A1=A1+Q(R)*N(I)^(R-1)
1255 NEXT R
1260 LET S=S+ABS (A(I)-A1)^2
1265 IF Z<=1 THEN  GO TO 1275
1270 LET N(I)=N(I)*1000
1275 PRINT TAB 0;N(I);TAB 10;A(I);TA 20;A1
1280 NEXT I
1285 PRINT ''"   SUM OF SQUARE ERRORS :-"
1290 PRINT "        ";S
1295 PRINT #0;"FOR A COPY PRESS P": PAUSE 0
1300 IF INKEY$="P" OR INKEY$="p" THEN  GO SUB 1755
1305 CLS : PRINT AT 4,4; INVERSE 1;"DIFFERENTIAL OF CURVE":
  INVERSE 0
1310 DIM G(V)
1315 PRINT ''TAB 2;"N";TAB 12;"A";TAB 22;"dA/dN"
1320 PRINT "--------------------------------"
1325 IF Z>=2 THEN  GO TO 1400
1330 IF Z=1 THEN  GO TO 1370
1335 FOR J=1 TO V
1340 LET B=Q(2)-1
1345 LET G(J)=Q(1)*Q(2)*(N(J)^B)
1350 LET G(J)=G(J)/1000
1355 PRINT TAB 0;N(J);TAB 10;A(J);TAB 19;G(J)
1360 NEXT J
```

```
1365 GO TO 1450
1370 FOR J=1 TO V
1375 LET G(J)=EXP (Q(2)*N(J))+(Q(1)*Q(2)*EXP (Q(2)*N(J)))
1380 LET G(J)=G(J)/1000000
1385 PRINT TAB 0;N(J);TAB 10;A(J);TAB 19;G(J)
1390 NEXT J
1395 GO TO 1450
1400 FOR J=1 TO V
1405 LET N(J)=N(J)/1000
1410 FOR R=3 TO Z
1415 LET G(J)=G(J)+Q(R)*(R-1)*N(J)^(R-2)
1420 NEXT R
1425 LET G(J)=G(J)+Q(2)
1430 LET G(J)=G(J)/1000000
1435 LET N(J)=N(J)*1000
1440 PRINT TAB 0;N(J);TAB 10;A(J);TAB 19;G(J)
1445 NEXT J
1450 PRINT #0;"    PRESS ENTER TO CONTINUE": PAUSE 0
1480 CLS : PRINT AT 2,6; INVERSE 1;"DELTA K CALCULATION":
  INVERSE 0
1485 PRINT AT 4,2;"ENTER YOUR VALUE OF DELTA P"
1490 INPUT DP
1495 PRINT ''"          DELTA P = ";DP
1500 PRINT ''"ENTER SPECIMEN THICKNESS  B(mm)"
1505 INPUT TH
1510 PRINT ''"         THICKNESS = ";TH;" mm"
1515 PRINT ''" ENTER SPECIMEN WIDTH  W(mm)"
1520 INPUT WD
1525 PRINT ''"           WIDTH = ";WD ;" mm"
1530 PRINT ''" ENTER SPECIMEN LENGTH  L(mm)"
1535 INPUT LN
1540 PRINT ''"          LENGTH = ";LN;" mm"
1545 DIM K(V): DIM M(V)
1550 PAUSE 100
1555 CLS : PRINT  FLASH 1''"          COMPUTING RESULTS          "
1560 FLASH 0
1565 LET WD=WD/1000: LET TH=TH/1000: LET LN=LN/1000
1570 LET DP=DP/1000
1575 FOR I=1 TO V
1576 LET A(I)=A(I)/1000
1580 LET K(I)=(1.93*(A(I)/WD)^0.5)-(3.07*(A(I)/WD)^1.5)+
 (14.53*(A(I)/WD)^2.5)-(25.11*(A(I)/WD)^3.5)+(25.8*(A(I)/WD)^4.5)
1585 LET M(I)=(6*DP*K(I))/(TH*WD^0.5)
1590 NEXT I
1595 CLS
1600 PRINT TAB 3;"DELTA K";TAB 18;"dA/dN"
1605 PRINT "--------------------------------"
1610 FOR I=1 TO V
1615 PRINT TAB 2;M(I);TAB 16;G(I)
1617 LET A(I)=A(I)*1000
1620 NEXT I
1625 PRINT #0;"FOR A COPY PRESS P"
1630 PAUSE 0
1635 IF INKEY$="P" OR INKEY$="p" THEN  GO SUB 1665
1640 CLS
1645 PRINT ''"   IF YOU WISH TO REPEAT THE"
```

```
1646 PRINT "  ANALYSIS USING A DIFFERENT"
1647 PRINT "   POWER VALUE THEN PRESS Y"
1650 PAUSE 0
1655 IF INKEY$="Y" OR INKEY$="y" THEN  GO TO 465
1660 STOP
1665 LPRINT ''TAB 3;"DELTA K";TAB 18;"dA/dN"
1670 LPRINT "------------------------------"
1675 FOR I=1 TO V
1680 LPRINT TAB 2;M(I);TAB 16;G(I)
1685 NEXT I
1690 RETURN
1695 LPRINT ''"          POWER FUNCTION"
1700 LPRINT ''"       A = Q(1) * N ^ Q(2)"
1705 LPRINT "WHERE"
1710 LPRINT "Q(1) = ";Q(1)
1715 LPRINT "Q(2) = ";Q(2)
1720 RETURN
1725 LPRINT ''"        EXPONENTIAL FUNCTION"
1730 LPRINT ''"     A = Q(1) * EXP (Q(2) * N)"
1735 LPRINT "WHERE"
1740 LPRINT "Q(1) = ";Q(1)
1745 LPRINT "Q(2) = ";Q(2)
1750 RETURN
1755 LPRINT ''TAB (2);"N";TAB 12;"A";TAB 22;"A CALC"
1760 LPRINT "------------------------------"
1765 FOR I=1 TO V
1770 IF Z>=2 THEN  GO TO 1800
1775 IF Z=1 THEN  GO TO 1790
1780 LET A1=Q(1)*N(I)^Q(2)
1785 GO TO 1820
1790 LET A1=Q(1)*EXP (Q(2)*N(I))
1795 GO TO 1820
1800 LET A1=Q(1)
1805 FOR R=2 TO Z
1807 LET N(I)=N(I)/1000
1810 LET A1=A1+Q(R)*N(I)^(R-1)
1813 LET N(I)=N(I)*1000
1815 NEXT R
1820 LPRINT TAB 0;N(I);TAB 10;A(I);TAB 20;A1
1825 NEXT I
1830 LPRINT ''"   SUM OF SQUARE ERRORS :-"
1835 LPRINT "        ";S
1840 RETURN
1845 LPRINT ''"        POLYNOMIAL FUNCTION"
1850 LPRINT ''"      A = Q(1) + Q(2) * N"
1855 LPRINT "WHERE"
1860 LPRINT "Q(1) = ";Q(1)
1865 LPRINT "Q(2) = ";Q(2)
1870 IF Z=2 THEN  RETURN
1875 FOR R=3 TO Z
1880 LPRINT "            + Q(";R;") * N ^ ";R-1
1885 LPRINT "WHERE"
1890 LPRINT "Q(";R;") = ";Q(R)
1895 NEXT R
1900 RETURN
1905 SAVE "FATIGUE" LINE 5
```